UNIVERSIDADE DE BRASÍLIA

INSTITUTO DE GEOCIÊNCIAS

GEOLOGIA, PETROLOGIA E POTENCIAL PARA MINERALIZAÇÕES MAGMÁTICAS DOS CORPOS MÁFICO-ULTRAMÁFICOS DA REGIÃO DE CANAÃ DOS CARAJÁS, PROVÍNCIA MINERAL DE CARAJÁS.

Lincoln Siepierski

Tese de Doutorado nº 129

Brasília-DF

2016

UNIVERSIDADE DE BRASÍLIA

INSTITUTO DE GEOCIÊNCIAS

GEOLOGIA, PETROLOGIA E POTENCIAL PARA MINERALIZAÇÕES MAGMÁTICAS DOS CORPOS MÁFICO-ULTRAMÁFICOS DA REGIÃO DE CANAÃ DOS CARAJÁS, PROVÍNCIA MINERAL DE CARAJÁS.

TESE DE DOUTORADO

Autor: Lincoln Siepierski

Orientador: Prof. Dr. Cesar Fonseca Ferreira Filho

Brasília-DF

2016

UNIVERSIDADE DE BRASÍLIA

INSTITUTO DE GEOCIÊNCIAS

Geologia, petrologia e potencial para mineralizações magmáticas dos corpos máfico-ultramáficos da região de Canaã dos Carajás, Província Mineral de Carajás.

Autor: Lincoln Siepierski

Examinadores:

Prof. Dr. Cesar Fonseca Ferreira Filho (Orientador)

Prof. Dr. Farid Chemale Júnior

Profª. Drª. Catarina Labouré B. Toledo

Prof. Dr. Raimundo Netuno Nobre Villas - UFPA

Prof. Dr. José Haroldo Silva Sá - UFBA

Brasília, junho de 2016

AGRADECIMENTOS

"Tudo que possas ou sonhas fazer, comece.

A audácia contém gênio, poder e magia."

Johann Wolfgang Goethe

"A mente que se abre a uma nova idéia jamais

voltará ao seu tamanho original."

Albert Einstein

ÍNDICE

ÍNDICE DE FIGURAS

ÍNDICE DE TABELAS

RESUMO

A região de Canaã dos Carajás está situada na borda sul da serra dos Carajás, dentro do Subdomínio de Transição (ST), e faz parte da Província Mineral de Carajás (PMC) onde ocorrem importantes depósitos de classe mundial de Fe, Cu, Ni e Mn. Esta região do ST apresenta numerosas ocorrências de rochas máfico-ultramáficas (MUM) e, dentro desta diversidade de associações MUM, três ocorrências foram selecionadas como foco do presente estudo em função do ambiente geológico, idades e aspectos petrológicos: (**1**) Complexo Acamadado do Vermelho; (**2**) Complexo Acamadado Touro; e (**3**) área Selva, que representa uma ocorrência de rochas vulcânicas ultramáficas portadoras de textura *spinifex*.

(**1**). O Complexo Acamadado do Vermelho, que contém importantes mineralizações de Ni laterítico, está localizado a cerca de 2 km NW da localidade de Canaã dos Carajás. Corresponde a uma intrusão MUM bem preservada de dimensões médias sem evidências de deformação ou metamorfismo regional, considerada como pertencente a um conjunto de intrusões acamadadas regionais interpretadas como parte de um grande evento magmático Neoarqueano (ca. 2,76 Ga). Apresenta cerca de 9,5 km de comprimento por 1,5 km de largura média, com alinhamento segundo a direção NE-SW, e ocorre encaixado em gnaisses do Complexo Xingú (>2,85 Ga) e granitóides indiferenciados. A arquitetura da intrusão do Vermelho abrange um conjunto de rochas ultramáficas acamadadas horizontalizadas denominada Zona Superior (UZ), que recobre uma sequência complexa, porém, no geral sub-horizontalizada, de rochas máfico-ultramáficas definida como Zona Inferior (LZ). O conteúdo de MgO varia de 40,12 % em peso (base anidra) em harzburgitos, até 2,22 % em peso nas rochas gabroicas mais fracionadas. Dados de química mineral comprovam olivinas com conteúdo de forsterita entre $Fo_{85,6}$ e $Fo_{90,5}$ que indicam um magma parental mais primitivo (ou mais rico em MgO). A sequência basal da LZ consiste em rochas ultramáficas interacamadadas, possivelmente formadas por múltiplos influxos de magma na câmara, não evidenciando o desenvolvimento de um claro fracionamento reverso da sequência de fases cumulus ou trends de fracionamento das rochas localizadas junto ao contato inferior com as encaixantes. A morfologia atual da intrusão, com destaque para os *plateaus* V1 e V2, foi principalmente esculpida a partir do Meso-Cenozoico, com a exumação da porção inferior da intrusão. Os dados obtidos no presente trabalho indicam que dois principais eventos de injeção de magma foram responsáveis pela evolução do Complexo Acamadado do Vermelho, o primeiro associado à formação da LZ e um segundo evento

posterior relacionado à formação da UZ. Esta evolução magmática, marcada por sucessivas injeções de magma, indica um sistema dinâmico e favorável para a geração de depósitos magmáticos.

As análises U-Pb em zircões, disponíveis para intrusões acamadadas MUM da PMC, indicam idades neoarqueanas (ca. 2680-2780 Ma) e, portanto, cronocorrelatas com as idades reportadas para o extensivo vulcanismo basáltico da região de Carajás (e.g. 2759±2 Ma; 2760±11 Ma). Estes resultados suportam a interpretação que as intrusões acamadadas e o vulcanismo da PMC resultam de um importante evento magmático Neoarqueano (ca. 2,76 Ga). O ambiente tectônico desse evento magmático é controverso, porém, evidências litogeoquímicas e isotópicas de contaminação crustal significativa em rochas basálticas têm sido utilizadas para corroborar o modelo de *rifting* continental. O Complexo Acamadado do Vermelho, caracterizado pela presença de rochas com texturas primitivas, estratigrafia e estrutura magmática sub-horizontalizada intrusiva em rochas granito-gnáissicas de alto grau metamórfico, bem como os aspectos composicionais que indicam contaminação de rochas crustais mais antigas, é também consistente com uma origem associada a *rifting* continental.

(**2**). O Complexo Acamadado Touro está localizado aproximadamente a 47 km WNW da localidade de Canaã dos Carajás. Corresponde a uma intrusão acamadada MUM sub-horizontalizada de pequenas dimensões com cerca de 4,8 km de comprimento por 1,2 km de largura média, alinhada segundo a direção ENE-WSW. Apresenta texturas primárias bem presenvadas e sem evidências de deformação, e ocorre encaixado em granitóides sin-orogênicos indiferenciados (ca. 2,73-2,76 Ga). Possui arcabouço estratigráfico e litogeoquímico característico de um único pulso magmático, sendo constituído por uma Zona Ultramáfica inferior (UZ) e uma Zona Máfica superior (MZ). O Complexo Touro apresenta conteúdo de MgO variando de 10 a 24,4 % em peso. Outra característica litogeoquímica marcante deste complexo é o baixo conteúdo de sílica nas rochas analisadas, o que aponta para um magma parental do tipo subsaturado em sílica, contribuindo para ausência de ortopiroxênio como fase cumulus nas rochas desta intrusão. Dados de química mineral indicam um magma moderadamente primitivo com olivinas apresentando conteúdo de forsterita variando de $Fo_{76,3}$ até $Fo_{67,9}$. O Complexo Touro apresenta estrutura magmática e evolução petrológica semelhantes aos complexos acamadados intrusivos em crosta continental estável. Estas características são compatíveis com o modelo tectônico de rift intraplaca proposto por vários autores para a PMC.

(**3**). As rochas komatiiticas portadoras de textura *spinifex* do *Greenstone Belt* Selva são os primeiros exemplos inequívocos da presença de komatiitos dentro do ST da PMC. Os afloramento destas rochas estão localizados a cerca de 1,5 km ao sul da Serra dos Carajás e foram descobertos durante trabalhos de prospecção regional para Ni-Cu (PGE) pela equipe de exploração da VALE. Essas ocorrências encontram-se associadas a uma faixa de 3,8 km de comprimento por aproximadamnete 1 km de largura média, contendo diversos tipos de rochas ultramáficas (talco xistos, serpentinitos e komatiitos portadores de textura *spinifex*). Esta unidade ultramáfica acompanha o *trend* NW-SE com mergulhos geralmente acentuados do *Greenstone Belt* Selva, que é composto dominantemente por quatzo-clorita xistos e clorita-actinolita xistos. Apesar das texturas *spinifex* e cumulus estarem bem preservadas em campo, a mineralogia primária dos komatiitos foi completamente substituída por minerais da fácies metamórfica xisto-verde. Os komatiitos com textura *spinifex* do *Greenstone Belt* Selva apresentam conteúdo de MgO variando de 22,8 a 26,8% em peso, enquanto que os komatiitos com textura cúmulus possuem conteúdo de MgO até 40,6% em peso. As lavas komatiíticas da sequência Selva foram comparadas com os komatiítos com textura *spinifex* da sequência Seringa (localizada dentro do Domínio Rio Maria), ambas são Al-não empobrecidas e apresentam uma razão Al_2O_3/TiO_2 próximo de 20. Os resultados de CaO, Na_2O e ETR dos komatiitos do Selva sugerem mobilidade destes elementos. Esta mobilidade pode estar relacionada à alteração hidrotermal associada a mineralização Cu-Au presente na região.

A identificação de lavas komatiíticas com textura *spinifex* próximo à Bacia de Carajás sugere a continuidade dos *greenstone belts* do Domínio Rio Maria (3,0-2,9 Ga) para o interior do Subdomínio de Transição, ampliando a área potencialmente favorável a hospedar depósitos de Ni-Cu-PGE associados a komatiitos.

ABSTRACT

Canaã dos Carajás region is located at south side of Carajás ridge, inside the Transition Subdomain-TS, and is part of Carajás Mineral Province-CMP. This Province presents several world class mineral deposits and represents a very important source of Fe, Cu, Ni and Mn. This region presents several mafic-ultramafic (MUM) occurrences and, considering this diversity of assembleges that occur inside the TS, three occurrences were selected as the focous of this study regarding geological setting and petrological features: (**1**) Vermelho Layered Complex; (**2**) Touro Layered Complex; and (**3**) spinifex-textured komatiites of Selva area.

(**1**). The Vermelho Layered Complex is a remarkably well preserved magmatic structure located in the Carajás Mineral Province. This medium-size mafic-ultramafic layered intrusion, located at about 2 kilometers NW from Canaã dos Carajás city, is best known for hosting world class nickel laterite resources. It is part of a cluster of mafic-ultramafic layered intrusions interpreted to be part of a large Neoarchean (ca. 2.76 Ga) magmatic event. This complex comprises an average 9.5 kilometer long per 1.5 kilometer wide NE-SW trending mafic-ultramafic intrusion, hosted by banded gneiss of the Xingú Complex (> 2.85 Ga) and massive granitic rocks. The intrusive architecture of the Vermelho Complex consists of an Upper Zone (UZ) of horizontally layered ultramafic rocks overlying a Lower Zone (LZ) of a complex but broadly subhorizontal sequence of mafic-ultramafic rocks. The MgO contents ranges from 40.12 wt.% (anhydrous base) in harzburgitic rocks, up to 2.22 wt.% in more fractionated gabbroic rocks. Mineral chemistry data from olivine crystals confirmed forsterite contents between $Fo_{90.5}$ and $Fo_{85.6}$, indicating a primitive parental magma source. The basal sequence of the LZ consists of interlayered ultramafic rocks, possibly resulting from successive influxes of primitive magma, and do not presents a clear evidence for a fully developed marginal reversal as indicated by the sequence of cumulates or fractionation trends of the rocks located close to the lower contact of the Vermelho Complex with country rocks. The actual landscape composed of plateaus (V1 and V2) and flat areas started to be formed at the transition from Meso-Cenozoic time and has exposed the lower portion of this layered intrusion. The data obtained in this study indicate that two major events of magma emplacement were involved in the evolution of the Vermelho Complex, the first one associated with the LZ and the second with the UZ. This dynamic magmatic evolution, composed by multiple influxes of magma, indicate favorable conditions for magmatic deposits generation.

Limited reported U-Pb zircon ages for layered intrusions of the Carajás Mineral Province indicate Neoarchean ages (ca. 2680-2780 Ma) that overlap with reported ages of the extensive basaltic volcanism of the region (e.g. 2759±2 Ma; 2760±11 Ma). These results support the interpretation that layered intrusions and volcanism of the Carajás Province result from a major Neoarchean (ca. 2.76 Ga) magmatic event. The tectonic setting of this magmatic event is controversial, but lithogeochemical and isotopic evidence for significant crustal contamination of basaltic rocks have been used to suggest a continental rifting model. The structure of the Vermelho Complex, characterized by pristine rock textures, stratigraphy and magmatic structure intrusive into high metamorphic gneiss-migmatite terrains, together with compositional features indicating contamination with older crustal rocks, is consistent with an origin associated with a continental rifting.

(**2**). The Touro Layered Complex is small size MUM intrusion located at about 47 kilometers WNW from Canaã dos Carajás city. This layered intrusion comprise an average 4.8 kilometers long per 1.2 kilometers wide trending ENE-WSW mafic-ultramafic intrusion, hosted by syn-orogenic granitoid rocks (ca. 2.73-2.76 Ga). The stratigraphic framework and lithogeochemical data follows the normal sequence of fractionation observed in single pulse magmatic layered intrusions, composed by a lower Ultramafic Zone (UZ) and an upper Mafic Zone (MZ). Touro Layered Complex have MgO contents ranging from 10 and 24.4 wt.%. Another remarkable issue is the low silica content in all assayed rocks, constraining the Touro Complex lithologies to silica-undersaturated parental magma type, contributing to the absence of orthopyroxene as cumulus phase in the rocks of this intrusion. Mineral chemistry data from olivine crystals showed forsterite contents ranging from $Fo_{76.3}$ to $Fo_{67.9}$, indicating a moderately fractionated parental magma for the Touro Complex. The magmatic structure and the petrological evolution of this complex are compatible with other layered complexes emplaced in stable continental crust. These features are compatible with the tectonic setting model for intraplate rift proposed by several authors for the CMP.

(**3**). Spinifex-textured komatiites in the Selva greenstone belt are the first unequivocal examples of komatiites in the Transition Subdomain of the Carajás Mineral Province. Outcrops of spinifex-textured komatiites, located ~ 1.5 kilometers to the south of the Carajás ridge, were discovered during regional exploration for Ni-Cu-(PGE) sulfide deposits by VALE. They are associated with a 3.8 kilometers long per 1 kilometers wide unit consisting of variable types of ultramafic rocks (talc schist, serpentinite and spinifex-textured komatiite). This ultramafic unit follows the steep dipping NW-SE trending Selva Greenstone

Belt composed mainly by quartz-chlorite schists and chlorite-actinolite schists. Although the spinifex and cumulus textures are well preserved in the field, the primary mineralogy of the komatiites has been completely replaced by greenschist facies metamorphic minerals. Spinifex-textured komatiites have MgO contents bracket between 22.8 and 26.9 wt.%, and cumulate textured komatiites have MgO contents up to 40.6 wt.%. Komatiites from the Selva and Seringa (located in the Rio Maria Granite-Greenstone Terrain) belts are Al-undepleted with Al_2O_3/TiO_2 ratios close to 20. Results for CaO, Na_2O, and REE suggest that these elements were mobile and their abundances have been modified during metasomatic alteration. This mobility may be related to hydrothermal alteration associated to Cu-Au mineralization in the region.

The identification of spinifex-textured komatiites close to the Carajás Basin suggests the continuation of 3.0-2.9 Ga greenstone belts of the Rio Maria Granite-Greenstone Terrain within the Transition Subdomain, and enlarges the area with potential to host komatiite associated Ni-Cu-PGE deposits.

CONSIDERAÇÕES GERAIS

Introdução

A Província Mineral de Carajás-PMC (Hirata et al., 1982; Docegeo, 1988, e outros) está localizada na porção sudeste do Estado do Pará (Figura A). É constituída por dois domínios geotectônicos distintos (Vasquez et al., 2008): Domínio Rio Maria (DRM), de idade Mesoarqueana, a sul; e Domínio Carajás (DC), de idade Neoarqueana, a norte (Figura B); uma zona de transição (Subdomínio de Transição-ST), situada no interior do DC, foi proposta para separar o DRM das rochas Neoarqueanas do Supergrupo Itacaiúnas, que representariam a Bacia de Carajás (Dall'Agnol et al., 2006; Feio & Dall'Agnol, 2012). A PMC é conhecida por hospedar numerosos depósitos de classe mundial (e.g. Fe, Cu, Ni e Mn). Este aspecto tem motivado importantes avanços do conhecimento geológico regional nas últimas décadas, particularmente na contextualização geológico-geocronológica das rochas englobadas no Complexo Xingú (Dall'Agnol et al., 2006; Vasquez et al., 2008; Feio & Dall'Agnol, 2012; Feio et al., 2013, e referências neles contidas) e também no estudo e caracterização das importantes mineralizações de ferro (Lobato et al., 2005a e 2005b) e cobre tipo IOCG (Tallarico et al., 2005; Monteiro et al., 2008a e 2008b; Xavier et al., 2012; Moreto et al., 2015, e referências neles contidas). Apesar desses avanços, os trabalhos mais recentemente publicados sobre complexos máfico-ultramáficos (MUM) e mineralizações associadas estão limitados aos complexos Puma-Onça (Macambira et al., 2002 e 2005; e referências neles contidas) e complexo Luanga (Ferreira Filho et al., 2007; Teixeira et al., 2015, e referências neles contidas), localizados respectivamente nas regiões de Tucumã e Curionópolis.

A região de Canaã dos Carajás encontra-se situada ao sul da serra dos Carajás, dentro do Subdomínio de Transição (Dall'Agnol et al., 2006; Feio & Dall'Agnol, 2012), e apresenta em seu entorno inúmeras ocorrências de rochas MUM (Figura B). Trabalhos de mapeamento geológico executados nos últimos anos, incluindo os programas de referência de levantamento e integração geológica regional da CPRM (Vasquez et al., 2008), bem como aqueles desenvolvidos por empresas de exploração mineral, mostraram que estas associações MUM incluem uma diversidade muito grande de corpos acamadados de porte médio a pequeno com destaque para o Complexo Acamadado do Vermelho, que contém importantes

mineralizações de Ni laterítico (Alves et al., 1986; Kuck, 2003), bem como ocorrências recentemente identificadas de rochas vulcânicas ultramáficas portadoras de textura *spinifex*. Estes corpos MUM estão encaixados em rochas do Complexo Xingú ou granitos arqueanos, inseridos no contexto do ST. Não existem dados geocronológicos robustos que permitam correlacionar essas associações com a evolução magmática da região de Carajás.

No sentido de ampliar o conhecimento dessas associações MUM na PMC e particularmente no ST, a presente tese de doutorado aborda o estudo de três ocorrências distintas de rochas MUM localizadas na região de Canaã dos Carajás, sendo dois complexos acamadados intrusivos (Vermelho e Touro) e a ocorrência de vulcânicas ultramáficas komatiíticas com textura *spinifex* na área denominada de Selva (Figura B).
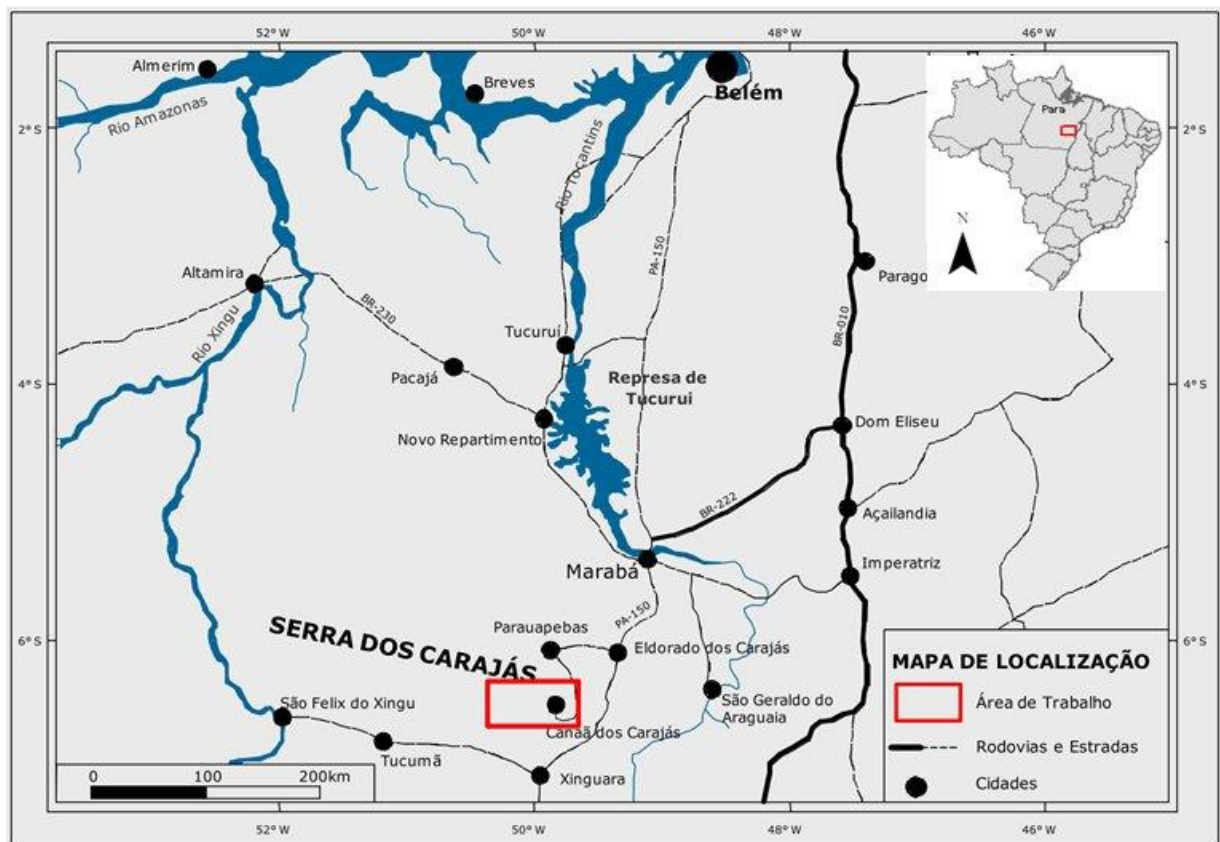
Figura A. Mapa de localização e acesso. Em vermelho, área onde estão inseridos os corpos MUM estudados.

O Complexo Acamadado do Vermelho (Figura B) encontra-se localizado a cerca de 2 km NW da localidade de Canaã dos Carajás e 10 km ao sul da serra dos Carajás, compreende um corpo com cerca de 9,5 km de comprimento por 1,5 km de largura média, alinhado segundo a direção NE-SW. Possui como principal aspecto morfológico dois *plateus*

conhecidos como V1 (porção NE) e V2 (porção SW) que se destacam das áreas aplainadas circunvizinhas. A geologia foi interpretada a partir de trabalhos de campo e dados de sondagem. Abrange um conjunto de rochas MUM acamadadas sub-horizontalizadas, não apresentando evidências de metamorfismo regional nem deformação, porém profundamente intemperizadas. O presente trabalho apresenta uma nova proposta de estratigrafia que abrange duas unidades assim distribuidas: (i) Zona Inferior (LZ), composta da base para o topo por: dunito e harzburgito (LZa); ortopiroxenito e norito (LZb) e gabronorito e gabro (LZc); (ii) Zona Superior (UZ), composta da base para o topo por ortopiroxenito com intercalações de cromitito (UZa) e dunito e harzburgito (UZb).

O Complexo Acamadado Touro (Figura B) situa-se a aproximadamente 47 km WNW de Canaã dos Carajás e cerca de 5 km sul da serra dos Carajás. Apresenta cerca de 4,8 km de comprimento por 1,2 km de largura média, alinhado segundo a direção ENE-WSW. Trabalhos de campo, dados de sondagem e levantamento geofísico terrestre (MAG), disponibilizados pela AVANCO, permitiram caracterizar que este complexo apresenta um conjunto de rochas MUM sub-hotizontalizadas, também sem evidências de metamorfismo regional, porém, localmente deformadas e hidrotermalizadas. A estratigrafia proposta para esse complexo é subdividida em: (i) Zona Ultramáfica inferior (UZ), composta por dunitos, wehrlitos e clinopiroxenitos; (ii) Zona Máfica superior (MZ), composta por melagabros, gabros e gabros pegmatoides no topo. No furo de sondagem utilizado e no mapeamento foi identificada, na borda do complexo, ocorrência descontínua de rocha gabroica profundamente intemperizada.

O *Greenstone Belt* Selva (Figura B) compreende parte de sequência vulcano-sedimentar metamorfisada na fácies xisto-verde, localizada a cerca de 11 km ao norte do Complexo Acamadado do Vermelho e a 1,5 km ao sul da serra de Carajás. Apresenta aproximadamente 3,8 km de comprimento alinhado no *trend* NW-SE e aflora discordantemente das rochas do Supergrupo Itacaiúnas (Figura B). Litologicamente, destaca-se nessa sequência a ocorrências rochas vulcânicas ultramáficas de natureza komatiítica e com textura *spinifex* preservada. No mesmo contexto geológico regional, foi datada metavulcânica ácida localizada no entorno da mina do Sossego (ca. 2,97 Ga-Moreto et al., 2015), este resultado confirma que os komatiitos do *Greenstone Belt* Selva fazem parte do Supergrupo Andorinhas e demonstra que o Domínio Rio Maria se estendeu bem mais ao norte, constituindo o embasamento onde se formou Cinturão Vulcano-Sedimentar Itacaiúnas.
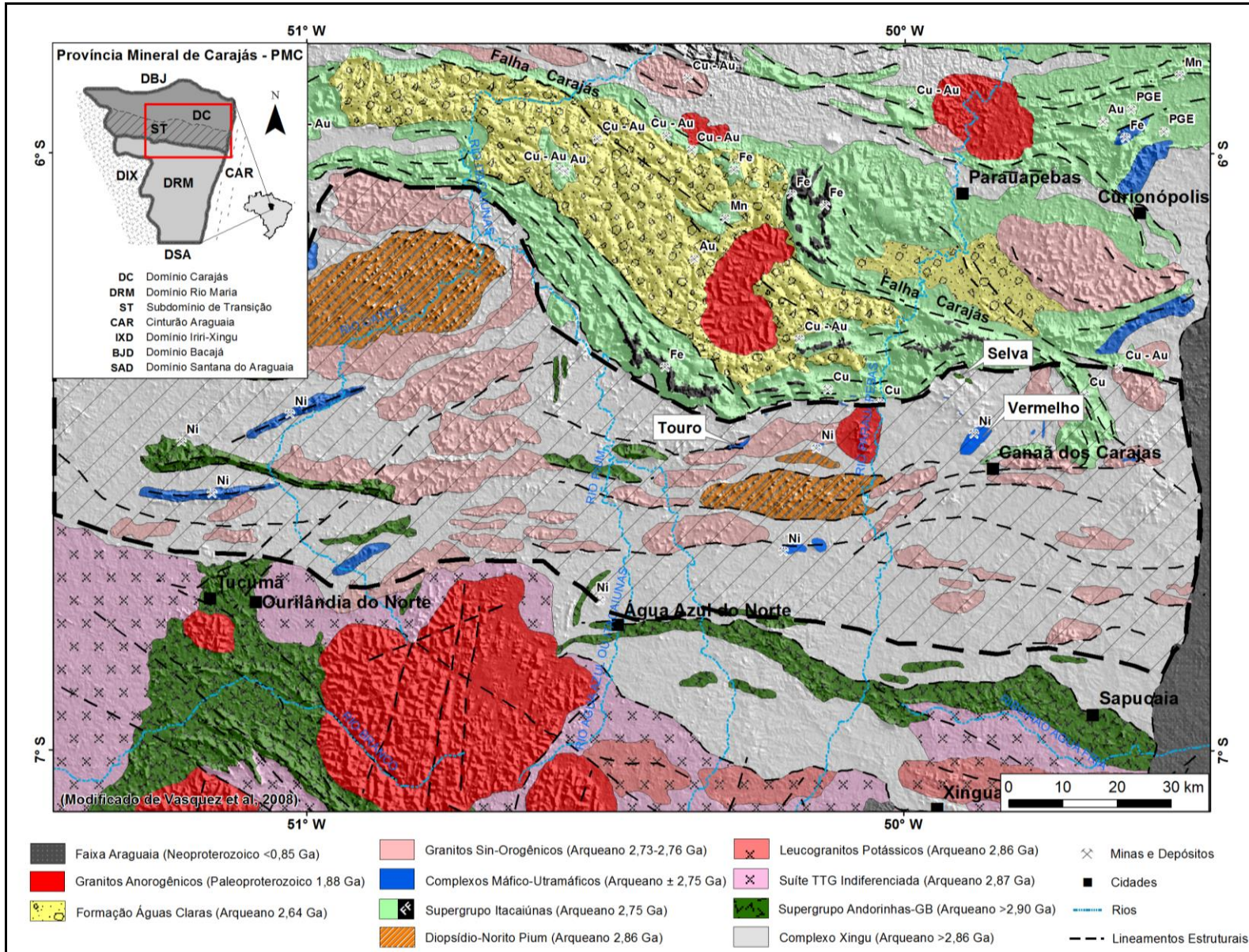
Figura B. Mapa geológico regional de parte da Provincia Mineral de Carajás com destaque dos corpos MUM estudados. No detalhe as principais unidades geotectônicas da PMC e adjacentes (modificado de Vasquez et al., 2008). Área hachurada representa o Subdomínio de Transição-ST (Dall´Agnol et al., 2006; Feio & Dall'Agnol, 2012).

A evolução do conhecimento não está sendo realizada somente na escala local das ocorrências estudadas, mas também regionalmente com o enquadramento petrológico destes e de outros corpos do entorno de Canaã dos Carajás no contexto do magmatismo MUM regional e sua integração na evolução geológica de Carajás.

A presente tese de doutorado está inserida na proposta do Projeto Integrado de Pesquisa do coordenador, "**Desenvolvimento de parâmetros comparativos da fertilidade do magmatismo máfico-ultramáfico de Carajás para mineralizações magmáticas (Ni, Cu, EGP, Cr, Ti-V) com base em estudos geocronológicos, petrológicos e do seu posicionamento tectônico-estratigráfico**", aprovado no Edital MCT/CTMineral/VALE/ CNPq 12/2009, com recursos liberados em 08/2010 e conta com a parceria da VALE.

Objetivo

Uma vez que não existem dados geocronológicos e petrológicos do Complexo do Vermelho e outros corpos máficos-ultramáficos menores situados na região do entorno de Canaã dos Carajás, a atual caracterização desses corpos como parte de uma suíte magmática maior, designada Suíte Cateté, é meramente especulativa. Em função do posicionamento destes corpos na porção sul da Serra dos Carajás, no limite entre os terrenos neoarqueanos de Carajás ao norte (ca. 2,7 Ga) e os terrenos granito-greenstone ao sul (ca. 2,9 Ga), o entendimento do posicionamento cronológico-estrutural deste magmatismo MUM é muito relevante para a geologia da região de Carajás.

Portanto, o presente doutorado se justifica e tem por objetivo contribuir para o melhor conhecimento de alguns desses corpos presentes na porção sul da Serra dos Carajás, nas vizinhanças de Canaã dos Carajás, com foco particularmente nas intrusões acamadadas do Vermelho e Touro, bem como nas rochas komatiíticas da área Selva (Figura B). O presente doutorado abrange também como objetivos específicos os seguintes pontos:

- Análise da estratigrafia e caracterização petrológica dos Complexos Acamadados do Vermelho e Touro;

- Caracterização do magmatismo komatiítico da sequência tipo *greenstone belt* da área Selva, presente no ST e correlação com os komatiitos do Supergrupo Andorinhas (área Seringa), presentes no DRM;

- Enquadramento dos Complexos Acamadados estudados e outros corpos do entorno de Canaã dos Carajás no contexto do magmatismo máfico-ultramáfico regional e sua integração no contexto da evolução geológica de Carajás;

- Estabelecimento de critérios prospectivos para estes corpos.

Metodologia e Escopo do Estudo

Para atingir estes objetivos propostos na pesquisa foi efetuada revisão bibliográfica, inclusive de relatórios internos disponibilizados pela VALE (Vermelho e Selva) e AVANCO (Touro). Procedeu-se a trabalhos de campo nas ocorrências MUM de interesse, inclusive na área Seringa (DRM), incluindo amostragem e descrição para estudos petrográficos e químicos de rochas e, exclusivamente para os Complexos Vermelho e Touro, também de testemunhos de sondagem de furos selecionados.

Foram efetuados estudos petrográficos em 143 amostras selecionadas, sendo 105 amostras do Complexo Acamadado Vermelho; 14 amostras do Complexo Acamadado Touro; e em ocorrências de rochas komatiíticas, 11 amostras na área Selva e 13 na área Seringa. Estes estudos permitiram o reconhecimento dos diversos litotipos que compõem os Complexos Acamadados do Vermelho e Touro, bem como das rochas komatiíticas que compõem os derrames das áreas Selva e Seringa, estas situadas respectivamente no Subdomínio de Transição e no Domínio Rio Maria.

Em amostras selecionadas dos Complexos Acamadados do Vermelho e Touro foram executadas um total de 524 análises de química mineral via microssonda eletrônica, sendo 353 no Complexo Acamadado Vermelho e 171 no Complexo Acamadado Touro. Essas análises foram realizadas no Laboratório de Microssonda Eletrônica da Universidade de Brasília, em equipamento Cameca SX-50. O tratamento dos dados foi feito por meio de planilha eletrônica Excel e os resultados analíticos representativos são apresentados nas Tabelas 1.1, 1.2, 2.2, 2.3 e 2.4.

Foram efetuadas análises litoquímicas em 53 amostras, sendo 17 no Complexo Acamadado Vermelho; 12 no Complexo Acamadado Touro; 11 nos komatiitos da área Selva e 13 nos komatiitos da área Seringa. As análises foram executadas no laboratório ALS Chemex (Canadá). Os ensaios compreenderam elementos maiores em rocha total (método: ME-XRF06), ICP-MS 47 elementos com abertura a 4 ácidos (método: ME-MS61) e Terras Raras (método: ME-MS82), os resultados analíticos encontram-se expressos nas Tabelas 1.3, 2.1 e 3.1.

Estudos isotópicos Sm-Nd foram executados apenas no Complexo Acamadado do Vermelho (17 análises) e todos foram realizados no Laboratório de Geocronologia da Universidade de Brasília. O procedimento segue os métodos descritos em Goia & Pimentel (2000). Os valores de TDM foram calculados com base no modelo de DePaolo (1981).

Estrutura da Tese

Este doutorado está estruturado em três capítulos na forma de artigos direcionados para publicação em periódicos científicos internacionais especializados sobre os temas abordados.

Os artigos contemplam tópicos propostos conforme os objetivos e respondem a importantes questões relacionadas à evolução petrológica e estratigráfica das intrusões acamadadas MUM selecionadas, bem como sobre a ocorrência de lavas komatiíticas, todos presentes na porção sul da serra dos Carajás, nas vizinhanças da localidade de Canaã dos Carajás. O detalhamento de cada tópico proposto, com metodologias utilizadas e resultados obtidos encontram-se presentes em cada um dos capítulos abaixo.

Capítulo 1

Este Capítulo apresenta o artigo intitulado de "**STRATIGRAPHY AND PETROLOGY OF THE VERMELHO COMPLEX, CARAJÁS PROVINCE, BRAZIL: EVIDENCE FOR MAGMATIC PROCESSES AT THE LOWER CONTACT ZONE OF A LAYERED MAFIC-ULTRAMAFIC INTRUSION**", a ser submetido ao periódico "Lithos". O manuscrito, figuras e legendas do artigo encontram-se em anexo neste volume.

Este artigo objetiva conceituar e discriminar quimicamente a estratigrafia das sequências magmáticas (e.g. Superior, Inferior), que refletem pulsos magmáticos distintos, presentes no Complexo Acamadado do Vermelho. A abordagem tem como base o estudo petrológico, a apresentação de dados isotópicos inéditos, o entendimento do sistema magmático, e os processos magmáticos relacionados à zona de contato inferior, bem como a proposta de enquadramento desses corpos dentro do magmatismo máfico-ultramáfico regional e possíveis implicações para exploração mineral.

Capítulo 2

Este Capítulo apresenta o artigo denominado "**STRATIGRAPHY AND PETROLOGY OF THE TOURO MAFIC-ULTRAMAFIC COMPLEX, CARAJÁS PROVINCE, BRAZIL**" e possivelmente será submetido ao periódico "Applied Earth Sciences - IMM". O manuscrito, figuras e legendas do artigo encontram-se em anexo neste volume.

Este artigo tem por finalidade apresentar a estratigrafia da sequência magmática ultramáfica e máfica, bem como a conceituação do Complexo Acamadado do Touro com base na geologia, em estudos petrológicos e na caracterização do sistema magmático, visando ao enquadramento dentro do magmatismo máfico-ultramáfico regional assim como possíveis implicações para exploração mineral.

Capítulo 3

Este Capítulo apresenta o artigo "**SPINIFEX-TEXTURED KOMATIITES IN THE SOUTH BORDER OF THE CARAJAS RIDGE, SELVA GREENSTONE BELT, CARAJÁS PROVINCE, BRAZIL**". Submetido ao periódico "Journal of South American Earth Sciences-SAMES" em junho de 2015 e publicado em janeiro de 2016. O artigo já publicado faz parte deste volume.

Este artigo traz a primeira descrição de komatiitos situados no Subdomínio de Transição da Província Mineral de Carajás. O objetivo deste trabalho é caracterizar as rochas komatiíticas que ocorrem na área Selva, inclusive estabelecendo comparação com *flows*

komatiíticos da área Seringa, localizada dentro do Domínio Rio Maria, bem como propor sua contextualização na evolução geológica da Província Mineral de Carajás e possíveis implicações para exploração mineral.

Referências

Alves, C.A., Bernardelli, A.L., and Beisiegel, V.R., 1986. A jazida de níquel laterítico do Vermelho, serra dos Carajás, Pará. In: Schobbenhaus, C.R. & Coelho, C.E.S. (Coords.). Principais Depósitos Minerais do Brasil. Rio de Janeiro, DNPM, 2, 325-340.

Kuck, P.H., 2003. U.S. Geological Survey Mineral Yearbook: Nickel-2003. In: http://minerals.usgs.gov/minerals/pubs/commodity/nickel/nickemyb03.pdf

Dall'Agnol R., Oliveira M.A., Almeida J.A.C., Althoff F.J., Leite A.A.S., Oliveira D.C., Barros C.E.M., 2006. Archean and Paleoproterozoic granitoids of the Carajás metallogenetic province, eastern Amazonian craton. In: Dall'Agnol R., Rosa-Costa L.T., Klein E.L. (Eds.) Symposium on Magmatism, Crustal Evolution, and Metallogenesis of the Amazonian Craton, Abstracts Volume and Field Trips Guide. Belém, PRONEXUFPA/SBG-NO, 150 p.

DePaolo, D.J., 1981. A neodymium and strontium isotopic study of the Mesozoic calc-alcaline granitic batholiths of the Sierra Nevada and Penisular Ranges, California. Journal of Geophysical Research 86 (B11), 10470-10488.

Docegeo-Rio Doce Geologia e Mineração, 1988. Revisão Litoestratigráfica da Província Mineral de Carajás. In: Provincia Mineral de Carajás, Litoestratigrafia e principais depósitos minerais. CVRD/SBG, Congresso Brasileiro de Geologia (Belém), *Anexo aos anais*, 35, 11-59.

Feio, G.R.L., Dall'Agnol, R., 2012. Geochemistry and petrogenesis of the Mesoarchean granites from the Canaã dos Carajás area, Carajás Province, Brazil: Implications for the origin of Archean granites, Lithos 154, 33-52.

Feio, G.R.L., Dall'Agnol, R., Dantas, E.L., Macambira, M.J.B., Santos, J.O.S., Althoff, F.J., Soares, J.E.B., 2013. Archean granitoid magmatism in the Canaã dos Carajás area: Implications for crustal evolution of the Carajás province, Amazonian craton, Brazil. Precambrian Research 227, 157-185.

Ferreira Filho, C.F., Cançado, F., Correa, C., Macambira, E.M.B., Siepierski, L., Brod, T.C.J., 2007, Mineralizações estratiformes de EGP-Ni associadas a complexos acamadados em Carajás: os exemplos de Luanga e Serra da Onça: *in* Contribuições à Geologia da Amazônia, Sociedade Brasileira de Geologia - Núcleo Norte, v. 5, p. 01-14.

Gioia, S.M.C.L., Pimentel, M.M., 2000. The Sm-Nd isotopic method in the geochronology laboratory of the University of Brasília. An. Acad. Bras., 72, 220-245.

Hirata, W.K., Rigon, J.C., Kadekaru, K., Cordeiro, A.A.C., Meireles, E.A., 1982. Geologia Regional da Província Mineral de Carajás. In: Simpósio Geologia da Amazônia, 1, Belém, Anais Belém, SBG/NO, 1, 100-110.

Lobato, L.M., Figueiredo e Silva, R.C., Rosière, C.A., Zucchetti, M., Baars, F.J., Seoane, J.C.S., Rios, F.J. Monteiro, A.M., 2005a. Hydrothermal origin for the iron mineralisation, Carajás province, Pará State, Brazil. In: Proceedings Iron Ore 2005. The Australian Institute of Mining and Metallurgy, Publication Series no 8, 99-110.

Lobato, L.M., Rosière, C.A., Figueiredo e Silva, R.C., Zucchetti, M., Baars, F.J., Seoane, J.C.S., Rios, F.J., Pimentel, M.M., Mendes, G., Monteiro, A.M., 2005b. A mineralização hidrotermal de ferro da Província Mineral de Carajás, controle estrutural e contexto na evolução metalogenética da província. In: O J Marini; E T de Queiroz; B W Ramos. (Org.). Caracterização de depósitos minerais em distritos mineiros da Amazônia. 1 ed. Brasília, DNPM/FINEP/ADIMB, 1, 21-92.

Macambira, E.M.B., Ferreira Filho, C.F., 2002. Fracionamento Magmático dos Corpos Máfico-Ultramáficos da Suíte Intrusiva Cateté - Sul do Pará. In: Klein E.L., Vasques M.L. & Rosa Costa L.T. (Eds.) *Contribuições à Geologia da Amazônia v. 3.* SBG-Núcleo Norte, pp. 105-114.

Macambira, E.M.B., Ferreira Filho, C.F., 2005. Exploration and origin of stratiform PGE mineralization in the Serra da Onça layered complex, Carajás Mineral Province, Brazil. In: 10th International Platinum Symposium Extended Abstract, Oulu-Finland, pp. 178-181.

Monteiro, L.V.S, Xavier, RP, Carvalho, E.R., Hitzman, M.W., Johnson, C.A., Souza Filho, C.R., Torresi, I., 2008a. Spatial and temporal zoning of hydrothermal alteration and mineralization in the Sossego iron oxide-copper-gold deposit, Carajás Mineral Province, Brazil: paragenesis and stable isotope constraints. Miner Depos 43, 129-159.

Monteiro, L.V.S., Xavier, R.P., Hitzman, M.W., Juliani, C., Souza Filho, C.R., Carvalho, E.R., 2008b. Mineral chemistry of ore and hydrothermal alteration at the Sossego iron oxide-copper-gold deposit, Carajás Mineral Province, Brazil. Ore Geol Rev 34, 317-336.

Moreto, C.P.N., Monteiro, L.V.S., Xavier, R.P., Creaser, R.A., DuFrane, S.A., Tassinari, C.C.G., Sato, K., Kemp, A.I.S., Amaral, W.S., 2015. Neoarchean and Paleoproterozoic Iron Oxide-Copper-Gold Events at the Sossego Deposit, Carajás Province, Brazil: Re-Os and U-Pb Geochronological Evidence. Economic Geology, 110, 809-835.

Naldrett, A.J., 2004. Magmatic sulfide deposits - geology, geochemistry and exploration. Springer, Berlin, 724 pp.

Tallarico, F.H.B., Figueiredo, B.R., Groves, D.I., Kositcin, N., McNaughton, N.J., Fletcher, I.R., Rego, J.L., 2005. Geology and SHRIMP U-Pb geochronology of the Igarapé Bahia deposit, Carajás copper-gold belt, Brazil: an Archean (2.57 Ga) example of iron-oxide-Cu-Au-(U-REE) mineralization. Econ Geol 100, 7-28.

Teixeira, A.S., Ferreira Filho, C.F., Della Giustina, M.E.S., Araujo, S.M., Silva, H.H.A.B., 2015. Geology, petrology and geochronology of the Lago Grande layered complex: Evidence for a PGE-mineralized magmatic suite in the Carajas Mineral Province, Brazil. Journal of South American Earth Sciences 64, 116-138.

Vasquez, M.L., Rosa-Costa, L.T., 2008. Geologia e recursos minerais do Estado do Pará: texto explicativo do mapa geológico e de recursos minerais do Estado do Pará-escala 1:1.000.000. Programa Geologia do Brasil (PGB), CPRM, 328 pp.

Xavier, R.P., Monteiro, L.V.S., Moreto, C.P.N., Pestilho, A.L.S., Melo, G.H.C., Silva, M.A.D., Aires, B., Ribeiro, C., Silva, F.H.F., 2012. The iron oxide copper-gold systems of the Carajás mineral province, Brazil. Society of Economic Geologists, Special Publication 16, 433-454.

"STRATIGRAPHY AND PETROLOGY OF THE VERMELHO COMPLEX, CARAJÁS PROVINCE, BRAZIL: EVIDENCE FOR MAGMATIC PROCESSES AT THE LOWER CONTACT ZONE OF A LAYERED MAFIC-ULTRAMAFIC INTRUSION."

LINCOLN SIEPIERSKI, CESAR FONSECA FERREIRA FILHO

STRATIGRAPHY AND PETROLOGY OF THE VERMELHO COMPLEX, CARAJÁS PROVINCE, BRAZIL: EVIDENCE FOR MAGMATIC PROCESSES AT THE LOWER CONTACT ZONE OF A LAYERED MAFIC-ULTRAMAFIC INTRUSION

Lincoln Siepierski [a,b] and Cesar Fonseca Ferreira Filho[a]

a - Instituto de Geociência, Universidade de Brasília, Brasília, DF, 70910-900, Brazil

b - VALE S/A, Rodovia BR-381/km 450, 33040-900, Santa Luzia, MG, Brazil

Corresponding author: Cesar Fonseca Ferreira Filho[a]

Abstract

The Vermelho Complex is a remarkably well preserved magmatic structure located in the Carajás Mineral Province. This medium-size mafic-ultramafic layered intrusion, located at about 10 km south from Carajás ridge, is best known for hosting world class nickel laterite resources. It is part of a cluster of mafic-ultramafic layered intrusions interpreted to be part of a large Neoarchean (ca. 2.76 Ga) magmatic event which includes a thick pile of coeval continental basalts.

The Vermelho Complex comprises an average 9.5 kilometer long per 1.5 kilometer wide NE-SW trending mafic-ultramafic intrusion, hosted by banded gneiss of the Xingú Complex (> 2.85 Ga) and massive granitic rocks. The main topographic feature comprises two plateau-type hills (known as V1 and V2) up to 280 meters above surrounding

flat areas. These plateaus are sustained by weathered ultramafic rocks, which are characterized by silica-rich laterites in the upper portions of the weathered profile. The intrusive architecture of the Vermelho Complex consists of a horizontally layered ultramafic zone (UZ = Upper Zone) overlying a complex but broadly subhorizontal sequence of mafic-ultramafic rocks (LZ = Lower Zone). The UZ outcrops in the isolated hills while the LZ occurs in flat areas close to country rocks. The actual landscape started to be formed at the transition from Meso-Cenozoic time and has exposed the lower portion of this layered intrusion. The data obtained in this study indicate that two major events of magma emplacement were involved in the evolution of the Vermelho Complex, the first one associated with the LZ and the second with the UZ. The LZ follows the normal sequence of fractionation characterized for the Vermelho Complex (Ol + Chr $\rightarrow$ Opx + Chr $\rightarrow$ Opx $\rightarrow$ Opx + Pl $\rightarrow$ Opx + Pl + Cpx), evolving from primitive dunite and harzburgite in the base (where most primitive olivine composition is $Fo_{90.5}$) up to highly fractionated quartz-bearing gabbronorite in the upper portions (where most fractionated Opx composition is $En_{57.5}$). This zone extends for more than 400 meters below the V1 plateau but becomes progressively shallower toward the northeast and southwestern portions of the intrusion. Change in thickness in the Lower Zone is likely to indicate the existence of a conduit-type structure below the V1 plateau, as by deep MAG anomalies restricted to this portion of the intrusion. The basal sequence of the LZ, located close to the contact with country rocks, consists of interlayered harzburgites and orthopyroxenites, possibly resulting from successive influxes of primitive magmas. The most primitive mineral compositions of these basal sequences are located dozens of meters away from the contact of country rocks, possibly due to fractionation of the parental magma in the feeding system during initial heating associated with first batches of magmas filling the magma chamber. However, evidence for a fully developed marginal reversal is not indicated by the sequence of cumulates or fractionation trends of the sequence of rocks located close to the lower contact of the Vermelho Complex.

The UZ indicates a remarkable break in the fractionation sequence and mineral compositions of the upper portions of the LZ. This zone consists of two major subhorizontal layers that were just preserved from erosion in the V1 and V2 plateaus. The UZ has a minimum thickness of about 175 meters, broadly corresponding to the maximum height of the V1 plateau above the surrounding flat lands. The lower layer is up to 50 meters thick and consists of orthopyroxenite with minor associated chromitite. The contact of this layer with underlying gabbroic rocks does not outcrop but a sharp contact is indicated by the abrupt transition from overlying orthopyroxenite and underlying gabbroic boulders in the slopes of

the plateaus, as well as rock chips from percussive drilling. The orthopyroxenite of the UZ has coarse- to medium-grained adcumulate texture, consisting of cumulus orthopyroxene and chromite (1-3 vol. %). Chromite occurs mainly as disseminated fine-grained euhedral crystals in orthopyroxenite, but may also occurs in few centimeter thick chromite-rich pods or discontinuous layers. Compostional features of orthopyroxenites of the UZ are comparable to those observed at the lower portions of the LZ, suggesting that the magma composition associated with stages 1 and 3 are similar. The orthopyroxenite layer is interpreted to result from mixing of a large new influx of primitive magma with a small volume of highly fractionated silica-rich resident magma. The associated chromitites possibly result from chromite saturation induced by the mixing of highly distinct magmas, following the model proposed for the origin of chromitites in several layered intrusions. The location of feeders associated with this second major influx of primitive magma is not constrained by geological or geophysical features. The upper and basal subhorizontal contacts of the UZa suggest however that primitive magma may have been filled from lateral conduits (not preserved at the actual erosion level) rather than from the same conduit that filled the first major influx primitive magma.

Limited reported U-Pb zircon ages for layered intrusions of the Carajás Mineral Province indicate Neoarchean ages (ca. 2680-2780 Ma) that overlap with reported ages of the extensive basaltic volcanism of the region (e.g. 2759±2 Ma ; 2760±11 Ma). These results support the interpretation that layered intrusions and volcanism of the Carajás Province result from a major Neoarchean (ca. 2.76 Ga) magmatic event. The tectonic setting of this magmatic event is controversial, but lithogeochemical and isotopic evidence for significant crustal contamination of basaltic rocks have been used to suggest a continental rifting model. The structure of the Vermelho Complex, characterized by pristine rock textures, stratigraphy and magmatic structure intrusive into high metamorphic gneiss-migmatite terrains, together with compositional features indicating contamination with older crustal rocks, is consistent with an origin associated with a continental rifting.

Introduction

The Vermelho Complex in the Carajás Mineral Province is known for hosting world-class Ni laterite resources (220 Mt @ 1.23% Ni; Kuck, 2003). Previous studies of the Vermelho Complex have focused on the nickel-laterite deposit and the stratigraphy and petrology of the mafic-ultramafic rocks were mainly disregarded. This study is part of an assessment of the mafic-ultramafic bodies of the Canaã region (Fig. 1.1; Siepierski, in prep.), and provides the first systematic geological and petrological study of the layered rocks of the Vermelho Complex. Results of this study provide new insights of the intrusive architecture of the Vermelho Complex, which consists of a horizontally layered ultramafic zone overlying a complex sequence of mafic-ultramafic rocks in contact with host sialic rocks. The latter is interpreted as the lower marginal zone of the Vermelho Complex, thus providing new geological and petrological evidences for the processes that occur at the base of layered intrusions.

Geological features and petrological processes associated with the lower marginal zones of layered intrusions were extensively described in several layered intrusions (e.g. Huppert and Sparks, 1989; Eales and Cawthorn, 1996; McBirney, 1996; McCallum, 1996) and reviewed by Latypov (2003a) and Latypov et al. (2007; 2011). Geological features of these lower marginal zones, usually described as chilled margins or lower border groups, are highly variable for different layered intrusions. However, the presence of compositional reversals seem to be a frequently feature in basic-ultrabasic sills and layered intrusions. Compositional reversals are characterized by phase layering and cryptic variation in cumulates of the lower marginal zones following and inverted trend compared to the trend described for the overlying cumulates. Several different processes (e.g. crystal settling, in situ crystallization, multiple magma injection, compositionally zoned magma, Soret fractionation) and models were proposed to explain this common feature. Diversity of models and petrological processes reflects the geological-petrological variability of the marginal lower zones in layered intrusions. Our findings in the Vermelho Complex provide further evidence for the geological and petrological variability of marginal lower zones of layered complexes. They are used in this study to review the current models for the development of the lowermost portions of layered intrusions and chromitite deposits.

16

Geological Setting

Regional Geological Setting

The regional geology of the Carajás Mineral Province and adjacent areas (Fig. 1.1) is described, among others, by Hirata et al. (1982), Meireles et al. (1984), Docegeo (1988), Araújo and Maia (1991), Costa et al. (1995), Vasquez et al. (2008). The Carajás Province is best known for hosting several world-class deposits, including the largest iron ore resources in the world, as well as Cu-Au, Ni, PGE, Au and Mn deposits.

The Carajás Province (Fig. 1.1) lies in the eastern portion of the Amazon Craton, being bordered (Vasquez et al., 2008) to the east by the Neoproterozoic Araguaia Belt; to the west by overlying Paleoproterozoic volcanic sequences and plutonic rocks of the Iriri-Xingu Domain; limits to the south comprises mainly Paleoproterozoic to Archean granite-gneiss rocks of the Santana do Araguaia Domain; and geological limits to the north, where Paleoproterozoic gneiss-migmatite-granulite terrains predominate (e.g. Faraco et al., 2005), are not precisely defined and is referred as Bacajá Domain.

Carajás Province have been subdivided in two geotectonic domains (Vasquez et al., 2008): a typical granite-greenstone terrains of the Rio Maria Domain further south; and the complex terrain of the Carajás Domain including mainly Neoarchean volcano-sedimentary sequences and granitic-gneissic-granulite rocks. A E-W Transition Subdomain zone (Dall'Agnol et al., 2006; Feio and Dall'Agnol, 2012), was proposed to separate the Neoarchean volcano-sedimentary sequences of Carajás Domain and the Rio Maria Domain.

The Xingu Complex consists mainly of gneiss, migmatite and granulites (Docegeo, 1988). U-Pb zircon dating of high-grade metamorphic rocks yielded Archean ages, 2,859±9 Ma for the diopside-norite Pium (Pidgeon et al., 2000; Vasquez et al., 2008) and 2,859±2 Ma for migmatites (Machado et al., 1991). These are interpreted to represent ages of metamorphic recrystallization. These basement rocks experienced several episodes of reactivation during the Archean and Paleoproterozoic (Pinheiro and Holdsworth, 1997; Holdsworth and Pinheiro, 2000). The Andorinhas Supergroup consists of typical Archean (2,904 ± 29 Ma; Macambira and Lancelot, 1996) greenstone belts (Docegeo, 1988), including spinifex-textured komatiitc flows and pillowed basalts (Huhn et al., 1986); these greenstone

rocks were intruded by TTG-granitoids (ca. 2,877 ± 6 Ma; Rolando and Macambira, 2003) and late potassic leucogranites (ca. 2,865 ± 1 Ma; Leite et al., 2004).

The Itacaiúnas Supergroup includes several Archean (ca. 2.75 Ga; Machado et al., 1991; Trendall et al., 1998) volcano-sedimentary sequences (Docegeo, 1988). These include the large sequence of metabasalts of the Grão Pará Group, footwall to the jaspilite-hosted, giant iron deposits of Carajás (Figueiredo and Silva et al., 2008; Lobato et al., 2005). This extensive basaltic volcanism is usually considered to result from intra-plate rifting of older continental crust (Gibbs et al., 1986; Docegeo, 1988; Olszewski et al., 1989; Villas and Santos, 2001) but subduction-related environments have also been proposed (Dardenne et al., 1988; Teixeira and Eggler, 1994; Zuccheti, 2007; Zuchetti et al., 2007).

The Águas Claras Formation (Araújo et al., 1988; Soares et al., 1994) comprises sandstone and siltstone formed in shallow marine to fluvial environment (Nogueira et al., 1994; 2000). This sequence of clastic sedimentary rocks covers different sequences of the Itacaiúnas Supergroup. A minimum age for the Águas Claras Formation was determined by Dias et al. (1996) from zircons obtained from cross cutting gabbroic dikes (2,645±12 Ma). The Gorotire Formation is a clastic immature sequence covering the Itacaiúnas Supergroup and Águas Claras Formation (Docegeo, 1988).

The Carajás Province was intruded by granititic magmas of distinct ages and compositions. These intrusions are mainly correlated to four main distinct periods. Mesoarchean (ca. 2.96-2.93 Ga and 2.87-2.83 Ga) granitic intrusions (Sardinha et al., 2004; Feio et al., 2012 and 2013); Neoarchean (ca. 2.76-2.73 Ga) intrusions include the Plaquê Suite and other syn-orogenic granites (Avelar et al., 1999; Huhn et al., 1999; Dall'Agnol et al., 1997; Barros et al., 2001; Sardinha et al., 2006; Barros et al., 2009; Feio et al; 2012 and 2013); younger (ca. 2.56 Ga) intrusions include alkaline granites (Machado et al., 1991 and Souza et al., 1996); and Paleoproterozoic (ca. 1.88 Ga) intrusions include several anorogenic granitic plutons (e.g. Dall'Agnol et al., 2005 and 2006) that belong to an extensive A-type Proterozoic province of the Amazon Craton (e.g. Santos et al., 2001).

Several mafic-ultramafic intrusions intrude the Xingu Complex and the Itacaiúnas Supergroup (Docegeo, 1988). These include large lateritic Ni-mineralized layered intrusions of the Cateté Suite (Macambira, 1997), as well as the PGE-mineralized Luanga (Ferreira Filho et al., 2007) and Lago Grande (Teixeira et al., 2015) complexes. The latter crystallized at 2,763±6 Ma (Machado et al., 1991) and is coeval with the extensive mafic magmatism of

the Itacaiúnas Supergroup, whereas the age of the Archean Cateté Suite is poorly constrained (Macambira, 1997; Macambira and Tassinari, 1998).

The Vermelho Complex is interpreted as part of the Cateté Suite (Macambira, 1997), a subject that is being revised based on ongoing geological, petrological studies of the mafic-ultramafic complexes of the Canaã region (Siepierski, in prep.). Preliminary results indicate a large diversity of mafic-ultramafic intrusions in the Canaã region, suggesting that they belong to different magmatic suites (Siepierski, in prep.).

Vermelho Complex

The Vermelho Complex is located at about 10 km south from Carajás ridge and hosted by basement granitic-gneissic rocks of the Xingu Complex. This layered intrusion was discovered in 1974 during exploration for nickel laterite deposits. After the discovery several advanced projects were undertaken in the area to evaluate the nickel-laterite deposit. The latest published report indicates total resources of 220 Mt @ 1.23% Ni (Kuck, 2003). Studies of the Vermelho Complex focused mainly in the nickel-laterite deposit (Bernardelli et al., 1983; Correa et al., 1984; Alves et al., 1986), and the stratigraphy and petrology of the layered rocks were just cursorily described.

Alves et al. (1986) described the Vermelho Complex as two NE-SW trending contiguous mafic-ultramafic bodies. These two bodies, designated V1 and V2, are described as two concentric differentiated units, each of them consisting of an ultramafic core and a mafic rim. These two ultramafic cores, comprising the plateau-type hills of the V1 and V2 ore bodies, consist of serpentinized olivine-rich rocks (dunite and peridotite) and pyroxenite. The mafic rim, as decribed by Alves et al. (1986), surrounds the V1 and V2 plateaus and is mainly composed by gabbro, metagabbro, gabbronorite and minor pyroxenite.

Nickel mineralization results of deep weathering of olivine-rich protoliths on the V1 and V2 plateaus (Alves et al., 1986; Silva and Oliveira, 1995). The Vermelho nickel deposit has a 30-40 meter deep weathering profile, which consists from top to bottom of the following units: (1) Lateritic soil: brown to red ferruginous magnetic soil with pisolitic and laterite fragments, deeply weathered rock and silcrete fragments could be present; (2) Laterite zone: not-textured brown to red ferruginous and magnetic fine-grained material, chemical

assays returned Ni from 0.5wt% to 1.0wt%; (3) Siliceous zone: composed of silica-rich massive to boxwork-type blocks or bodies, pores are filled by brown to dark-red argillaceous and magnetic material; (4) Saprolite: poor-structured, brown to yellow color, deeply weathered but not consistently decomposed ultramafic rock, Ni contents increase from 0.5wt% on top to about 4.0wt% at the lower zone where smectite is abundant; (5) Saprolitized serpentinite: light-green to yellow to grey very decomposed ultramafic rock with some preserved primary structure, in this zone the Ni-rich garnieritic ore with Ni contents ranging from 4wt% up to 9wt%; and (6) Serpentinite: fresh ultramafic rock green to black color with preserved primary structures, chemical assays results Ni ranging from 0.2wt% to 0.4wt%.

The geological interpretation of the Vermelho Complex as two concentric mafic-ultramafic bodies, as indicated by Alves et al. (1986), is at variance with the results obtained in this study. This subject will be considered in the section describing the geology and stratigraphy of the Vermelho Complex.
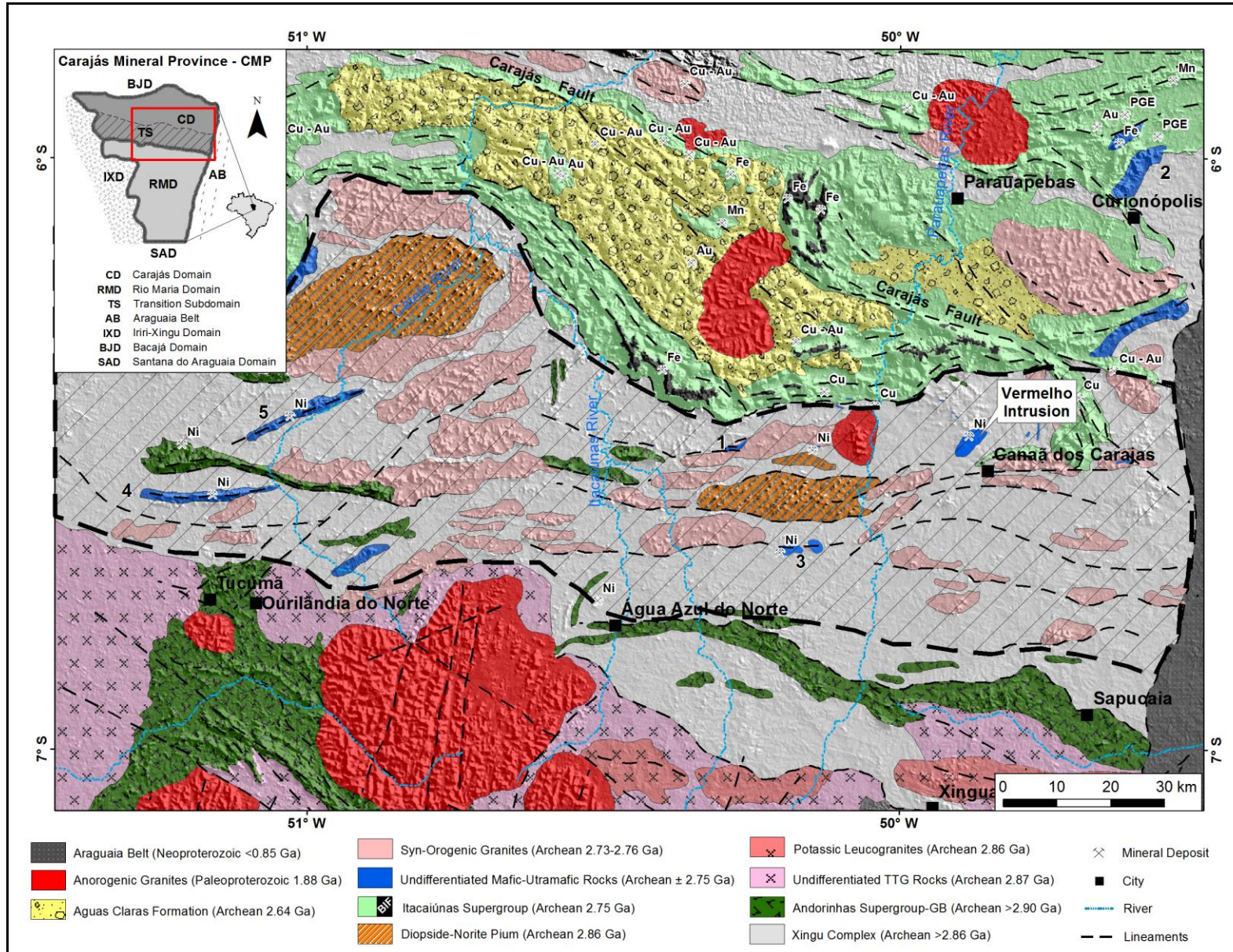
Figure 1.1. Regional geological map showing part of the CMP (partially modified from Vasquez et al., 2008). Some MUM layered intrusions are indicated: (1) Touro; (2) Serra Leste Magmatic Suite (e.g. Luanga and Lago Grande); (3) Buzios; (4) Onça and (5) Puma. Hatched area: Transition Subdomain-TS (partially modified from Dall´Agnol et al., 2006; Feio and Dall'Agnol, 2012).

21

Analytical Procedures

Microprobe analyses

Mineral analyses were performed on polished thin section using a 5-spectrometer JEOL JXA-8230 SuperProbe at the Electron Microprobe Laboratory of the University of Brasília (Brazil). The wavelength dispersive (WDS) analyses were performed at an accelerating voltage of 15 kV and a beam current of 10 nA. Both synthetic and natural mineral standards were used for the analyses and the same standards and procedure were retained throughout. Fe^{3+} contents were estimated using site and charge balance calculations on cation-normalised analyses. Routine analyses (EDS) of several minerals were also used to support petrographic studies. Systematic WDS analyses were obtained for olivine, orthopyroxene, clinopyroxene, and plagioclase. Tables 1.1 and 1.2 show representative analyses of olivine and orthopyroxene.

Bulk rock analyses (ICP-MS)

Sample preparation and lithogeochemistry analyses were performed at the ALS Chemex (Canada). A total of 17 representative samples from two diamond drill holes were analysed using three different procedures. These include the whole rock package plus LOI (ALS Chemex codes: ME-XRF12st and OA-GRA05x), total S plus total C (ALS Chemex codes: S-IR08 and C-IR07) and 38 elements fusion ICP-MS package (ALS Chemex code: ME-MS81). A complete description of analytical methods is available in the ALS Chemex Home Page (www.alsglobal.com). Analysed samples (Table 1.3) were arranged into three different groups representative of the main lithotypes.

Sm-Nd isotopic analyses

Sm-Nd isotopic analyses followed the method described by Gioia and Pimentel (2000) and were carried out at the Geochronology Laboratory of the University of Brasilia. Whole-rock powders (~ 3000 mg) were mixed with 149Sm-150Nd spike solution and dissolved in Savillex bombs. Sm and Nd extraction of whole-rock samples followed conventional cation exchange techniques. The isotopic measurements were carried out on a multi-collector Finnigan MAT 262 mass spectrometer in static mode. The 143Nd/144Nd ratios were normalized to 146Nd/144Nd of 0.7219 and the decay constant used was 6.54 × 10-12 a-1. The TDM values were calculated using the model of DePaolo (1981). Nd procedure blanks were better than 100 pg. Sm-Nd results for 15 samples are shown in Table 1.4.

The Vermelho Mafic-Ultramafic Complex

Geology and stratigraphy

Based upon field studies and a review of the extensive exploration data (including maps, soil geochemistry surveys, drilling, geophysical surveys) developed by VALE for the evaluation of Ni laterite resources, this study provides new insights regarding the geology and stratigraphy of the Vermelho Complex. This complex comprises an average 9.5 kilometer long per 1.5 kilometer wide NE-SW trending mafic-ultramafic intrusion (Fig. 1.2). The main topographic feature comprises two plateau-type hills (known as V1 and V2) up to 280 meters above surrounding flat areas (Fig. 1.3A). These plateaus are sustained by weathered ultramafic rocks, which are characterized by silica-rich laterites in the upper portions of the weathered profile. The most remarkable geological feature of the Vermelho Complex is the subhorizontal distribution of different mafic-ultramafic rocks in the V1 and V2 plateaus. The horizontal contact between different mafic-ultramafic rocks, indicated by the topographic contours in Figure 1.2, is well exposed in the edge of the hills (Fig. 1.3B and 1.3C). The horizontal contact of upper weathered serpentinite and lower orthopyroxenite (Fig. 1.3C) exposed in the slopes of both V1 and V2 hills, were intercepted all the way through these hills by the detailed drilling program (grid of 50x50 meters) developed by VALE. This

subhorizontal layering of the intrusion indicates that the upper portions of V1 and V2 hills, where the Ni-laterite deposits are located, represent outcrops of the same layer of dunite-harzburgite (Fig. 1.4). These hills thus represent two inselbergs preserved from erosion by the weathered-resistant silica-rich cap of the lateritic profile (Fig. 1.3A).

The stratigraphy of the Vermelho Complex proposed in this study is based on two main geological evidences. Firstly it considers the existence of an upper sequence of horizontally layered ultramafic rocks, designated here as the Upper Zone. Secondly, it considers the existence of a lower sequence of ultramafic to mafic rocks developed in the base of the intrusion, designated here as the Lower Zone. The geological description presented in this study follows the stratigraphy indicated in Figures 1.2, 1.4 and 1.5.

Host rocks of the Vermelho Complex include banded gneiss of the Xingú Complex, massive granitic rocks and metagabbroic rocks (Fig. 1.2). Intrusive contacts with banded gneiss and massive granitic rocks are exposed close to the V1 and V2 hills, but are mainly covered in the NE and SW portions of the Vermelho Complex.

Late diabase dikes of unkown absolute age cross cut the Vermelho Complex and country rocks. Diabase dikes consist of fine-grained rocks with intergranular texture. These rocks consist mainly of saussuritized plagioclase laths (50-55 vol. %), anhedral pseudomorphs of clinopyroxene replaced by amphibole (35-45 vol. %), ilmenite (up to 5 vol. %), rutile (< 1 vol. %) and minor quartz (< 5 vol. %).
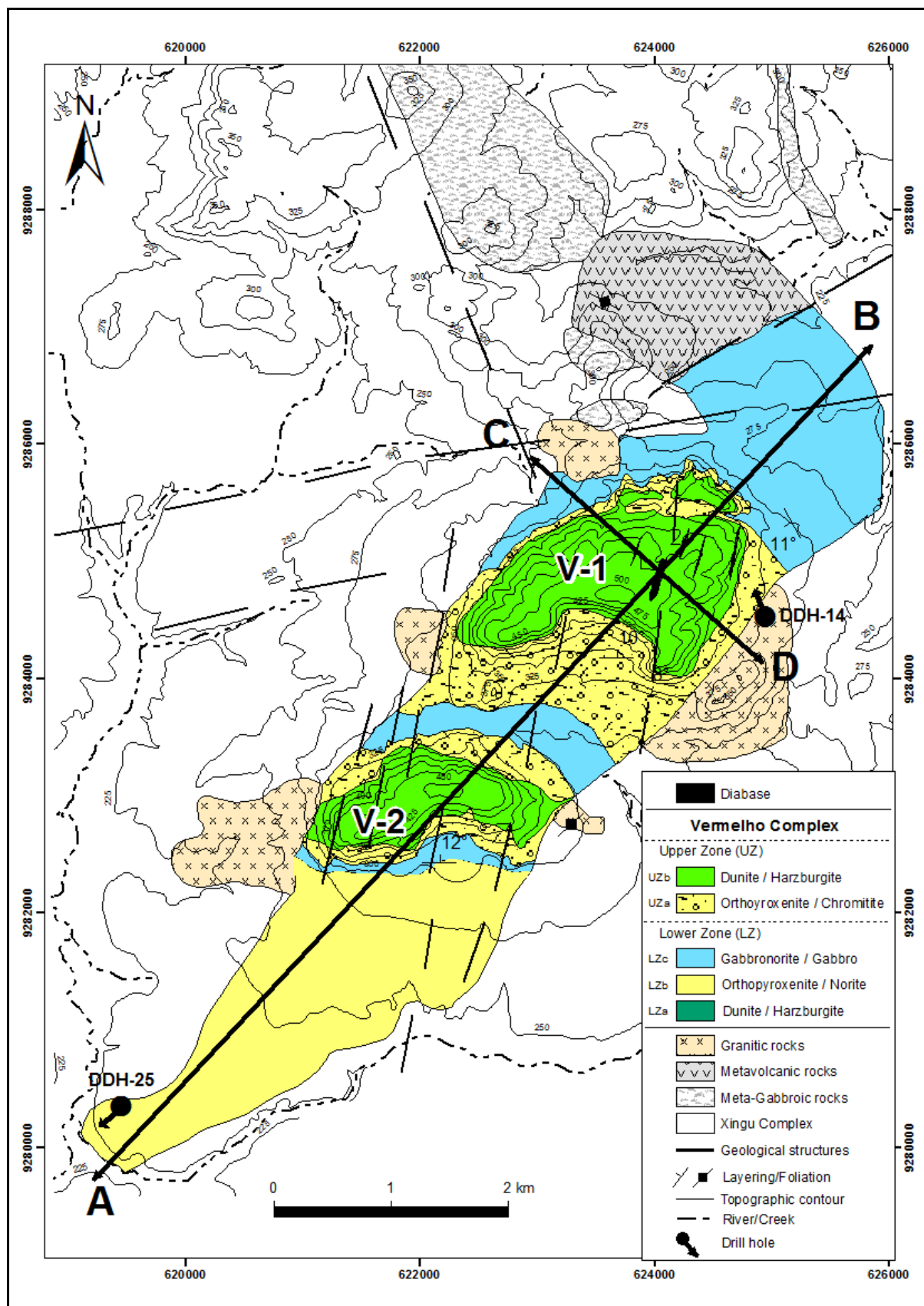
Figure 1.2. Geological map of the Vermelho Complex. Modified from CVRD (2004).
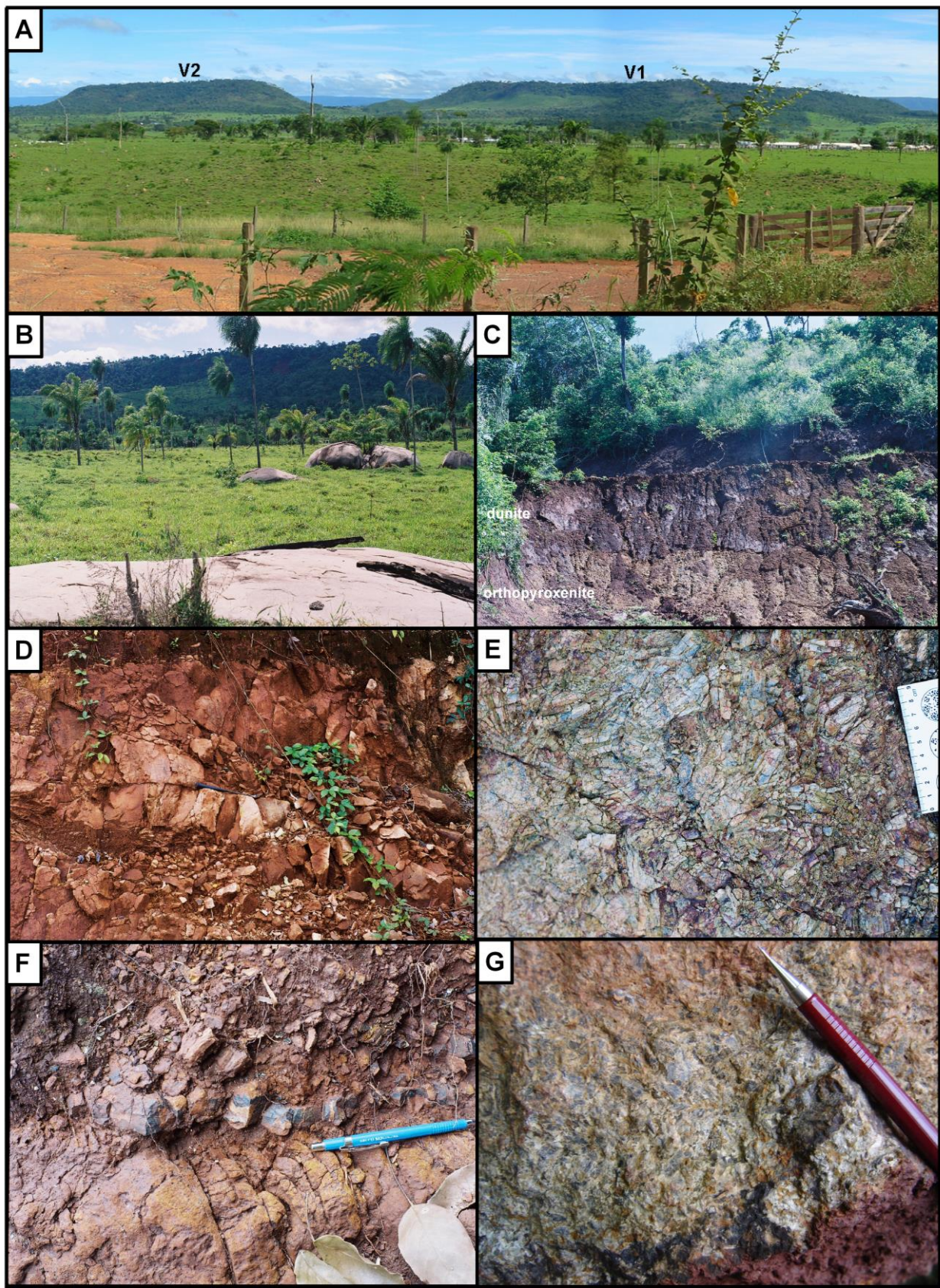
Figure 1.3. A) Panoramic view of the Vermelho Complex showing V1 and V2 plateau-like hills (looking northwest). B) Outcrop of granitoid basement rocks, V1 hill on the background. C) Horizontal contact of weathered dunite (above) and orthopyroxenite (below) from the Upper Zone of the V1 hill. D) Outcrop of dunite of the Upper Zone (V1 hill). E) Outcrop of coarse-grained orthopyroxenite of the Upper Zone (V1 hill). F) Subhorizontal chromitite layer

(black) hosted by orthopyroxenite of the Upper Zone (V2 hill). G) Coarse-grained gabbronorite of the Lower Zone (V2 hill).

Lower Zone

The Lower Zone is just well exposed close to the V1 and V2 hills, where outcrops of unweathered gabbroic rocks occur. Away from the V1 and V2 hills, or stratigraphically below the gabbroic rocks, geological data are mainly provided by drill cores, including two deep holes (DDH-14 and DDH-25; Fig. 1.5) and several shallow holes (< 100 meters). The thickness of the Lower Zone is highly variable and the contact border is variable but generally subhorizontal away from the V1 hill (Fig. 1.5). This zone extends for more than 400 meters below the V1 hill, as indicated by DDH-14 (Fig. 1.4 and 1.5), but becomes progressively shallower toward the northeastern and southwestern portions of the intrusion (Fig. 1.4 and 1.5). Change in thickness in the Lower Zone is likely to indicate the existence of a conduit-type structure below the V1 hill, as suggested in the interpreted geological section in Figure 1.4. This interpretation is supported by deep MAG anomalies restricted to this portion of the intrusion. Based on different rock assemblages three subzones (LZa, LZb, LZc) are distinguished in the Lower Zone (Fig. 1.4).

The LZa consists mainly of dunite and harzburgite with minor orthopyroxenite (Fig. 1.6A to 1.6D). Lza does not outcrop (Fig. 1.2 and 1.4) and the following description is based on drill core description. In drill core DDH-14 a sequence of ultramafic rocks has a steep contact with host granitic rocks (Fig. 1.5). The contact zone intercepted in DDH-14 is characterized by few meters of poorly preserved core consisting of highly altered fine-grained mafic rock. This contact zone is followed inward by interlayered orthopyroxenite, harzburgite and dunite (Fig. 1.6C and 1.6D), the latter prevailing at the lower portion of the core. In drill core DDH-25 a sharp subhorizontal basal contact of harzburgite with gneissic rocks (country rocks) was intercepted (Fig. 1.5). DDH-25 consists of harzburgite (Ol+Chr cumulate with intercumulus Opx) in the lower part of the core (Fig. 1.6A), followed by plagioclase orthopyroxenite (Opx+Chr cumulate with intercumulus Pl) of the LZb. Dunite and harzburgite of both DDH-14 and DDH-25 are partially to extensively serpentinized, but primary igneous textures are largely preserved. This alteration is heterogeneous, varying from extensive in dunite to moderate or minor in harzburgite and orthopyroxenite. Description of these samples are based on the original primary mineralogy, such that several rocks described/mapped as dunite or harzburgite consist mainly of serpentine, talc and magnetite (e.g. serpentinite, talc-serpentinite). Samples of dunite, restricted to core samples from DDH-

14, are medium-grained adcumulate rocks (Fig. 1.7A), consisting of cumulus Ol+Chr and minor interstitial Opx. Harzburgite has coarse- to medium-grained meso- to orthocumulate texture, consisting of cumulus Ol+Chr and abundant interstitial Opx (Fig. 1.7B). Orthocumulate texture is characterized by large (up to few centimeter) Opx oikocrysts enclosing several olivine crystals. These olivine crystals have rounded edges and gulf-like textures, indicating a reaction relation with Opx oikocrysts.

The LZb consists mainly of orthopyroxenite, melanorite and norite. The thickness of the LZb is not constrained by drilling below the V1 and V2 plateaus, where the thickest portion of the LZ is expected (Fig. 1.4). The LZb has scattered outcrops of weathered orthopyroxenites located to the south of the V2 hill and has been intercepted in shallow exploration drill holes. However, a complete section of unweathered rocks is restricted to bore hole DDH-25 (Fig. 1.2, 1.4 and 1.5). The contact of LZb with the underlying LZa in the drill hole DDH-25 is gradational. This contact is characterized by 20 meters of interlayered harzburgite and orthopyroxenite, that is followed upwards by plagioclase orthopyroxenite and melanorite (Opx cumulate with intercumulus Pl). Above this gradational contact, orthopyroxene cumulates with variable amounts of intercumulus plagioclase prevail. Depending on the amount of interstitial plagioclase textures vary from adcumulate (orthopyroxenite; Fig. 1.7C), to mesocumulate (Pl orthopyroxenite or melanorite; Fig. 1.7D) and orthocumulate (norite). Accessory magmatic minerals in these rocks include chromite and phlogopite. Chromite is a conspicuous accessory mineral (up to 2 vol. %) that occurs as fine-grained euhedral crystals. Phlogopite occurs in variable proportions (from none to 3 vol. %) as interstitial crystals to Opx (Fig. 1.7D).

The LZc outcrops in several boulders and blocks close to V1 and V2 plateaus. Contact with underlying Pl-orthopyroxenite and norite of the LZb is poorly preserved. Medium- to coarse-grained massive gabbroic to leucogabbroic rocks predominate in the LZc (Fig. 1.3G). Compositions vary from gabbronorite, gabbro and quartz-bearing leucogabbro or leucogabbronorite. Quartz occurs as an interstitial mineral in several gabbroic rocks (up to10 vol. %), but may reach up to 25 vol. % in coarse-grained leucogabbroic rocks. Gabbro and gabbronorite with abundant quartz (> 5 vol %) have accessory ilmenite (up to 5 vo. %), magnetite (up to 4 vol. %), phlogopite (up to 1 vol. %), hornblende (up to 1 vol. %), apatite (up to 1 vol. %) and zircon (< 1 vol. %). Some of these quartz-bearing rocks have orthopyroxene with abundant exsolution lamellae of clinopyroxene (and herringbone structures) indicating that it is an inverted pigeonite (Fig. 1.7E).

Upper Zone

The Upper Zone (UZ), exposed in the V1 and V2 hills (Fig. 1.2, 1.3A and 1.4), consists of two major subhorizontal layers that were partially preserved from erosion in these hills (Fig. 1.3C). The UZ has a minimum thickness of about 175 meters, broadly corresponding to the maximum height of the V1 plateau above the surrounding flat lands. The UZ is subdivided in two subzones (UZa and UZb).

The UZa consists of a thick layer (up to 50 meter) of orthopyroxenite with minor associated chromitite. Rocks of the UZa are usually partially to extensively weathered such that fresh rocks are restricted to road cuts in the slopes of the V1 and V2 hills or in drill cores. The contact of the UZa with the underlying LZc does not outcrop, but a sharp transition from overlying orthopyroxenite and underlying gabbroic boulders is indicated at the base of the V1 and V2 hills. The orthopyroxenite of the UZa has coarse- to medium-grained adcumulate texture (Fig. 1.3E and 1.7F), consisting of cumulus orthopyroxene and chromite (1-3 vol. %). Chromite occurs mainly as disseminated fine-grained euhedral crystals in orthopyroxenite, but may also occurs in chromite-rich pods (Fig. 1.3E and 1.3F). These pods (or discontinuous layers) are few centimeter thick and have modal chromite varying from massive (Fig. 1.3F and 1.7G) to just above regular cotetic concentration (> 5 vol. %). Chromite crystals in chromitite pods are fine-grained and usually form annealed aggregates around prismatic Opx crystals.

The UZb consists of a thick layer (up to 125 meter) of extensively weathered dunite and harzburgite. These rocks are the protolith of the Ni-laterite ore of the Vermelho deposit. The contact of the UZb and the underlying UZa is sharp and well exposed in the slopes of the V1 and V2 hills (Fig. 1.3B and 1.3C). Due to pervasive weathering or serpentinization none primary silicates are preserved in rocks from the UZb. Unweathered to mildly weathered rocks of the UZb are restricted to few road cuts (Fig. 1.3D) and the base of drill holes. These rocks are mainly serpentinite with preserved medium-grained adcumulate (pseudomorphs of Ol; Fig. 1.7H) to mesocumulate (pseudomorphs of cumulus Ol and intercumulus Opx) texture. These rocks, consisting mainly of fine-grained serpentine and magnetite with variable proportions of talc, carbonate and minor chlorite, are interpreted as serpentinized dunite and harzburgite. Chromite is partially to highly altered to Fe-hydroxides and occurs as disseminated (2-3 vol. %) fine-grained euhedral crystals in both dunite and harzburgite.
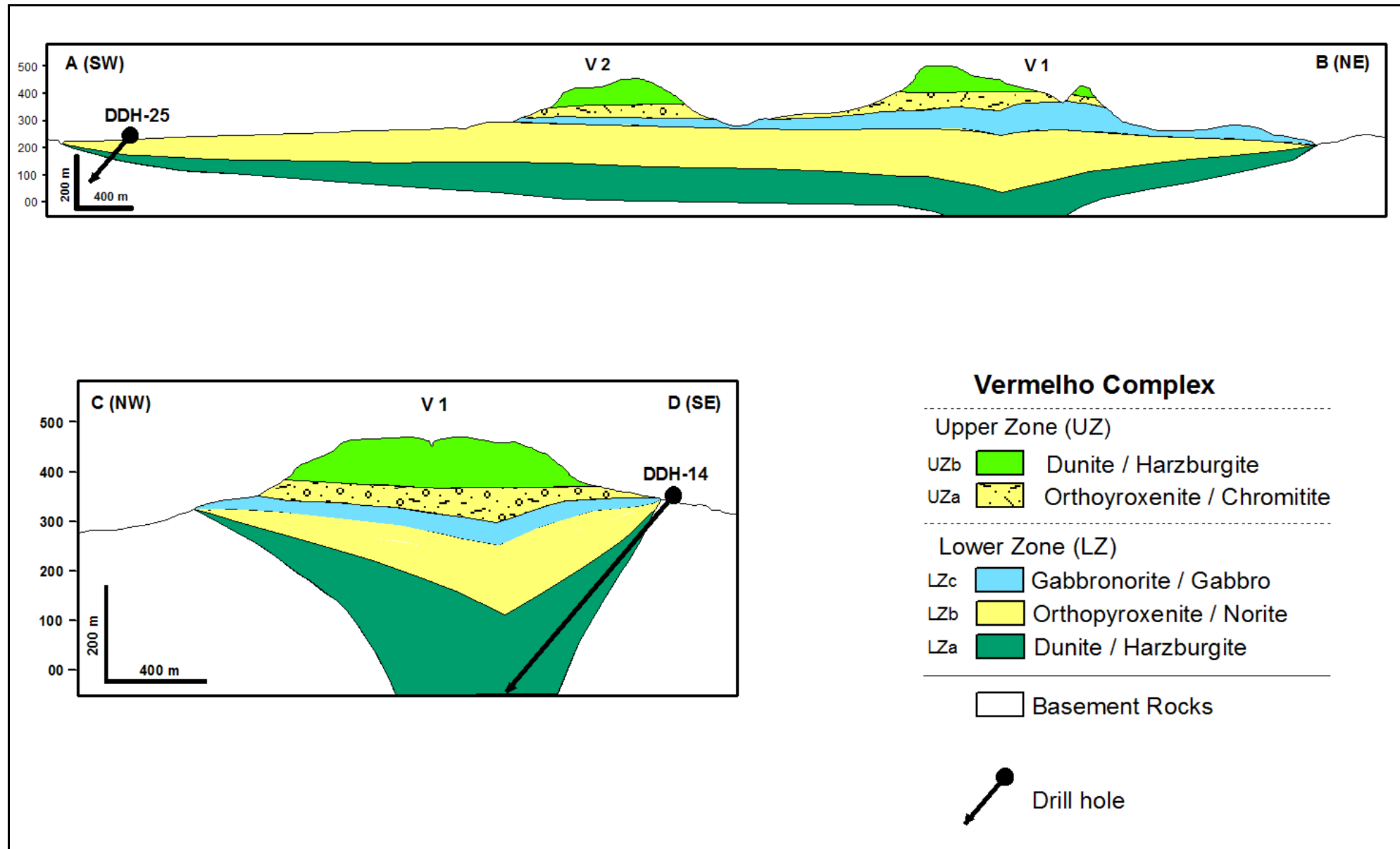
Figure 1.4. Geological sections "A-B" and "C-D" in the Vermelho Complex. (see Fig. 1.2 for location of vertical profiles).
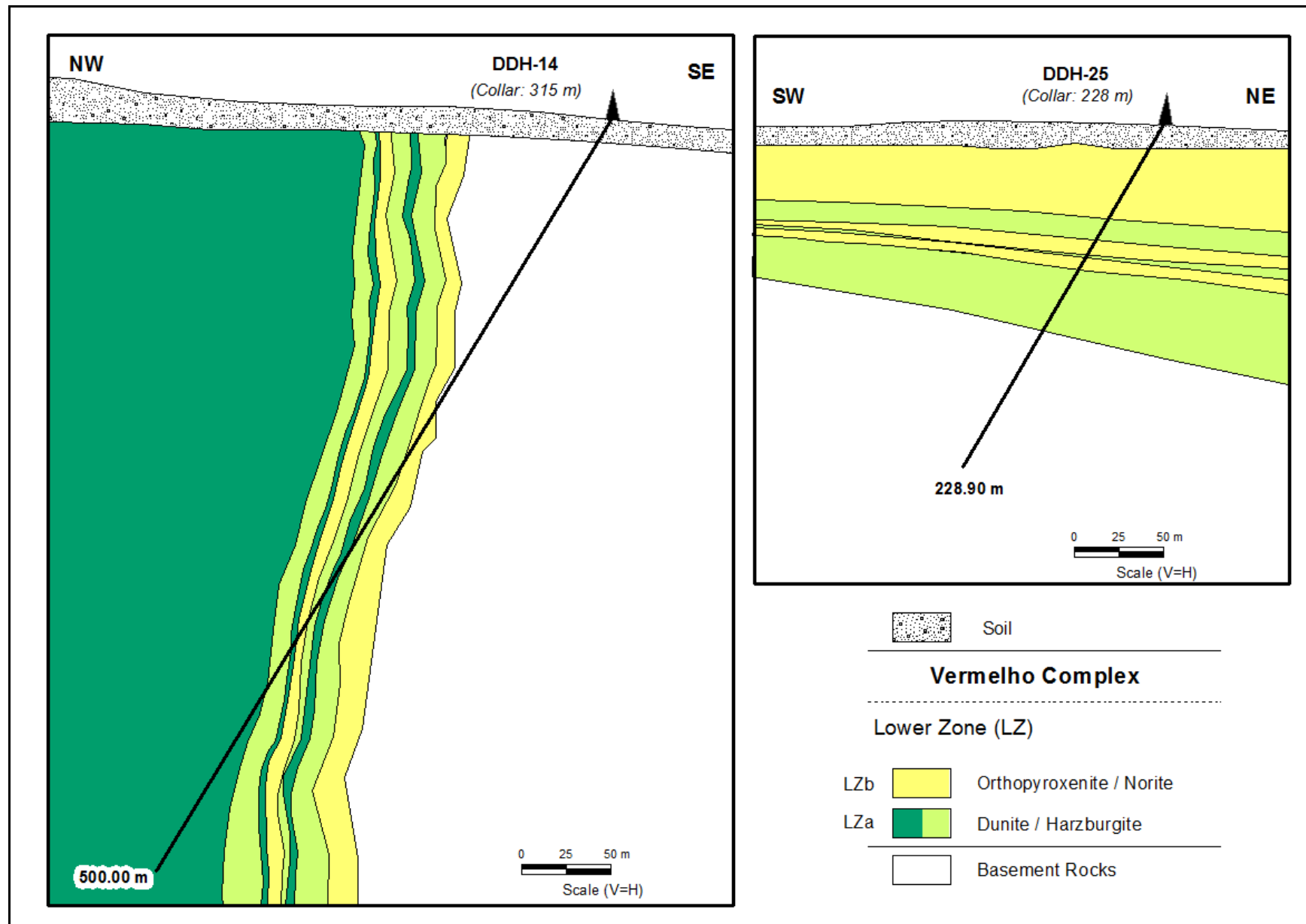
Figure 1.5. Geological sections "DDH-14" and "DDH-25". (see Fig. 1.2 for location of drill holes).

Figure 1.6. A) Oikocrysts of orthopyroxene in harzburgite of the LZa (DDH-25). B) Gradational contact of harzburgite and orthopyroxenite from the LZa (DDH-14). C) Contact of dunite and orthopyroxenite layer of the LZa (DDH-14). D) Close-up of dunite-orthopyroxenite contact of the LZa (DDH-14). Core is 4.5 cm wide.
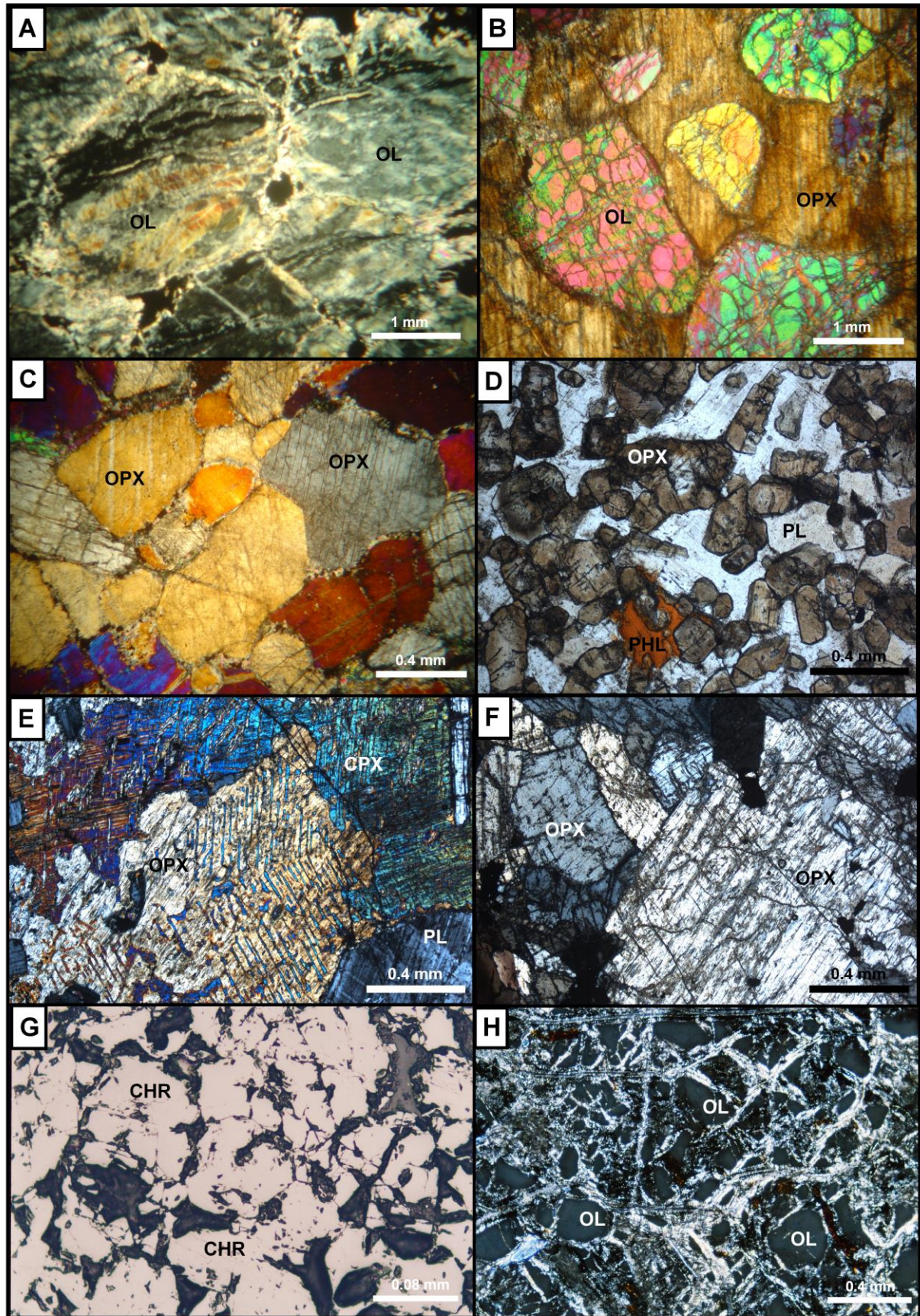
Figure 1.7. Photomicrographs of representative rocks of the Vermelho Complex. A) Serpentinized dunite of the LZa. Adcumulate texture is defined by olivine pseudomorphs (OL) replaced by serpentine-talc-magnetite. View in cross-polarized light (XPL). B) Harzburgite of the LZa. Orthocumulate texture consisting of cumulus olivine (OL) enclosed

in orthopyroxene (OPX) oikocryst (XPL). C) Orthopyroxenite of the LZb with adcumulate texture (XPL). D) Mesocumulate melanorite of the LZc with cumulus orthopyroxene (OPX) and intercumulus plagioclase (PL) and phlogopite (PHL). View in plane-polarized light (PPL). E) Gabbronorite of the LZc with orthopyroxene (OPX) showing exsolution lamellae of clinopyroxene (CPX) in herringbone structures (XPL). F) Orthopyroxenite of the UZa. Note variable sized Opx crystals and adcumulate texture (XPL). G) Massive chromitite of the UZa. View in reflected light (PPL). H) Dunite of the UZb showing pervasive serpentinization and euhedral pseudomorphs of olivine (XPL).

Mineral Chemistry

Systematic analyses of Opx and Ol crystals were performed in unweathered samples from the LZ collected in bore holes DDH-14 (9 samples) and DDH-25 (14 samples). Additional analyses of Opx, Pl and Cpx were acquired in 3 samples from outcrops of gabbroic rocks (gabbronorite and leuco-gabbronorite) from the LZc. Analyses of orthopyroxenite were also acquired in two samples of fresh orthopyroxenite from the UZa. Due to the extensive weathering or serpentinization of dunite and harzburgite from the UZb, no magmatic silicates (Ol or Opx) were preserved in this zone for compositional studies.

Systematic compositional variation of Ol and Opx throughout the drill holes DDH-14 and DDH-25 (Fig. 1.8) provide cryptic variation data for harzburgite and olivine orthopyroxenite in sections of the LZ. In these samples Ol compositions range from $Fo_{88.0}$ to $Fo_{85.6}$ and $Fo_{90.5}$ to $Fo_{86.6}$ in the DDH-14 and DDH-25 bore holes respectively. Ol compositions are primitive (i.e. have high Fo content) and have a limited compositional variation in samples for both drill holes. Ni contents in olivine range from 2200-3950 ppm and from 1750-3400 ppm in the DDH-14 and DDH-25 bore holes respectively (Fig. 1.8). Ni contents are positively correlated with Fo contents in both bore holes but are distinctively lower in bore hole DDH-25, specially when compared with similar Fo compositions (Fig. 1.9). Distinct Ni contents for olivine crystals from bore holes DDH-14 and DDH-25 suggest minor Ni depletion in olivine crystals formed in distal portions of the LZ. Because significant amount of sulfides where not identified in any of the bore holes of the LZ, and not indicated by the results of exploration geophysical surveys, the identified depletion of Ni should be associated with minor segregation of sulfides toward the SW border of the intrusion. Opx compositions range from $En_{92.1}$ to $En_{85.6}$ and $En_{91.0}$ to $En_{77.2}$ in the DDH-14 and DDH-25 bore holes respectively. Opx compositions are primitive and have a limited compositional variation in few analysed samples from the bore hole DDH-14, while in bore hole DDH-25 the

composition of Opx vary from primitive in harzburgite to more fractionated in the upward Ol orthopyroxenite and melanorite (Fig. 1.8). Compositional variations of Ol and Opx are limited in the border contact zone (about 100 meter thick) intercepted by bore hole DDH-14 (Fig. 1.5 and 1.8), such that no systematic fractionation is indicated in this border zone. In bore hole DDH-25 the compositional variation of Opx and Ol indicates a lower portion (below 94 m) of harzburgite characterized by primitive mineral compositions, an intermediate portion (from 94 to 70 m) of harzburgite characterized by the most primitive mineral compositions interlayered with orthopyroxenites with more fractionated mineral compositions, and an upper portion (above 70 m) of melanorite where Opx have more fractionated compositions within a limited compositional range. Compositional variations of Ol and Opx throughout bore hole DDH-25 is consistent with an upward fractionation from the base of the LZa toward the overlying melanorite of the LZb.

The composition of Opx crystals was obtained for three gabbroic rocks (gabbronorite and leuco-gabbronorite) from outcrops of the LZc. Opx compositions in these samples range from $En_{63.8}$ to $En_{57.5}$ and are significantly more fractionated than Opx compositions obtained in crystals from orthopyroxenite and melanorite from the LZb (Fig. 1.10). Even though absolute values for TiO_2 and Cr_2O_3 for Opx analyses are highly scattered, a result of overall lower contents together with analyses including small portions of fine-grained Cpx exsolution, results indicate that Opx compositions of rocks from the LZc have higher TiO_2 contents and lower Cr_2O_3 contents compared to Opx compositions of rocks from the LZb (Fig. 1.10). The composition of Cpx ($En_{49.5}$ to $En_{28.1}$) and Pl crystals ($An_{58.8}$ to $An_{43.8}$) are consistent with the results obtained for Opx crystals of the same gabbroic rocks.

Opx crystals from two samples of orthopyroxenite of the UZa have primitive compositions ($En_{85.7}$ to $En_{83.0}$). These samples have Opx compositions with higher En contents compared to samples of the underlying gabbroic rocks, as well as samples of orthopyroxenites of the LZb (Fig. 1.10).

Table 1.1. Representative analyses of olivine.

Sample	244OL1.2	275OL3.2	297OL2.1	306OL2.2	311OL5.2	323OL1.2	330OL1.2	370OL3.2	RAV64	RAV65	RAV66	RAV60	RAV61	RAV63	RAV59
Location	GT14-244	GT14-275.3	GT14-297.9	GT14-306.1	GT14-311.3	GT14-323.6	GT14-330.8	GT14-370.8	GT25-108.75	GT25-102.2	GT25-96.2	GT25-130.75	GT25-123.6	GT25-114.4	GT25-134.79
Rock type	Hbz-LZ	Hbz-LZ	Hbz-LZ	Hbz-LZ	Hbz-LZ	Hbz-LZ	Hbz-LZ	Ol-Opxt-LZ	Hzb-LZ	Hzb-LZ	Hzb-LZ	Hzb-LZ	Hzb-LZ	Hzb-LZ	Hzb-LZ
SiO_2	40.77	40.49	40.57	40.96	39.95	40.63	40.53	40.83	38.82	38.15	39.24	40.55	40.44	40.68	40.57
TiO_2	0.04	0.03	<0.01	0.02	0.02	0.00	0.01	0.01	<0.01	<0.01	<0.01	<0.01	<0.01	<0.01	<0.01
Al_2O_3	0.12	0.02	<0.01	0.07	0.06	<0.01	<0.01	<0.01	<0.01	<0.01	<0.01	0.03	<0.01	<0.01	0.08
Cr_2O_3	0.09	0.04	<0.01	0.05	<0.01	<0.01	0.03	0.01	0.02	0.03	<0.01	0.01	<0.01	0.03	<0.01
FeO	13.42	12.92	11.70	12.04	13.50	13.22	12.64	13.37	12.42	13.00	11.84	12.04	11.98	12.60	11.94
MnO	0.07	0.11	0.08	0.05	0.07	0.04	0.07	0.07	0.10	0.15	0.08	0.09	0.14	0.14	0.12
MgO	46.00	46.20	47.71	47.37	46.16	46.39	46.74	45.78	48.14	47.68	48.50	46.89	47.17	47.03	46.87
NiO	0.41	0.45	0.49	0.42	0.32	0.31	0.32	0.33	0.37	0.40	0.45	0.40	0.35	0.28	0.44
Total	100.92	100.26	100.54	100.98	100.06	100.59	100.34	100.40	99.87	99.40	100.10	100.01	100.07	100.76	100.03
Si	1.006	1.005	0.998	1.004	0.996	1.005	1.003	1.012	0.969	0.961	0.974	1.003	1.001	1.002	1.006
Al	0.004	0.001	<0.001	0.002	0.002	<0.001	<0.001	<0.001	<0.001	<0.001	<0.001	0.001	<0.001	<0.001	0.002
Ti	0.001	0.001	<0.001	<0.001	<0.001	<0.001	<0.001	<0.001	<0.001	<0.001	<0.001	<0.001	<0.001	<0.001	<0.001
Cr	0.002	0.001	<0.001	0.001	<0.001	<0.001	<0.001	<0.001	<0.001	0.001	<0.001	<0.001	0.000	0.001	<0.001
Fe	0.277	0.268	0.241	0.247	0.281	0.273	0.262	0.277	0.259	0.274	0.246	0.249	0.248	0.260	0.248
Mn	0.001	0.002	0.002	0.001	0.001	0.001	0.002	0.002	0.002	0.003	0.002	0.002	0.003	0.003	0.003
Mg	1.692	1.708	1.750	1.731	1.715	1.710	1.723	1.691	1.791	1.791	1.794	1.730	1.740	1.726	1.733
Ni	0.008	0.009	0.010	0.008	0.006	0.006	0.006	0.006	0.007	0.008	0.009	0.008	0.007	0.006	0.009
Total	2.99	3.00	3.00	2.99	3.00	3.00	3.00	2.99	3.03	3.04	3.02	2.99	3.00	3.00	3.00
Fo	85.87	86.33	87.87	87.47	85.86	86.19	86.78	85.87	87.35	86.73	87.96	87.41	87.53	86.93	87.50
Ni ppm	3255	3498	3821	3294	2492	2429	2539	2555	2297.00	2445.19	2760.10	2469.89	2179.68	1747.45	2723.05

Table 1.2. Representative analyses of orthopyroxene.

Sample	297-OPX1.1	330-OPX2.1	473-OPX1.1	RAV68	RAV69	RAV70	RAV71	RAV65	RAV66	RAV67	RAV60	RAV61	RAV61	RAV62	RAV63	RAV73	RAV74	80	16	29	38
Location	GT14-297.9	GT14-330.8	GT14-473.6	GT25-85.9	GT25-77.9	GT25-73.15	GT25-71.5	GT25-102.2	GT25-96.2	GT25-90.4	GT25-130.75	GT25-123.6	GT25-123.6	GT25-120.3	GT25-114.4	GT25-60.85	GT25-50.25	V1-04C	V1-04D	62	94
Rock type	Hzb-LZ	Hzb-LZ	Hzb-LZ	Hzb-LZ	Pl-Opxt-LZ	Hzb-LZ	Hzb-LZ	Hzb-LZ	Hzb-LZ	Opxt-LZ	Hzb-LZ	Hzb-LZ	Hzb-LZ	Hzb-LZ	Hzb-LZ	Pl-Opxt-LZ	Pl-Opxt-LZ	Opxt-UZ	Opxt-UZ	Gbnor-LZ	Lgbnor-LZ
SiO_2	56.57	56.92	57.32	56.53	54.94	56.46	56.15	55.50	54.80	53.63	56.90	56.39	55.87	56.67	56.74	54.70	55.70	56.38	56.65	52.35	52.37
TiO_2	0.08	0.09	0.02	0.03	0.03	0.04	0.06	<0.01	0.11	0.03	<0.01	<0.01	0.04	0.08	<0.01	0.06	0.06	<0.01	<0.01	0.19	0.01
Al_2O_3	1.15	1.53	0.87	1.54	1.17	0.88	1.74	0.47	1.82	1.17	1.45	1.02	1.55	1.55	1.13	0.85	1.17	1.01	1.10	0.95	0.73
Cr_2O_3	0.41	0.60	0.06	0.16	0.34	0.27	0.67	<0.01	0.42	0.04	0.37	0.13	0.13	0.38	0.07	0.23	0.38	0.23	0.15	0.01	<0.01
FeO	8.65	7.59	9.77	8.63	15.28	6.53	5.74	8.87	7.99	14.99	9.07	8.88	8.29	8.09	8.79	14.78	13.48	10.15	10.90	23.68	25.64
MnO	0.07	0.06	0.10	0.17	0.32	0.19	0.18	0.19	0.18	0.25	0.16	0.14	0.13	0.09	0.09	0.28	0.25	0.09	0.08	0.52	0.63
MgO	32.61	33.13	32.60	33.28	29.10	35.17	32.75	34.40	33.88	29.65	32.71	32.40	32.93	32.74	33.01	28.01	29.58	32.05	31.25	21.16	19.50
NiO	0.08	0.07	0.05	0.08	0.05	0.13	0.07	0.06	0.08	0.08	0.09	0.06	0.04	0.03	0.07	0.06	0.10	0.01	0.05	0.03	0.05
CaO	0.48	0.37	0.05	0.16	0.33	0.92	3.58	0.13	1.01	0.15	0.11	0.08	0.15	0.89	0.09	1.32	0.22	0.04	0.14	1.07	0.48
Na_2O	<0.01	<0.01	<0.01	0.03	<0.01	0.05	0.09	0.02	0.02	0.01	0.08	<0.01	<0.01	0.01	0.02	0.07	0.05	0.01	<0.01	0.00	0.01
K_2O	0.02	0.29	0.02	<0.01	<0.01	0.03	<0.01	0.01	0.03	0.01	0.02	0.08	0.22	0.00	<0.01	0.01	<0.01	0.02	0.01	0.03	<0.01
Total	100.10	100.66	100.86	100.60	101.56	100.66	101.03	99.64	100.32	100.02	100.98	99.22	99.33	100.54	100.01	100.36	100.99	99.99	100.32	99.98	99.42
Si	1.970	1.955	1.985	7.828	7.791	7.782	7.743	7.794	7.647	7.725	7.867	7.920	7.835	7.848	7.899	7.854	7.865	7.900	7.932	7.867	7.968
Al	0.047	0.062	0.036	0.251	0.195	0.143	0.283	0.078	0.299	0.199	0.237	0.170	0.256	0.253	0.186	0.144	0.195	0.167	0.181	0.169	0.131
Ti	0.002	0.002	<0.001	0.003	0.004	0.004	0.006	<0.001	0.012	0.004	<0.001	0.005	0.004	0.008	<0.001	0.007	0.006	<0.001	<0.001	0.022	0.002
Cr	0.011	0.016	0.002	0.017	0.039	0.030	0.073	<0.001	0.046	0.005	0.041	0.015	0.015	0.042	0.007	0.027	0.043	0.026	0.017	0.002	<0.001
Fe	0.252	0.218	0.283	0.999	1.813	0.753	0.662	1.042	0.932	1.806	1.049	1.043	0.972	0.937	1.024	1.775	1.591	1.189	1.276	2.976	3.262
Mn	0.002	0.002	0.003	0.020	0.039	0.022	0.022	0.022	0.022	0.030	0.019	0.017	0.016	0.011	0.010	0.033	0.030	0.011	0.010	0.066	0.081
Mg	1.693	1.696	1.683	6.870	6.152	7.225	6.732	7.202	7.048	6.366	6.741	6.783	6.884	6.759	6.850	5.996	6.225	6.695	6.523	4.740	4.423
Ni	0.002	0.002	0.001	0.009	0.005	0.014	0.008	0.007	0.009	0.009	0.010	0.007	0.005	0.003	0.008	0.007	0.011	0.001	0.006	0.003	0.006
Ca	0.018	0.013	0.002	0.023	0.049	0.135	0.529	0.019	0.150	0.024	0.017	0.012	0.022	0.132	0.014	0.203	0.034	0.006	0.021	0.173	0.079
Na	<0.001	<0.001	<0.001	0.009	<0.001	0.013	0.024	0.005	0.006	0.002	0.023	<0.001	<0.001	0.004	0.006	0.018	0.013	0.003	<0.001	0.001	0.003
K	0.001	0.013	0.001	<0.001	<0.001	0.005	<0.001	0.002	0.005	0.001	0.004	0.014	0.039	<0.001	<0.001	0.001	<0.001	0.004	0.001	0.005	<0.001
Total	4.00	3.98	4.00	16.03	16.09	16.13	16.08	16.17	16.17	16.17	16.01	15.99	16.05	16.00	16.01	16.06	16.01	16.00	15.97	16.02	15.95
En	86.17	87.91	85.40	87.30	77.24	90.56	91.04	87.37	88.32	77.90	86.53	86.67	87.63	87.83	87.00	77.16	79.64	84.92	83.64	61.43	57.55
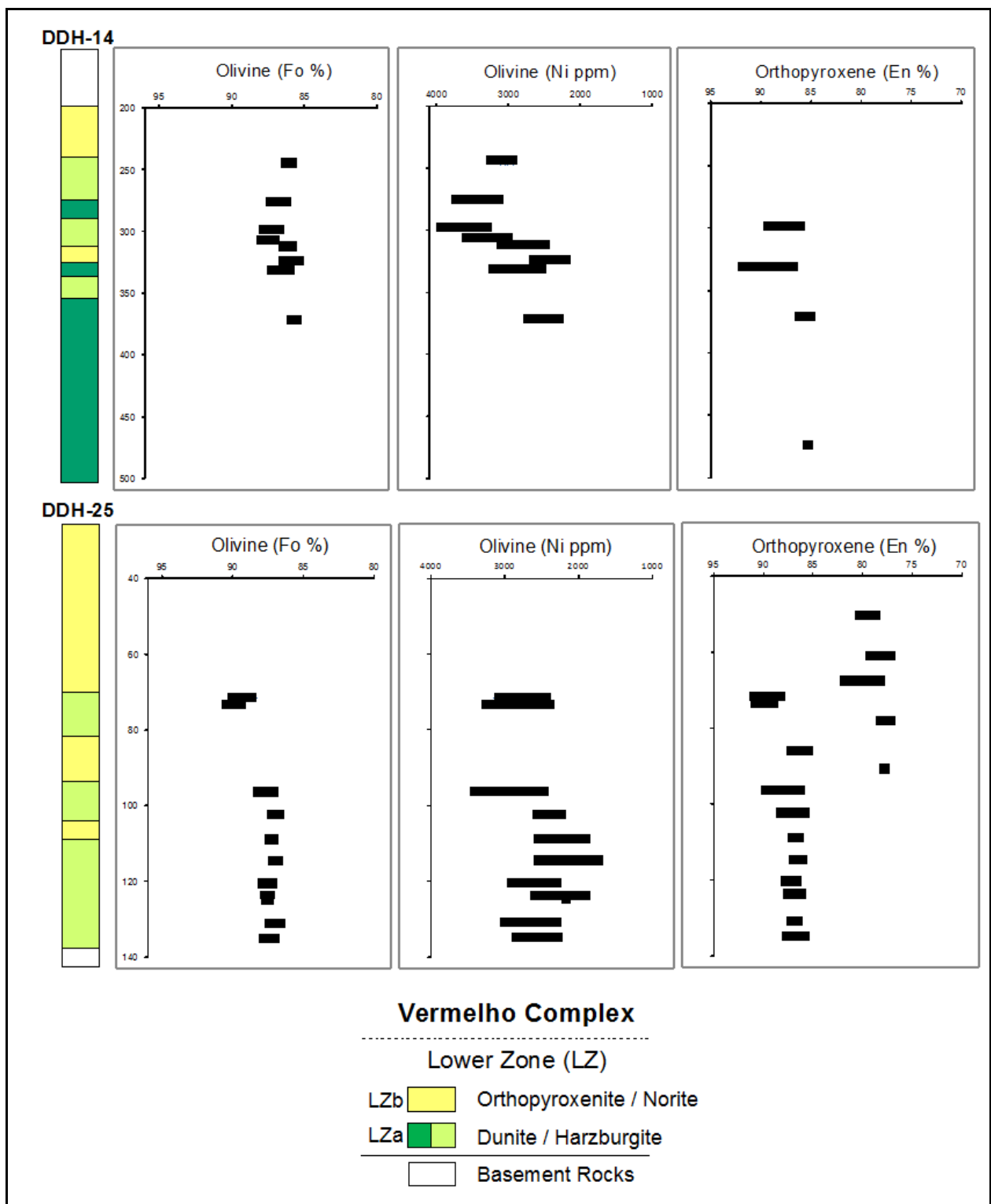
Figure 1.8. Compositional variation of olivine and orthopyroxene throughout bore holes DDH-14 and DDH-25.
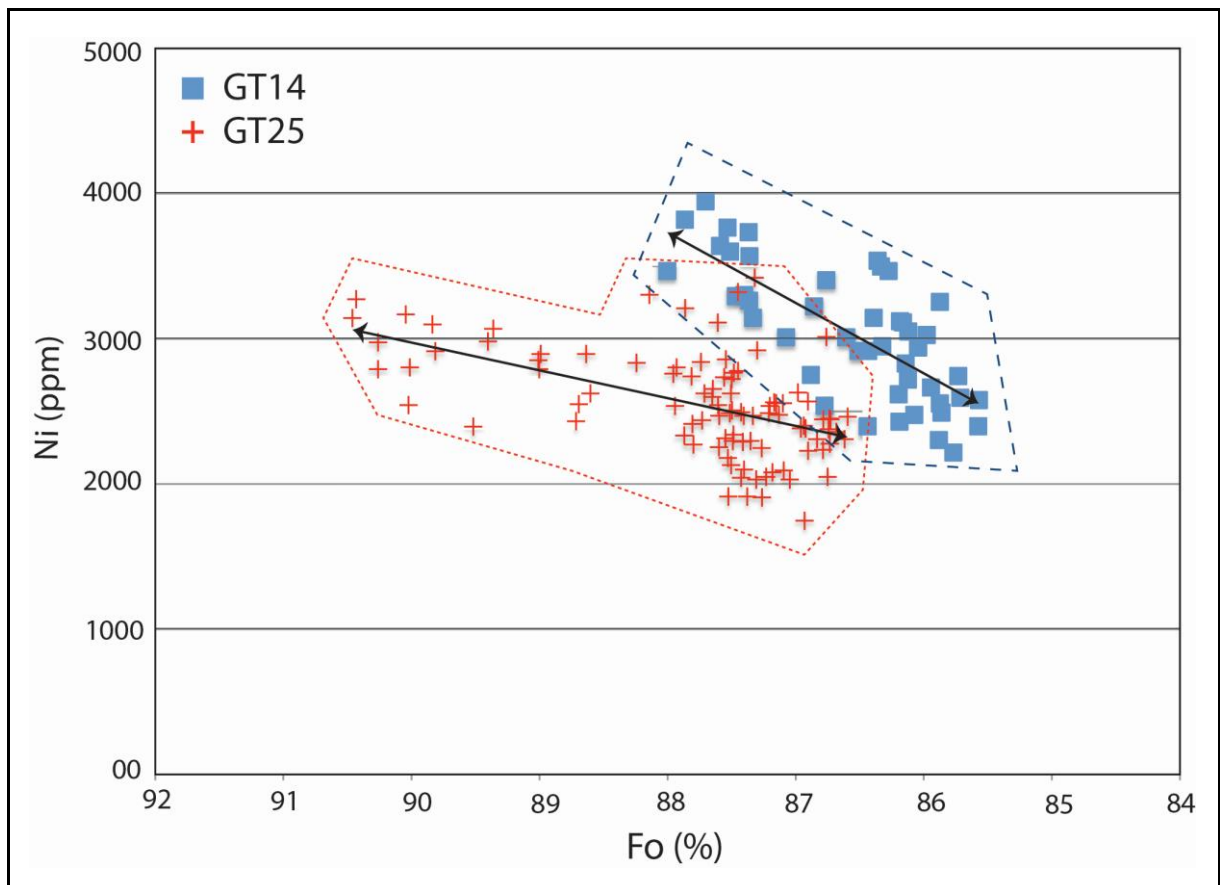
Figure 1.9. Plot of Fo versus Ni content of olivine from samples of harzburgite and olivine orthopyroxenite of the LZ. Data from DDH-14 and DDH-25 bore holes.
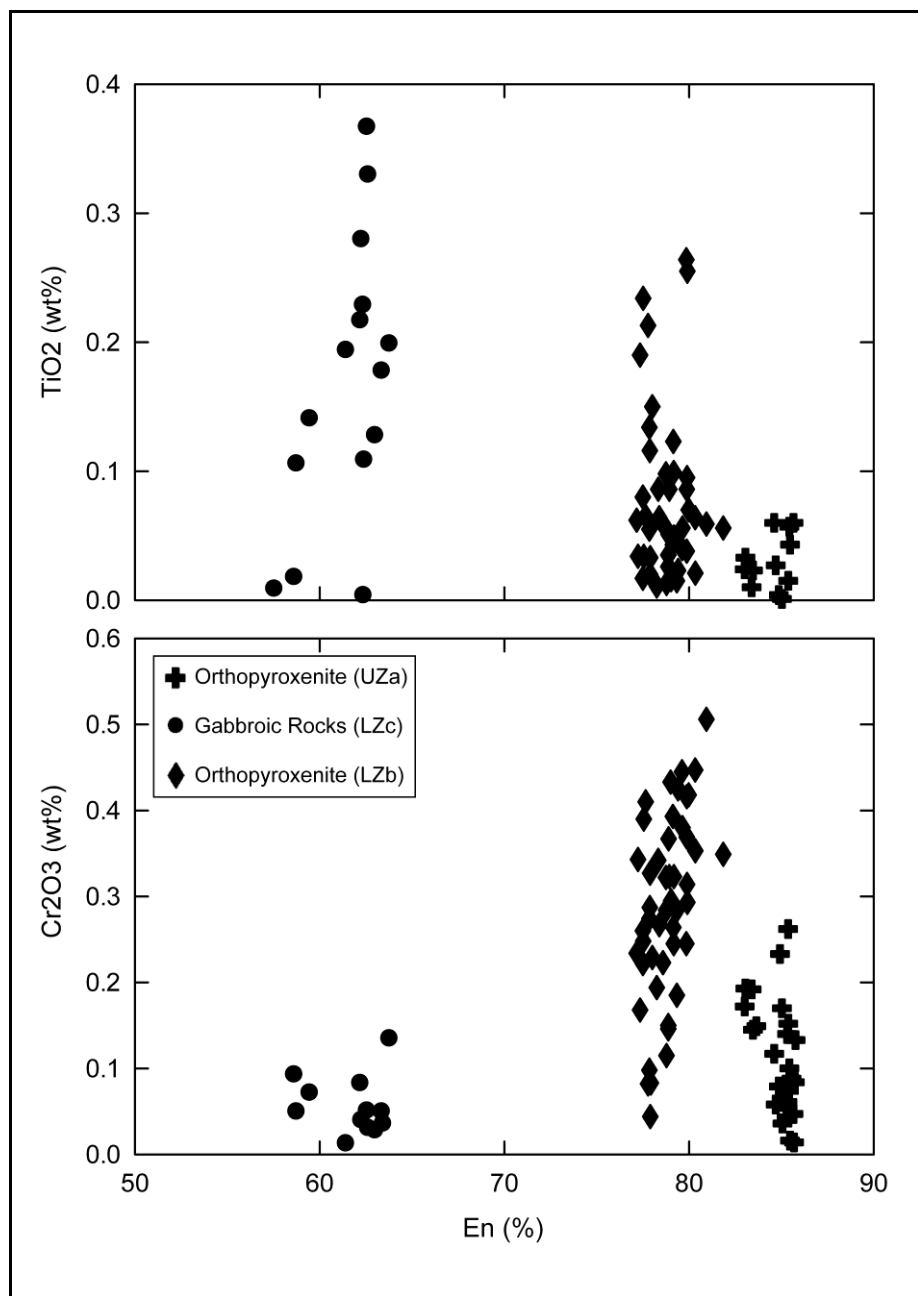
Figure 1.10. Plot of En versus TiO₂ and Cr₂O₃ contents of orthopyroxene of orthopyroxenite (LZb and UZa) and gabbroic rocks (LZc) of the Vermelho Complex.

Bulk Rock Geochemistry

Analysed samples (Table 1.3) were arranged into three groups representative of the main lithotypes of the Vermelho Complex. Harzburgitic rocks (8 samples) comprise variably serpentinized drill core samples from bore holes DDH-14 and DDH-25. Orthopyroxenitic rocks include two samples of plagioclase-orthopyroxenite from the LZb (bore hole DDH-25) and one sample of chromite-bearing orthopyroxenite from an outcrop of

the UZa. Gabbroic rocks (6 samples) include samples from outcrops located close to the V1 and V2 hills. The plots of major elements and selected trace elements versus MgO (Fig. 1.11) and chondrite-normalized REE patterns (Fig. 1.12) depict the main characteristics of these rocks. Because the Vermelho Complex consists of cumulate rocks, their major and minor element compositions are dominantly controlled by the type of cumulus minerals for each group of rocks.

Harzburgitic rocks have MgO contents bracket between 32.6 to 36.7 wt. % (or 34.29 to 40.12 wt.% anhydrous base) and very low CaO contents (0.10 to 0.35 wt. %), consistent with olivine and orthopyroxene cumulates. Al_2O_3 (1.26 to 5.20 wt. %) and K_2O contents (0.15 to 1.48 wt. %) are highly variable and related to the conspicuous presence of interstitial phlogopite. The contents of Ni and Cr in harzburgites are controlled by olivine and accessory chromite, respectively (Fig. 1.11). Cr_2O_3 contents (between 0.27 to 0.92 wt. %) are consistent with the occurrence of cumulus chromite in harzburgites. Harzburgitic rocks have relatively low contents of incompatible elements (Table 1.3), as expected for olivine and orthopyroxene cumulates. REE profiles for harzburgitic rocks are variable and discontinuous, possibly due to REE contents close to detection limits. In general REE profiles for harzburgitic rocks have slightly positive slope for LREE (average chondrite-normalized La/Sm = 2.62) and flat slope for HREE (average chondrite-normalized Sm/Yb = 1.18) (Fig. 1.12).

Plagioclase-orthopyroxenite samples from the LZb are characterized by MgO contents of 16.0-16.4 wt. % and high Al_2O_3 (9.63 and 10.12 wt. %), CaO (5.49 and 5.00 wt. %) and Na_2O (1.64 and 1.80 wt. %) contents, consistent with an orthopyroxene cumulate with abundant intercumulus plagioclase (Table 1.3). Contents of K_2O (0.53 and 0.78 wt. %) are high for this type of cumulate rock and result from conspicuous interstitial phlogopite as an accessory mineral. REE profiles for samples of plagioclase-orthopyroxenite (Fig. 1.12) have highly positive slope for LREE (chondrite-normalized La/Sm = 5.5 to 6.0) and positive slope for HREE (chondrite-normalized Sm/Yb = 1.17 to 1.85). Mantle-normalized alteration-resistant lithophile trace element profiles of plagioclase-orthopyroxenite samples are fractionated, as indicated by relative enrichment in LREE and Th, with pronounced negative Nb and Ta anomalies (Fig. 1.13). The composition of the chromite-bearing orthopyroxenite sample of the UZa is remarkably different when compared with plagioclase-orthopyroxenite samples of the LZb. The chromite-bearing orthopyroxenite is characterized by MgO content of 29.9 wt. % and very low Al_2O_3 (0.72 wt. %), CaO (0.08 wt. %), Na_2O (< 0.01 wt. %) and

K$_2$O (< 0.01 wt. %) contents, consistent with an orthopyroxene adcumulate. The high content of Cr$_2$O$_3$ (1.02 wt. %) is consistent with abundant accessory cumulus chromite in this sample. The chromite-bearing orthopyroxenite has relatively low contents of incompatible elements (Table 1.3), as expected for an orthopyroxene adcumulate. The REE profile for the chromite-bearing orthopyroxenite is comparable with those obtained for harzburgitic rocks of the LZb, characterized by a discontinuous profile with slightly positive slope for LREE (chondrite-normalized La/Sm = 2.1) and slightly negative slope for HREE (chondrite-normalized Sm/Yb = 0.49) (Fig. 1.12).

Gabbroic rocks of the LZc are characterized by low MgO content (2.22 to 6.77 wt. %) combined with high SiO$_2$ (53.2 to 66.0 wt. %), Al$_2$O$_3$ (14.60 to 17.99 wt. %), CaO (6.50 to 9.96 wt. %), Na$_2$O (3.38 to 5.37 wt. %) contents, consistent with fractionated plagioclase cumulates. Except for sample 110, REE profiles for samples of gabbroic rocks are similar (Fig. 1.12) and characterized by highly positive slope for LREE (average chondrite-normalized La/Sm = 4.2) and positive slope for HREE (average chondrite-normalized Sm/Yb = 1.9). These samples have none to mild positive anomaly of Eu. Sample 110 is the gabbroic rock with the lowest content of REE and is characterized by a distinctively high positive Eu anomaly. Mantle-normalized alteration-resistant lithophile trace element profiles of gabbroic rocks are fractionated, as indicated by relative enrichment in LREE and Th, with pronounced negative Nb anomalies (Fig. 1.13). Different trace element composition of gabbroic sample 110 may result from a plagioclase cumulate with lesser amounts of trapped intercumulus liquid, thus explaining a lower content of incompatible trace elements, combined with the presence of accessory zircon and ilmenite, which explain the relatively higher contents of Zr-Hf and Ti, respectively.

Table 1.3. Chemical composition of representative samples from Vermelho Complex. Major elements and S (wt. %), trace elements and REE (ppm).

Rock type	Hzb DDH-14 (LZa)				Hzb DDH-25 (LZa)				Pl-Opxt DDH-25 (LZb)		Gbnor/Gb rocks (LZc)						Opxt (UZa)
Sample	297	306	323	370	RAV-60	RAV-62	RAV-65	RAV-70	RAV-72	RAV-74	V2-10	V2-11	62	94	110	161	V1-04C
SiO2	41.20	40.80	43.10	46.40	43.40	41.90	39.10	41.50	53.24	56.00	66.00	58.20	53.20	57.90	55.40	54.40	53.30
TiO2	0.09	0.06	0.07	0.07	0.16	0.15	0.18	0.10	0.21	0.17	0.73	0.55	0.32	1.25	0.60	0.31	0.02
Al2O3	1.95	1.91	1.62	1.26	5.20	4.36	3.10	2.25	9.63	10.12	14.60	14.91	16.70	16.04	17.99	16.54	0.72
Cr2O3	0.80	0.59	0.27	0.48	0.92	0.71	0.42	0.78	0.21	0.18	<0.01	0.00	0.01	0.07	0.04	0.01	1.02
Fe2O3	9.76	9.52	10.32	9.17	11.21	10.36	10.83	9.52	13.53	9.11	3.68	8.81	8.05	5.24	7.22	7.11	13.85
MnO	0.10	0.11	0.06	0.15	0.10	0.10	0.08	0.09	0.19	0.16	0.05	0.12	0.08	0.10	0.09	0.12	0.10
MgO	36.69	35.61	35.44	34.52	32.67	34.68	35.51	36.18	16.06	16.43	2.22	4.44	6.44	3.87	6.77	6.53	29.90
CaO	0.20	0.15	0.23	0.30	0.10	0.24	0.13	0.35	5.49	5.00	6.50	7.55	9.85	9.38	7.32	9.96	0.08
Na2O	<0.01	<0.01	0.01	0.01	0.01	0.04	<0.01	<0.01	1.64	1.80	5.37	4.72	3.38	5.26	3.89	3.58	<0.01
K2O	0.67	0.87	0.68	0.43	1.48	0.99	0.30	0.15	0.53	0.78	0.27	0.46	0.66	0.32	0.35	0.93	0.00
P2O5	0.00	0.00	<0.01	0.00	<0.01	0.00	0.03	0.00	0.03	0.03	0.19	0.08	0.04	0.00	<0.01	0.03	<0.01
LOI	8.50	10.40	8.15	7.25	4.71	6.45	10.34	9.09	-0.79	0.23	0.34	0.16	1.22	0.48	0.32	0.43	0.99
Total	99.96	100.02	99.95	100.04	99.96	99.98	100.02	100.01	99.97	100.01	99.95	100.00	99.94	99.91	99.99	99.94	99.98
S	0.02	0.01	0.01	<0.01	0.01	0.01	0.05	0.03	0.03	0.02	<0.01	0.04	0.01	0.01	<0.01	0.02	0.01
C	0.04	0.1	0.03	0.07	0.03	0.07	0.03	0.09	0.16	0.04	0.03	0.03	0.03	0.02	0.01	0.01	0.03
Ag	<1	<1	<1	<1	<1	<1	<1	<1	<1	<1	<1	<1	<1	<1	<1	<1	<1
Ba	49.6	49.6	51.5	32.4	180.0	132.0	70.8	31.8	132.0	211.0	193.0	207.0	225.0	223.0	147.5	355.0	6.4
Co	87.0	74.5	83.9	51.4	90.8	97.5	89.8	108.0	67.0	67.2	12.5	40.4	37.7	20.6	33.7	38.5	41.8
Cr	6270	4580	2180	3800	7750	5660	3450	6280	1680	1480	10	40	130	40	280	100	7820
Cs	0.65	0.72	0.62	0.38	2.09	1.34	0.63	0.66	1.14	1.6	0.35	0.41	0.19	0.09	0.14	0.2	0.09
Cu	13	13	15	13	7	10	11	8	102	79	32	76	293	25	45	52	8
Ga	3.6	5.1	4.2	5	11.5	7.1	6.4	5.8	11.3	11.8	22.4	21.7	18.5	21.3	17.6	18.5	8.5
Hf	<0.2	<0.2	0.2	<0.2	0.6	0.4	0.3	<0.2	0.8	0.9	2.1	1.7	1.2	2.3	2.0	1.8	<0.2
Mo	2	3	2	3	2	2	6	3	7	3	3	3	3	3	2	3	2
Nb	<0.2	0.3	0.8	0.5	2.1	1.0	2.6	<0.2	2.0	1.5	5.1	3.8	1.8	6.7	3.7	2.0	<0.2
Ni	2500	1810	1560	783	1555	1845	1865	1950	429	414	92	107	210	105	266	216	365
Pb	<5	<5	<5	<5	<5	<5	<5	<5	5	8	6	6	<5	<5	5	6	<5
Rb	33.3	43.7	35.8	23.6	62.3	43.7	14.5	8.7	26.3	35.3	10.9	11.3	17.3	5.7	8.5	19.5	1.8
Sn	<1	<1	<1	<1	<1	<1	<1	<1	3	2	1	1	1	1	1	1	<1
Sr	5.3	5.5	4.6	3.6	6.1	6.6	6.5	3.5	174.0	192.0	351.0	355.0	338.0	386.0	428.0	484.0	1.2
Ta	<0.1	<0.1	<0.1	0.1	0.1	0.1	0.4	0.1	0.1	0.1	0.7	0.4	0.2	0.6	0.4	0.2	<0.1
Tl	<0.5	<0.5	<0.5	<0.5	<0.5	<0.5	<0.5	<0.5	<0.5	<0.5	<0.5	<0.5	<0.5	<0.5	<0.5	<0.5	<0.5
V	<5	<5	<5	<5	<5	<5	<5	<5	78	48	173	208	155	157	88	148	<5
W	2	5	3	4	2	1	2	2	9	2	3	6	4	5	6	9	3
Zn	63	47	26	35	182	148	237	152	73	79	33	55	50	45	40	51	34
Zr	7	8	6	3	20	16	13	8	30	28	50	49	46	77	69	55	<2
La	0.5	0.8	0.5	1	0.7	0.7	0.6	0.8	8.4	10.1	15.8	14.2	10.3	7.7	4.2	6.4	0.6
Ce	1.0	2.2	0.9	1.7	1.1	1.8	0.8	1.6	14.9	18.4	28.9	24.7	19.4	13.9	6.4	11.8	1.0
Pr	0.11	0.30	<0.03	0.19	0.11	0.26	0.08	0.16	1.62	1.93	3.64	2.76	2.29	1.80	0.62	1.48	0.10
Nd	0.5	1.4	0.4	0.7	0.4	1.0	0.3	0.6	5.8	6.6	13.8	10.3	8.6	8.0	2.4	6.0	0.4
Sm	0.19	0.44	<0.03	0.16	0.11	0.26	0.09	0.19	0.98	1.09	2.95	2.10	1.48	2.16	0.38	1.22	0.18
Eu	<0.03	0.07	0.05	0.03	<0.03	0.03	<0.03	0.03	0.29	0.30	0.96	0.79	0.82	0.84	0.67	0.55	<0.03
Gd	0.11	0.34	0.16	0.18	0.06	0.23	<0.05	0.13	1.17	1.08	3.19	2.02	1.67	2.17	0.43	1.55	0.12
Tb	0.02	0.03	0.04	0.03	<0.01	0.04	<0.01	0.01	0.17	0.15	0.43	0.33	0.28	0.35	0.06	0.22	0.01
Dy	0.17	0.32	0.18	0.24	0.06	0.32	<0.05	0.20	1.00	0.98	2.78	2.30	1.75	2.24	0.36	1.47	0.23
Ho	0.04	0.05	0.06	0.06	0.03	0.08	0.01	0.05	0.25	0.19	0.59	0.43	0.35	0.49	0.12	0.3	0.06
Er	0.09	0.15	0.23	0.24	0.08	0.18	0.05	0.12	0.63	0.59	1.60	1.42	1.05	1.51	0.30	0.81	0.18
Tm	0.02	0.02	0.04	0.03	0.01	0.04	<0.01	0.02	0.1	0.09	0.25	0.2	0.14	0.21	0.05	0.13	0.05
Yb	0.15	0.3	0.19	0.38	0.16	0.25	0.15	0.18	0.59	0.56	1.41	1.14	0.87	1.13	0.39	0.77	0.41
Lu	0.02	0.04	0.04	0.06	0.03	0.05	0.03	0.03	0.08	0.08	0.22	0.18	0.15	0.17	0.06	0.12	0.07
Y	1.2	1.8	1.1	1.9	0.8	2.3	0.6	1.5	5.8	4.9	15.3	12.1	9.3	13.5	2.7	8.7	1.7
Th	0.40	0.62	0.33	0.90	1.13	1.07	0.58	0.49	3.20	4.10	19.30	7.58	1.97	3.15	2.28	1.94	0.68
U	0.21	0.34	0.31	0.22	0.31	0.51	0.25	0.23	0.99	1.31	3.21	1.87	0.74	0.62	0.63	0.58	0.25
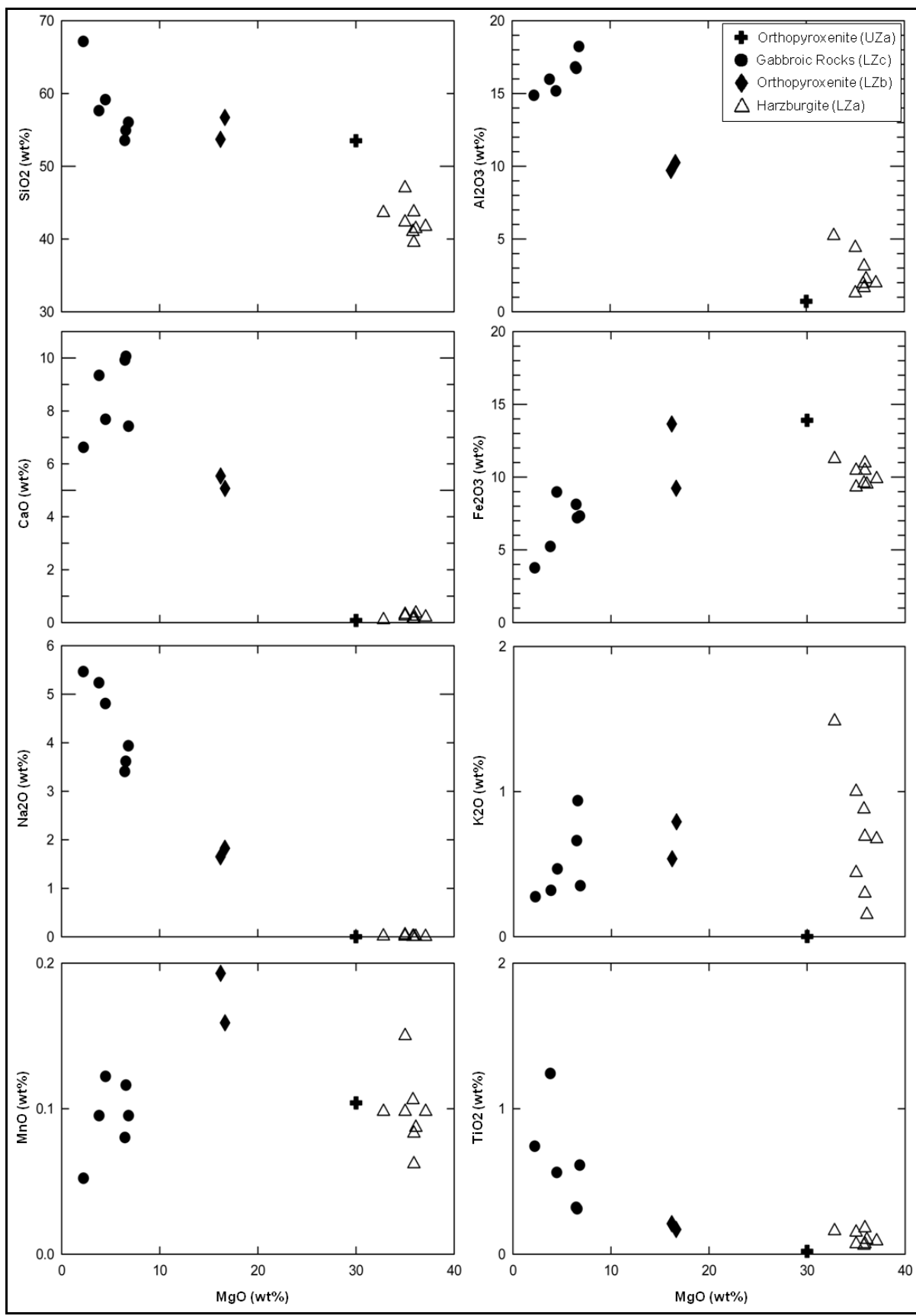
Figure 1.11. Plot of MgO content versus major oxides and selected trace elements for different group of rocks of Vermelho Intrusion. See Table 1.3 for chemical analyses.
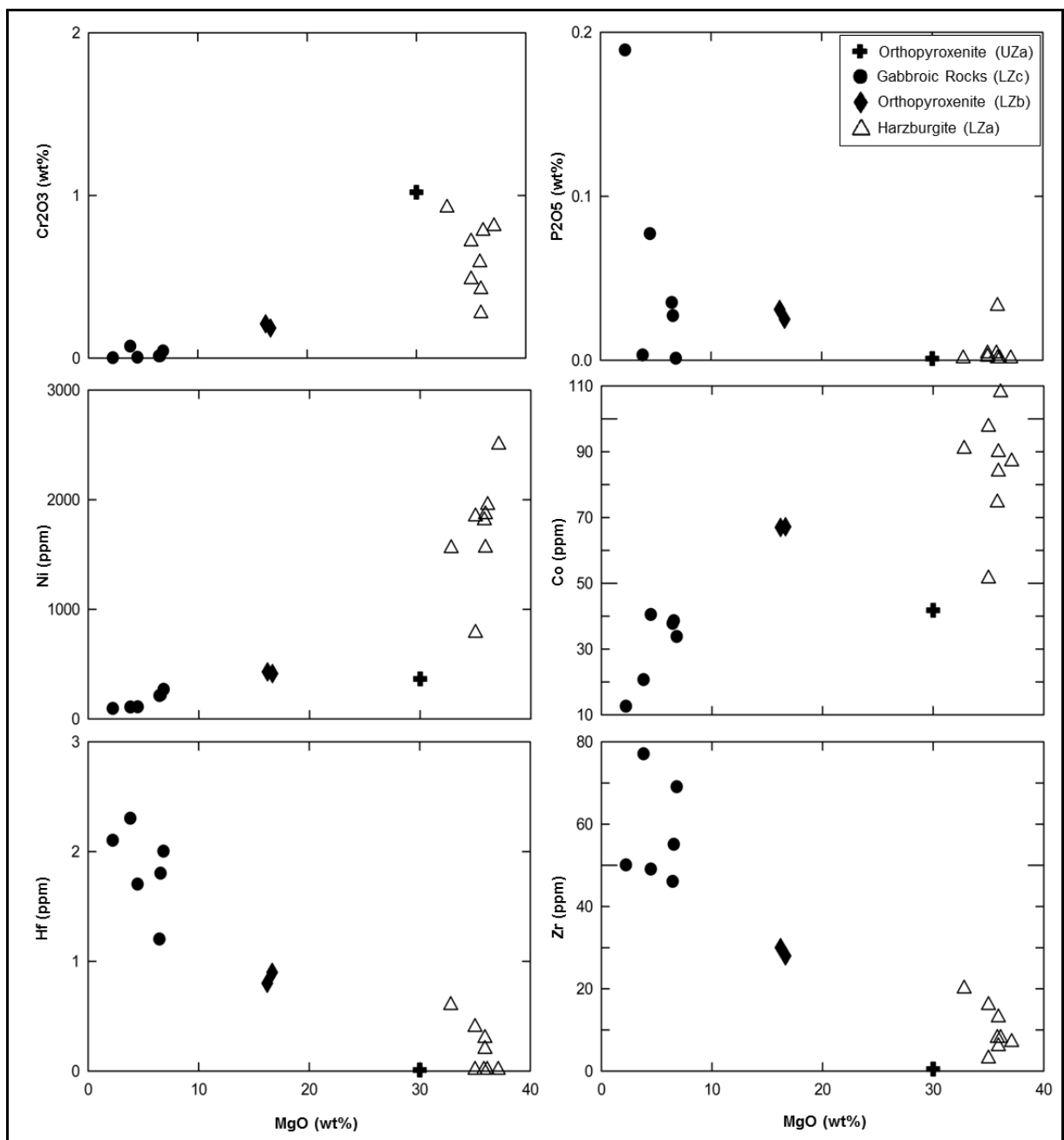
Figure 1.11 (cont.). Plot of MgO content versus major oxides and selected trace elements for different group of rocks of Vermelho Intrusion. See Table 1.3 for chemical analyses.
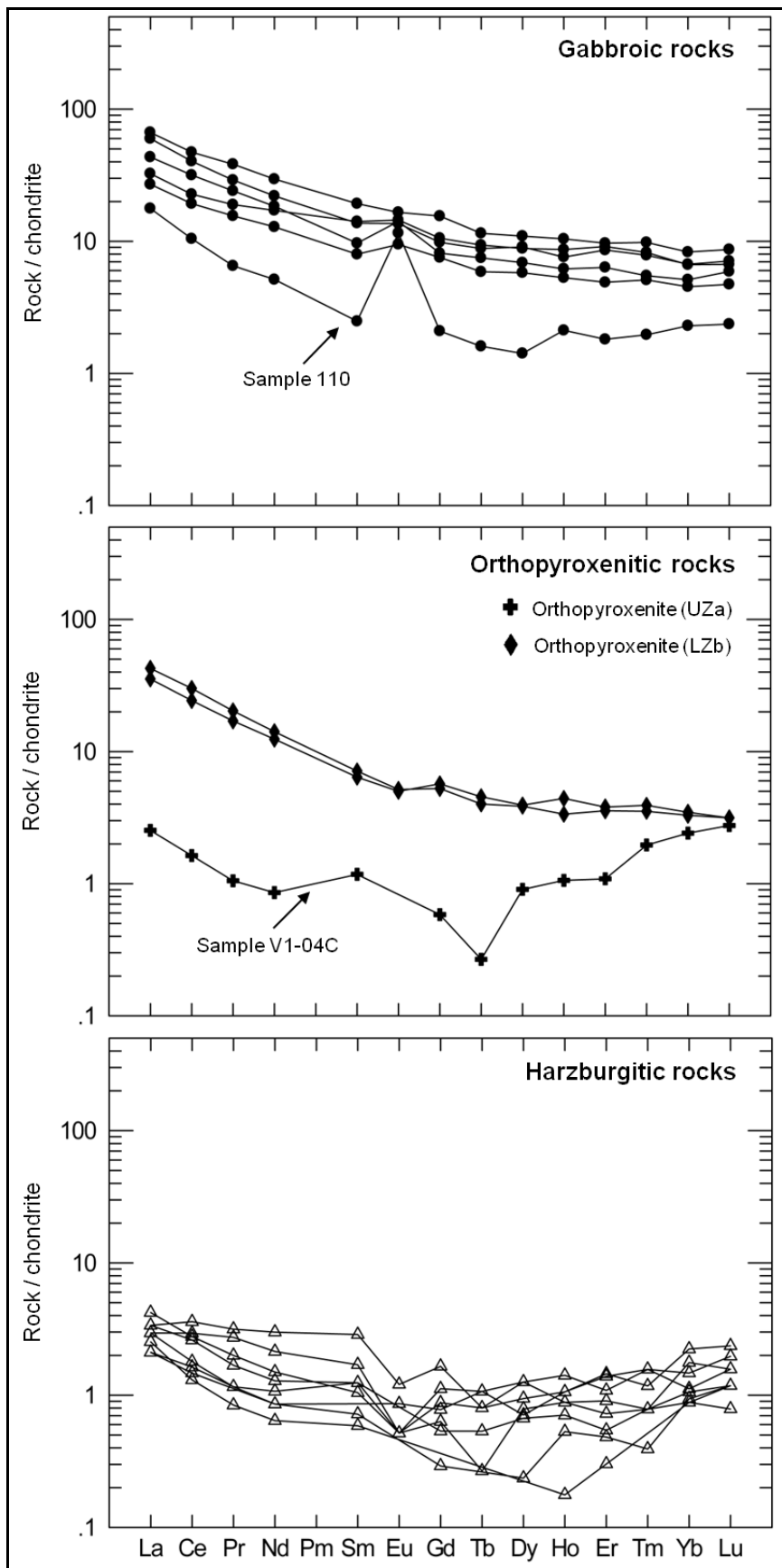
Figure 1.12. Chondrite-normalized REE patterns for different group of rocks of Vermelho Layered Intrusion. See Table 1.3 for chemical analyses. Normalization data from Sun and MacDonough (1989).
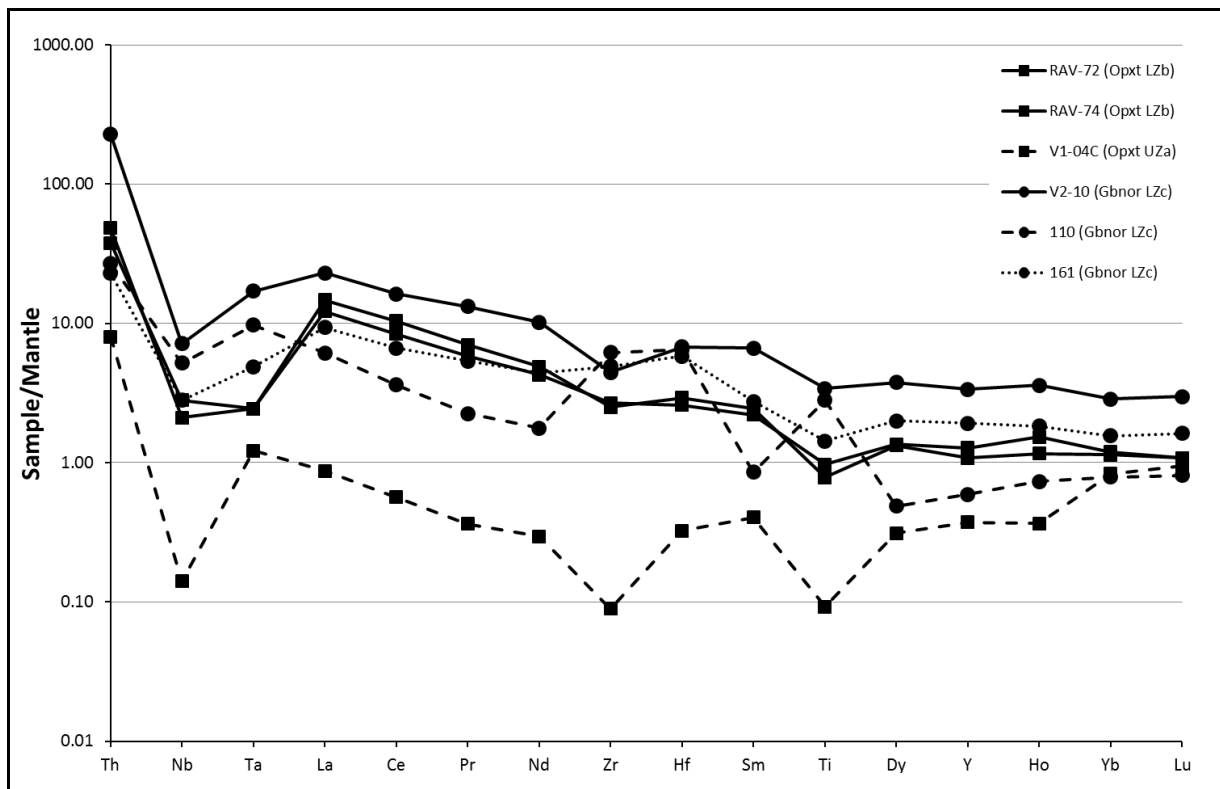
Figure 1.13. Primitive mantle-normalized alteration-resistant profiles for samples of orthopyroxenite from LZb and UZa (black squares) and representative gabbroic rocks from LZc (black circles) of the Vermelho Complex. Data from Table 1.3. Primitive mantle normalization values are from Sun and McDonough (1989).

Sm-Nd isotopes

The Sm-Nd isotopic data of the Vermelho Complex are listed in Table 1.4. Nd isotopic data obtained for both mafic and ultramafic lithotypes of the LZ render Nd model ages between 2.90 and 3.30 Ga, with variably εNd (T) values (+0.1 to -7.3). Plotted against the stratigraphy, the Sm–Nd data are scattered and do not correlate with the layering sequence, rock types or any fractionation index ($Mg_{\#}$; Fo and En content).

Table 1.4 - Sm–Nd isotopic data for the Vermelho Complex.

Sample	Rock Type	Nd(ppm)	Sm(ppm)	Sm/Nd	$^{147}Sm/^{144}Nd$	$^{143}Nd/^{144}Nd$	±2SE	$^{143}Nd/^{144}Nd_i$	$\varepsilon(0)$	$\varepsilon(T_{2.77Ga})$	$T_{DM}(Ma)$
V1-04C	Orthopyroxenite (UZa)	0.40	0.18	0.450	0.272	0.513643	16	0.508670	19.6	-7.3	-
V2-10	Gabbro (LZc)	13.80	2.95	0.214	0.129	0.511232	9	0.508870	-27.4	-3.4	3298
V2-11	Mag-Gabbro (LZc)	10.30	2.10	0.204	0.123	0.511199	12	0.508946	-28.1	-1.9	3125
62	Gabbro (LZc)	8.60	1.48	0.172	0.104	0.510866	12	0.508964	-34.6	-1.5	3033
94	Pegt Leucogabbro (LZc)	8.00	2.16	0.270	0.163	0.512005	10	0.509021	-12.3	-0.4	3190
110 (V2FP-425)	Pegt Leucogabbro (LZc)	2.40	0.38	0.158	0.096	0.510798	9	0.509048	-35.9	0.1	2902
161	Pegt Leucogabbro (LZc)	6.00	1.22	0.203	0.123	0.511203	12	0.508956	-28.0	-1.7	3106
RAV-62 (DDH-25)	Harzburgite (LZa)	1	0.26	0.260	0.157	0.511901	13	0.509028	-14.4	-0.3	3120
RAV-65 (DDH-25)	Harzburgite (LZa)	0.3	0.09	0.300	0.181	0.512299	18	0.508984	-6.6	-1.1	-
RAV-70 (DDH-25)	Harzburgite (LZa)	0.6	0.19	0.317	0.191	0.512449	15	0.508950	-3.7	-1.8	-
RAV-72 (DDH-25)	Orthopyroxenite (LZb)	5.8	0.98	0.169	0.102	0.510751	8	0.508884	-36.8	-3.1	3142
RAV-74 (DDH-25)	Orthopyroxenite (LZb)	6.6	1.09	0.165	0.100	0.510732	9	0.508907	-37.2	-2.7	3102
297 (DDH-14)	Harzburgite (LZa)	0.5	0.19	0.380	0.230	0.513001	18	0.508802	7.1	-4.7	-
306 (DDH-14)	Harzburgite (LZa)	1.4	0.44	0.314	0.190	0.512399	15	0.508926	-4.7	-2.3	-
370 (DDH-14)	Harzburgite (LZa)	0.7	0.16	0.229	0.138	0.511432	12	0.508906	-23.5	-2.7	3288

Discussion

Magmatic structure

Results of this study indicate that the intrusive architecture of the Vermelho Complex consists of a horizontally layered ultramafic zone (UZ) overlying a complex but broadly subhorizontal sequence of mafic-ultramafic rocks (LZ). The UZ occurs as two isolated hills and host a world-class Ni laterite deposit, while the LZ occurs in flat areas close to country rocks (Fig. 1.2, 1.3, 1.4). This architecture of the layered rocks will be used in the following discussions addressing the petrological evolution of the layered rocks and the tectonic setting of the Vermelho Complex in the Carajás Mineral Province. Before moving into these discussions, it is important to remind that the actual landscape where the lateritic plateau of the Vermelho Ni deposit is located, started to be formed at the transition from Meso-Cenozoic time (Vasconcelos et al., 1994; Costa et al., 1996). This ladscape indicates that the exposed UZ represents just a small portion of the original sequence of layered rocks, which survived the extensive erosion of the lateritic profile in recent times. It is likely that a thick sequence of layered rocks were originally located above the exposed UZ. On the other hand, the landscape has exposed most of the lower portion of this layered intrusion, thus allowing a discussion regarding the magmatic processes at the lower contact of this layered intrusion.

Constraints for the composition of parental magma and fractionation

The composition of the parental magma of the Vermelho Complex cannot be constrained by common approaches used to define their composition in well-exposed and unaltered intrusions (e.g., chilled margin, bulk composition, extrusive equivalents, related dykes, and melt inclusions). The world-class Ni laterite deposit developed from the thick pile of ultramafic rocks of the UZ provides an evidence for a primitive parental magma. This is supported by the compositional range of cumulus Ol ($Fo_{85.6-90.5}$) in the LZ of the Vermelho Complex. The composition of the most primitive cumulus Ol in the Vermelho Complex is

comparable with those reported for the Bushveld Complex (Fo_{91}; Wilson, 2012), Stillwater Complex (Fo_{90}; McCallum, 1996) and Bacuri Complex (Fo_{91}; Spier and Ferreira Filho, 2001), all of them originated from primitive parental magmas. Olivine compositions obtained for the Vermelho Complex is also consistent with primitive composition obtained for olivine in layered intrusions hosting large Ni-laterite deposits in Carajás (e.g., up to Fo_{92} for the Serra da Onça Complex and up to Fo_{89} for the Serra do Puma Complex; Ferreira Filho et al., 2007; Rosa, 2014; Rosa et al., submitted).

Additional constraint for the composition of the parental magma of the Vermelho Complex is provided by the crystallization sequence of the LZ. Cumulus mineral in layered rocks of the LZ indicate that the sequence of crystallization consists of Ol + Chr, Opx + Chr, Opx and Opx + Pl in the LZa and LZb, and then followed by Opx + Pl + Cpx in the LZc. The latter includes more fractionated rocks characterized by interstitial quartz as well as accessory zircon and apatite. Crystallization sequences in which Opx precedes Cpx are characteristic of major PGE-bearing intrusions (e.g. Bushveld, Great Dyke, Stillwater; Eales and Cawthorn, 1996). PGE-bearing layered intrusions in the Carajás Mineral Province (e.g. Luanga, Serra da Onça and Lago Grande) are also characterized by the same crystallization sequence (Ferreira Filho et al., 2007; Teixeira, 2013; Teixeira et al., 2015; Rosa, 2014; Rosa et al., submitted). The early crystallization of orthopyroxene relative to clinopyroxene indicates that the primary magma was silica saturated. Several studies also suggest that assimilation of continental crust by primitive parental magmas may have induced enrichment in silica in these magmas (Campbell, 1985). Evidence for assimilation of continental crust during the ascent and/or emplacement of the parental magma of the Vermelho Complex is also provided by lithogeochemical and isotopic results. Mantle-normalized alteration-resistant trace element profiles of gabbroic rocks are fractionated, as indicated by relative enrichment in LREE and Th, with pronounced negative Nb and Ta anomalies (Fig. 1.13). These alteration-resistant element profiles were compared with average compositions of the upper and lower crust (Wedepohl, 1995), with average composition of the B1 rocks of the Bushveld Complex (Barnes et al., 2010) and with data for gabbroic rocks of other layered intrusions of the Carajás Mineral Province (Luanga Complex, Ferreira Filho et al., 2007; Lago Grande Complex, Teixeira, 2013; Serra da Onça Complex, Rosa, 2014) in Figure 1.14. B1 rocks of the Bushveld Complex are chilled margins interpreted as representative of the composition of the parental magma of the cumulate rocks of the Lower Zone of the Bushveld Complex. The B1 magma is interpreted as the product of a mixture of a primitive mantle melt mixed with continental crust, and has been successfully modelled as the parental magma of the cumulate

rocks of Lower and Lower Critical Zones of the Bushveld Complex (Barnes et al., 2010, Godel et al., 2011). Even though the composition of the parental magma of the Vermelho Complex is not constrained by chilled margins, the similar distribution of alteration-resistant elements of the Vermelho Complex and B1 magma supports the suggestion that both complexes crystallized from crustal contaminated primitive magmas. Assimilation of older sialic crust during emplacement and/or ascent of the parental magma of the Vermelho Complex is supported by Sm-Nd isotopic data (Table 1.4). Nd isotopic data obtained for both mafic and ultramafic lithotypes render Nd model ages between 2.90 and 3.30 Ga, with variably εNd (T) values (+0.1 to -7.3). These results are consistent with an original mantle melt variably contaminated with older continental crust, which is compatible with an intrusive relationship with gneisses and migmatites of the ca. >2.8 Ga Xingu Complex.
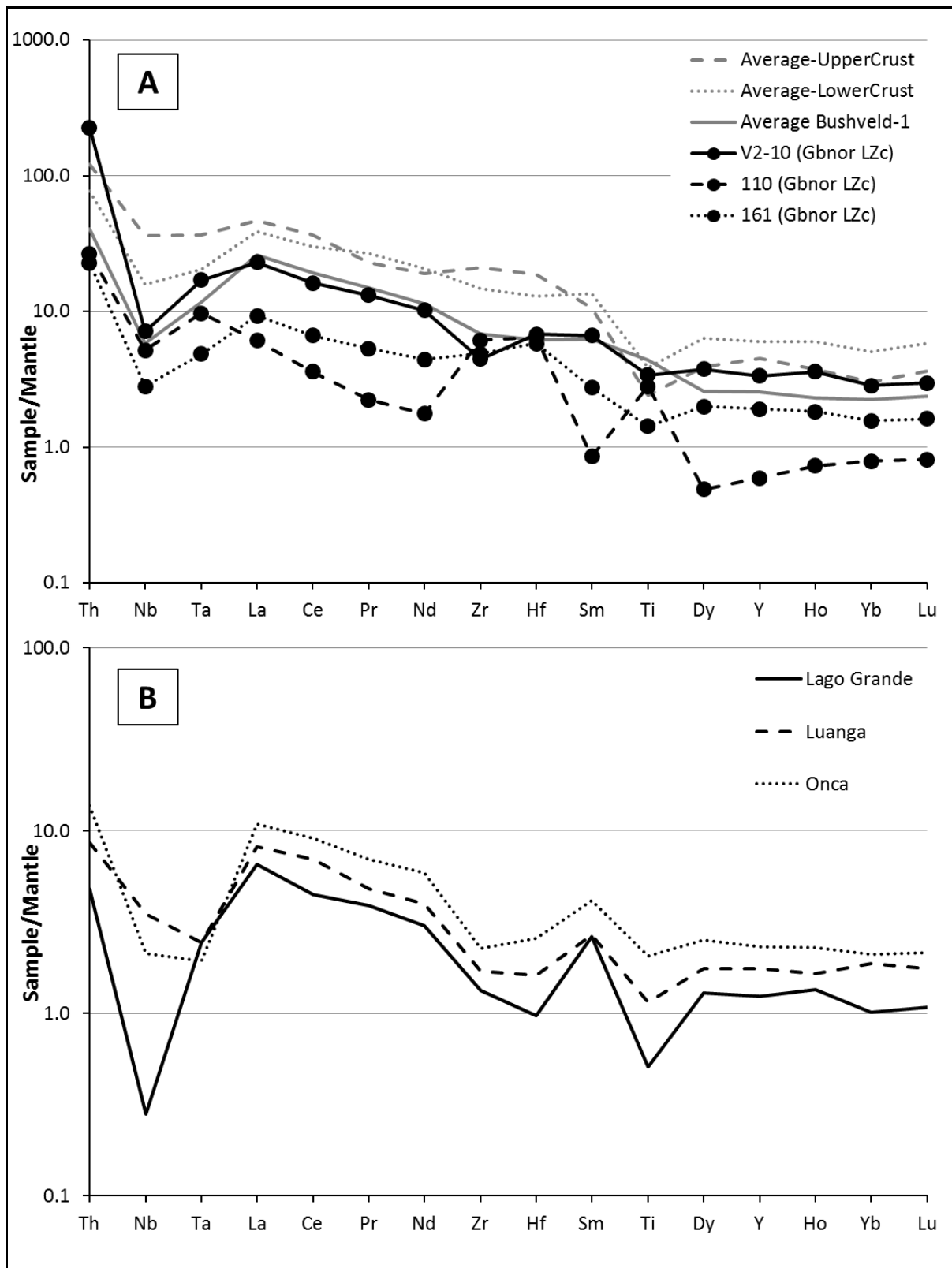
Figure 1.14. A) Primitive mantle-normalized alteration-resistant profiles for samples of gabbroic rocks of the Vermelho Complex (this paper), average composition of the upper and lower crust (Wedepohl, 1995), and average composition of the B1 rocks of the Bushveld Complex (Barnes et al., 2010). B) Primitive mantle-normalized alteration-resistant profiles for samples of gabbroic rocks of the Lago Grande Complex (Teixeira, 2013), Luanga Complex (Ferreira Filho et al., 2007) and Serra da Onça Complex (Rosa, 2014). Primitive mantle normalization values are from Sun and McDonough (1989).

Magmatic processes at the lower contact zone

The lower contact zone of the Vermelho Complex is well delineated due to shallow exposure in a subhorizontal structure (Fig. 1.2, 1.3, 1.4). This feature, combined with extensive drilling developed for evaluation of nickel laterite resources and few deep drilling for nickel sulfide exploration, provided a unique opportunity to investigate in detail the processes associated with the lower contact of a layered intrusion in the Carajás Mineral Province.

Marginal compositional reversals represent geological features commonly associated with different types of mafic-ultramafic sills, dykes and layered intrusion. These features are described in many mafic-ultramafic intrusions (e.g. Lightfoot and Naldrett, 1984; Huppert and Sparks, 1989; Eales and Cawthorn, 1996; McBirney, 1996; McCallum, 1996; Wilson and Engell-Sørensen, 1986; Egorova and Latypov, 2012; 2013) and were reviewed by Latypov (2003; 2003b, and references therein) and Latypov et al. (2007; 2011, and references therein). Compositional reversals represent zones along the margins of igneous intrusions in which rocks become progressively more primitive inwards (i.e. from the contact with country rocks to the interior of the intrusion), such that their crystallization sequence and compositional trends are opposite to the one expected from crystal fractionation of parental magmas. Even though these features are very common in mafic-ultramafic intrusions their interpretation is controversial (see Latypov et al. 2007; 2011, for a review of proposed models). The magmatic structure of the Vermelho Complex indicates the existence of a LZ consisting of more fractionated rocks located below a sequence of primitive dunite and orthopyroxenite that forms the UZ, thus broadly suggesting the existence of a compositional reversal at the base of the intrusion. In the following discussion the data collected in the lower portion of the Vermelho Complex, at the contact with country rocks, are compared with current models proposed for the processes that occur at the lower contact zone of mafic-ultramafic intrusions.

Basal compositional reversals are commonly characterized by inverted crystallization sequences and minerals that become gradually more primitive inwards (e.g. increase in Fo and/or En content of olivine and Opx, respectively). Current models assume an open-system evolution of magma chambers (Latypov et al., 2011; Egorova and Latypov, 2012) consisting of an initial stage where the inflowing magma becomes increasingly more primitive with time, followed by a stage where fractional crystallization in a closed system

prevail. The most primitive rocks and minerals would be located at the transition of these different stages (known as crossover horizon) and represent the rocks and minerals that crystallized from magmas with composition close to the parental magma of the sill or layered intrusion. A schematic model for a basal reversal assuming the same crystallization sequence identified in the Vermelho Complex is provided in figure 1.15A. This model is compared with our data obtained from two drill cores that intersects the basal contact of the Vermelho Complex with country rocks (Fig. 1.15B).

The borehole DDH-14 intersect a subvertical contact with country rocks at the deeper zone of the Vermelho Complex, likely to represent the feeder zone (Fig. 1.2, 1.4, 1.5). A deep zone of ultramafic rocks and subvertical structure at the central portion of the Vermelho Complex is supported by geophysical data (VALE unpublished reports). The sequence of ultramafic rocks close to the contact with country rocks consists of interlayered orthopyroxenite, harzburgite and dunite (Fig. 1.15B). The inverted crystallization sequence (e.g. Opx, orthopyroxenite; Ol+Opx, harzburgite; Ol, dunite) adjacent to the contact is followed inwards by a normal crystallization sequence (e.g. Ol; Ol+Opx; Opx), which resembles an expected sequence for a basal reversal (Fig. 1.15B). However, the crystallization sequence in the deeper portion (i.e. > 310 meter), consisting mainly of dunite (Ol cumulate) does not fit the model for basal reversals (Fig. 1.15B). Because the drill core DDH-14 possibly intersects the feeder zone of the Vermelho Complex, the sequence of dunite and harzburgite located away from the contact zone should represent dunites formed in successive events of magma flowing into the magma chamber. Mineral compositions for olivine and Opx throughout the borehole DDH-14 is limited to nine samples due to extensive serpentinization throughout the drill core and poorly preserved core close to the contact with country rocks (i.e. orthopyroxenites located at the contact with country rocks). Mineral compositional trends for olivine are consistent with a reversal (Fig. 1.15B), as indicated by the most primitive olivine compositions (Fo = 86.8-87.9 %; Ni= 3300-3950 ppm) located about 100 meters away from the contact with country rocks.

The borehole DDH-25 intersected a subhorizontal contact with country rocks at the southwestern limit of the Vermelho Complex (Fig. 1.2, 1.4, 1.5). The sequence of ultramafic rocks close to the contact with country rocks consists of interlayered harzburgite (Ol+Opx cumulate) and orthopyroxenite (Opx cumulate) (Fig. 1.15B). Plagioclase appears as an intercumulus mineral in the uppermost Opx cumulates and become progressively more abundant forming orthocumulate melanorites at the upper portions of the drill core. Mineral

compositional trends for olivine and Opx are characterized by a monotonous lower portion (from 90 to 140 meters) close to the contact with country rocks, followed upwards by abrupt compositional variations (Fig. 1.15B). Both crystallization sequence and mineral compositional trends of the borehole DDH-25 are different from what is expected in basal reversals (Fig. 1.15B). The sequence of ultramafic rocks is consistent with their origin within open system magma chambers, where crystal fractionation and concomitant successive influxes of magma occur. The most primitive olivine (Fo = 89.4-90.5; Ni= 2395-3275 ppm) and orthopyroxene (En = 89.7-90.8) compositions are located in the uppermost harzburgite layer, about 70 meters above the contact with country rocks. The most primitive composition of olivine from drill core DDH-25 has higher Fo content but lower Ni content when compared with the most primitive olivine composition from drill core DDH-14 (Fig. 1.15B). These features preclude any possibility that olivine from the drill core DDH-25, located away from the feeder zones of the Vermelho Complex, result from fractionation of the same primitive magma that crystallized the olivine from the drill core DDH-14, this one located at the feeder zone.

Results for DDH-14 and DDH 25 indicate that the sequence of rocks located close to the contact with country rocks do not perfectly fit the model for compositional reversals proposed by Latypov et al. (2011) and Egorova and Latypov (2012). This model was successfully tested in several dykes and sills suggesting that it is appropriate for several magmatic systems. These reversals are explained by the early separation of high-temperature phases in the feeder system in the early stage of intrusion, before more primitive magmas entered the chamber as the conduit and feeder system heated up (Latypov et al., 2011). An important question is whether the original contact zone of a layered intrusion is fully preserved in large layered intrusions. Magmatic systems originated from a single magma influx, like several sills and dykes used to support the model developed by Latypov (2011), are more likely to preserve original features. Large layered intrusions, generally accepted to originate from several influxes of primitive magma and successive inflation of the chamber, may not preserve the original contacts of primitive magma and country rocks. We suggest that the Vermelho Complex results from more than one major influx of primitive magma, such that original contacts with country rocks may have been obliterated during new influxes of magma. Detailed descriptions of rocks of the lower contact of large layered intrusions are not common, and our study of the Vermelho Complex together with those developed in the Bushveld Complex (Wilson, 2012) are few exceptions. These studies suggest that the lower contact of major layered intrusions is complex and variable, resulting from successive

influxes of primitive magmas. In the following section the evidence for a second major influx of primitive magma in the Vermelho Complex is discussed.
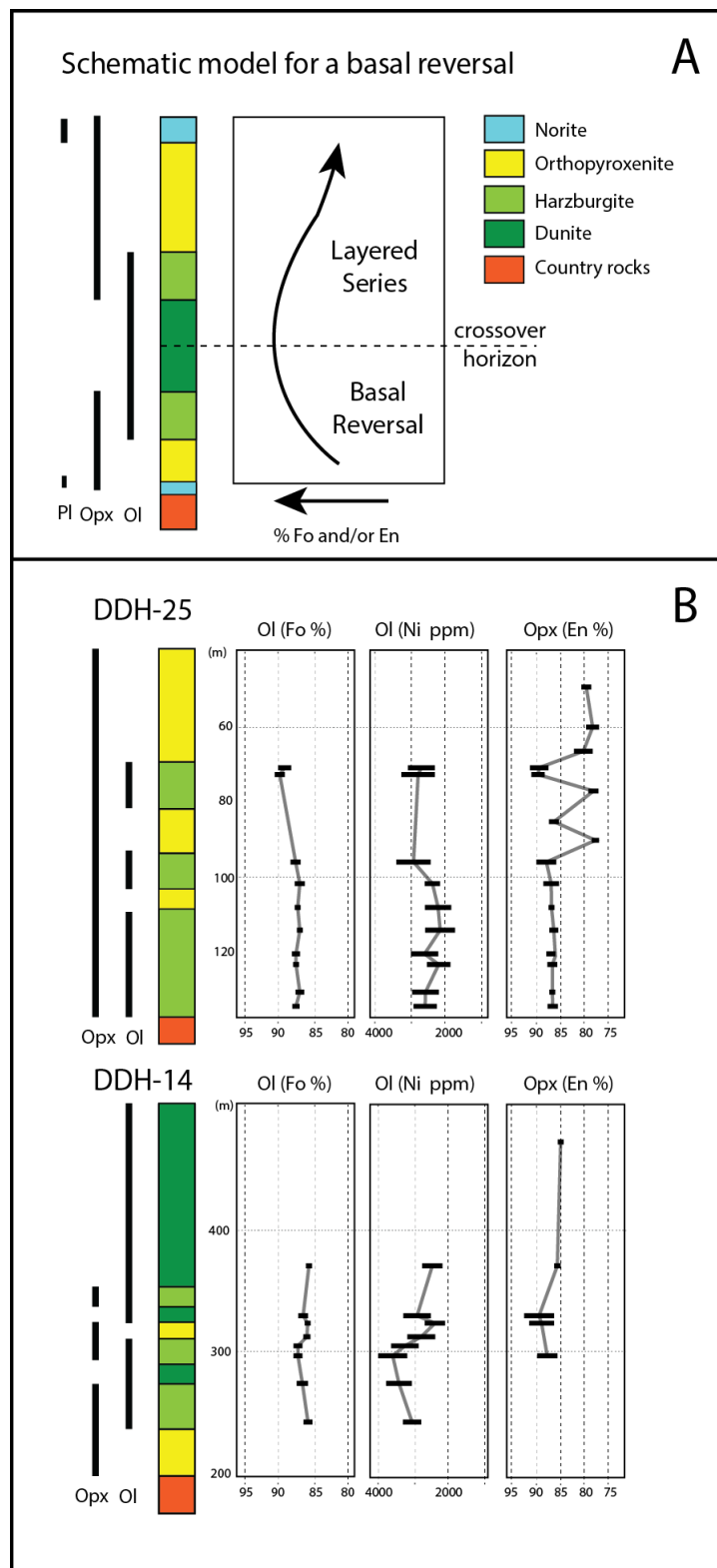
Figure 1.15. A) Sketch of an ideal basal compositional reversal. Based on Latypov et al. (2011) and Egorova and Latypov (2012). The crystallization sequence and rock types are adjusted to the Vermelho Complex. B) Data for GT14 and GT25 bore holes of the Vermelho Complex.

The origin of the UZ and associated chromitites

A remarkable feature of the stratigraphy of the Vermelho Complex is the subhorizontal layer of fractionated gabbroic rocks (LZc) located below ultramafic rocks (UZ) that host world class nickel laterite resources. The contact of fractionated quartz-bearing gabbroic rocks of the upper portion of the LZc with overlying orthopyroxenite and associated chromitite pods of the UZa indicates an abrupt break in the fractionation sequence of the LZ (Fig. 1.16). This break in the fractionation sequence is matched with significant reversals in composition of orthopyroxenes and La/Yb ratio of rocks (Fig. 1.16). Compositional features of orthopyroxenites of the UZa are comparable to those observed at the lower portions of the LZa, close to the contact with country rocks (Fig. 1.16). These features support the interpretation that the UZ results from a significant new influx of primitive magma, following an extensive fractionation of early injected primitive magmas. The layer of orthopyroxenite located at the base of the UZ (i.e. UZa) is interpreted to result from mixing of the new influx of primitive magma and fractionated magma resident in the magma chamber. Chromitite pods are restricted to the UZa of the Vermelho Complex. Chromitites do not occur in dunite of the lower portions of the UZb, a contact that was extensively investigated during drilling programs for evaluation of nickel laterite resources, as well as in the lower portions of the LZ. Chromitite pods of the Vermelho Complex provide an additional example of chromitites located in specific intervals of layered intrusions characterized by distinct petrological breaks on their regular fractionation path (e.g. Ferreira Filho and Araújo, 2009).

Even though chromitite are common rocks of the stratigraphy of mafic-ultramafic layered intrusions, their origin is a long-standing issue that was recently awakened by new interpretations (e.g. Maier et al., 2013). Chromitites broadly represent a special case of cumulate rock where chromite is the sole liquidus (cumulus) mineral. Formation of chromitites was thus interpreted based upon changes in phase relations of the appropriate system to allow the system to fall into the chromite stability field. The mechanisms for the formation of chromitite layers may now be separated into those that require that chromite was the sole liquidus phase in the site where it is concentrated or crystallized (e.g. Irvine, 1975; 1977; Lipin, 1993; Eales, 2000; Ferreira Filho and Araújo, 2009) and those that propose that chromite was mechanically introduced into their present position in the layered complex or sill as chromite-saturated slurries (Mondal and Mathez, 2007; Maier et al., 2013). The latter has an implication that chromitites originated from magmas that are saturated in chromite, independently of where (e.g. during ascent in the crust, within an underlying magma

chamber) and how this magma achieved chromite saturation (e.g. crustal contamination, pressure changes, magma mixing, an originally chromite-saturated mantle melt). Considering that magmas feeding magma chambers are initially chromite-saturated, the need for a specific process leading to changes in phase relations to reach chromite saturation within the layered intrusion or sill is not necessary. A detailed review of the arguments and examples favoring the different processes for the origin of chromitites is not intended in here (see Mondal and Mathez, 2007 or Maier et al. 2013 for a review and references). Our argument concerns the observation that chromitites in the Vermelho Complex, and layered intrusions of the Carajás region in general, are restricted to stratigraphic horizons where the fractionation sequence and petrological features were abruptly changed. It implies that the origin of chromitites does not follow the natural path of fractionation of a chromite-saturated parental magma, but demands the involvement of some internal process in the layered intrusion. In the following descriptive model we suggest that orthopyroxenites and associated chromitite pods and layers of the UZa in the Vermelho Complex were formed as the result of mixing of a new influx of primitive magma with fractionated resident magma.
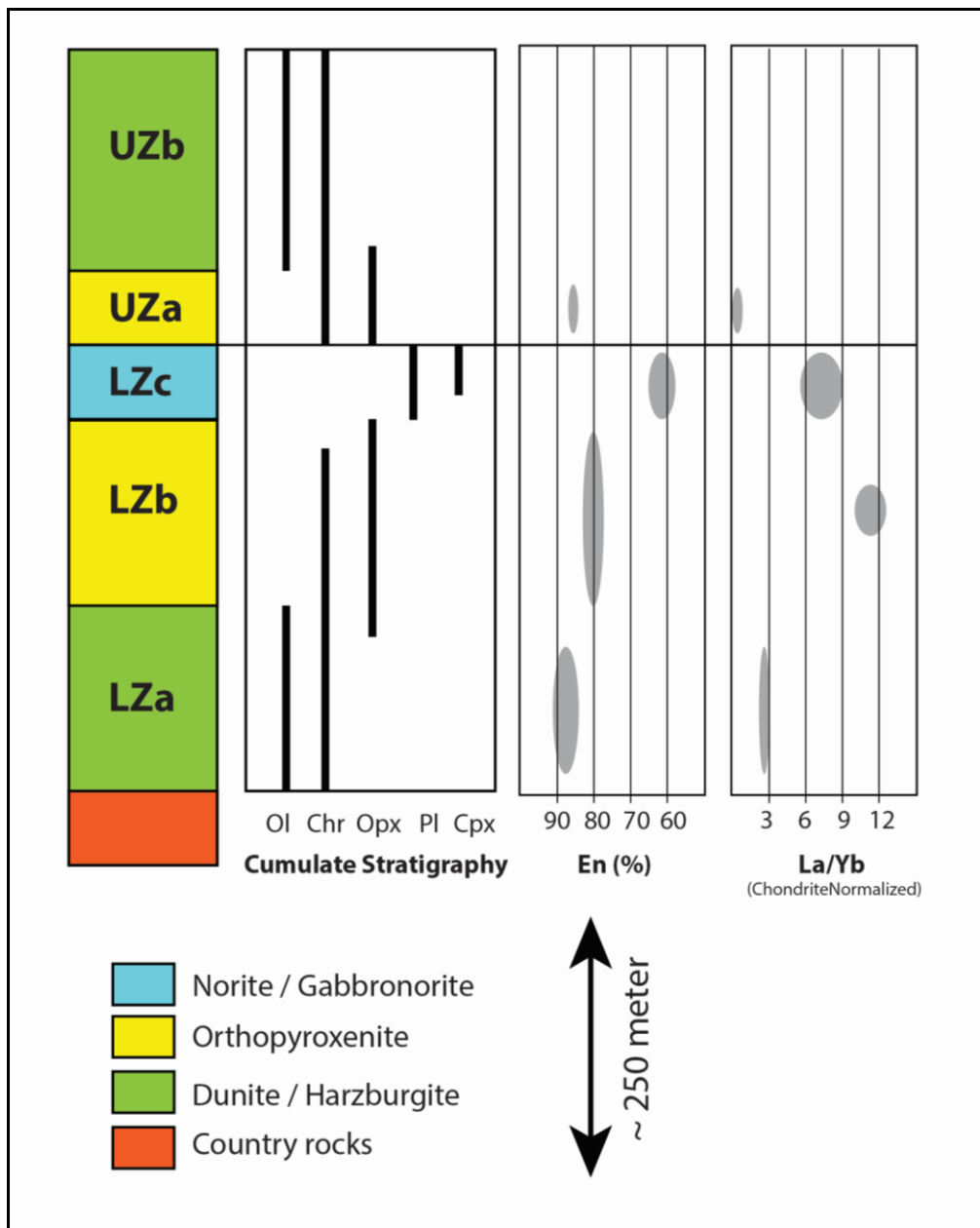
Figure 1.16. Key compositional features of the LZ and UZ of the Vermelho Complex. The indicated thickness of the exposed layered sequence is based on average thickness for the UZ and LZc on the slopes of the V1 plateau, as well as estimated thickness of the LZb and LZa in drill cores located to the southwest of the V2 plateau.

A descriptive model for the evolution of the Vermelho Complex

The evolution of the Vermelho layered complex is briefly described as the result of 5 major stages (Fig. 1.17). The data obtained in this study indicate that two major events of magma emplacement were involved in the evolution of the Vermelho Complex, the first one associated with the LZ and the second with the UZ.

Stage 1 consists of the initial stages of the evolution of the intrusion. Our results do not provide evidence for a thin chilled margin or a well developed marginal reversal. The basal sequence of rocks located close to the country rocks consists of interlayered harzburgites and orthopyroxenites, possibly resulting from successive influxes of primitve magmas. The most primitive mineral compositions are located dozens of meters away from the contact of country rocks (Fig. 1.15), possibly due to fractionation of the parental magma in the feeding system during initial heating associated with first batches of magmas filling the magma chamber (as described by Egorova and Latypov, 2012). Stage 2 consists of the crystallization of the Lower Zone that follows a normal sequence of fractionation, evolving from primitive harzburgites in the base (LZa) up to highly fractionated quartz-bearing gabbronorite in the upper portions (LZc) (Fig. 1.16). Stage 3 consists of a new major influx of primitive magma. Compostional features of orthopyroxenites of the UZa are comparable to those observed at the lower portions of the LZa, suggesting that the magma composition associated with stages 1 and 3 are similar. The location of feeders associated with the second major influx of primitive magma is not constrained. The upper and basal subhorizontal contacts of the UZa suggests that primitive magma may have been filled from lateral conduits (not preserved at the actual erosion level) rather than from the same conduit that filled the first major influx primitive magma. Stage 4 consists of the crystallization of the UZ, characterized by a remarkable break in the fractionation sequence and mineral compositions of the LZ (Fig. 1.16). The orthopyroxenite layer (UZa) is interpreted to result from mixing of a large volume of primitive magma with a small volume of highly fractionated silica-rich resident magma. Irregular pods or discontinuous layers of chromitites associated with orthopyroxenites of the UZa are interpreted to result from chromite saturation associated with the mixing of these highly distinct magmas. This model, originally proposed by Irvine (1977) to explain the origin of chromitite layers of the Muskox intrusion, has also been applied to explain the origin of chromitite layers of the Stillwater Complex (Raedeke and McCallum, 1984; Campbell and Murck, 1993), the Great Dyke (Wilson, 1982) and the Bacuri Complex (Spier and Ferreira Filho, 2001). Orthopyroxenites and associated chromitites of the UZa are followed upwards by a sequence of homogeneous olivine + chromite cumulates, just preserved in the V1 and V2 plateaus (Fig. 1.17). The lateral extension, thickness and composition of the layered sequence of the UZ are unconstrained due to extensive weathering and erosion in recent times. Stage 5 consists of the development of the weathering profile preserved in the lateritic plateau of the Vermelho Ni deposit, which started to be formed at the transition from Meso-Cenozoic time (Vasconcelos et al., 1994; Costa et al., 1996). It is worth mentioning that the original

resources of nickel laterites (i.e. the one existing before the erosion that carved the actual landscape) was much larger than the reported 220 Mt @ 1.23% Ni (Kuck, 2003).
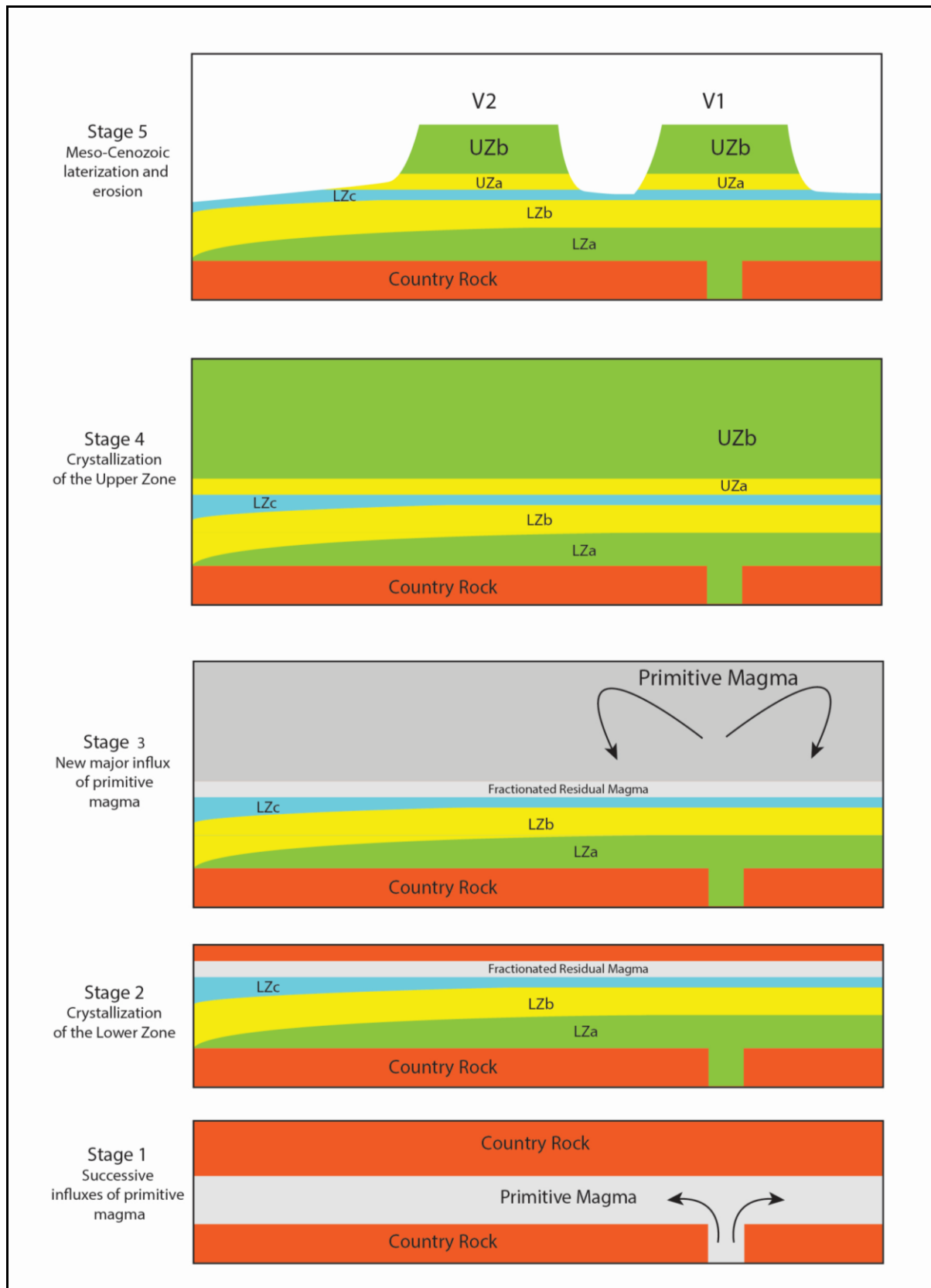
Figure 1.17. Schematic diagram summarizing the main stages during the evolution of the Vermelho Complex. Captions from figure 1.16.

How the Vermelho Complex fit into the tectonic framework of the CMP

Reported U-Pb zircon ages for layered intrusions of the Carajás Mineral Province (Fig. 1.18) indicate that they have Neoarchean ages broadly bracket between 2680-2780 Ma. U-Pb zircon ages for the Luanga (2763±6 Ma; Machado et al., 1991), Lago Grande (2722±53 Ma; Teixeira, 2013; Teixeira et al., 2015) and Serra da Onça (2766±6Ma; unpublished data reported by Lafon et al., 2000) complexes overlap with precise ages of the bimodal volcanism of the Grão Pará Group (2759±2 Ma, Machado et al., 1991; 2760±11 Ma, Trendall et al., 1998), thus supporting the interpretation that mafic volcanics and mafic-ultramafic layered intrusions resulted from coeval magmatic events (Machado et al., 1991; Ferreira Filho et al., 2007). Even though the available geochronological data are restricted to few complexes, and not sufficiently precise to indicate that dated layered intrusions were all coeval, they support the interpretation that layered intrusions and the bimodal volcanism of the Carajás Province result from a major Neoarchean (ca. 2.76 Ga) magmatic event.

The tectonic setting of the volcanic-sedimentary sequences of Carajás (Itacaiúnas Supergroup) is a highly debated issue. This extensive basaltic volcanism is usually considered to result from intra-plate rifting of older continental crust (Gibbs et al., 1986; Olszewski et al., 1989; Villas and Santos, 2001) but subduction-related environments have also been proposed (Dardenne et al., 1988; Teixeira and Eggler, 1994; Zucchetti, 2007). The basaltic volcanism in the Itacaiúnas Supergroup shows lithogeochemical and isotopic evidence for significant contamination of mantle-derived melts by continental crust, thus supporting the continental rifting model (Gibbs et al., 1986; Olszewski et al., 1989). According to Tallarico (2003), rifting and basaltic volcanism were associated with plume-derived mafic magma underplating.

The structure and composition of the layered intrusions of the Carajás are consistent with a Neoarchean intra-plate rifting environment in Carajás. A schematic model of the geologic setting of emplacement of the Carajás layered intrusions is provided in figure 1.19, based upon current models for the origin of Ni-Cu-PGE mineralized layered intrusions associated with continental rifting and volcanism (Barnes and Lightfoot, 2005; Lightfoot, 2007). Field evidence consistent with this model is provided by large layered intrusions with pristine rock textures, stratigraphy and magmatic structure intrusive into high metamorphic gneiss-migmatite terrains of the Xingú Complex. Such intrusive contacts are described in the Serra da Onça Complex (Rosa, 2014), Lago Grande Complex (Teixeira, 2013; Teixeira et al.,

2015) and Vermelho Complex (this study). Large and primitive layered intrusions, like the Serra da Onça and Vermelho complexes are emplaced within the Xingú Complex, while smaller and moderately primitive intrusions, like the Luanga and Lago Grande complexes, are partially emplaced into volcanic rocks of the Grão Pará Group (Fig. 1.19). These layered intrusions indicate that primitive (i.e. high MgO) magmas were transferred through continental crust and intruded older sialic rocks in the Carajás Province. The assimilation of older continental crust during the ascent and/or emplacement of the mafic-ultramafic magma is consistent with petrological (e.g. crystallization sequence, lithogeochemistry; Fig. 1.14) and isotopic (e.g. Sm-Nd systematics; Fig. 1.18) results reported for the Luanga and Lago Grande complexes in the Serra Leste region (Ferreira Filho et al., 2007; Teixeira 2013; Teixeira et al., 2015), the Serra da Onça Complex in the Tucumã region (Rosa, 2014) and the Vermelho Complex in the Canaã dos Carajás region (this study). The location of the layered complexes in the CMP is controlled by major regional faults, interpreted as dip crustal discontinuities where ponded mantle melts (mafic underplate) were transferred through the crust (Fig. 1.19).

U-Pb age (Ma)	Age	Complex	Fo (%)	$\varepsilon_{Nd(T=2.77)}$
LA-ICPMS	2722±53	Lago Grande	80.4 - 86.7	- 4.2 to - 0.3
ID-TIMS	2763±6	Luanga	80.0 - 84.7	na
		Vermelho	85.6 - 90.5	- 7.3 to + 0.1
SHRIMP	2766±6	Onça	86.2 - 92.4	- 3.1 to - 2.1
ID-TIMS	2759±2	Grão Pará		
SHRIMP	2760±11	Grão Pará		
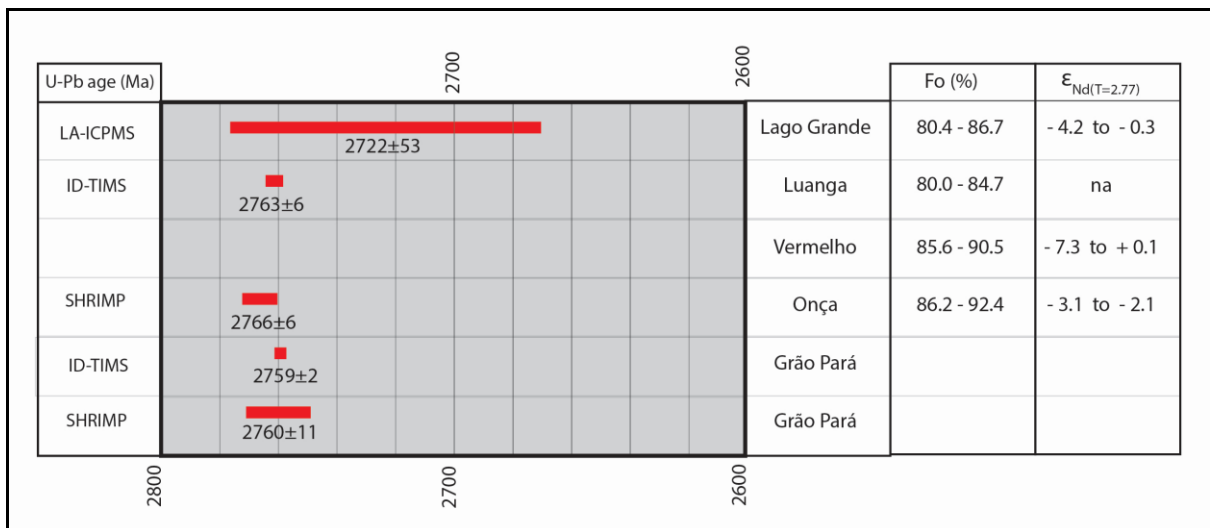
Figure 1.18. Summary of U-Pb zircon ages, Fo contents of olivine and Sm-Nd isotopes for layered intrusions of the CMP. Data from the following references: Lago Grande (Teixeira, 2013; Teixeira *et al.*, 2015); Luanga (Machado *et al.*, 1991; Ferreira Filho *et al.*, 2007); Serra da Onça (Lafon et al., 2000; Rosa, 2014; Rosa et al., submitted); Vermelho (this study); Grão Pará (Machado *et al.* 1991; Trendall *et al.*, 1998).
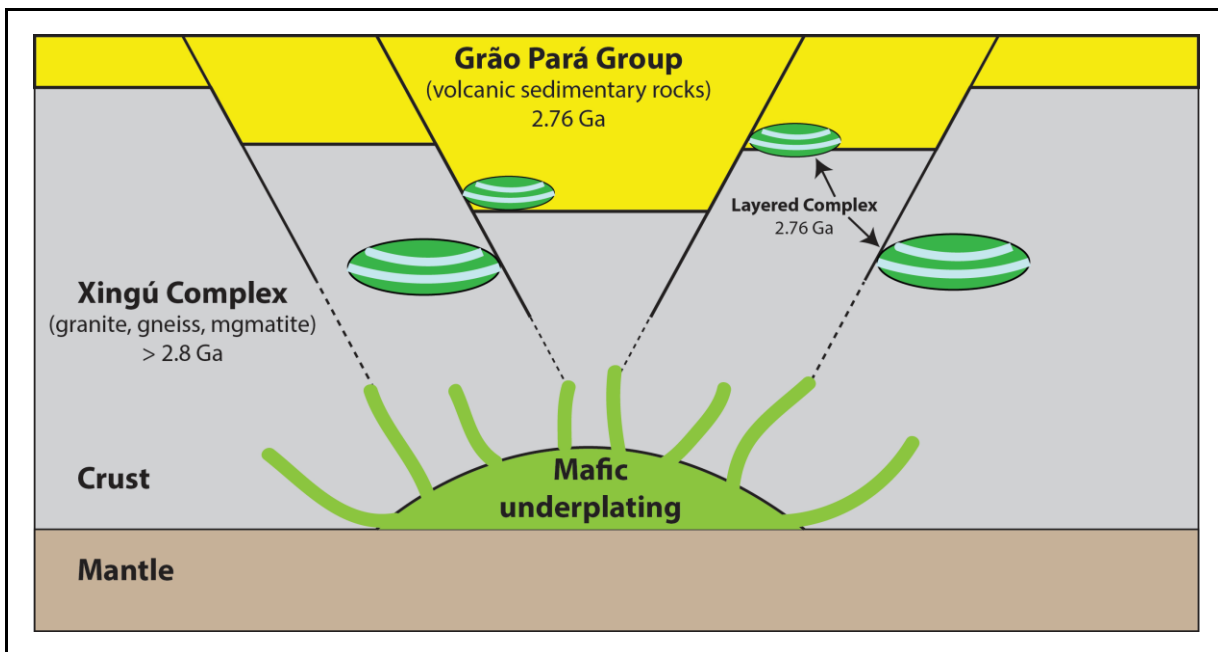
Figure 1.19. Schematic model of the geologic setting for emplacement of the Carajás layered intrusions. See text for discussion.

Acknowledgments

References

Alves, C.A., Bernardelli, A.L., Beisiegel, V.R., 1986. A jazida de níquel laterítico do Vermelho, serra dos Carajás, Pará. In: Schobbenhaus, C.R. & Coelho, C.E.S. (Coords.). Principais Depósitos Minerais do Brasil. Rio de Janeiro, DNPM, 2, 325-340.

Araújo, O.J.B., Maia, R.G.N., João, X.S.J., Costa, J.B.S., 1988, A megaestruturação arqueana da Folha Serra dos Carajás. In: Congresso Latino Americano de Geologia, Anais, Belém-Brasil, 1, 324-338.

Araújo, O.J.B. de, Maia R.G.N., 1991. Programa Levantamentos Geológicos Básicos do Brasil. Serra de Carajás. Folha SB.22- Z-A. Estado do Pará. Brasília, DNPM-CPRM, 136 pp.

Avelar, V.G., Lafon, J.M., Correia JR., F.C., Macambira, E.M.B., 1999. O magmatismo arqueano da região de Tucumã-Província Mineral de Carajás: Novos dados geocronológicos. Revista Brasileira de Geociências 29, 453-460.

Barnes, S-J., Lightfoot, P.C., 2005. Formation of magmatic nickel-sulfide ore deposits and processses affecting their copper and platinum-group element contents. In Hedenquist, J.W., Thompson, J.F.H., Goldfarb, R.J. and Richards, J.P. (Eds.). Economic Geology 100th Anniversary Volume, 179-213.

Barnes, S-J., Maier, W.D., Curl, E., 2010. Composition of the marginal rocks and sills of the Rustenburg layered suite, Bushveld Complex, South Africa: implications for the formation of the PGE deposits. Economic Geology 105, 1491–1511.

Barros, C.E.M., Sardinha, A.S., Barbosa, J.P.O., Krimski, R., Macambira, M.J.B., 2001. Pb–Pb and U–Pb zircon ages of Archean syntectonic granites of the Carajás metallogenic province, northern Brazil. In: Proceedings of the South American Symposium on Isotopic Geology 3, 94-97.

Barros, C.E.M., Sardinha, A.S., Barbosa, J.P.O., Macambira, M.J.B., 2009. Structure, petrology, geochemistry and zircon U/Pb and Pb/Pb geochronology of the synkinematic Archean (2.7Ga) A-type granites from the Carajás Metallogenic Province, northern Brazil. The Canadian Mineralogist 47, 1423-1440.

Bernardelli, A.L., Melfi, A.J., Oliveira, S.M.B. de, Trescases, J.J., 1983. The Carajás nickel deposit. In: Melfi, A.J. & Carvalho, A. (Eds). Laterization processes: Proceedings of the II Int. Sem. on Laterisation Processes. IAG, 107-118.

Campbell, I.H., 1985. The difference between oceanic and continental tholeiites: a fluid dynamic explanation. Contributions to Mineralogy and Petrology 91, 37-43.

Campbell, I.H., Murck, B.W., 1993. Petrology of the G and H chromitite zones in the Mountain View area of the Stillwater Complex, Montana. Journal of Petrology, 34, 291-316.

Cawthorn, R.G., Walraven, F., 1998. Emplacement and crystalization time for the Bushveld Complex. Journal of Petrology 39, 1669-1687.

Correa, S.L.A., Oliveira, N.P., Schwab, R.G., 1984. Alguns aspectos mineralógicos e geoquímicos da laterita niquelífera do Vermelho, serra dos Carajás, e suas implicações genéticas. In: Congresso Brasileiro de Geologia, 33, Rio de Janeiro, SBG, Anais 10, 4838-4849.

Costa, J.B.S., Araújo, O.J.B., Santos, A., João, X.S.J., Macambira, M.J.B., Lafon, J.M., 1995. A Província Mineral de Carajás: aspectos tectono estruturais, estratigráficos e geocronológicos. In: Boletim do Museu Paraense Emílio Goeldi, Série Ciências da Terra 7, 199-235.

Costa, J.B.S., Bemerguy, R.L., Hasui, Y., Borges, M. da S., Ferreira Júnior, C.R.P., Bezerra, P.E.L., Costa, M.L. da, Fernandes, J.M.G., 1996, Neotectônica da região amazônica: aspectos tectônicos, geomorfológicos e deposicionais: Geonomos 4 (2), 23-44.

CVRD-Companhia Vale do Rio Doce S.A., 2004. Projeto Níquel do Vermelho. Relatório Interno-CVRD, Carajás-PA (inédito), 194 pp.

Dall'Ágnol, R., Souza, Z.S., Althoff, F.J., Barros, C.E.M., Leite, A.A.S., João, X.S.J., 1997. General aspects of the granitogenesis of the Carajás metallogenetic province. In: Proceedings of the International Symposium on Granites and Associated Mineralizations, Salvador, Excursion Guide, 135-161.

Dall'Agnol, R., Teixeira, N.P., Rämö, O.T., Moura, C.A.V., Macambira, M.J.B., Oliveira, D.C. 2005. Petrogenesis of the Paleoproterozoic, rapakivi, A-type granites of the Archean Carajás Metallogenic Province, Brazil. Lithos 80, 101-129.

Dall'Agnol, R., Oliveira, M.A., Almeida, J.A.C., Althoff, F.J., Leite, A.A.S., Oliveira, D.C., Barros, C.E.M., 2006. Archean and Paleoproterozoic granitoids of the Carajás metallogenetic province, eastern Amazonian craton. In: Dall'Agnol, R., Rosa-Costa L.T., Klein E.L. (Eds.) Symposium on Magmatism, Crustal Evolution, and Metallogenesis of the Amazonian Craton, Abstracts Volume and Field Trips Guide. Belém, PRONEXUFPA/SBG-NO, 150 pp.

Dardenne, M.A., Ferreira Filho, C.F., Meirelles, M.R., 1988. The role of shoshonitic and calc-alkaline suites in the tectonic evolution of the Carajás District, Brazil. Journal of South American Earth Science 1, 363-372.

DePaolo, D.J. 1981. A neodymium and strontium isotopic study of the Mesozoic calc-alcaline granitic batholiths of the Sierra Nevada and Penisular Ranges, California. Journal of Geophysical Research 86 (B11), 10470-10488.

Dias, G.S., Macambira, M.J.B., Dall'Agnol, R., Soares, A.D.V., Barros, C.E.M., 1996. Datação de zircões de Sill de metagabro: Comprovação da idade arqueana da Formação Águas Claras, Carajás, Pará. In: Simpósio de Geologia da Amazônia, V, Belém, Sociedade Brasileira de Geologia, Extended Abstracts Bulletin, 376-379.

Docegeo-Rio Doce Geologia e Mineração, 1988. Revisão Litoestratigráfica da Província Mineral de Carajás. In: Provincia Mineral de Carajás, Litoestratigrafia e principais depósitos minerais. CVRD/SBG, Congresso Brasileiro de Geologia (Belém), *Anexo aos anais*, 35, 11-59.

Eales, H.V., 2000. Implications of the chromium budget of the Western Limb of the Bushveld Complex. South African Journal of Geology 103, 141-150.

Eales, H.V., Cawthorn, R.G., 1996. The Bushveld Complex. In: Cawthorn, R.G. (Ed.), Layered Intrusions. Developments in Petrology, vol. 15. Elsevier Science B. V. 181-229.

Egorova, V., Latypov, R.M., 2012. Processes operating during the initial stage of magma chamber evolution: insights from marginal reversal of the Imandra Layered Intrusion, Russia. Journal of Petrology 53, 3-26.

Egorova, V., Latypov, R.M., 2013. Mafic-ultramafic sills: new insights from M- and S-shaped mineral and whole-rock compositional profiles. Journal of Petrology 54, 2155-2191.

Faraco, M.T.L., Vale, A.G., Santos, J.O.S., Luzardo, R., Ferreira, A.L., Oliveira, M.A., Marinho, P.A.C., 2005. Levantamento Geológico da Região ao Norte da Província Carajás In: Souza, V. & Horbe, A.C. (Eds.). Contribuições a Geologia da Amazônia 4, 32-44.

Feio, G.R.L., Dall'Agnol, R., 2012. Geochemistry and petrogenesis of the Mesoarchean granites from the Canaã dos Carajás area, Carajás Province, Brazil: Implications for the origin of Archean granites, Lithos 154, 33-52.

Feio, G.R.L., Dall'Agnol, R., Dantas, E.L., Macambira, M.J.B., Santos, J.O.S., Althoff, F.J., Soares, J.E.B., 2013. Archean granitoid magmatism in the Canaã dos Carajás area:

Implications for crustal evolution of the Carajás province, Amazonian craton, Brazil. Precambrian Research 227, 157-185.

Ferreira Filho, C.F., Araujo, S.M., 2009. Review of Brazilian chromite deposits associated with layered intrusions: geological and petrological constraints for the origin of stratiform chromitites. Applied Earth Sciences (Trans. Inst. Min. Metall. B) 118, 86-100.

Ferreira Filho, C.F., Cançado, F., Correa, C., Macambira, E.M.B., Siepierski, L., Brod, T.C.J., 2007. Mineralizações estratiformes de EGP-Ni associadas a complexos acamadados em Carajás: os exemplos de Luanga e Serra da Onça. In: Contribuições à Geologia da Amazônia, Sociedade Brasileira de Geologia - Núcleo Norte, 5, 01-14.

Figueiredo e Silva, R.C., Lobato, L.M., Rosière, C.A., Zucchetti, M., Hagemann, S.H., Baars, F.J., Morais, R. Andrade, I., 2008. A hydrothermal origin for the jaspilite-hosted, giant iron ore of the Serra Norte deposits in the Carajás Province, Pará State, Brazil. In: Hagemann, S.G., Rosière, C.A., Gutzmer, J., and Beukes, N.J., (Eds.), BIF-related high-grade iron mineralization. Reviews in Economic Geology 15, 255-290.

Gibbs, A.K., Wirth, K.R., Hirata, W.K., Olszewski Jr., W.J., 1986. Age and composition of the Grão Pará Group volcanics, Serra dos Carajás. Revista Brasileira de Geociências 16, 201-211.

Gioia, S.M.C.L., Pimentel, M.M., 2000. The Sm-Nd isotopic method in the geochronology laboratory of the University of Brasília. An. Acad. Bras., 72, 220-245.

Godel B., Barnes, S-J., Maier, W.D., 2011. Parental magma composition inferred from in situ trace elements in cumulus and intercumulus silicate minerals: example from the lower and lower critical zones of the Bushveld Complex (South Africa). Lithos 125, 537-552.

Hirata, W.K., Rigon, J.C., Kadekaru, K., Cordeiro, A.A.C., Meireles, E.A., 1982. Geologia Regional da Província Mineral de Carajás. In: Simpósio Geologia da Amazônia, 1, Belém, Anais Belém, SBG/NO, 1, 100-110.

Holdsworth, R.E., Pinheiro, R.V.L., 2000. The anatomy of shallow-crustal transpressional structures: insights from the Archean Carajás fault zone, Amazon, Brazil. Journal Structural Geology 22, 1105-1123.

Huhn, S.R.B., Santos, A.B.S., Amaral, A.F., Ledsham, E.J., Gouveia, J.L., Martins, L.P.B., Montalvão, R.M.G., Costa, V.C., 1986. O terreno granito-greenstone da região de Rio Maria-Sul do Pará. In Congresso Brasileiro de Geologia, 35, Anais, Sociedade Brasileira de Geologia 3, 1438-1452.

Huhn, S.R.B., Macambira, M.J.B., Dall'Agnol, R., 1999. Geologia e Geocronologia Pb/Pb do Granito Alcalino Arqueano Planalto, Região da Serra do Rabo, Carajás-PA. In: Simpósio de Geologia da Amazônia, 6. Manaus, Anais, Sociedade Brasileira de Geologia - Núcleo Norte 1, 463-466.

Huppert, H.E., Sparks, R.S.J., 1989. Chilled margins in igneous rocks. Earth and Planetary Science Letters 92, 397-405.

Irvine, T. N., 1975. Crystallization sequences in the Muskox intrusion and other layered intrusions-II. Origin of chromitite layers and similar deposits of other magmatic ores. Geochimica et Cosmochimica Acta 39, 991-1020.

Irvine, T.N., 1977. Origin of chromitite layers in the Muskox intrusion and other layered intrusions: a new interpretation. Geology 5, 573-577.

Irvine, T.N., Smith, C.H., 1967. The ultramafic rocks of the Muskox intrusion, Northwest Territories, Canada. In: Wyllie, P.J. (ed.) Ultramafic and Related Rocks. New York: John Wiley & Sons, Inc., 38-49.

Kuck, P.H., 2003. U.S. Geological Survey Mineral Yearbook: Nickel-2003. In: http://minerals.usgs.gov/minerals/pubs/commodity/nickel/nickemyb03.pdf

Lafon, J.M., Macambira, M.J.B., Pidgeon, R.T., 2000. Zircon U-Pb SHRIMP dating of Neoarchean magmatism in the southwestern part of the Carajás Province (eastern Amazonian Craton, Brazil). In: International Geological Congress, 30, Abstract Volume, CD-ROM.

Latypov, R.M., 2003a. The origin of marginal compositional reversals in basic-ultrabasic sills and layered intrusions by Soret fractionation. Journal of Petrology 44, 1579-1618.

Latypov, R.M., 2003b. The origin of basic-ultrabasic sills with S-, D-, and I-shaped compositional profiles by in situ crystallization of a single input of phenocryst-poor parental magma. Journal of Petrology 44, 1619-1656.

Latypov, R.M., Chistyakova, S.Yu, Alapieti, T.T., 2007. Revisiting problem of chilled margins associated with marginal reversals in mafic-ultramafic intrusive bodies. Lithos 99, 178-206.

Latypov, R.M., Hanski, E., Lavrenchuk, A., Huhma, H., Havela, T., 2011. A 'Three-Increase Model' for the Origin of the Marginal Reversal of the Koitelainen Layered Intrusion, Finland. Journal of Petrology 52, 733-764.

Leite, A.A.S., Dall'Agnol, R., Macambira, M.J.B., Althoff, F.J., 2004. Geologia e geocronologia dos granitóides arqueanos da região de Xinguara (PA) e suas implicações na evolução do Terreno Granito-Greenstone de Rio Maria. Rev. Bras.Geoc., 34, 447-458.

Lightfoot, P.C., Naldrett, A.J., 1984. Chemical variation in the Insizwa complex, Transkei, and the nature of the parent magma. Canadian Mineralogist 22, 111-123.

Lightfoot, P.C., 2007. Advances in Ni-Cu-PGE Sulphide Deposit Models and Implications for Exploration Technologies. In "Proceedings of Exploration 07: Fifth Decennial International Conference on Mineral Exploration" edited by B. Milkereit, 629-646.

Lipin, B.R., 1993. Pressure increases, the formation of chromite seams, and the development of the ultramafic series in the Stillwater Complex, Montana. Journal of Petrology 34, 955-976.

Lobato, L.M., Figueiredo e Silva, R.C., Rosière, C.A., Zucchetti, M., Baars, F.J., Seoane, J.C.S., Rios, F.J., Monteiro, A.M., 2005. Hydrothermal origin for the iron mineralisation, Carajás province, Pará State, Brazil. In: Proceedings Iron Ore 2005. The Australian Institute of Mining and Metallurgy, Publication Series no 8, 99-110.

Macambira, E.M.B., 1997. Geologia e aspectos metalogenéticos dos elementos do Grupo Platina no Complexo Máfico-ultramáfico da Serra da Onça-Sul do Pará. Belém-UFPA. MSc thesis, 178 pp.

Macambira, E.M.B., Tassinari, C.C.G., 1998. Estudos Sm-Nd no Complexo Máfico-ultramafico da Serra da Onça-Sul do Para. Implicações geocronológicas e geotectônicas. In: Congresso Brasileiro de Geologia, 40, Belo Horizonte, SBG, Anais, 1, 463-463.

Macambira, M.J.B., Lancelot, J.R., 1996. Time constraints for the formation of the Archean Rio Maria crust, Southeastern Amazonian Craton, Brazil: International Geology Review 38, 1134-1142.

Machado, W., Lindenmayer, Z.G., Krogh, T.E., Lindenmayer, D., 1991. U-Pb geochronology of Archean magmatism and basement reactivation in the Carajás área, Amazon shield, Brazil. Precambrian Research 49, 329-354.

Maier, W.D., Barnes, S-J., Groves, D.I., 2013. The Bushveld Complex, South Africa: formation of platinum-palladium, chrome- and vanadium-rich layers via hydrodynamic sorting of a mobilized cumulate slurry in a large, relatively slowly cooling, subsiding magma chamber. Mineralium Deposita 48, 1-56.

McBirney, A.R., 1996. The Skaergaard Intrusion. In: Cawthorn, R.G. (Ed.), Layered Intrusions. Developments in Petrology, vol. 15. Elsevier Science B. V., 147-180.

McCallum, I.S., 1996. The Stillwater Complex. In: Cawthorn, R.G. (Ed.), Layered Intrusions. Developments in Petrology, vol. 15. Elsevier Science B. V., 441-483.

Meireles, E.M., Hirata, W.K., Amaral, A.F., Medeiros Filho, C.A., Gato, W.C., 1984. Geologia das Folhas Carajás e Rio Verde, Província Mineral de Carajás, Estado do Pará. In: SBG, Congresso Brasileiro de Geologia, 34, Rio de Janeiro, Anais, 5, 2163-2174.

Mondal, S.K., Mathez, E.A., 2007. Origin of the UG2 chromitite layer, Bushveld Complex. Journal of Petrology 48, 495-510.

Naslund, H.R., MacBirney, A.R., 1996. Mechanisms of Formation of Igneous Layering. In: Cawthorn, R.G. (Ed.), Layered Intrusions. Developments in Petrology, vol. 15. Elsevier Science B. V., 1-43.

Nogueira, A.C.R., Truckenbrod, W., Costa, J.B.S., Pinheiro, R.V.L., 1994. Análise faciológica e estrutural da Formação Águas Claras, Pré-Cambriano da Serra dos Carajás. In: Simpósio de Geologia da Amazônia, 4, Belém, Sociedade Brasileira de Geologia, Resumos Expandidos, 363-364.

Nogueira, A.C.R., Truckenbrod, W., Pinheiro, R.V.L., 2000. Storm and tide-dominated siliciclastic deposits of the Archean Águas Claras Formation, Serra dos Carajás, Brazil. In: 31th International Geological Congress, Rio de Janeiro, Brazil, Extended Abstracts, CD-ROM.

Olszewski, W.J., Wirth, K.R., Gibbs, A.K., Gaudette, H.E., 1989. The age, origin, and tectonics of the Grão Pará Group and associated rocks, Serra dos Carajás, Brazil: Archean continental volcanism and rifting. Precambrian Research 42, 229-254.

Pidgeon, R.T., Macambira, M.J.B., Lafon, J.M., 2000. Th-U-Pb isotopic systems and internal structures of complex zircons from an enderbite from the Pium Complex, Carajás Province, Brazil: evidence for the ages of granulite facies metamorphism and the protolith of the enderbite. Chemical Geology 166, 159-171.

Pinheiro, R.V.L., Holdsworth, R.E., 1997. Reactivation of Archaean strike-slip fault systems, Amazon region, Brazil. Journal of the Geological Society, London, 154, 99-103.

Rolando, A.P., Macambira, M.J.B., 2003. Archean crust formation in Inajá range area, SSE of Amazonian craton, Brazil, based on zircon ages and Nd isotopes. In: SOUTH AMERICAN SYMPOSIUM ON ISOTOPE GEOLOGY, 4, Salvador. Short Papers. Salvador: CBPM, 268-270.

Raedeke, L.D., McCallum, I.S., 1984. Investigations of the Stillwater Complex: Part II. Petrology and petrogenesis of the Ultramafic Series. Journal of Petrology, 25, 395-420.

Rosa, W.D., 2014. Complexos acamadados da Serra da Onça e Serra do Puma: Geologia e petrologia de duas intrusões máfico-ultramáficas com sequência de cristalização distinta na província arqueana de Carajás, Brasil. Unpbl. M.Sc. thesis, Universidade de Brasília, Brazil, 73 pp.

Rosa, W.D., Ferreira Filho, C.F., Pimentel, M.M., submitted. Serra da Onça and Serra do Puma layered complexes: Geology and petrology of two intrusions with distinct crystallization sequences in the Archean Carajás Provinde, Brazil. Submitted to Applied Earth Sciences - IMM.

Santos, J.O.S., Groves, D.I., Hartmann, L.A., Moura, M.A., Mc-Naughton, N.J., 2001. Gold deposits of the Tapajós and Alta Floresta domains, Tapajós-Parima orogenic belt, Amazon craton, Brazil. Mineralium Deposita 36, 278-299.

Sardinha, A.S., Dall'Agnol, R., Gomes, A.C.B., Macambira, M.J.B., Galarza, M.A., 2004. Geocronologia Pb–Pb e U–Pb em zircão de granitóides arqueanos da região de Canaã dos Carajás, Província Mineral de Carajás. Congresso Brasileiro de Geologia, 42. CDrom (in Portuguese).

Sardinha, A.S., Barros, C.E.M., Krymsky, R., 2006. Geology, geochemistry, and U–Pb geochronology of the Archean (2.74Ga) Serra do Rabo granite stocks, Carajás Province, northern Brazil. Journal of South American Earth Sciences 20, 327-339.

Silva, M.L.M.C., Oliveira, S.M.B., 1995. As fases portadoras de níquel do minério laterítico de níquel do Vermelho, Serra dos Carajás (PA). Revista Brasileira de Geociências 25, 69-78.

Simkin, T., Smith, J.V., 1970. Minor-element distribution in olivine. Journal of Geology 78, 304-325.

Soares, A.D.V., Santos, A.B., Vieira, E.A., Bella, V.M., Martins, L.P.B., 1994. Área Águas Claras: Contexto geológico e mineralizações. In: Simpósio de Geologia da Amazônia, 4, Belém, Anais, Sociedade Brasileira de Geologia, 379-382.

Souza, S.R.B., Macambira, M.J.B., Sheller, T., 1996. Novos dados geocronológicos para os granitos deformados do Rio Itacaiúnas (Serra dos Carajás, PA), implicações estratigráficas. In: Simpósio de Geologia da Amazônia, 5, Belém, Anais, Sociedade Brasileira de Geologia, 380-383.

Spier, C.A., Ferreira Filho, C.F., 2001. The chromite deposits of the Bacuri mafic-ultramafic layered complex, Guyana Shield, Amapá´ State, Brazil, Economic Geology 96, 817-835.

Sun, S.S., McDonough, W.F., 1989. Chemical and isotopic systematics of oceanic basalts: Implications for mantle composition and processes. In: Saunders, A.D., Norry, M.J. (Eds.), Magmatism in Oceanic Basins, Geol. Soc. London Spec. Pub. 42, 313-345.

Tait, S., Jaupart, C., 1996. The producing of chemically stratified and accumulate plutonic igneous rocks. Mineralogical Magazine 60, 99–114.

Tallarico, F.H.B., 2003. O Cinturão Cupro-Aurífero de Carajás, Brasil. PhD Thesis. Universidade Estadual de Campinas, Brazil, 229 pp.

Teixeira, A.S., 2013. Geologia, Petrologia e Geocronologia do Complexo Acamadado Lago Grande: Evidência para uma Suite Magmática Mineralizada a PGE na Província Carajás – Brasil. Unpbl. M.Sc. thesis, Universidade de Brasília, Brazil, 108 pp.

Teixeira, A.S., Ferreira Filho, C.F., Giustina, M.E.S.D., Araújo, S.M., Silva, H.H.A.B., 2015. Geology, petrology and geochronology of Lago Grande Layered Complex: evidence for a PGE-mineralized magmatic suite in Carajás Mineral Province, Brazil. J. S. Am. Earth Sci. 64, 116-138.

Teixeira, J.B.G., Eggler, D.H., 1994. Petrology, Geochemistry, and Tectonic Setting of Archaean Basaltic and Dioritic Rocks from the N4 Iron Deposit, Serra dos Carajás, Pará, Brazil. Acta Geologica Leopoldensia 17, 71-114.

Trendall, A.F., Basei, M.A.S., De Laeter, J.R., Nelson, D.R., 1998. SHRIMP zircon U-Pb constraints on the age of the Carajás Formation, Grão Pará Group, Amazon Craton: Journal of South American Earth Sciences 11, 265-277.

Vasconcelos, P.M., Renne, P.R., Brimhall, G.H., Becker, T.A., 1994. Direct dating of weathering phenomena by 40Ar/39Ar and K-Ar analysis of supergene K-Mn oxides: Geochimica et Cosmochimica Acta 58, 1635-1665.

Vasquez, M.L., Rosa-Costa, L.T., 2008. Geologia e recursos minerais do Estado do Pará: texto explicativo do mapa geológico e de recursos minerais do Estado do Pará-escala 1:1.000.000. Programa Geologia do Brasil (PGB), CPRM. 328 pp.

Villas, R.N., Santos, M.D., 2001. Gold deposits of the Carajás mineral province: Deposit types and metallogenesis. Mineralium Deposita 36, 300-331.

Wedepohl, K.H., 1995. The composition of the continental crust. Geochim Cosmochim Acta 59, 1217-1232.

Wilson, A.H., 1982. The Geology of the Great 'Dyke', Zimbabwe: The Ultramafic Rocks. Journal of Petrology 23, 240-292.

Wilson, A.H., 2012. A Chill Sequence to the Bushveld Complex: Insight into the First Stage of Emplacement and Implications for the Parental Magmas. Journal of Petrology 53, 1123-1168.

Wilson, J.R., Engell-Sørensen, O., 1986. Marginal reversals in layered intrusions are evidence for emplacement of compositionally stratified magma. Nature 323, 616-618.

Zucchetti, M., 2007. Rochas máficas do Grupo Grão Pará e sua relação com a mineralização de ferro dos depósitos N4 e N5, Carajás, PA. Phd thesis, Belo Horizonte, Instituto de Geociências, UFMG, 116 pp.

Zucchetti, M., Lobato, L.M., Hagemann, S., 2007. Hydrothermal alteration of basalts that host the giant Northern Range Carajás iron deposits, Brazil. In: C.J. Andrew et al. (Eds.), Proceedings of 9th Biennial SGA Meeting, Dublin, 1231-1234.

"STRATIGRAPHY AND PETROLOGY OF THE TOURO MAFIC-ULTRAMAFIC COMPLEX, CARAJÁS PROVINCE, BRAZIL."

LINCOLN SIEPIERSKI, CESAR FONSECA FERREIRA FILHO, EDUARDO T. MANSUR

STRATIGRAPHY AND PETROLOGY OF THE TOURO MAFIC-ULTRAMAFIC COMPLEX, CARAJÁS PROVINCE, BRAZIL

Lincoln Siepierski[a,b,] Cesar Fonseca Ferreira Filho[a] and Eduardo Teixeira Mansur[a]

a - Instituto de Geociência, Universidade de Brasília, Brasília, DF, 70910-900, Brazil

b - VALE S/A, Rodovia BR-381/km 450, 33040-900, Santa Luzia, MG, Brazil

Abstract

The Touro Complex is part of a cluster of mafic-ultramafic layered intrusions located in the Transition Subdomain of the Carajás Mineral Province. This medium size complex (4.8 x 1.2 km) consists of an Ultramafic Zone (UZ), a Mafic Zone (MZ) and a thin and discontinuos gabbroic zone located at the lower contact of the Ultramafic Zone and hosted granitoid rocks (designated Basal Gabbroic Rock - BGR). The UZ consists of variably replaced olivine clinopyroxenite (Ol + Cpx + Chr cumulate), wehrlite (Ol + Chr cumulate with intercumulus Cpx) and dunite (Ol + Chr cumulate), while the MZ consists mainly of medium- to coarse-grained gabbro with adcumulate texture, and minor melagabbro with Cpx (or Cpx+Ol) cumulus and Pl intercumulus.

The magmatic structure of the Touro Complex, indicated by geological sections supported by limited diamond drilling and geophysical surveys, suggests a thick subvertical ultramafic feeder capped by a subhorizontal zone of gabbroic rocks. The BGR consists of a narrow and discontinuous zone of fine- to medium-grained gabbro mapped along the southeastern contact of the UZ and host rocks, as well as in few outcrops in the northwestern contact of the MZ. This gabbroic zone located at the lower contact of the Touro Complex

similar to what is described at the base of several layered intrusions. The indicated architecture of the Touro Complex suggests that the extension of the feeder zone remains unexplored, a feature that enhances the potential for hosting deep-seated Ni-Cu-PGE sulfides.

The layered rocks of the Touro Complex originated mainly from crystallization of cumulus olivine, clinopyroxene and plagioclase, following a crystallization sequence consisting of Ol+Chr → Ol+Cpx+Chr → Ol+Cpx+Pl → Cpx+Pl. The absence of Opx as a cumulus mineral in the Touro Complex suggests that the primary magma was silica undersaturated. The compositional range of cumulus Ol ($Fo_{76.3-67.9}$) supports a moderately fractionated parental magma for the Touro Complex. Mantle-normalized alteration-resistant trace element profiles of ultramafic and gabbroic rocks in the Touro Complex are fractionated, as indicated by relative enrichment in LREE and Th, with pronounced negative Nb anomalies.

Distinct crystallization sequences described for the Touro and Vermelho complexes suggest that each complex evolved from a different parental magma. The crystallization sequence of the Vermelho Complex (Ol+Chr → Opx+Chr → Opx → Opx+Pl → Opx+Pl+Cpx) in which Opx precedes Cpx indicates that the magma is silica-saturated, while the crystallization sequence of the Touro Complex suggests that the primary magma was silica undersaturated. Contrasting crystallization sequences were also described for the Serra da Onça (silica-saturated) and Serra do Puma (silica-unsaturated) complexes located in the western portion of the Carajás Mineral Province. Both silica-saturated and silica-unsaturated layered complexes in the Carajás Mineral Province have similar trace element patterns, suggesting that they were derived from a similar mantle source that followed different fractionation path during ascent and/or emplacement in the crust.

Introduction

The medium size (4.8 x 1.2 km) Touro Complex is part of a cluster of different mafic-ultramafic bodies located in the Transitional Subdomain of the Carajás Mineral Province

(CMP). Recent studies of mafic-ultramafic rocks in the CMP (e.g., Rosa, 2014; Teixeira et al., 2015; Silva, 2015; Siepierski and Ferreira Filho, in prep.) indicate the existence of layered intrusions with different size, magmatic structure, crystallization sequence and mineralizations, suggesting that the Neoarchean mafic-ultramafic involved different parental magmas and/or different fractionation processes during magma ascent and emplacement in the crust.

This study provides the first geological and petrological description of the Touro Complex. Results from the exploration program for nickel sulfide deposits developed by AVANCO RESOURCES LIMITED, including geological maps, soil geochemistry data, drill cores and geophysical surveys, provided a basic framework for the geological-stratigraphic interpretation of the layered rocks of this study. Our results indicate that the crystallization sequences described for the Touro and Vermelho (Siepierski and Ferreira Filho, in prep.) complexes (see Fig. 2.1 for location) are different, suggesting that each complex evolved from a different parental magma. The implications of this result for the evolution of the Neoachean magmatism in Carajás is further evaluated in this study.

Geological Setting

Regional Geological Setting

The regional geology of the Carajás Mineral Province and adjacent areas (Fig. 2.1) is described, among others, by Hirata et al. (1982), Meireles et al. (1984), Docegeo (1988), Araújo and Maia (1991), Costa et al. (1995), Vasquez et al (2008), and others. The Carajás Province is best known for hosting several world-class deposits, including the largest iron ore resources in the world, as well as Cu-Au, Ni, PGE, Au and Mn deposits.

The Carajás Mineral Province-CMP (Fig. 2.1) lies in the eastern portion of the Amazon Craton. Regional geotectonic framework for CMP (Vasquez et al., 2008) indicate it is bordered by: Neoproterozoic Araguaia Belt to the east; Paleoproterozoic vulcanic and plutonic rocks of the Iriri-Xingu Domain to the west; Proterozoic to Archean granite-gneiss rocks of the Santana do Araguaia Domain; and geological limits to the north, where Paleoproterozoic gneiss-migmatite-granulite terrains predominate (e.g. Faraco et al., 2005),

are not precisely defined and is referred as Bacajá Domain. Carajás Province have been subdivided in two geotectonic domains (Vasquez et al., 2008): a typical granite-greenstone terrains of the Rio Maria Domain further south; and the complex terrain of the Carajás Domain including mainly Neoarchean volcano-sedimentary sequences and granitic-gneissic-granulite rocks. A E-W Transition Subdomain zone (Dall'Agnol et al., 2006; Feio and Dall'Agnol, 2012), was proposed to separate the Neoarchean volcano-sedimentary sequences of Carajás Domain and the Rio Maria Domain.

The Xingu Complex consists mainly of gneiss, migmatite and granulites (Docegeo, 1988). U-Pb zircon dating of high-grade metamorphic rocks yielded Archean ages, 2,859±9 Ma for the diopside-norite Pium (Pidgeon et al., 2000; Vasquez et al., 2008) and 2,859±2 Ma for migmatites (Machado et al., 1991). These are interpreted to represent ages of metamorphic recrystallization. These basement rocks experienced several episodes of reactivation during the Archean and Paleoproterozoic (Pinheiro and Holdsworth, 1997; Holdsworth and Pinheiro, 2000). The Andorinhas Supergroup consists of typical Archean (2,904 ± 29 Ma; Macambira and Lancelot, 1996) greenstone belts (Docegeo, 1988), including spinifex-textured komatiitc flows and pillowed basalts (Huhn et al., 1986).

The Itacaiúnas Supergroup includes several Archean (ca. 2.75 Ga; Machado et al., 1991; Trendall et al., 1998) volcano-sedimentary sequences (Docegeo, 1988). These include the large sequence of metabasalts of the Grão Pará Group, footwall to the jaspilite-hosted, giant iron deposits of Carajás (Figueiredo and Silva et al., 2008; Lobato et al., 2005). This extensive basaltic volcanism is usually considered to result of intra-plate rifting of older continental crust (Gibbs et al., 1986; Docegeo, 1988; Olszewski et al., 1989; Villas and Santos, 2001) but subduction-related environments have also been proposed (Dardenne et al., 1988; Teixeira and Eggler, 1994; Zuccheti, 2007; Zuchetti et al., 2007).

The Águas Claras Formation (Araújo et al., 1988; Soares et al., 1994) comprises sandstone and siltstone formed in shallow marine to fluvial environment (Nogueira et al., 1994; 2000). This sequence of clastic sedimentary rocks covers different sequences of the Itacaiúnas Supergroup. A minimum age for the Águas Claras Formation was determined by Dias et al. (1996) from zircons obtained from cross cutting gabbroic dikes (2,645±12 Ma). The Gorotire Formation is a clastic immature sequence covering the Itacaiúnas Supergroup and Águas Claras Formation (Docegeo, 1988).

Granititic intrusions of distinct ages and compositions occur in the Carajás Province. These intrusions are mainly correlated to four main distinct periods. Mesoarchean (ca. 2.96-2.93 Ga and 2.87-2.83 Ga) granitic intrusions (Sardinha et al., 2004; Feio et al., 2013); Neoarchean (ca. 2.76-2.73 Ga) intrusions include the Plaquê Suite and other syn-orogenic granites (Avelar et al., 1999; Huhn et al., 1999; Dall'Agnol et al., 1997; Barros et al., 2001; Sardinha et al., 2006; Barros et al., 2009; Feio et al., 2013); younger (ca. 2.56 Ga) intrusions include alkaline granites (Machado et al., 1991 and Souza et al., 1996); and Paleoproterozoic (ca. 1.88 Ga) intrusions include several anorogenic granitic plutons (e.g. Dall'Agnol et al., 2005 and 2006) that belong to an extensive A-type Proterozoic province of the Amazon Craton (e.g. Santos et al., 2001).

Several mafic-ultramafic intrusions intrude the Xingu Complex or the Itacaiúnas Supergroup (Docegeo, 1988). These include large lateritic Ni-mineralized Onça, Puma and Vermelho layered intrusions of the Cateté Suite (Macambira, 1997), as well as the PGE-mineralized Luanga (Ferreira Filho et al., 2007) and Lago Grande complexes (Teixeira et al., 2015). The latter crystallized at 2,763±6 Ma (Machado et al., 1991) and is coeval with the extensive mafic magmatism of the Itacaiúnas Supergroup, whereas the age of the Archean Cateté Suite is poorly constrained (Macambira, 1997; Macambira and Tassinari, 1998).

The Touro Layered Complex was interpreted as part of the Cateté Suite (Macambira, 1997), a subject that is being revised based on ongoing geological, petrological and geochronological studies of the mafic-ultramafic complexes of the Carajás Mineral Province. Recent results (e.g., Rosa, 2014; Teixeira et al., 2015; Silva, 2015; Mansur and Ferreira Filho, in prep.) indicate a large diversity of Neoarchean mafic-ultramafic intrusions in the Carajás region, suggesting that they belong to different magmatic suites.
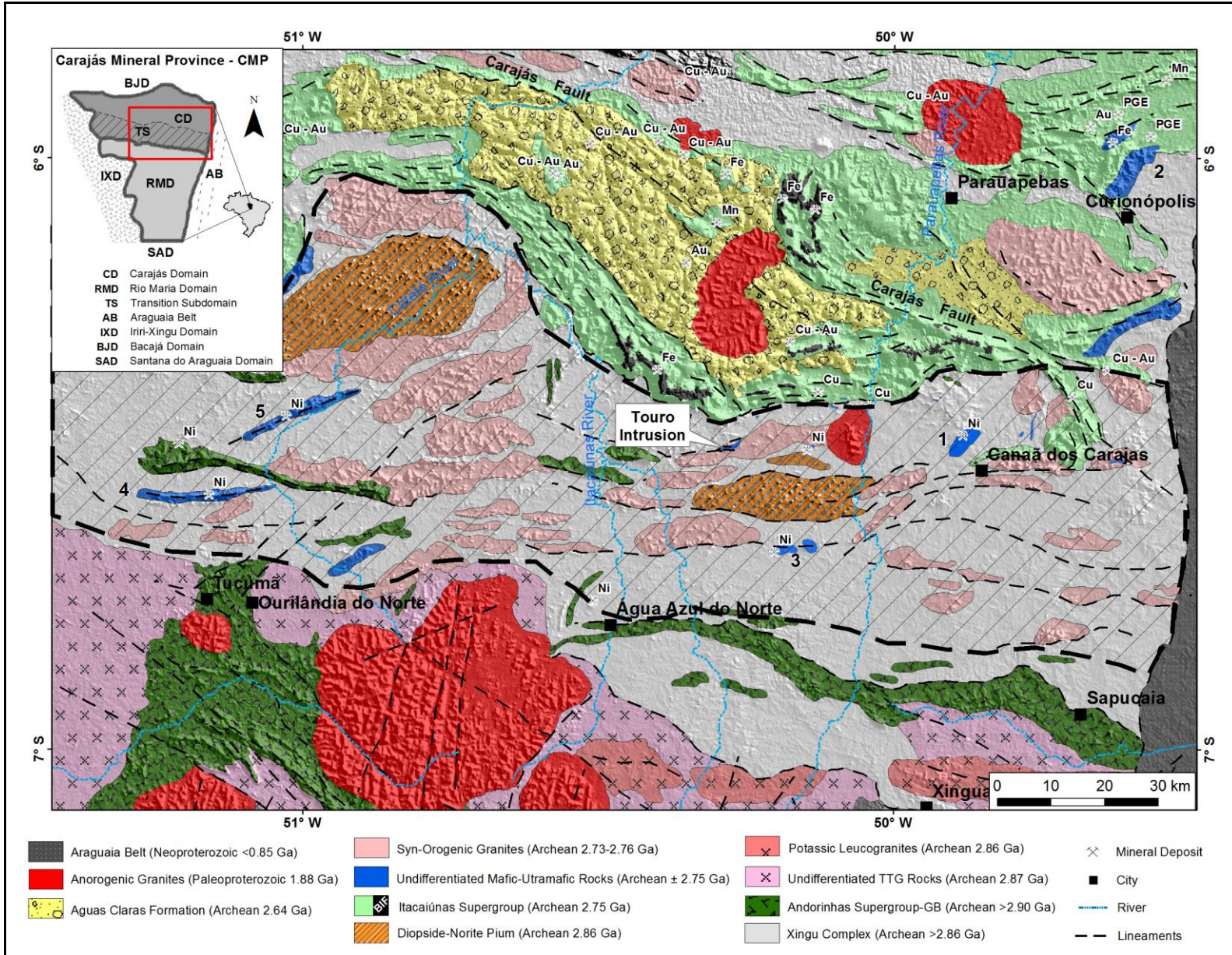
Figure 2.1. Main geological units of part of the Carajás Mineral Province (partially modified from Vasquez et al., 2008). Some mafic-ultramafic layered intrusions are indicated: (1) Vermelho; (2) Serra Leste Magmatic Suite (e.g. Luanga and Lago Grande); (3) Buzios; (4) Onça and (5) Puma. Hatched area: Transition Subdomain-TS (partially modified from Dall´Agnol et al., 2006; Feio and Dall'Agnol, 2012).

Analytical Procedures

Bulk rock analyses (ICP-MS)

Sample preparation and lithogeochemistry analyses were performed at the ALS Chemex (Canada). A total of 12 representative samples from outcrops and drill cores were analysed using three different procedures. These include the whole rock package plus LOI (ALS Chemex codes: ME-XRF12st and OA-GRA05x), total S plus total C (ALS Chemex codes: S-IR08 and C-IR07) and 38 elements fusion ICP-MS package (ALS Chemex code: ME-MS81). A complete description of analytical methods is available in the ALS Chemex Home Page (www.alsglobal.com). Analysed samples (Table 2.1) were arranged into three different groups representative of the main lithotypes.

Microprobe analyses

Mineral analyses were performed on polished thin section using a 5-spectrometer JEOL JXA-8230 SuperProbe at the Electron Microprobe Laboratory of the University of Brasília (Brazil). The wavelength dispersive (WDS) analyses were performed at an accelerating voltage of 15 kV and a beam current of 10 nA. Both synthetic and natural mineral standards were used for the analyses and the same standards and procedure were retained throughout. Fe^{3+} contents were estimated using site and charge balance calculations on cation-normalised analyses. Routine analyses (EDS) of several minerals were also used to support petrographic studies. Systematic WDS analyses were obtained for olivine, clinopyroxene, and plagioclase. Tables 2.2, 2.3 and 2.4 show representative analyses of olivine and clinopyroxene and plagioclase.

The Touro Mafic-Ultramafic Complex

The Touro Mafic-Ultramafic Complex is located at about 5 km south from Carajás ridge and hosted by syn-orogenic granitoid rocks (Feio et al., 2013). This layered intrusion was targeted by AVANCO RESOURCES LIMITED for nickel sulfide deposits in 2009.

Geology and stratigraphy

Based upon field studies and the review of the exploration data (e.g., geological maps, soil geochemistry surveys, drilling) developed by AVANCO, this study provides the first description of the geology and stratigraphy of the Touro Complex. This complex comprises an average 4.8 kilometer long per 1.2 kilometer wide ENE-WSW trending mafic-ultramafic intrusion (Fig. 2.2).

The most prominent geomorphologic feature of the Touro Complex consists of smooth hills, up to 110 meters higher than surrounding flat areas, sustained by weathered mafic rocks (Fig. 2.3A). The mafic-ultramafic rocks occur mainly as blocks and boulders (Fig. 2.3B and 2.3F) with rare outcrops, such that layering and geological contacts are not well exposed in the field and were supported by ground geophysics (Fig. 2.2) and drilling data.

The stratigraphy of the Touro Complex consists of an Ultramafic Zone, a Mafic Zone and a thin and discontinuos gabbroic zone located at the contact of the Ultramafic Zone and host rocks. The latter is interpreted as a border unit and referred to as the Border Gabbroic Rocks. The ground MAG survey indicated NE-SW linear anomalies coincident with the UZ and extending beneath hosts rocks to the south of bore hole TSD-01. This feature suggests that ultramafic rocks extend below the basement rocks in this region and may represent the feeder zone of the intrusion (see Fig. 2.4 for an interpreted section of the Touro Complex). The geological description presented in this study follows the stratigraphy indicated in Figures 2.2 and 2.4.

Host rocks of the Touro Complex include syn-orogenic granitoid rocks (Fig. 2.2). These granitoid rocks are poorly exposed but are mapped by the typical light-grey quartz-rich soil produced from the weathering of these rocks.
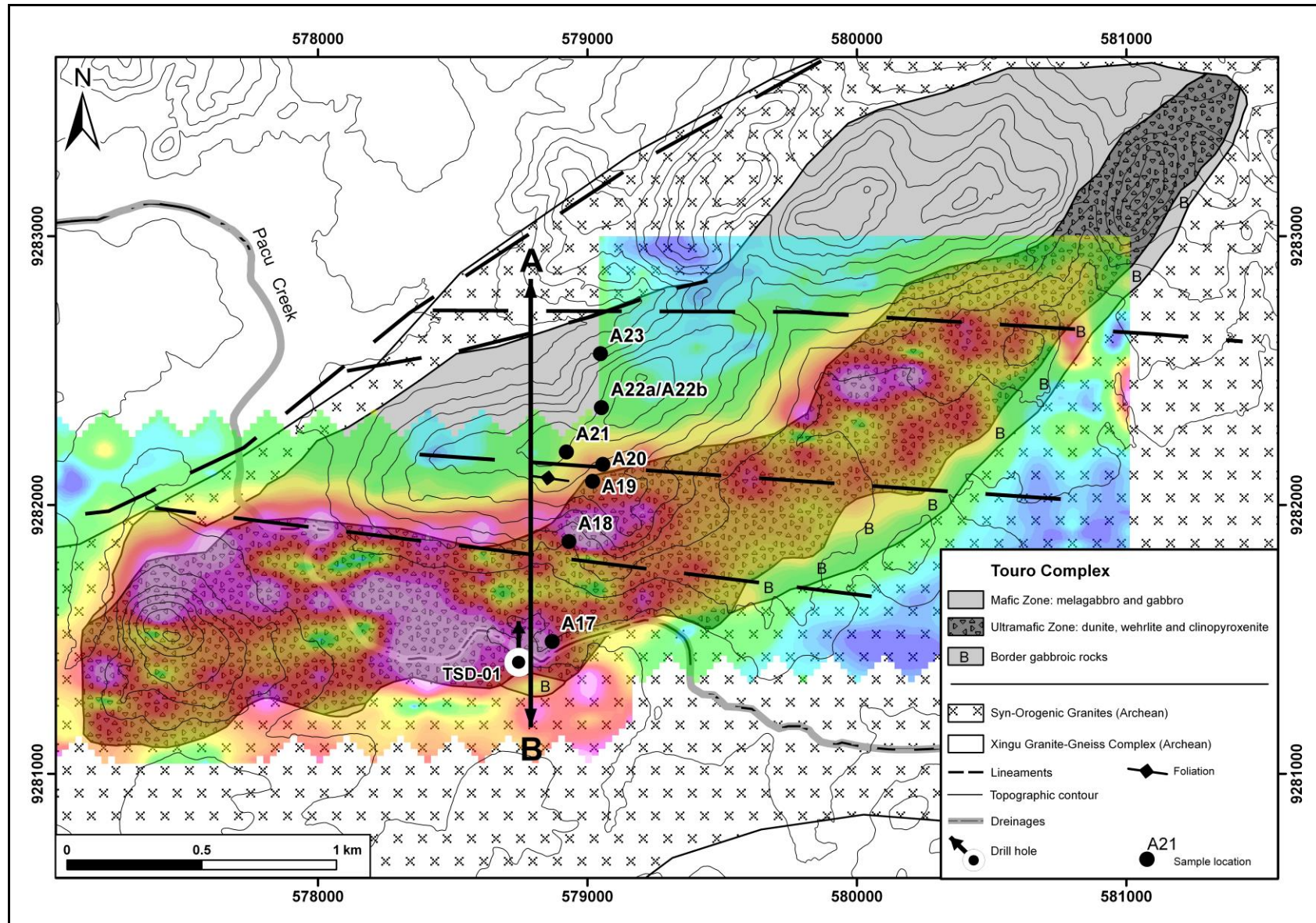
Figure 2.2. Geological map of the Touro Complex (ground MAG-AS on overlay). Partially modified from AVANCO (2009).
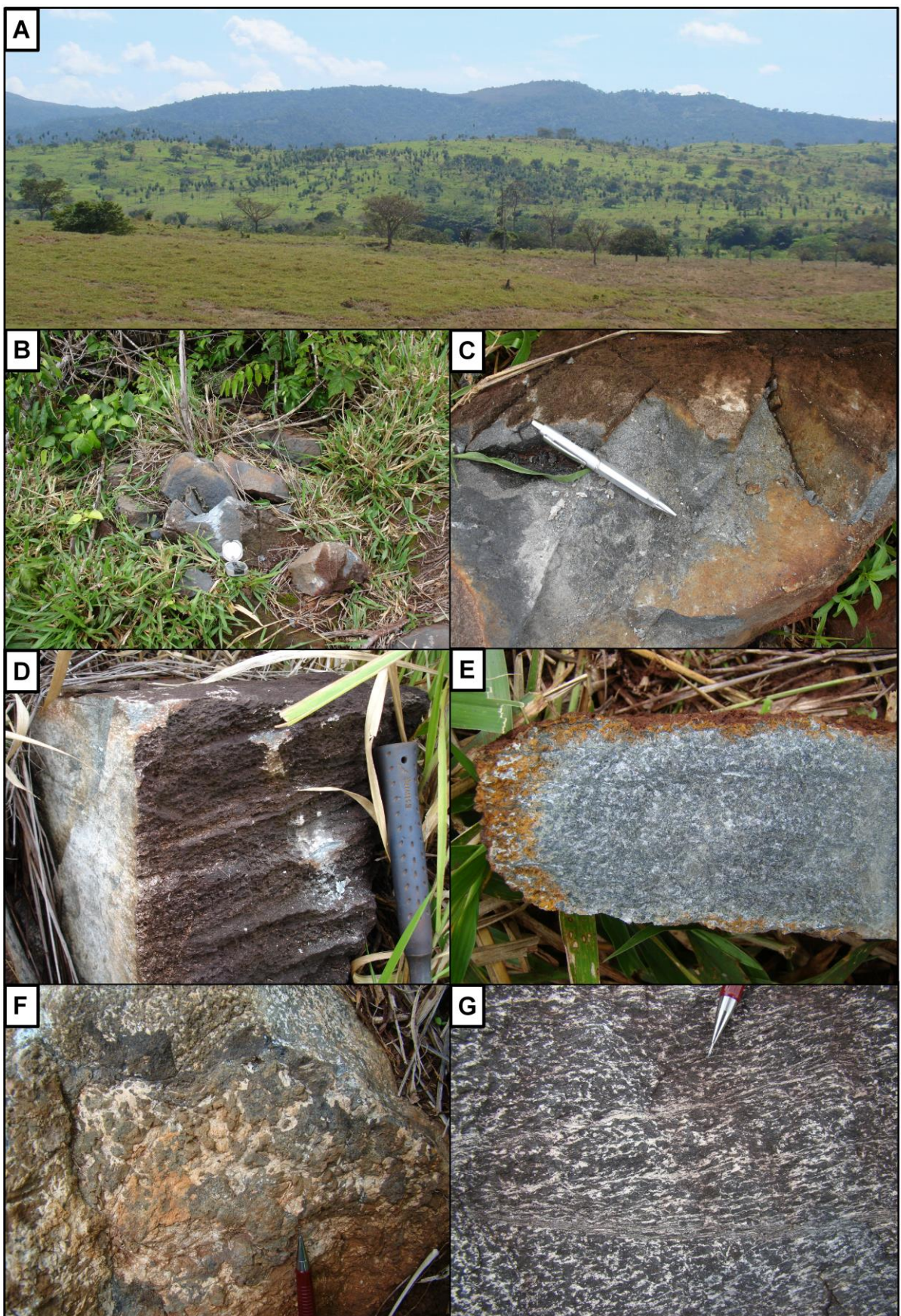
Figure 2.3. A) Panoramic view of the Touro Complex hill with the Carajás ridge on the background (looking northwest). B) Outcrop of olivine-clinopyroxenite of the Ultramafic Zone. C) Detail of olivine-clinopyroxenite showing spots with dark-grey color due to olivine serpentinization. D) Outcrop of clinopyroxenite of the Ultramafic Zone. E) Outcrop of

coarse-grained equigranular gabbro of Mafic Zone. F) Outcrop of pegmatoid gabbro of the Mafic Zone). G) Coarse-grained sheared amphibole-rich gabbroic rock of the Mafic Zone.

Border Gabbroic Rocks

The Border Gabbroic Rocks (BGR) is exposed at the southeastern flank of the Touro Complex following the contact of the Ultramafic Zone and host granitic rocks (Fig. 2.2 and 2.4). The BGR forms a poorly outcropping narrow zone consisting of variably textured gabbroic rocks. Geological information is restricted to limited drill core and weathered outcrops. The thickness of the Border Gabbroic Rocks is highly variable and may be up to 200 meters in some places. Unweathered core samples from the BGR consist mainly of fine to medium-grained gabbro with subophitic texture. Plagioclase crystals are partially to extensively saussuritized while clinopyroxene crystals are mainly transformed to amphibole (actinolite).

Ultramafic Zone

The Ultramafic Zone (UZ) crops out as an ENE-WSW zone at the southeastern flank of the hill and nearby lowlands (Fig. 2.2, 2.3A and 2.4). The following description is based on drill cores and outcrops. Drill core TSD-01 intersects a thick sequence of ultramafic rocks suggesting steep contact with the country rocks and the BGR to the east, as well as MZ rocks outcropping in the hill (Fig. 2.4). The ultramafic rocks consists of interlayered magnetite-serpentine amphibolitite and magnetite-talc amphibolitite (after olivine clinopyroxenite), followed by massive, fine to medium-grained, dark grey color ($\pm$amphibole)-magnetite-serpentine-rich rocks. These lithotypes are variably replaced olivine clinopyroxenite (Ol + Cpx + Chr cumulate), wehrlite (Ol + Chr cumulate with intercumulus Cpx) and dunite (Ol + Chr cumulate). Dunite prevails in the lower portion of the drill core, consisting of extensively serpentinized olivine pseudomorphs and accessory phlogopite. Scattered outcrops and frequent boulders/blocks of the UZ rocks consist of medium-grained, dark grey color, strong magnetic olivine-clinopyroxenite and wehrlite (Fig. 2.3B and 2.3C). These lithotypes have adcumulate to mesocumulate textures consisting of variably replaced sub-milimeter to millimeter-scale cumulus olivine (variable replaced by serpentine and magnetite) and chromite, with intercumulus clinopyroxene variably replaced by actinolite and/or chlorite (Fig. 2.5A). Chromite is a conspicuous accessory mineral (up to 2 vol. %) that occurs as fine-grained euhedral crystals, and phlogopite occurs in highly variable proportions

(from none to 3 vol. %) as interstitial crystals. Clinopyroxenite, a medium to coarse-grained, green color, Cpx + Chr adcumulate (Fig. 2.3D) and plagioclase clinopyroxenite, a Cpx mesocumulate with interstial plagioclase, occur in the UZ close to the contact with the MZ. These rock types are also variably replaced such that both pristine igneous minerals (e.g., Cpx, Pl) and pseudomorphs (e.g., Cpx replaced by amphibole, saussuritized plagioclase) occur.

Mafic Zone

The Mafic Zone (MZ), exposed in hills (Fig. 2.2, 2.3A and 2.4), consists mainly of medium- to coarse-grained gabbro with adcumulate texture, and minor melagabbro with Cpx (or Cpx+Ol) cumulus and Pl intercumulus (Fig. 2.3E, 2.5B). Clinopyroxene crystals are partially to extensively replaced by amphibole (actinolite), and plagioclase crystals show widespread saussuritization (Fig. 2.5C). Locally metric-scale pods of pegmatoidal gabbroic rock were hosted in medium-grained gabbro (Fig. 2.3F). These pods are interpreted as concentration of trapped intercumulus liquid enriched in volatiles and incompatible elements. Outcrops of sheared gabbroic rocks occur close to E-W structural lineaments. These rocks exhibit strong planar orientation and millimeter-scale shear-bands. Within sheared zone clinopyroxene crystals are mainly replaced by amphibole and chlorite (Fig. 2.3G and 2.5D).
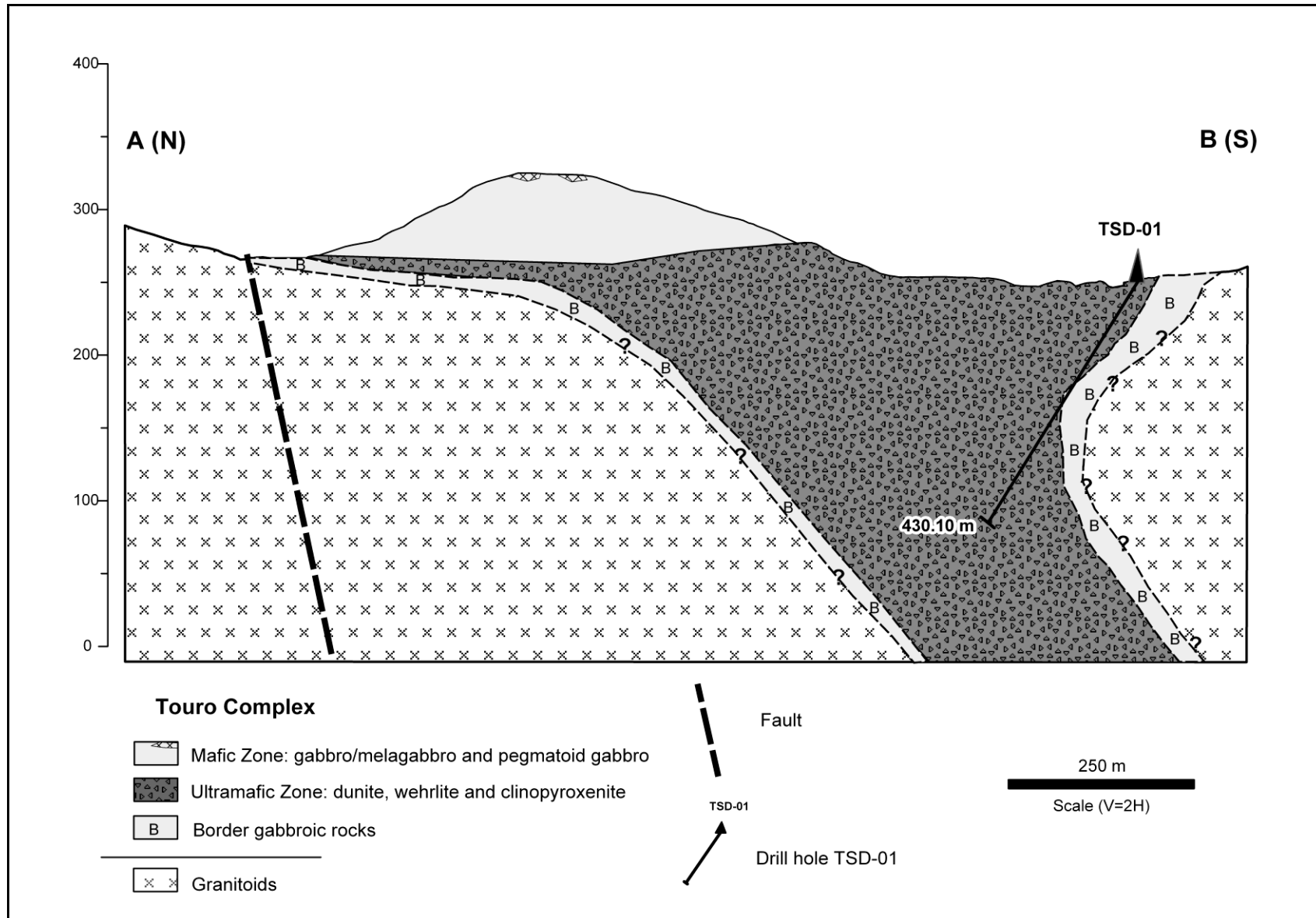
Figure 2.4. Interpreted geological section of the Touro Complex (see Fig. 2.2 for location of the A-B section).
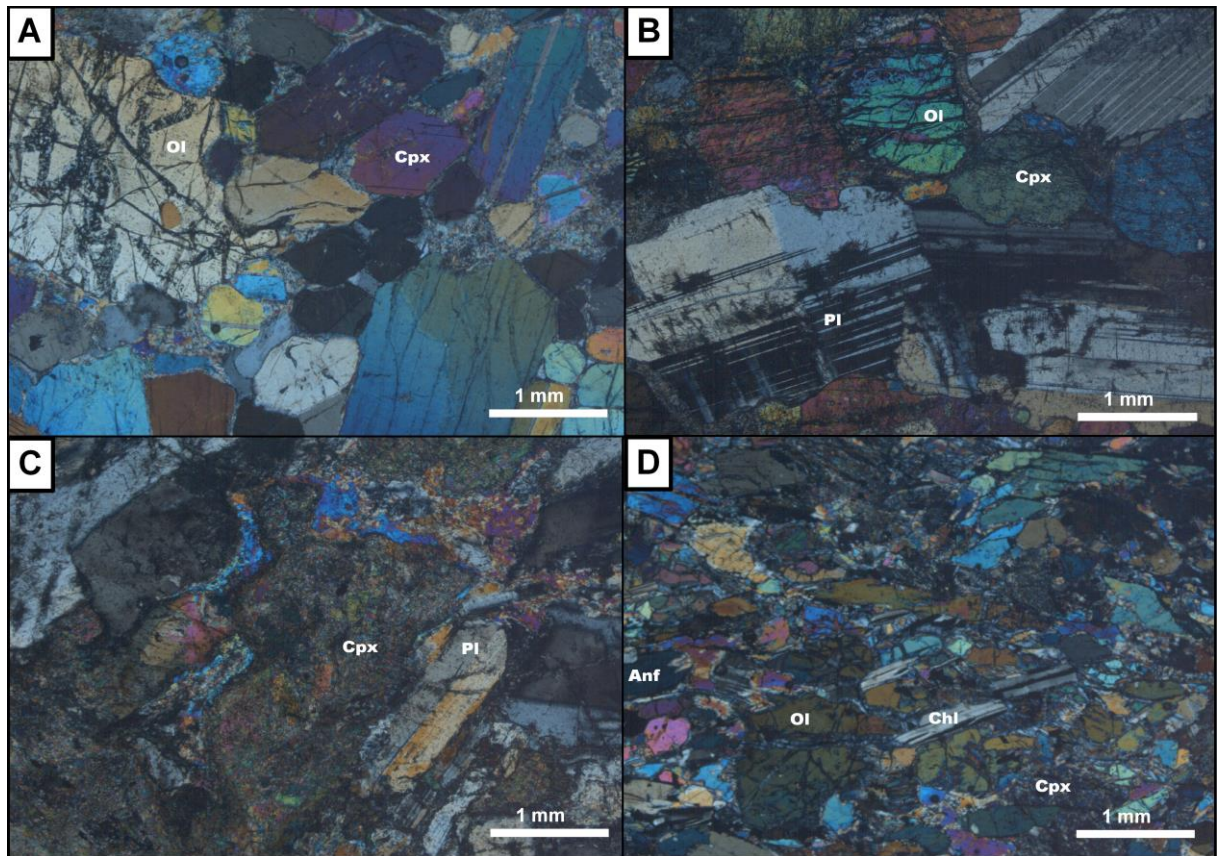
Figure 2.5. Photomicrographs of representative rocks of the Touro Complex. A) Serpentinized olivine-clinopyroxenite of the UZ. Adcumulate texture is defined by olivine pseudomorphs (OL) replaced by serpentine-talc-magnetite and clinopyroxene (Cpx). View in cross-polarized light (XPL). B) Olivine-melagabbro of the MZ. Mesocumulate texture consisting of cumulus olivine (OL) and clinopyroxene (Cpx) and intercumulus plagioclase (Pl) (XPL). C) Gabbro of the MZ with mesocumulate texture and extensive replacement of clinopyroxene by amphibole and saussuritized plagioclase (Pl) (XPL). D) Sheared gabbro of the MZ showing planar fabric and some preserved primary assemblage (XPL).

Bulk Rock Geochemistry

Analysed samples (Table 2.1) are representative of different cumulate rocks with preserved igneous minerals and textures of the Touro Complex. These samples include olivine clinopyroxenite (4 drill core and 2 outcrop samples), olivine-bearing gabbroic rocks (2 outcrop samples) and gabbroic rocks (4 outcrop samples). The plots of major elements and selected trace elements versus MgO (Fig. 2.6) and chondrite-normalized REE patterns (Fig. 2.7) indicate the main characteristics of these distinct rocks.

Olivine clinopyroxenite are characterized by higher MgO (19.1 to 24.4 wt. %) and Fe_2O_3 (9.8 to 14.1 wt. %) contents combined with lower Al_2O_3 (2.7 to 4.2 wt. %) and Na_2O

(0.3 to 0.7 wt. %) contents (Fig. 2.6; Table 2.1), which is expected when Ol + Cpx cumulates are compared with Pl cumulates (olivine gabbro and gabbro). The overall distribution of major and minor elements is mainly controlled by the type and proportion of cumulus minerals, as indicated by strong positive correlation of compatible elements (e.g., Cr and Ni) with MgO and negative correlation of incompatible elements (e.g., Na and Ti) with MgO. High Cr_2O_3 contents of olivine clinopyroxenite (0.3 to 0.4 wt. %) are consistent with the cotetic crystallization of chromite in this rock type.

The analysed lithotypes of the Touro Complex have relatively low contents of incompatible trace elements (Table 2.1), as expected for olivine, clinopyroxene and plagioclase cumulates. Variations in contents of incompatible trace elements in cumulate rocks from layered complexes result from the combined effect of variable assemblages of cumulate minerals, fractionation of the parental magma and variable amounts of trapped intercumulus liquid (Barnes, 1986; Ferreira Filho et al., 1998). Chondrite-normalized rare earth element (REE) profiles are similar for different lithotypes of the Touro Complex (Fig. 2.7). REE profiles for olivine clinopyroxenite have slightly positive slopes (i.e., progressive enrichment toward lighter REE) with chondrite-normalized Ce/Yb ratios (Ce/Yb_{CN}) ranging from 2.96 to 3.55. REE profiles for olivine gabbro and gabbroic rocks have moderately positive slopes with Ce/Yb_{CN} ranging from 3.59-3.25 and 3.22-5.35 respectively. The sample with the most fractionated content of REE is a pegmatoidal gabbro with positive slope and Ce/Yb_{CN} of 6.36.

Table 2.1. Chemical composition of representative samples from Touro Complex. Major elements and S (wt. %), trace elements and REE (ppm).

Sample	A17	A18	A19	A20	A21	A22a	A22b	A23	TSD01-424	TSD01-272	TSD01-211	TSD01-069
Rock	Ol-clinopyroxenite	Ol-gabbro	Ol-clinopyroxenite	Gabbro	Gabbro	Peg Gabbro	Gabbro	Ol-melagabbro	Ol-clinopyroxenite	Ol-clinopyroxenite	Ol-clinopyroxenite	Ol-clinopyroxenite
SiO2	49.0	50.6	49.9	50.2	50.6	51.5	50.6	48.7	48.0	44.5	44.6	48.9
TiO2	0.32	0.30	0.30	0.32	0.44	0.46	0.38	0.46	0.25	0.21	0.22	0.31
Al2O3	4.21	10.40	3.14	10.00	13.40	14.80	13.20	8.38	2.86	2.68	2.86	3.89
Cr2O3	0.31	0.17	0.39	0.15	0.08	0.04	0.08	0.24	0.39	0.37	0.30	0.33
Fe2O3	11.0	7.9	9.8	8.0	8.6	7.6	8.6	12.7	11.1	12.9	14.1	11.5
MnO	0.19	0.15	0.19	0.16	0.13	0.12	0.13	0.21	0.14	0.17	0.14	0.19
MgO	19.1	13.1	19.6	12.6	10.0	8.4	10.4	16.1	22.0	24.2	24.4	20.0
CaO	15.0	15.4	16.4	15.1	13.3	11.3	13.3	11.2	12.6	10.9	8.1	14.2
Na2O	0.70	1.70	0.62	1.91	2.66	3.99	2.63	1.44	0.46	0.33	0.44	0.75
K2O	0.14	0.22	0.11	0.18	0.47	0.69	0.47	0.39	0.18	0.26	0.11	0.17
P2O5	0.02	0.02	0.01	0.02	0.04	0.02	0.03	0.02	0.01	0.01	0.02	0.02
BaO	0.020	0.017	0.017	0.014	0.019	0.023	0.024	0.022	0.006	0.005	0.003	0.012
SrO	0.007	0.012	0.006	0.011	0.018	0.025	0.019	0.010	0.001	0.001	<0.001	0.004
LOI	1.16	0.77	0.42	1.15	1.14	1.72	1.39	1.40	2.42	3.40	4.89	1.11
Total	101.1	100.7	100.9	99.8	100.9	100.7	101.2	101.2	100.4	99.9	100.1	101.3
Mg#	60	59	63	58	50	49	51	52	63	62	60	60
S	<0.01	<0.01	<0.01	0.01	0.01	<0.01	0.01	<0.01	0.01	0.01	<0.01	0.01
C	0.1	0.05	0.11	0.05	0.06	0.17	0.11	0.06	0.05	0.17	0.09	0.1
Ag	<1	<1	<1	<1	<1	<1	<1	<1	<1	<1	<1	<1
As	0.7	0.2	0.4	0.1	0.1	0.2	0.5	0.9	0.5	0.2	0.2	0.1
Ba	60.9	68.4	44.6	62.8	90.1	126	131	146	13.2	32.7	11.8	28.2
Co	78.2	51.6	74.5	53.3	50.5	42	51.3	75.7	85.3	108.5	115.5	84
Cr	2190	1300	2680	1150	610	340	640	1710	2770	2590	2120	2290
Cs	0.15	0.26	0.14	0.14	0.27	0.47	0.22	0.21	0.16	0.21	0.16	0.06
Cu	17	31	22	35	46	32	56	22	19	18	8	22
Ga	5.7	8.6	4.4	9	11.8	12.5	11.5	8.9	3.7	3.4	4.1	5.4
Hf	0.3	0.3	0.3	0.4	0.9	1	0.6	0.8	0.3	0.2	0.2	0.4

Table 2.1 (cont.). Chemical composition of representative samples from Touro Complex. Major elements and S (wt. %), trace elements and REE (ppm).

Sample	A17	A18	A19	A20	A21	A22a	A22b	A23	TSD01-424	TSD01-272	TSD01-211	TSD01-069
Rock	Ol-clinopyroxenite	Ol-gabbro	Ol-clinopyroxenite	Gabbro	Gabbro	Peg Gabbro	Gabbro	Ol-melagabbro	Ol-clinopyroxenite	Ol-clinopyroxenite	Ol-clinopyroxenite	Ol-clinopyroxenite
Mo	2	2	2	2	2	2	2	2	2	2	2	2
Nb	0.3	0.2	<0.2	0.3	1.1	0.9	0.8	1	<0.2	<0.2	0.3	0.3
Ni	514	317	535	308	236	186	234	457	665	826	874	546
Pb	<5	<5	<5	<5	<5	5	<5	<5	<5	<5	<5	<5
Rb	4.5	11.6	3	8.9	23	70.3	16.5	12.1	6.1	13.7	3.2	3.2
Sn	1	1	1	1	1	1	1	1	2	1	1	1
Sr	31.2	96.3	28.1	89.7	141.5	209	147	70.6	7.5	13.2	8.2	21.5
Ta	0.1	<0.1	<0.1	<0.1	0.1	0.1	0.1	0.1	<0.1	<0.1	0.2	<0.1
Tl	<0.5	<0.5	<0.5	<0.5	<0.5	<0.5	<0.5	<0.5	<0.5	<0.5	<0.5	<0.5
V	206	184	184	197	186	166	179	165	170	136	160	217
W	3	2	2	5	2	4	6	4	3	2	2	6
Zn	76	94	62	61	62	63	64	83	57	87	56	99
Zr	15	14	12	17	32	44	25	29	15	11	13	15
La	2	2.2	1.6	2.5	4.7	5.5	4.4	4.2	2	1.5	1.8	2
Ce	4.8	5	3.9	5.6	9.7	9.6	9	9.5	4.2	3.8	4.1	4.9
Pr	0.67	0.67	0.58	0.79	1.21	1.07	1.14	1.25	0.59	0.5	0.6	0.64
Nd	3.1	3.3	2.8	3.5	5.5	4.5	4.8	5.2	2.7	2.2	2.6	3.3
Sm	0.86	1.07	1	1.18	1.53	1.14	1.22	1.46	0.9	0.77	0.91	0.95
Eu	0.38	0.39	0.35	0.39	0.52	0.44	0.47	0.5	0.24	0.21	0.31	0.35
Gd	1.41	1.43	1.33	1.47	1.86	1.28	1.54	1.87	1.18	1.06	1.13	1.49
Tb	0.22	0.23	0.24	0.27	0.32	0.23	0.29	0.35	0.21	0.17	0.19	0.27
Dy	1.67	1.59	1.59	1.78	1.91	1.38	1.71	2	1.38	1.23	1.24	1.76
Ho	0.32	0.3	0.35	0.37	0.44	0.3	0.37	0.41	0.26	0.27	0.26	0.31
Er	0.95	0.96	0.93	1.06	1.06	0.77	0.95	1.25	0.78	0.72	0.76	0.92
Tm	0.14	0.13	0.14	0.16	0.18	0.1	0.2	0.18	0.12	0.1	0.11	0.14
Yb	0.82	0.73	0.69	0.91	0.95	0.79	1	1.17	0.62	0.62	0.61	0.79
Lu	0.13	0.12	0.13	0.16	0.17	0.13	0.15	0.18	0.11	0.1	0.11	0.14
Y	8.8	8.1	8.6	9.6	11.3	8.3	10	11.4	7.4	6.2	6.6	8.6
Th	0.31	0.34	0.18	0.42	0.95	0.62	0.64	0.8	0.26	0.19	0.28	0.34
U	0.26	0.26	0.24	0.26	0.43	0.4	0.37	0.32	0.21	0.19	0.23	0.22
(Ce/Yb)N	3.07	3.59	2.96	3.22	5.35	6.36	4.71	4.25	3.55	3.21	3.52	3.25
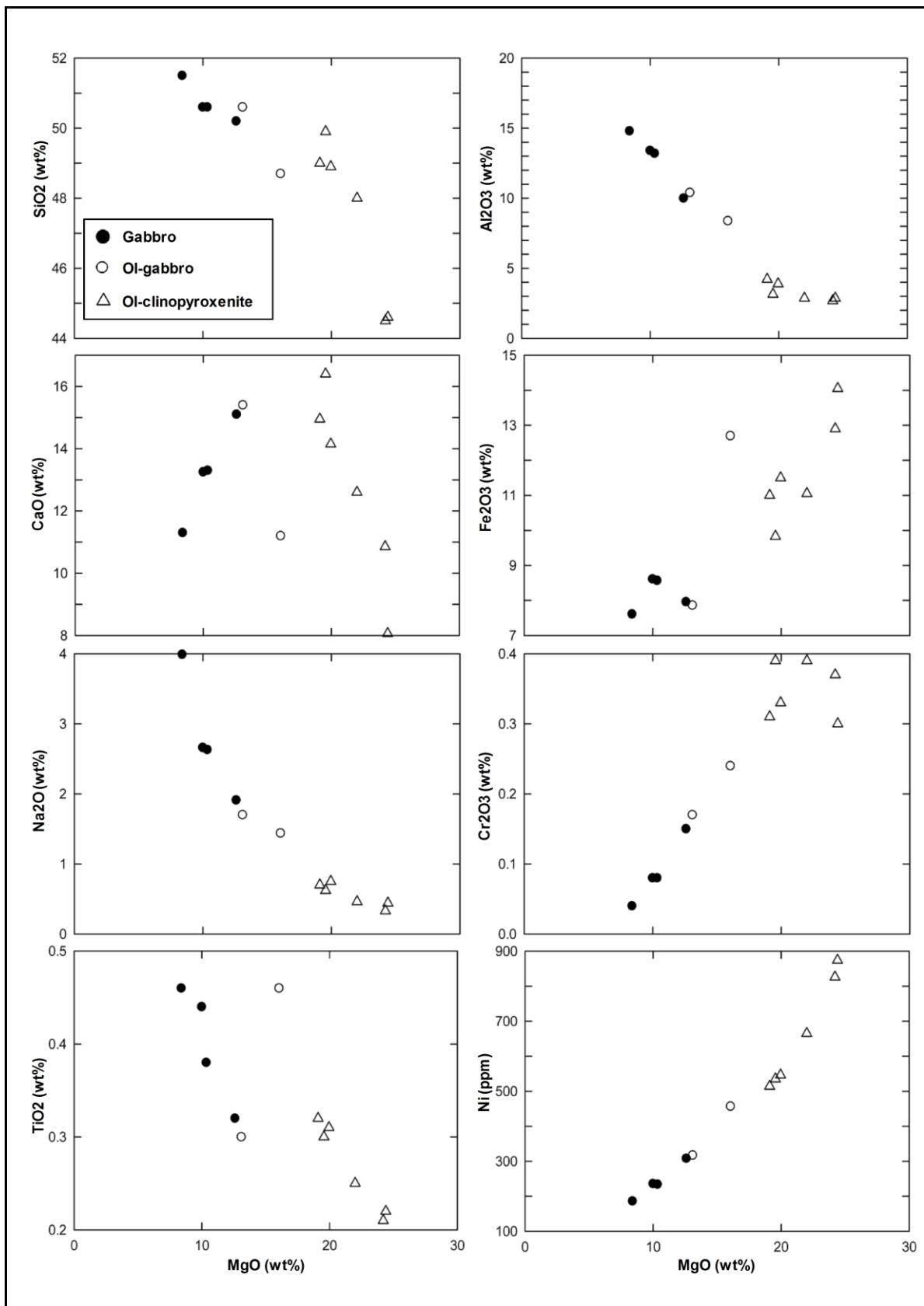
Figure 2.6. Plot of MgO content versus major oxides and selected trace elements for different group of rocks of the Touro Complex. See Table 2.1 for chemical analyses.
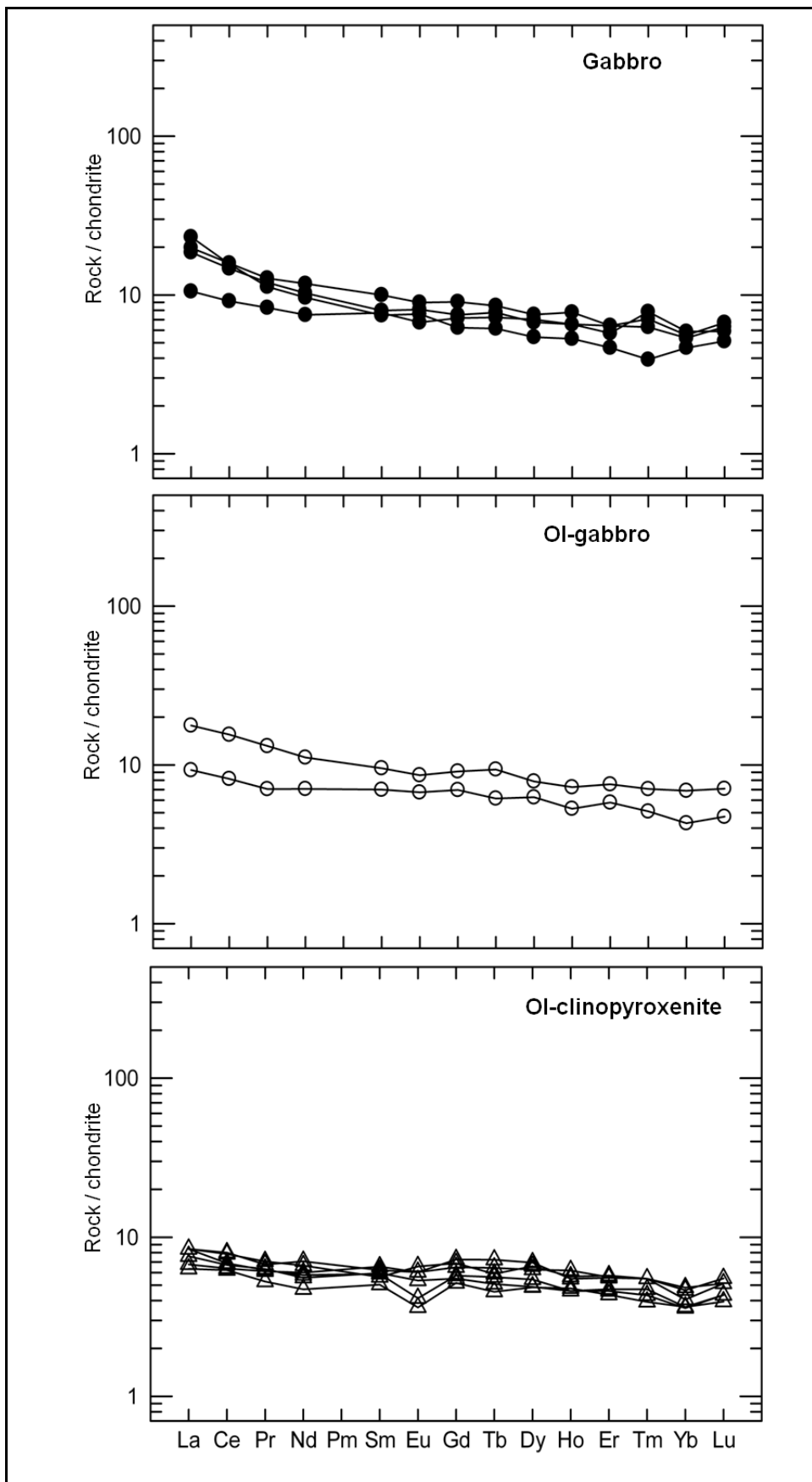
Figure 2.7. Chondrite-normalized REE patterns for different group of rocks of Touro Complex. See Table 2.1 for chemical analyses. Normalization data from Sun and MacDonough (1989).

High-field strength elements (HFSE) and rare-earth elements (REE) are relatively immobile in many altered mafic-ultramafic rocks (e.g., Arndt and Lesher, 1992; Lesher and Arndt, 1995; Lahaye et al., 1995) and were successfully applied in studies of variably altered rocks in the Carajás Province (e.g., Teixeira et al., 2015; Siepierski and Ferreira Filho, 2016). Unfortunately, several HFSE have very low contents that are close to or below their lower limits of quantification in the analyses of obtained for this study (e.g., Th, Nb, Ta, U: Table 2.1), and should be considered with discretion. Mantle-normalized spidergram of selected incompatible trace elements were plot for samples with higher contents of these elements (Fig. 2.8). Profiles for olivine clinopyroxenite and gabbroic rocks are fractionated, as indicated by relative enrichment in LREE and Th, with pronounced negative Nb anomalies.
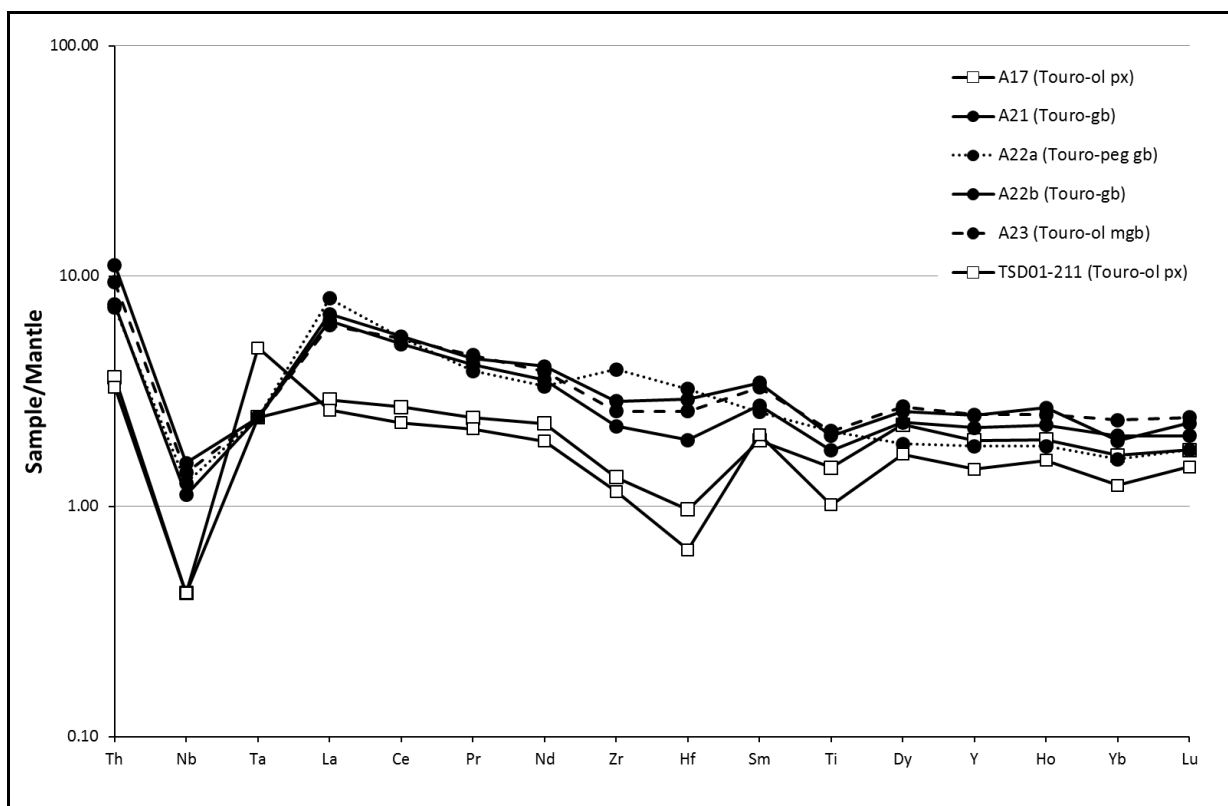
Figure 2.8. Primitive mantle-normalized alteration-resistant profiles for samples of pyroxenites (squares) and representative gabbroic rocks (black circles) of the Touro Complex. Data from Table 2.1. Primitive mantle normalization values are from Sun and McDonough (1989).

Mineral Chemistry

Systematic analyses of olivine and clinopyroxene crystals (Tables 2.2 and 2.3) were performed in unweathered drill core samples from bore hole TSD-01 (5 samples of the

UZ) and outcrops of the UZ and the MZ (6 samples). Additional analyses of plagioclase crystals (Table 2.4) were acquired in 5 samples from outcrops of gabbroic rocks from the MZ.

Systematic compositional variation of Ol and Cpx throughout the drill hole TSD-01 and outcrops provide cryptic variation data for olivine-clinopyroxenite and clinopyroxenite in a composed section of the Touro Complex (Fig. 2.9). In these samples Ol compositions range from $Fo_{67.9}$ to $Fo_{76.3}$, with Ni contents ranging from 990 to 2488 ppm, and is also compared with the compositional trend for olivine from layered complexes (Fig. 2.10). Clinopyroxene compositions range from $En_{42.5}$ in a gabbroic rock of the MZ to $En_{49.5}$ in an olivine-clinopyroxenite of the UZ. Compositional variations of Ol and Cpx do not follow a continuous fractionation trend, a subject to be addressed in the following discussions. Plagioclase composition in gabbroic rocks of the MZ ranges from $An_{61.4}$ to $An_{41.4}$ and becomes more fractionated toward the upper portion of the Touro Complex.
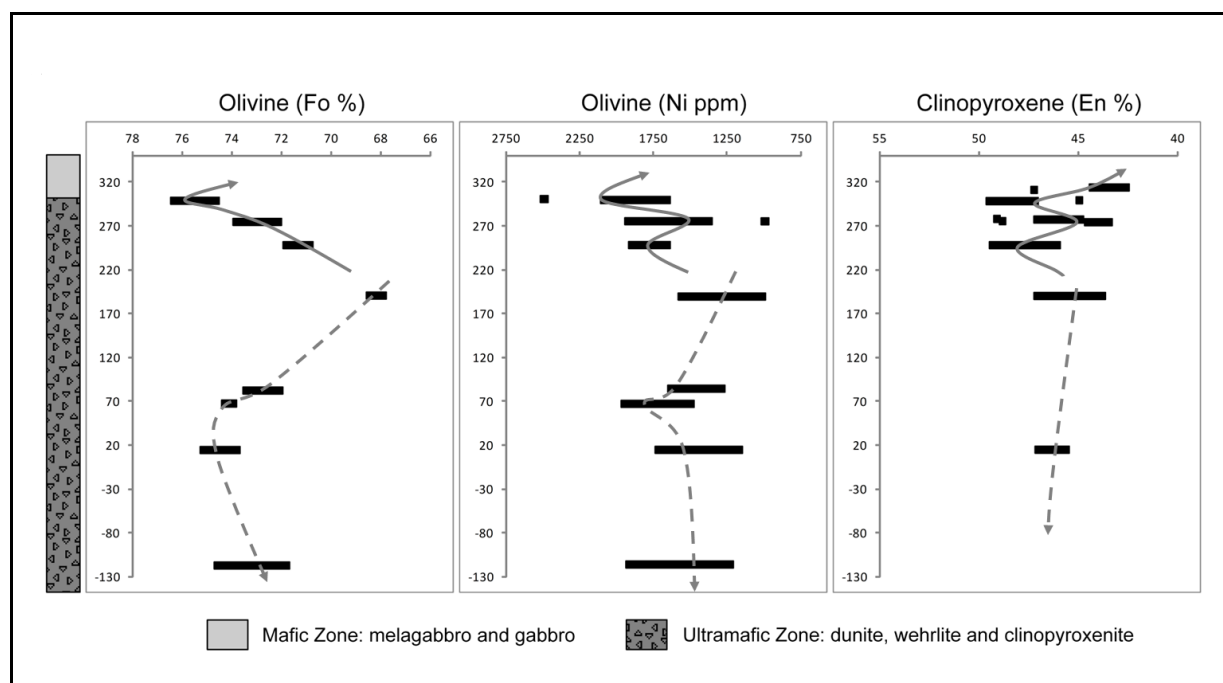
Figure 2.9. Stratigraphy and compositional variation trends of olivine and clinopyroxene throughout drill core TSD-01 (highlighted by dashed grey line) and surface outcrops (grey line).

Table 2.2. Representative analyses of olivine.

Sample	A17	A17	A18	A18	A18	A18	A19	A19	A19	A19	TSD69	TSD69	TSD69	TSD69	TSD69	TSD69	TSD194	TSD194	TSD211	TSD211	TSD211	TSD211	TSD272	TSD272	TSD272	TSD272	TSD424	TSD424	TSD424	TSD424
Rock type	Ol-Cpxt	Ol-Cpxt	Ol-Gab	Ol-Gab	Ol-Gab	Ol-Gab	Ol-Cpxt	Ol-Cpxt	Ol-Cpxt	Ol-Cpxt	Ol-Cpxt	Ol-Cpxt	Ol-Cpxt	Ol-Cpxt	Ol-Cpxt	Ol-Cpxt	Ol-Cpxt	Ol-Cpxt	Ol-Cpxt	Ol-Cpxt	Ol-Cpxt	Ol-Cpxt	Ol-Cpxt	Ol-Cpxt	Ol-Cpxt	Ol-Cpxt	Ol-Cpxt	Ol-Cpxt	Ol-Cpxt	Ol-Cpxt
SiO2	38.21	38.25	38.43	38.70	38.19	38.58	37.19	38.09	37.61	37.94	37.02	37.40	37.60	38.15	37.84	37.60	38.44	38.78	38.49	38.53	38.47	38.66	39.21	38.61	38.65	39.23	38.45	38.12	38.56	38.31
FeO	25.49	25.53	24.55	24.22	24.62	23.87	22.30	22.43	22.28	22.76	28.11	28.21	28.41	27.67	28.24	28.27	23.87	25.27	23.35	23.49	23.42	23.43	22.98	22.96	22.46	22.77	25.27	24.86	24.37	24.35
MnO	0.43	0.39	0.30	0.26	0.35	0.35	0.29	0.27	0.36	0.28	0.52	0.54	0.53	0.56	0.52	0.52	0.38	0.45	0.42	0.39	0.45	0.41	0.33	0.33	0.35	0.43	0.40	0.42	0.42	0.42
MgO	35.98	36.61	36.33	36.54	36.45	37.04	38.13	37.46	37.80	37.54	33.80	33.64	33.64	33.79	33.48	33.66	37.05	36.52	37.57	37.92	37.65	37.89	38.27	38.22	38.07	38.06	36.05	36.59	36.32	36.67
NiO	0.22	0.22	0.13	0.18	0.24	0.22	0.22	0.21	0.27	0.32	0.19	0.19	0.13	0.16	0.13	0.20	0.18	0.21	0.20	0.25	0.19	0.21	0.15	0.21	0.22	0.17	0.18	0.17	0.23	0.22
Total	100.36	101.08	99.87	100.14	99.88	100.16	98.16	98.55	98.43	98.92	99.74	100.15	100.42	100.45	100.34	100.54	100.16	101.32	100.14	100.69	100.32	100.73	101.00	100.42	99.82	100.73	100.49	100.30	99.97	100.10
Si	1.008	1.001	1.016	1.020	1.009	1.013	0.986	1.011	0.997	1.003	0.996	1.004	1.007	1.019	1.014	1.007	1.011	1.012	1.008	1.003	1.006	1.006	1.015	1.005	1.011	1.019	1.014	1.004	1.018	1.009
Fe2	0.562	0.558	0.543	0.534	0.544	0.524	0.467	0.498	0.489	0.503	0.624	0.633	0.636	0.618	0.633	0.633	0.525	0.552	0.511	0.511	0.512	0.510	0.498	0.500	0.492	0.494	0.557	0.547	0.538	0.536
Mn	0.010	0.009	0.007	0.006	0.008	0.008	0.007	0.006	0.008	0.006	0.012	0.012	0.012	0.013	0.012	0.012	0.008	0.010	0.009	0.009	0.010	0.009	0.007	0.007	0.008	0.009	0.009	0.009	0.009	0.009
Mg	1.415	1.428	1.432	1.436	1.435	1.450	1.508	1.481	1.495	1.480	1.356	1.346	1.343	1.346	1.338	1.344	1.452	1.421	1.467	1.472	1.468	1.470	1.477	1.483	1.485	1.474	1.417	1.436	1.429	1.440
Ni	0.005	0.005	0.003	0.004	0.005	0.005	0.005	0.004	0.006	0.007	0.004	0.004	0.003	0.003	0.003	0.004	0.004	0.004	0.004	0.005	0.004	0.004	0.003	0.004	0.005	0.004	0.004	0.004	0.005	0.005
Total	3.000	3.000	3.000	3.000	3.000	3.000	2.973	3.000	2.995	3.000	2.992	3.000	3.000	3.000	3.000	3.000	3.000	3.000	3.000	3.000	3.000	3.000	3.000	3.000	3.000	3.000	3.000	3.000	3.000	3.000
Fo	71.56	71.88	72.52	72.90	72.52	73.45	76.33	74.86	75.35	74.62	68.46	68.01	67.86	68.52	67.88	67.97	73.45	72.03	74.15	74.21	74.13	74.25	74.81	74.79	75.13	74.88	71.77	72.41	72.65	72.86
Ni ppm	1758	1697	990	1443	1873	1735	1720	1651	2088	2488	1528	1482	1052	1244	1021	1559	1436	1643	1597	1950	1489	1666	1159	1681	1720	1374	1443	1351	1835	1750

Table 2.3. Representative analyses of clinopyroxene.

Sample	A17	A17	A18	A18	A18	A19	A19	A19	A19	A20	A22b	A22b	A22b	A23	A23	A23	TSD69	TSD69	TSD69	TSD69	TSD272	TSD272	TSD272
Rock type	Ol-Cpxt	Ol-Cpxt	Ol-gab	Ol-gab	Ol-gab	Ol-Cpxt	Ol-Cpxt	Ol-Cpxt	Ol-Cpxt	Gab	Gab	Gab	Gab	Ol-Mgab	Ol-Mgab	Ol-Mgab	Ol-Cpxt	Ol-Cpxt	Ol-Cpxt	Ol-Cpxt	Ol-Cpxt	Ol-Cpxt	Ol-Cpxt
SiO_2	53.75	52.90	53.47	54.07	54.19	53.29	53.00	53.00	54.56	54.55	53.76	53.25	54.07	56.07	54.24	55.59	54.14	54.90	54.56	54.98	54.21	55.14	54.83
TiO_2	0.29	0.34	0.29	0.17	0.04	0.23	0.25	0.27	0.14	0.02	0.10	0.13	0.37	0.05	0.26	0.04	0.00	0.00	0.00	0.00	0.19	0.09	0.16
Al_2O_3	2.29	2.94	2.14	1.03	0.80	2.11	1.59	1.66	0.77	0.49	0.77	0.68	2.89	0.44	0.98	0.37	0.20	0.18	0.19	0.19	0.65	0.64	0.86
Cr_2O_3	0.28	0.51	0.39	0.17	0.20	0.63	0.10	0.18	0.23	0.05	0.17	0.15	0.16	0.12	0.15	0.19	0.10	0.05	0.03		0.52	0.25	0.07
FeO	5.71	5.18	5.18	5.20	4.81	5.61	5.19	5.56	4.22	5.96	5.09	5.09	5.72	6.87	6.23	5.40	3.55	3.66	3.85	3.71	4.04	2.89	3.10
MnO	0.11	0.23	0.10	0.12	0.15	0.14	0.15	0.14	0.10	0.24	0.20	0.21	0.26	0.17	0.17	0.18	0.04	0.12	0.14	0.21	0.06	0.11	0.16
MgO	16.56	16.23	15.32	15.32	15.65	16.65	16.43	16.91	16.00	15.08	15.25	15.49	15.12	16.68	15.86	15.32	16.58	16.45	16.53	16.37	16.39	16.90	16.80
NiO	0.04	0.06	0.00	0.04	0.04	0.02	0.00	0.07	0.04	0.00	0.04	0.03	0.00	0.04	0.01	0.02	0.00	0.03	0.01	0.00	0.04	0.00	0.02
CaO	21.45	21.91	22.72	23.77	24.19	21.20	22.86	21.88	23.97	23.70	24.38	24.54	20.51	18.72	22.67	23.23	25.24	24.90	24.68	24.81	24.56	24.16	24.79
Na_2O	0.26	0.59	0.46	0.28	0.29	0.42	0.32	0.34	0.35	0.28	0.36	0.27	0.91	0.16	0.39	0.35	0.08	0.07	0.03	0.07	0.17	0.17	0.17
Total	100.74	100.88	100.07	100.17	100.37	100.30	99.89	100.00	100.39	100.36	100.11	99.84	100.01	99.31	100.96	100.70	99.85	100.42	100.05	100.37	100.85	100.35	100.94
Fe_2O_3		0.00	0.72	0.00	0.00	0.99	1.18	1.99	2.08	0.83	0.00	1.17	0.00	0.00	0.00	0.50	0.00	1.34	0.00	0.00	0.70	0.00	0.08
FeO		5.71	5.45	5.18	6.62	4.95	4.32	3.40	3.69	4.83	5.96	4.03	4.90	5.72	6.87	5.78	5.40	2.42	3.66	3.71	3.41	2.89	3.03
AFU																							
Tetraedro																							
Si	1.96	1.92	1.96	1.99	1.98	1.94	1.94	1.94	1.99	2.01	1.97	1.96	1.98	2.08	1.98	2.03	1.98	2.00	2.00	2.01	1.97	2.00	1.98
Al	0.04	0.08	0.04	0.01	0.02	0.06	0.06	0.06	0.01	0.00	0.03	0.03	0.02	0.00	0.02	0.00	0.01	0.00	0.00	0.00	0.03	0.00	0.02
Σ	2.00	2.00	2.00	2.00	2.00	2.00	2.00	2.00	2.00	2.01	2.00	1.99	2.00	2.08	2.00	2.03	1.99	2.00	2.00	2.01	2.00	2.00	2.00
M1																							
Al		0.05	0.03	0.05	0.07	0.04	0.02	0.01	0.01	0.04	0.02	0.01	0.02	0.11	0.02	0.02	0.02	0.00	0.01	0.01	0.00	0.03	0.02
Fe^{3+}		0.00	0.02	0.00	0.00	0.03	0.03	0.05	0.06	0.02	0.00	0.03	0.00	0.00	0.00	0.01	0.00	0.03	0.00	0.00	0.02	0.00	0.00
Mg		0.90	0.89	0.84	0.84	0.90	0.93	0.90	0.92	0.89	0.83	0.84	0.83	0.83	0.92	0.86	0.84	0.93	0.89	0.89	0.89	0.92	0.91
Fe^{2+}		0.03	0.04	0.09	0.08	0.02	0.01	0.03	0.00	0.03	0.15	0.12	0.14	0.05	0.05	0.09	0.14	0.05	0.09	0.10	0.07	0.05	0.07
ΣM1		1.00	1.00	1.00	1.00	1.00	1.00	1.00	1.00	1.00	1.00	1.00	1.00	1.00	1.00	1.00	1.00	1.00	1.00	1.00	1.00	1.00	1.00
M2																							
Fe^{2+}		0.14	0.13	0.07	0.13	0.13	0.13	0.08	0.11	0.12	0.03	0.01	0.01	0.12	0.16	0.08	0.02	0.03	0.02	0.01	0.03	0.04	0.02
Ca		0.84	0.84	0.89	0.84	0.84	0.85	0.90	0.86	0.85	0.93	0.96	0.96	0.81	0.74	0.89	0.91	0.96	0.97	0.97	0.96	0.94	0.96
Na		0.02	0.03	0.03	0.03	0.03	0.02	0.02	0.02	0.02	0.02	0.03	0.02	0.06	0.01	0.03	0.02	0.01	0.00	0.00	0.01	0.01	0.01
ΣM2		1.00	1.00	1.00	1.00	1.00	1.00	1.00	1.00	1.00	0.99	1.00	1.00	1.00	0.92	1.00	0.97	1.00	1.00	0.99	1.00	1.00	1.00
En		47.08	47.10	44.34	44.60	47.84	48.59	47.26	48.66	47.22	42.54	43.53	42.91	45.73	49.08	44.81	43.72	47.15	45.20	45.11	45.58	47.10	46.27

Table 2.4. Representative analyses of plagioclase.

Sample	A18	A18	A18	A20	A20	A20	A21	A21	A22b	A22b	A22b	A22b	A23	A23	A23	A23
Rock type	Ol-gab	Ol-gab	Ol-gab	Gab	Gab	Gab	Gab	Gab	Gab	Gab	Gab	Gab	Ol-Mgab	Ol-Mgab	Ol-Mgab	Ol-Mgab
SiO2	56.08	54.90	54.72	53.53	54.50	54.24	54.61	54.32	54.93	54.15	54.55	55.27	55.88	58.83	56.30	57.18
Al2O3	27.13	27.74	27.65	27.28	27.28	26.93	26.98	27.81	26.64	27.14	26.77	26.18	27.18	25.65	26.25	26.15
CaO	11.79	12.66	12.31	13.43	12.73	12.40	12.15	12.89	12.02	12.62	12.72	12.32	12.07	9.72	10.99	10.52
Na2O	5.29	4.86	4.77	4.64	5.14	5.10	5.09	4.74	5.44	4.96	5.12	5.31	5.08	6.39	5.76	6.07
K2O	0.08	0.08	0.22	0.04	0.08	0.05	0.10	0.04	0.03	0.05	0.03	0.05	0.07	0.08	0.12	0.08
SrO	0.19	0.11	0.00	0.02	0.00	0.15	0.23	0.04	0.14	0.07	0.02	0.02	0.00	0.03	0.19	0.17
Total	100.58	100.51	100.48	99.02	99.79	99.02	99.24	99.90	99.40	99.05	99.42	99.37	100.34	100.79	99.82	100.38
% An	54.94	58.75	58.04	61.37	57.54	57.14	56.57	59.93	54.88	58.29	57.79	56.02	56.52	45.45	50.99	48.72
% Ab	44.62	40.80	40.70	38.39	42.03	42.57	42.89	39.84	44.98	41.45	42.05	43.71	43.06	54.08	48.32	50.85
% Or	0.44	0.45	1.25	0.24	0.43	0.29	0.54	0.23	0.14	0.26	0.16	0.26	0.41	0.47	0.69	0.43
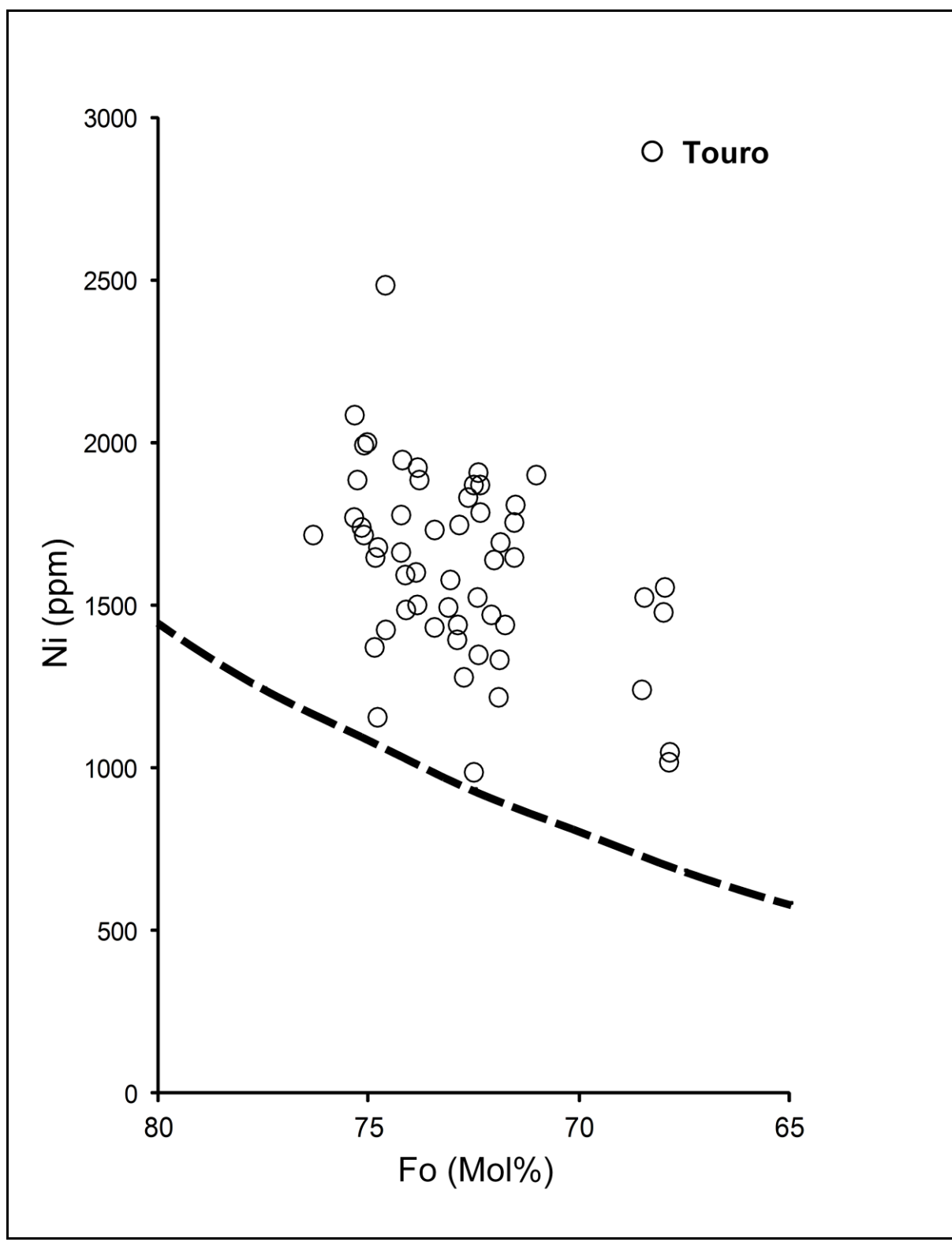
Figure 2.10. Plot of Fo versus Ni content of olivine from samples of the Touro Complex. The dashed line is the compositional trend for olivine from layered complexes (Simkin and Smith, 1970).

Discussion

Magmatic Structure

Layered intrusions in the CMP have distinct architecture resulting from different primary structure as well as distinct tectonic features. The latter is illustrated by tectonically undisturbed horizontal layering of the Vermelho Complex (Siepierski and Ferreira Filho, in prep.) and tectonically overturned layering of the Luanga (Ferreira Filho et al., 2007) and Lago Grande complexes (Teixeira et al., 2015). An interpreted magmatic structure of the Touro Complex is indicated in geological sections (e.g., Fig. 2.4). This interpretation is supported by MAG anomalies associated with the UZ that extend below the basement rocks close to bore hole TSD-01. The thick sequence of ultramafic rocks indicates steep contact with the country rocks and the BGR to the east, suggesting a sub-vertical ultramafic feeder supported by not continuous fractionation trend, capped by a subhorizontal zone of gabbroic rocks (Fig. 2.4). MAG anomalies do not extend below the MZ suggesting that ultramafic cumulates outcropping to the northwest of the UZ represent a thin extension of the UZ. The BGR consists of a narrow and discontinuous zone of fine- to medium-grained gabbroic mapped along the southeastern contact of the UZ and host rocks, as well as in few outcrops in the northwestern contact of MZ. This gabbroic zone located at the lower contact of the Touro Complex similar to what is described at the base of several layered intrusions (Eales et al., 1996; McBirney, 1996; McCallum, 1996; Latypov, 2003), including recent descriptions of layered intrusions in the CMP (e.g., Serra da Onça Complex: Rosa, 2014).

The suggested architecture of the Touro Complex has significant implications for the interpretation of available exploration data and for planning further activities. Despite the depletion of Ni in olivine not be evident in the investigated interval (Fig. 2.10), it is particularly relevant the suggestion that the extension of the feeder zone remains unexplored, a feature that enhances the potential for hosting deep-seated Ni-Cu-PGE sulfides.

Fractionation and constraints for the composition of the parental magma

The characterization of the parental magma of a layered intrusion provides clues on the nature of the mantle source and the prospectivity of an igneous suite to host magmatic mineral deposits. However, defining the composition of parental magmas in layered

intrusions is not always straightforward, and their compositions are frequently inferred from the crystallization sequences of the intrusions and the geochemistry of cumulate minerals and rocks (e.g., Chai and Naldrett, 1992; Ferreira Filho et al. 1998; Godel et al. 2011; Teixeira et al., 2015). Results obtained in this study indicate that the layered rocks originated mainly from crystallization of cumulus olivine, clinopyroxene and plagioclase, suggesting a crystallization sequence consisting of Ol+Chr $\rightarrow$ Ol+Cpx+Chr $\rightarrow$ Ol+Cpx+Pl $\rightarrow$ Cpx+Pl. The absence of Opx as a cumulus mineral in the Touro Complex suggests that the primary magma was silica undersaturated (Campbell, 1985). Layered intrusions with abundant and early crystallization of cumulus Opx (e.g., Serra da Onça and Luanga complexes: Ferreira Filho et al., 2007; Vermelho Complex: Siepierski and Ferreira Filho, in prep.) and those that do not contain cumulus Opx (e.g., Serra do Puma Complex: Rosa, 2014; Ézio Complex: Silva, 2015) occur in the CMP, indicating the presence of both silica-saturated and silica-unsaturated magmas. The compositional range of cumulus Ol ($Fo_{76.3-67.9}$) supports a moderately fractionated parental magma for the Touro Complex.

Mantle-normalized alteration-resistant trace element profiles of ultramafic and gabbroic rocks in the Touro Complex are fractionated, as indicated by relative enrichment in LREE and Th, with pronounced negative Nb anomalies (Fig. 2.8). Trace element profiles are very close to results obtained in several layered intrusions in the CMP (Fig. 2.11), including the Lago Grande Complex (Teixeira et al., 2015), Serra da Onça and Serra do Puma complexes (Rosa, 2014) and Vermelho Complex (Siepierski and Ferreira Filho, in prep.), and were interpreted as the result of an original mantle melt contaminated with older continental crust (see Teixeira et al., 2015 for further discussion).
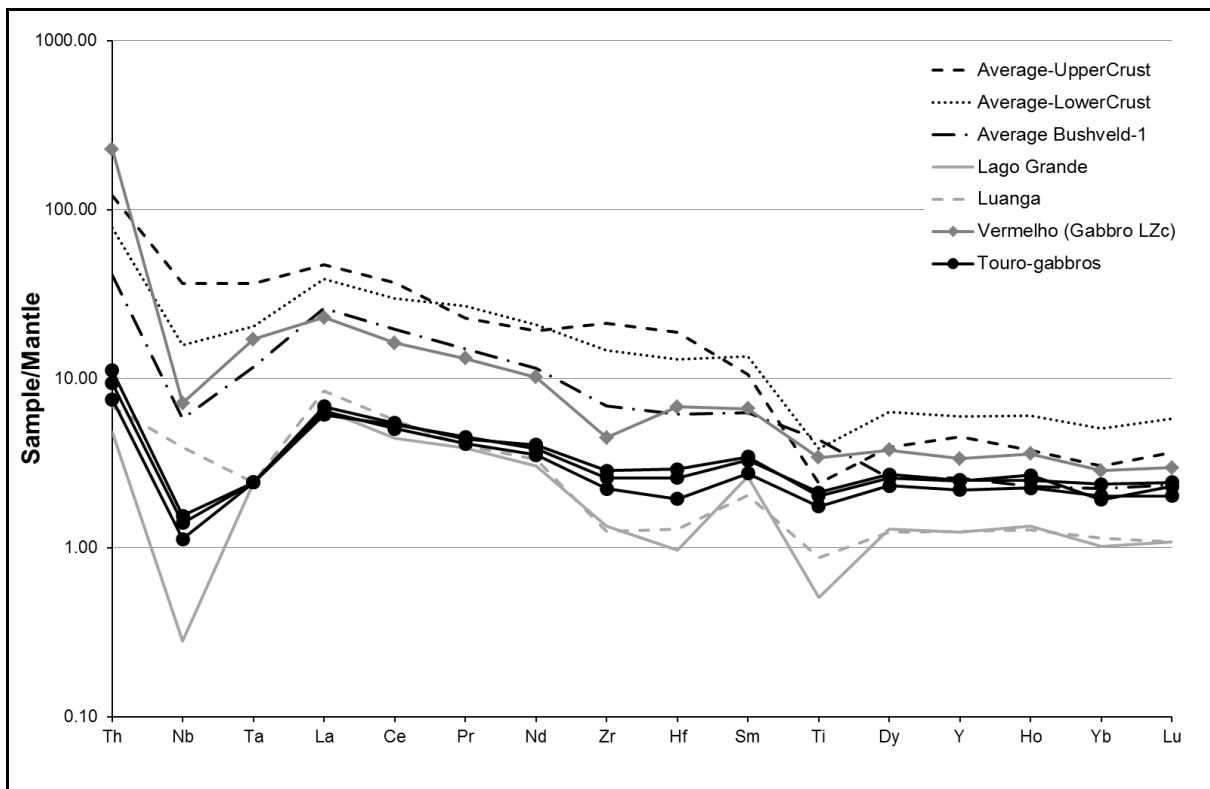
Figure 2.11. Primitive mantle-normalized alteration-resistant profiles for gabbroic of the Touro Complex (this study) and other layered intrusions of the CMP. Primitive mantle normalization values are from Sun and McDonough (1989).

Conclusions

Distinct crystallization sequences described for the Touro (this study) and Vermelho (Siepierski and Ferreira Filho, in prep.) complexes (see Fig. 2.1 for location) suggests that each complex evolved from a different parental magma. The crystallization sequence of the Vermelho Complex (Ol+Chr → Opx+Chr → Opx → Opx+Pl → Opx+Pl+Cpx) in which Opx precedes Cpx indicates that the magma is silica-saturated, while the crystallization sequence of the Touro Complex (Ol+Chr → Ol+Cpx+Chr → Ol+Cpx+Pl → Cpx+Pl) is characterized by the absence of Opx as a cumulus mineral suggesting that the primary magma was silica-unsaturated. Contrasting crystallization sequences were also described for the Serra da Onça (silica-saturated) and Serra do Puma (silica-unsaturated) complexes located in the western portion of the CMP (Rosa, 2014). Both silica-saturated and silica-unsaturated layered complexes in the CMP have broad similarity in the trace element data, suggesting that they were derived from a similar mantle source. Mantle-normalized alteration-resistant trace element profiles of gabbroic rocks in silica-saturated and silica-unsaturated complexes in the CMP are fractionated, as indicated by relative enrichment in

LREE and Th, with pronounced negative Nb and Ta anomalies. Trace elements and Sm-Nd isotopic results obtained for the Serra da Onça (silica-saturated) and Serra do Puma (silica-unsaturated) suggest that they derived from similar primitive magmas that followed different fractionation path during ascent and/or emplacement in the crust (Rosa, 2014). The tectonic model of intra-plate rifting of older continental crust for the CMP (Gibbs et al., 1986; Olszewski et al., 1989; Villas and Santos, 2001) provides an appropriate setting for crustal assimilation of primitive mantle derived primitive magmas.

Acknowledgments

References

Araújo, O.J.B., Maia, R.G.N., João, X.S.J., Costa, J.B.S., 1988. A megaestruturação arqueana da Folha Serra dos Carajás. In: Congresso Latino Americano de Geologia, Anais, Belém-Brasil, 1, 324-338.

Araújo O.J.B., Maia R.G.N., 1991. Programa Levantamentos Geológicos Básicos do Brasil. Serra de Carajás. Folha SB.22- Z-A. Estado do Pará. Brasília, DNPM-CPRM, 136 pp.

Arndt, N.T., Lesher, C.M., 1992. Fractionation of REE by olivine and the origin of Kambalda komatiites, Western Australia. Geochimica et Cosmochimica Acta 56, 4191-4204.

Avanco Resources, 2009. Carajás Project – Touro Target. Internal Report, 3 pp.

Avelar, V.G., Lafon, J.M., Correia JR., F.C., Macambira, E.M.B., 1999. O magmatismo arqueano da região de Tucumã-Provínica Mineral de Carajás: Novos dados geocronológicos. Revista Brasileira de Geociências 29, 453-460.

Barnes, S.J., 1986. The effect of trapped liquid crystallization on cumulus mineral compositions in layered intrusions. Contributions to Mineralogy and Petrology 93, 524-531.

Barros, C.E.M., Sardinha, A.S., Barbosa, J.P.O., Krimski, R., Macambira, M.J.B., 2001. Pb-Pb and U-Pb zircon ages of Archean syntectonic granites of the Carajás metallogenic province, northern Brazil. In: Proceedings of the South American Symposium on Isotopic Geology, 3, 94-97.

Barros, C.E.M., Sardinha, A.S., Barbosa, J.P.O., Macambira, M.J.B., 2009. Structure, petrology, geochemistry and zircon U/Pb and Pb/Pb geochronology of the synkinematic Archean (2.7Ga) A-type granites from the Carajás Metallogenic Province, northern Brazil. The Canadian Mineralogist 47, 1423-1440.

Campbell, I.H., 1985. The difference between oceanic and continental tholeiites: a fluid dynamic explanation. Contributions to Mineralogy and Petrology 91, 37-43.

Chai, F.M., Naldrett, A.J., 1992. The Jinchuan ultramafic intrusion: cumulate basaltic magma. Journal of Petrology, 33, 277-303.

Costa, J.B.S., Araújo, O.J.B., Santos, A., João, X.S.J., Macambira, M.J.B., Lafon, J.M., 1995. A Província Mineral de Carajás: aspectos tectono estruturais, estratigráficos e geocronológicos. In: Boletim do Museu Paraense Emílio Goeldi, Série Ciências da Terra 7, 199-235.

Dall'Ágnol, R., Souza, Z.S., Althoff, F.J., Barros, C.E.M., Leite, A.A.S., João, X.S.J., 1997. General aspects of the granitogenesis of the Carajás metallogenetic province. In: Proceedings of the International Sy mposium on Granites and Associated Mineralizations, Salvador, Excursion Guide, 135-161.

Dall'Agnol, R., Teixeira, N.P., Rämö, O.T., Moura, C.A.V., Macambira, M.J.B., Oliveira, D.C. 2005. Petrogenesis of the Paleoproterozoic, rapakivi, A-type granites of the Archean Carajás Metallogenic Province, Brazil. Lithos 80, 101-129.

Dall'Agnol R., Oliveira M.A., Almeida J.A.C., Althoff F.J., Leite A.A.S., Oliveira D.C., Barros C.E.M., 2006. Archean and Paleoproterozoic granitoids of the Carajás metallogenetic province, eastern Amazonian craton. In: Dall'Agnol R., Rosa-Costa L.T., Klein E.L. (Eds.) Symposium on Magmatism, Crustal Evolution, and Metallogenesis of the Amazonian Craton, Abstracts Volume and Field Trips Guide. Belém, PRONEXUFPA/SBG-NO, 150 pp.

Dardenne, M.A., Ferreira Filho, C.F., Meirelles, M.R., 1988. The role of shoshonitic and calc-alkaline suites in the tectonic evolution of the Carajás District, Brazil. Journal of South American Earth Science 1, 363-372.

Dias, G.S., Macambira, M.J.B., Dall'Agnol, R., Soares, A.D.V., Barros, C.E.M., 1996. Datação de zircões de Sill de metagabro: Comprovação da idade arqueana da Formação Águas Claras, Carajás, Pará. In: Simpósio de Geologia da Amazônia, V, Belém, Sociedade Brasileira de Geologia, Extended Abstracts Bulletin, 376-379.

Docegeo-Rio Doce Geologia e Mineração, 1988. Revisão Litoestratigráfica da Província Mineral de Carajás. In: Provincia Mineral de Carajás, Litoestratigrafia e principais depósitos minerais. CVRD/SBG, Congresso Brasileiro de Geologia (Belém), *Anexo aos anais*, 35, 11-59.

Eales, H.V., Cawthorn, R.G., 1996. The Bushveld Complex. In: Cawthorn, R.G. (Ed.), Layered Intrusions. Developments in Petrology, vol. 15. Elsevier Science B. V., pp. 181–229.

Faraco, M.T.L., Vale, A.G., Santos, J.O.S., Luzardo, R., Ferreira, A.L., Oliveira, M.A., Marinho, P.A.C., 2005. Levantamento Geológico da Região ao Norte da Província Carajás In: Souza, V. & Horbe, A.C. (Eds.). Contribuições a Geologia da Amazônia, v.4, 32-44.

Feio, G.R.L., Dall'Agnol, R., Dantas, E.L., Macambira, M.J.B., Santos, J.O.S., Althoff, F.J., Soares, J.E.B., 2013. Archean granitoid magmatism in the Canaã dos Carajás area: Implications for crustal evolution of the Carajás province, Amazonian craton, Brazil. Precambrian Research, 227, 157-185.

Ferreira Filho, C.F., Naldrett, A.J., Gorton, M.P., 1998. REE and pyroxene compositional variation across the Niquelandia mafic and ultramafic layered intrusion, Brazil: Petrological and metallogenetic implications. Transaction of the Institution of Mining and Metallurgy, England, v. 107, 1-22.

Ferreira Filho, C.F., Cançado, F., Correa, C., Macambira, E.M.B., Siepierski, L., Brod, T.C.J., 2007. Mineralizações estratiformes de EGP-Ni associadas a complexos acamadados em

Carajás: os exemplos de Luanga e Serra da Onça. In: Contribuições à Geologia da Amazônia, Sociedade Brasileira de Geologia - Núcleo Norte, 5, 01-14.

Figueiredo e Silva, R.C., Lobato, L.M., Rosière, C.A., Zucchetti, M., Hagemann, S.H., Baars, F.J., Morais, R., Andrade, I., 2008. A hydrothermal origin for the jaspilite-hosted, giant iron ore of the Serra Norte deposits in the Carajás Province, Pará State, Brazil. In: Hagemann, S.G., Rosière, C.A., Gutzmer, J., and Beukes, N.J., (Eds.), BIF-related high-grade iron mineralization. Reviews in Economic Geology 15, 255-290.

Gibbs, A.K., Wirth, K.R., Hirata, W.K., Olszewski Jr., W.J., 1986. Age and composition of the Grão Pará Group volcanics, Serra dos Carajás. Revista Brasileira de Geociências 16, 201-211.

Godel, B., Barnes, S-J., Maier, W.D., 2011. Parental magma composition inferred from in situ trace elements in cumulus and intercumulus silicate minerals: example from the lower and lower critical zones of the Bushveld Complex (South Africa). Lithos 125, 537-552.

Hirata, W.K., Rigon, J.C., Kadekaru, K., Cordeiro, A.A.C., Meireles, E.A., 1982. Geologia Regional da Província Mineral de Carajás. In: Simpósio Geologia da Amazônia, 1, Belém, Anais Belém, SBG/NO, 1, 100-110.

Holdsworth, R.E., Pinheiro, R.V.L., 2000. The anatomy of shallow-crustal transpressional structures: insights from the Archean Carajás fault zone, Amazon, Brazil. Journal Structural Geology 22, 1105-1123.

Huhn, S.R.B., Santos, A.B.S., Amaral, A.F., Ledsham, E.J., Gouveia, J.L., Martins, L.P.B., Montalvão, R.M.G., Costa, V.C., 1986. O terreno granito-greenstone da região de Rio Maria-Sul do Pará. In Congresso Brasileiro de Geologia, 35, Anais, Sociedade Brasileira de Geologia, 3, 1438-1452.

Huhn, S.R.B., Macambira, M.J.B., Dall'Agnol, R., 1999. Geologia e Geocronologia Pb/Pb do Granito Alcalino Arqueano Planalto, Região da Serra do Rabo, Carajás-PA. In: Simpósio de Geologia da Amazônia, 6. Manaus, Anais, Sociedade Brasileira de Geologia - Núcleo Norte, 1, 463-466.

Lahaye, Y., Arndt, N.T., Byerly, G., Gruau, G., Fourcade, S., Chauvel, C., 1995. The influence of alteration on the trace-element and Nd isotope compositions of komatiites. Chemical Geology, 126, 43-64.

Latypov, R.M., 2003. The origin of marginal compositional reversals in basic-ultrabasic sills and layered intrusions by Soret fractionation. Journal of Petrology 44, 1579-1618.

Lesher, C.M., Arnt, N.T., 1995. REE and Nd geochemistry, petrogenesis and volcanic evolution of contaminated komatiites at Kambalda, Western Australia. Lithos 34, 127-157.

Lobato, L.M., Figueiredo e Silva, R.C., Rosière, C.A., Zucchetti, M., Baars, F.J., Seoane, J.C.S., Rios, F.J., Monteiro, A.M., 2005. Hydrothermal origin for the iron mineralisation, Carajás province, Pará State, Brazil. In: Proceedings Iron Ore 2005. The Australian Institute of Mining and Metallurgy, Publication Series no 8, 99-110.

Macambira, E.M.B., 1997. Geologia e aspectos metalogenéticos dos elementos do Grupo Platina no Complexo Máfico-ultramáfico da Serra da Onça-Sul do Pará. Belém-UFPA. MSc thesis, 178 pp.

Macambira, E.M.B., Tassinari, C.C.G., 1998. Estudos Sm-Nd no Complexo Máfico-ultramafico da Serra da Onça-Sul do Para. Implicações geocronológicas e geotectonicas. In: Congresso Brasileiro de Geologia, 40, Belo Horizonte, SBG, Anais, 1, 463-463.

Macambira, M.J.B., Lancelot, J.R., 1996. Time constraints for the formation of the Archean Rio Maria crust, Southeastern Amazonian Craton, Brazil: International Geology Review 38, 1134-1142

Machado, W., Lindenmayer, Z.G., Krogh, T.E., Lindenmayer, D., 1991. U-Pb geochronology of Archean magmatism and basement reactivation in the Carajás área, Amazon shield, Brazil. Precambrian Research 49, 329-354.

Mansur, E.T., Ferreira Filho, C.F., in prep. Magmatic structure and geochemistry of the Luanga Mafic-Ultramafic Complex: further constraints for the PGE-mineralized magmatism in Carajás, Brazil.

McBirney, A.R., 1996. The Skaergaard Intrusion. In: Cawthorn, R.G. (Ed.), Layered Intrusions. Developments in Petrology, vol. 15. Elsevier Science B. V., pp. 147–180.

McCallum, I.S., 1996. The Stillwater Complex. In: Cawthorn, R.G. (Ed.), Layered Intrusions. Developments in Petrology, vol. 15. Elsevier Science B. V., pp. 441–483.

Meireles, E.M., Hirata, W.K., Amaral, A.F., Medeiros Filho, C.A., Gato, W.C., 1984. Geologia das Folhas Carajás e Rio Verde, Província Mineral de Carajás, Estado do Pará. In: SBG, Congresso Brasrasileiro de Geologia, 34, Rio de Janeiro, Anais, 5, 2163-2174.

Nogueira, A.C.R., Truckenbrod, W., Costa, J.B.S., Pinheiro, R.V.L., 1994. Análise faciológica e estrutural da Formação Águas Claras, Pré-Cambriano da Serra dos Carajás. In: Simpósio de

Geologia da Amazônia, 4, Belém, Sociedade Brasileira de Geologia, Resumos Expandidos, 363-364.

Nogueira, A.C.R., Truckenbrod, W., Pinheiro, R.V.L., 2000. Storm and tide-dominated siliciclastic deposits of the Archean Águas Claras Formation, Serra dos Carajás, Brazil. In: 31th International Geological Congress, Rio de Janeiro, Brazil, Extended Abstracts, CD-ROM.

Olszewski, W.J., Wirth, K.R., Gibbs, A.K., Gaudette, H.E., 1989. The age, origin, and tectonics of the Grão Pará Group and associated rocks, Serra dos Carajás, Brazil: Archean continental vulcanism and rifting. Precambrian Research 42, 229-254.

Pidgeon, R.T., Macambira, M.J.B., Lafon, J.M., 2000. Th-U-Pb isotopic systems and internal structures of complex zircons from an enderbite from the Pium Complex, Carajás Province, Brazil: evidence for the ages of granulite facies metamorphism and the protolith of the enderbite. Chemical Geology 166, 159-171.

Pinheiro, R.V.L., Holdsworth, R.E., 1997. Reactivation of Archaean strike-slip fault systems, Amazon region, Brazil. Journal of the Geological Society, London, 154, 99-103.

Rosa, W.D., 2014. Complexos acamadados da Serra da Onça e Serra do Puma, Geologia e petrologia de duas intrusões máfico-ultramáficas com sequência de cristalização distinta na Província Arqueana de Carajás, Brasil. Unpbl. M.Sc. thesis, Universidade de Brasília, Brazil, 73 pp.

Santos, J.O.S., Groves, D.I., Hartmann, L.A., Moura, M.A., Mc-Naughton, N.J., 2001. Gold deposits of the Tapajós and Alta Floresta domains, Tapajós-Parima orogenic belt, Amazon craton, Brazil. Mineralium Deposita 36, 278-299.

Sardinha, A.S., Dall'Agnol, R., Gomes, A.C.B., Macambira, M.J.B., Galarza, M.A., 2004. Geocronologia Pb-Pb e U-Pb em zircão de granitóides arqueanos da região de Canaã dos Carajás, Província Mineral de Carajás. Congresso Brasileiro de Geologia, 42. CD-ROM (in Portuguese).

Sardinha, A.S., Barros, C.E.M., Krymsky, R., 2006. Geology, geochemistry, and U-Pb geochronology of the Archean (2.74Ga) Serra do Rabo granite stocks, Carajás Province, northern Brazil. Journal of South American Earth Sciences 20, 327-339.

Siepierski, L., Ferreira Filho, C.F., 2016. Spinifex-textured komatiites in the south border of the Carajas ridge, Selva Greenstone belt, Carajas Province, Brazil. Journal of South American Earth Sciences 66, 41-55.

Siepierski, L., Ferreira Filho, C.F., in prep. Stratigraphy and petrology of the Vermelho Complex, Carajás Province, Brazil: evidence for magmatic processes at the lower contact zone of a layered mafic-ultramafic intrusion.

Silva, K.S., 2015. Geologia, petrologia, geocronologia e mineralizações sulfetadas do Complexo Ézio, Província Mineral de Carajás, Brasil. Unpbl. M.Sc. thesis, Universidade de Brasília, Brazil, 158 pp.

Simkin, T., Smith, J.V., 1970. Minor-element distribution in olivine. Journal of Geology 78: 304-325.

Soares, A.D.V., Santos, A.B., Vieira, E.A., Bella, V.M., Martins, L.P.B., 1994. Área Águas Claras: Contexto geológico e mineralizações. In: Simpósio de Geologia da Amazônia, 4, Belém, Anais, Sociedade Brasileira de Geologia, 379-382.

Souza, S.R.B., Macambira, M.J.B., Sheller, T., 1996. Novos dados geocronológicos para os granitos deformados do Rio Itacaiúnas (Serra dos Carajás, PA), implicações estratigráficas. In: Simpósio de Geologia da Amazônia, 5, Belém, Anais, Sociedade Brasileira de Geologia, 380-383.

Sun, S.S., McDonough W.F., 1989. Chemical and isotopic systematics of oceanic basalts: Implications for mantle composition and processes. In: Saunders, A.D., Norry, M.J. (Eds.), Magmatism in Oceanic Basins, Geol. Soc. London Spec. Pub., 42, p. 313-345.

Teixeira, J.B.G., Eggler, D.H., 1994. Petrology, Geochemistry, and Tectonic Setting of Archaean Basaltic and Dioritic Rocks from the N4 Iron Deposit, Serra dos Carajás, Pará, Brazil. Acta Geologica Leopoldensia 17, 71-114.

Teixeira, A.S., Ferreira Filho, C.F., Giustina, M.E.S.D., Araújo, S.M., Silva, H.H.A.B., 2015. Geology, petrology and geochronology of Lago Grande Layered Complex: evidence for a PGE-mineralized magmatic suite in Carajás Mineral Province, Brazil. J. S. Am. Earth Sci. 64, 116-138.

Trendall, A.F., Basei, M.A.S., De Laeter, J.R., Nelson, D.R., 1998. SHRIMP zircon U-Pb constraints on the age of the Carajás Formation, Grão Pará Group, Amazon Craton: Journal of South American Earth Sciences 11, 265-277.

Vasquez, M.L., Rosa-Costa, L.T., 2008. Geologia e recursos minerais do Estado do Pará: texto explicativo do mapa geológico e de recursos minerais do Estado do Pará-escala 1:1.000.000. Programa Geologia do Brasil (PGB), CPRM, 328 pp.

Villas, R.N., Santos, M.D., 2001. Gold deposits of the Carajás mineral province: Deposit types and metallogenesis. Mineralium Deposita 36, 300-331.

Zucchetti, M., 2007. Rochas máficas do Grupo Grão Pará e sua relação com a mineralização de ferro dos depósitos N4 e N5, Carajás, PA. Phd thesis, Belo Horizonte, Instituto de Geociências, UFMG, 116 pp.

Zucchetti, M., Lobato, L.M., Hagemann, S., 2007. Hydrothermal alteration of basalts that host the giant Northern Range Carajás iron deposits, Brazil. In: C.J. Andrew et al. (Eds.), Proceedings of 9th Biennial SGA Meeting, Dublin, 1231-1234.

"SPINIFEX-TEXTURED KOMATIITES IN THE SOUTH BORDER OF THE CARAJAS RIDGE, SELVA GREENSTONE BELT, CARAJÁS PROVINCE, BRAZIL"

LINCOLN SIEPIERSKI, CESAR FONSECA FERREIRA FILHO.

SPINIFEX-TEXTURED KOMATIITES IN THE SOUTH BORDER OF THE CARAJAS RIDGE, SELVA GREENSTONE BELT, CARAJÁS PROVINCE, BRAZIL

Lincoln Siepierski [a,b,] Cesar Fonseca Ferreira Filho[a]

a - Instituto de Geociências, Universidade de Brasília, Brasília, DF, 70910-900, Brazil

b - VALE S/A, Av. Getulio Vargas, 671/13º, 30112-020, Belo Horizonte, MG, Brazil

Abstract

Spinifex-textured komatiites in the Selva greenstone belt are the first unequivocal examples of komatiites in the Transition Subdomain of the Carajás Mineral Province. Outcrops of spinifex-textured komatiites, located ~ 1.5 km to the south of the Carajás ridge, were discovered during regional exploration for Ni-Cu-(PGE) sulfide deposits by VALE. They are associated with a 3.8 km long unit consisting of variable types of ultramafic rocks (talc schist, serpentinite and spinifex-textured komatiite). This ultramafic unit follows the steep dipping NW-SE trending Selva greenstone belt composed mainly of quartz-chlorite schists (interpreted as metasediments) and chlorite-actinolite schists (interpreted as metabasalts). Greenschist facies metamorphic parageneses characterize all rock types in the Selva greenstone belt.

The komatiitic rocks in the Selva belt comprise a sequence of flows consisting of an upper spinifex-textured layer and a lower olivine cumulate layer. Although the spinifex and cumulus textures are well preserved in the field, the primary mineralogy of the komatiites has been completely replaced by greenschist facies metamorphic minerals. Platy olivine spinifex texture, consisting of an array of roughly parallel olivine plates, and random spinifex texture, consisting of randomly oriented olivine plates, are the most common primary

volcanic textures in komatiites in the Selva greenstone belt. Platy and random spinifex texture is defined by former plates of olivine replaced by serpentine with minor actinolite, chlorite and magnetite, alternating with former matrix replaced by abundant actinolite and minor chlorite, talc, serpentine, and magnetite. The domains between olivine plates in both platy and random spinifex-textured rocks contain irregular arrays of fine-grained parallel crystals, representing primary fine-grained "quench" clinopyroxene crystals replaced by actinolite.

Spinifex-textured komatiites have MgO contents bracket between 22.8 and 26.9 wt.%, and cumulate textured komatiites have MgO contents up to 40.6 wt.%. When plotted vs MgO contents, most major and minor elements fall on well-defined linear trends indicating control by olivine fractionation or accumulation. Komatiites from the Selva and Seringa (located in the Rio Maria Domain) belts are Al-undepleted with Al_2O_3/TiO_2 ratios close to 20. Results for CaO, Na_2O, and REE suggest that these elements were mobile and their abundances have been modified during metasomatic alteration. REE contents in some samples are very high (up to 40 times primitive mantle values) and REE patterns vary from flat ($La/Yb_{MN} \sim 1$) to highly enriched in LREE (La/Yb_{MN} up to ~ 10). The REE mobility may be related to hydrothermal alteration associated to Cu-Au mineralization in the region.

The identification of spinifex-textured komatiites close to the Carajás Basin suggests the continuation of 3.0-2.9 Ga greenstone belts of the Rio Maria Domain within the Transition Subdomain, and enlarges the area with potential to host komatiite-associated Ni-Cu-PGE deposits.

Keywords:
Komatiite
Spinifex
Lithogeochemistry
Greenstone belt
Carajás Province

Introduction

The definition of komatiite proposed in the early 1980s in the Penrose conference comprises ultramafic volcanic or subvolcanic rocks (Arndt and Brooks, 1980). Precise chemical limits for komatiitic magmas (or the komatiitic magma series) as well as textural

criteria for their volcanic origin have provoked much discussion and are still not acceptable by all authors (see Arndt et al., 2008 for a review). Komatiites are usually distinguished from other magnesium-rich volcanic rocks, such as picrites and meimechites, by having spinifex texture, such that Brooks and Hart (1974) and Kerr and Arndt (2001) suggested that komatiites should be defined as ultramafic rocks that either contain spinifex texture or are spatially associated with spinifex-textured rocks. Apart from specific discussion on the definition of komatiite, the remarkable spinifex texture remains as an unequivocal distinctive evidence for this rock type. Ni-Cu-PGE deposits associated with komatiitic magmas occur in greenstone belts in different parts of the world (e.g., Australia, Canada, Brazil, Zimbabwe, Vietnan) and were described in numerous reviews (e.g., Lesher and Keays, 2002; Barnes, 2006). In Brazil, komatiite-associated Ni-Cu-PGE deposits were discovered in the Fortaleza de Minas (Brenner et. al., 1990) and Crixás greenstone belts (Costa et al., 1997). These studies emphasize the potential of komatiites to host Ni-Cu-PGE deposits and how the distinctive properties of komatiitic magmas influence ore-forming processes.

In this study we present the first description of spinifex-textured komatiites located in the Transition Subdomain of the Carajás Mineral Province (CMP). The Transition Subdomain (Dall'Agnol et al., 2006; Vasquez et al., 2008) separates two distinct domains, the older Mesoarchean Rio Maria Domain to the south and the Neoarchean Carajás Domain to the north. While greenstone belt sequences with komatiitic magmatism characterizes the Rio Maria Domain, the Carajás Domain is characterized by extensive basaltic magmatism. The recent identification of komatiites (this study) and Mesoarchean acid metavolcanic rocks (Moreto et al., 2015) are significant findings in the Transition Subdomain, suggesting the northern continuation of the Rio Maria greenstone belts. The implications of this discovery for the transition of the Carajás and Rio Maria domains, as well as for mineral exploration for Ni-Cu-PGE sulfide deposits in the Transition Subdomain are discussed.

Geological setting

The Carajás Mineral Province (CMP) is well known for hosting several world-class deposits, including the largest iron ore resources in the world, as well as significant Cu-Au, Ni, PGE, Au and Mn deposits. The CMP (Fig. 3.1) is located in the eastern portion of the Amazon Craton, bordered to the east by the Neoproterozoic Araguaia Belt and to the west by overlying Paleoproterozoic sequences of the Uatumã Supergroup (e.g., Docegeo, 1988;

Araújo and Maia, 1991). Geological limits to the north, where gneiss-migmatite-granulite terrains predominate (e.g., Faraco et al., 2005; Vasquez et al., 2008), are not precisely defined.

The CMP consists of two distinct domains, the older Mesoarchean Rio Maria Domain to the south and the Neoarchean Carajás Domain to the north (Fig. 3.1; Vasquez et al., 2008). A poorly defined zone, frequently designated as the Transition Subdomain (Fig. 3.1), separates the Mesoarchean units of the Rio Maria Domain and the mainly Neoarchean volcanic-sedimentary rocks of the Carajás Domain (Dall'Agnol et al., 2006). The Selva greenstone belt is located at the southern border zone of the Carajás Domain, within the Transition Subdomain. The CMP comprises multiple mapped lithological units (Fig. 3.1), the most important of which are described below.

The Xingu Complex consists mainly of gneisses, migmatites, and granulites (Docegeo, 1988). U-Pb zircon ages of the Xingú Complex includes an 2859 ± 9 Ma age for edembergites of the Pium Complex (Pidgeon et al., 2000) and an 2859 ± 2 Ma age for migmatites (Machado et al., 1991). These basement rocks experienced several episodes of reactivation during the Archean and Paleoproterozoic (Pinheiro and Holdsworth, 1997; Holdsworth and Pinheiro, 2000).

The Andorinhas Supergroup (Docegeo, 1988) comprises several individual volcano-sedimentary sequences (e.g., Seringa, Identidade, Sapucaia, Babaçu/Lagoa Seca), and consists of typical Mesoarchean (2904 ± 29 Ma: Macambira and Lancelot, 1996) greenstone belts, including spinifex-textured komatiitic flows, pillowed metabasalts, intermediate to acid metavolcanic rocks and metasedimentary rocks (Huhn et al., 1986; Souza and Dall'Agnol, 1996; Souza et al., 2001).

The Itacaiúnas Supergroup includes several Neoarchean (ca. 2.75 Ga: Machado et al., 1991; Trendall et al., 1998) volcano-sedimentary sequences (Docegeo, 1988). These include the large sequence of metabasalts of the Grão Pará Group, footwall to the giant jaspilite-hosted iron deposits of Carajás (Figueiredo and Silva et al., 2008; Lobato et al., 2005a, 2005b).

Several mafic-ultramafic intrusions intrude the Xingu Complex and the Itacaiúnas Supergroup (Docegeo, 1988). These include large layered intrusion hosting lateritic Ni-deposits (e.g., Vermelho, Serra da Onça, Serra do Puma and Serra do Jacaré complexes) as

well as PGE-mineralized medium-sized intrusions (e.g., Luanga and Lago Grande complexes). These layered complexes are Neoarchean (e.g., 2766 ± 6 Ma Serra da Onça Complex: Lafon et al., 2000; 2763 ± 6 Ma Luanga Complex: Machado et al., 1991) and represent a major magmatic event coeval with the extensive basaltic volcanism of the Grão Pará Group (Machado et al., 1991; Ferreira Filho et al., 2007).

The Águas Claras Formation (Araújo et al., 1988; Soares et al., 1994) comprises sandstones and siltstones formed in shallow marine to fluvial environment (Nogueira et al., 1994 and 2000). A minimum age is provided by U-Pb ages of zircons obtained from cross cutting gabbroic dikes (2645 ± 12 Ma: Dias et al., 1996).

The Carajás Mineral Province was intruded by granititic magmas of four main distinct periods: 1) Mesoarchean (ca. 2.96-2.93 Ga and 2.87-2.83 Ga) granitic intrusions (Sardinha et al., 2004; Feio and Dall'Agnol, 2012; Feio et al., 2013); 2) Neoarchean (ca. 2.76-2.73 Ga) syn-orogenic intrusions including the Plaquê Suite (Avelar et al., 1999; Huhn et al., 1999; Dall'Agnol et al., 1997; Barros et al., 2001; Sardinha et al., 2006; Feio and Dall'Agnol, 2012; Feio et al., 2013); 3) earliest Neoarchean (ca. 2.56 Ga) intrusions including alkaline granites (Machado et al., 1991; Souza et al., 1996); 4) Paleoproterozoic (ca. 1.88 Ga) intrusions include several anorogenic granitic plutons (e.g., Dall'Agnol et al., 2005 and 2006) that belong to an extensive A-type Proterozoic province of the Amazon Craton (e.g., Santos et al., 2001).
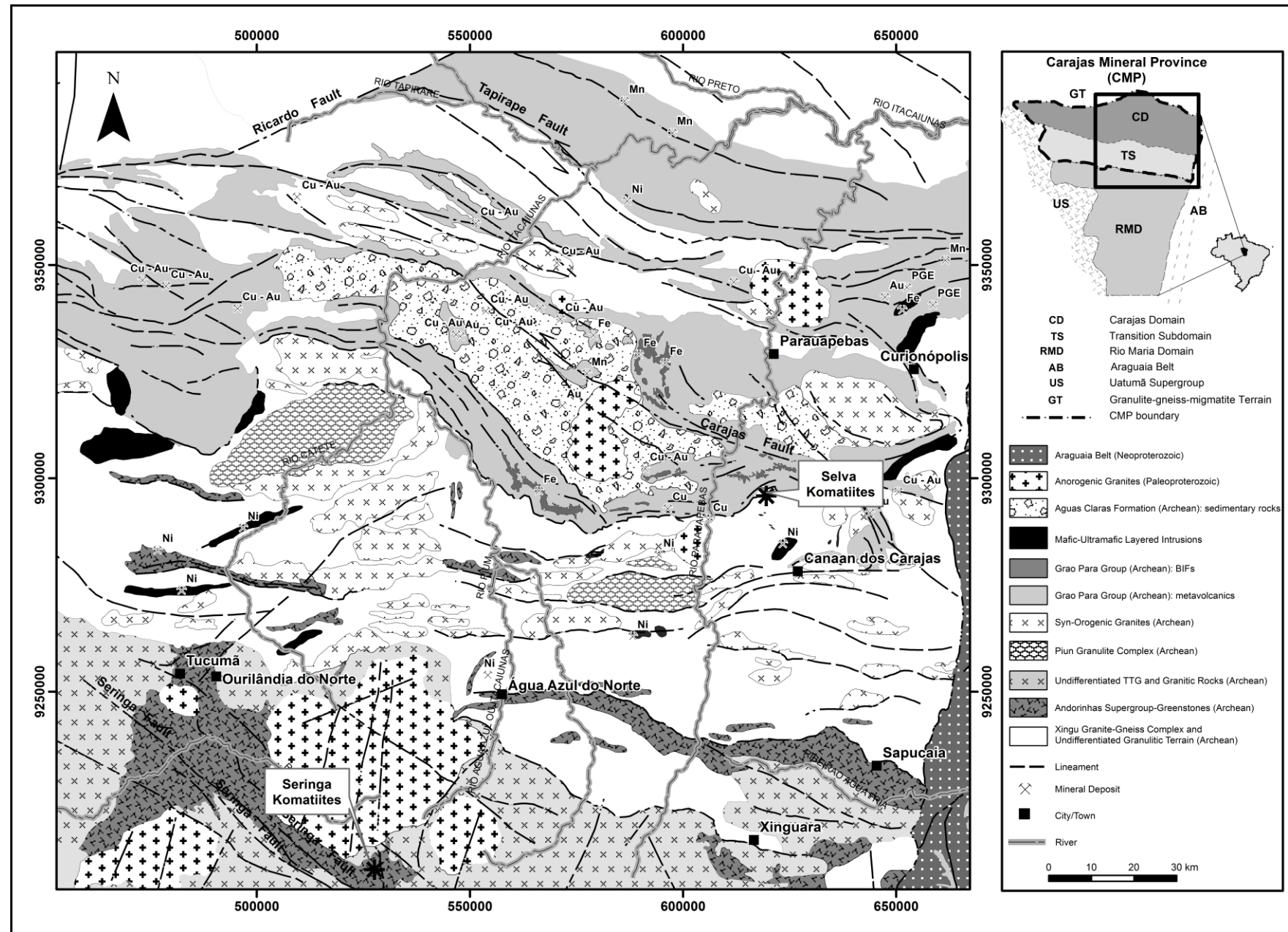
Figure 3.1. Main geological units of the Carajás Province (modified from Vasquez et al., 2008), showing locations of Selva and Seringa komatiite occurrences.

Sampling and analytical procedures

A total of 22 representative samples of unweathered komatiites from boulders or outcrops were selected for geochemical studies. Samples typically weight more than 1 kg to accommodate the coarse grain sizes of platy spinifex rocks. Sample preparation and lithogeochemistry analyses were performed at the ALS Chemex (Canada). Major and minor elements were determined by wavelength-dispersive X-ray fluorescence spectrometry (ALS Chemex method ME-XRF12st), loss-on-ignition was determined gravimetrically (ALS Chemex method OA-GRA05x), total S was determined by Leco® inductive combustion and infrared spectroscopy (ALS Chemex method S-IR08), and selected minor and trace elements were determined by fusion ICP-MS (ALS Chemex method ME-MS81). A complete description of analytical methods is available in the ALS Chemex Home Page (www.alsglobal.com). Analytical results are provided in Table 3.1.

Spinifex-textured komatiites

Local geology

Outcrops of spinifex-textured komatiites, located about 1.5 km to the south of the Carajás ridge (Fig. 3.1, 2 and 3A), were discovered during regional exploration for Ni-Cu-(PGE) sulfide deposits by VALE in 2004-2005. They are associated with a volcanic sedimentary sequence defined as the Selva greenstone belt by VALE (Fig. 3.2). The portion of the greenstone belt hosting most of the ultramafic rocks was mapped in detail during the exploration program (Fig. 3.2), which included soil geochemical and geophysical surveys. Ultramafic rocks extend for 3.8 kilometers following the NW-SE trending volcanic-sedimentary sequence. This NW-SE sequence and associated foliated granitic rocks have a sharp discordant contact with E-W trending basalts and iron formations of the Itacaiúnas Supergroup (Fig. 3.3A). The most prominent geomorphologic feature of the Selva greenstone belt consists of smooth hills, up to 130 meters higher than surrounding flat areas, sustained by highly weathered komatiitic rocks (Fig. 3.2, 3.3A) or quartz-chlorite schists. Unweathered

mafic-ultramafic rocks occur mainly as blocks and boulders with rare outcrops, especially of massive rocks.

Ultramafic rocks form irregular elongated zones of talc schist, serpentinite, and spinifex-textured komatiites. They are associated with quartz-chlorite schists, interpreted as metasedimentary rocks, and actinolite-chlorite schists, interpreted as metabasalts, that extend beyond the mapped area. Tectonic foliation is pervasive in schistose rocks (e.g., talc schist and actinolite-chlorite schist in Fig. 3.2) but limited to narrow discrete shear zones in massive rocks (e.g., serpentine and komatiite with spinifex texture in Fig. 3.2). This foliation is sub-vertical or dips steeply (> 65°) to the SW. Metamorphic parageneses indicate greenschist facies of metamorphism, consisting of chlorite-actinolite-epidote-albite-quartz assemblages in mafic rocks and chlorite-actinolite-talc-serpentine assemblages in ultramafic rocks. Rocks of the volcanic-sedimentary sequence are closely associated with foliated granitoids and cross cut by irregular bodies of gabbroic rocks (Fig. 3.2). All of these rocks are cut by concordant NW-SE trending quartz veins and partially covered by an iron-rich laterite (Fig. 3.2).
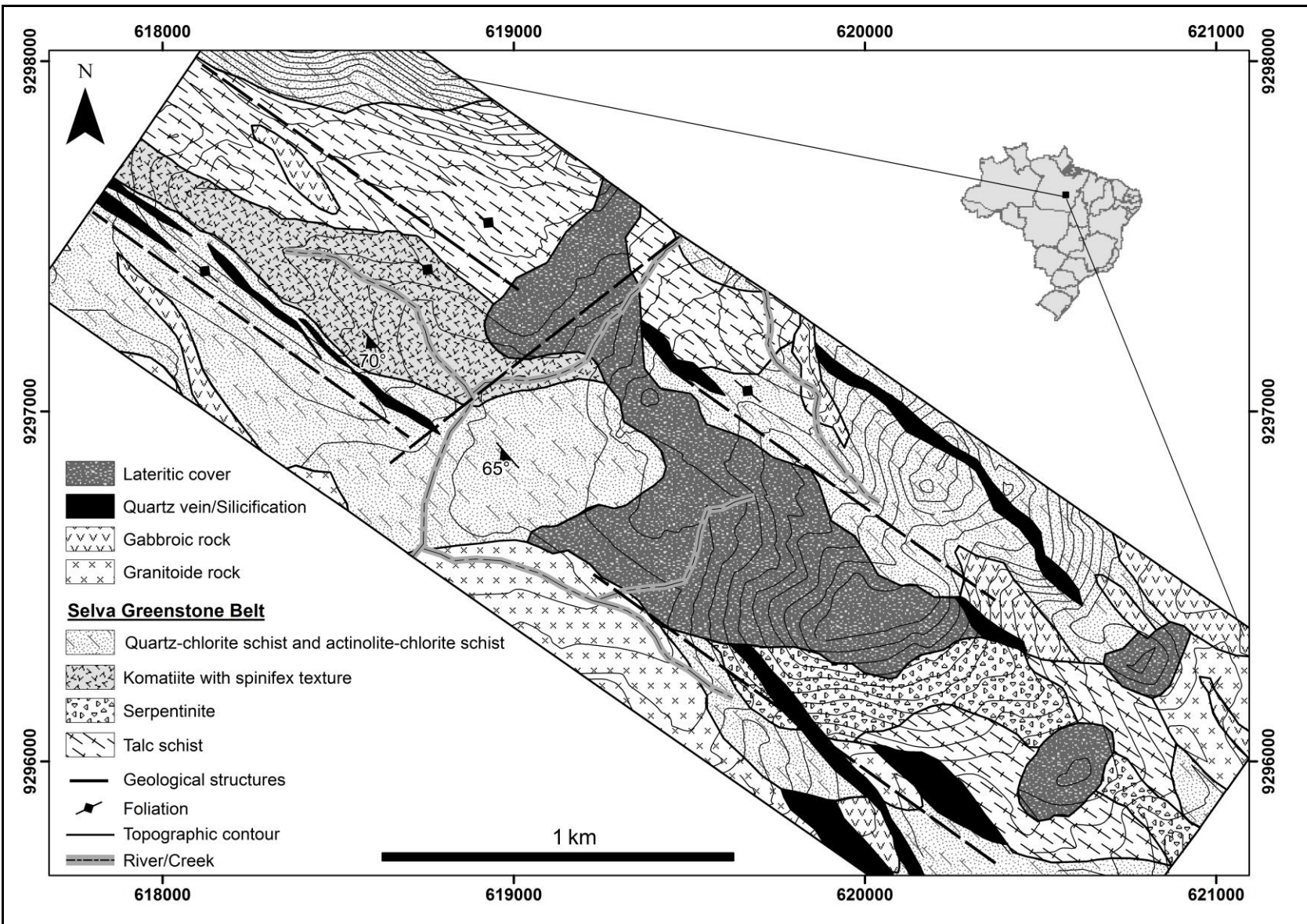
Figure 3.2. Geological map of the Selva greenstone belt (modified from CVRD, 2005)
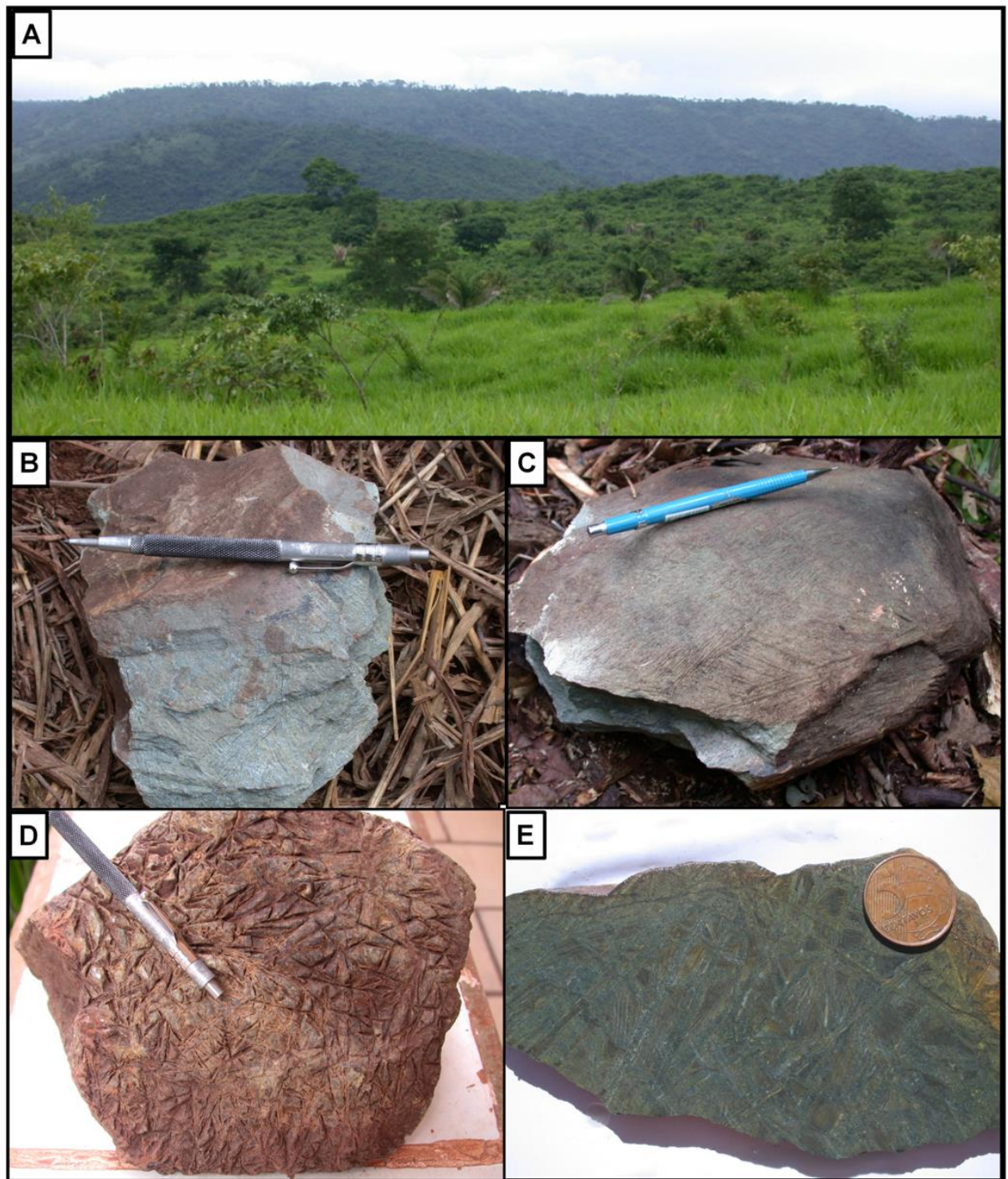
Figure 3.3. A) Panoramic view (looking to northeast) of the Selva greenstone belt. The first hill consists of komatiite with spinifex texture, whereas the higher hill in the back consists of iron formation and mafic volcanic rocks of the Itacaiúnas Supergroup. B) and C) Komatiite with centimeter-scale platy spinifex texture. D) and E) Komatiite with random spinifex texture.

Structure, petrography and mineralogy

Primary volcanic structures and textures are restricted to the northwestern portion of the mapped area, indicated in Figure 3.2 as komatiite with spinifex texture. The komatiites occur mainly as boulders and blocks and facing criteria based on volcanic features cannot be defined. Geological sections across this NW-SE trending zone of komatiites (Fig. 3.2) consist of a succession of up to tens-of-meters-wide domains with boulders/blocks of massive serpentinite alternating with boulders/blocks of spinifex-textured ultramafic rocks. This succession extends for hundreds-of-meters along strike and indicates that they represent a sequence of thin differentiated flows consisting of an upper spinifex-textured layer (A zone) and a lower olivine cumulate layer (B zone). This type of flow is the best-known and most diagnostic type of komatiitic flow and has been described in detail at many localities worldwide (e.g., Pyke et al., 1973; Saboia and Teixeira, 1983; see review by Arndt et al., 2008).

Platy olivine spinifex texture, consisting of an array of roughly parallel olivine plates (Fig. 3.4A-B and C-D), and coarse random spinifex, consisting of randomly oriented olivine plates (Fig. 3.4E and F), are the most common primary volcanic textures preserved in the komatiites in the Selva greenstone belt. Individual spinifex plates are up to 20 centimeters long, and may be partially disrupted by tectonism. Although the spinifex texture is well preserved in abundant blocks/boulders in the field, the primary mineralogy of the komatiites has been completely replaced by greenschist facies metamorphic minerals. Platy (Fig. 3.4A-B-C-D) and random (Fig. 3.4E-F) spinifex texture is defined by former plates of olivine replaced by chlorite and serpentine with minor actinolite and magnetite, alternating with former matrix replaced by abundant actinolite and minor chlorite, talc, serpentine, and magnetite. The domains between olivine plates in both platy and random spinifex-textured rocks contain irregular arrays of fine-grained parallel crystals (Fig. 3.4G), representing primary fine-grained "quench" clinopyroxene crystals replaced by actinolite.

Massive serpentinite blocks/boulders interlayered with spinifex-textured blocks/boulders do not show any distinctive volcanic structures in the field. They consist of a fine-grained diablastic aggregate of serpentine with minor actinolite, magnetite, talc and chlorite. Relicts of primary olivine mesocumulate texture are preserved in thin sections, represented by fine-grained euhedral olivine crystals completely pseudomorphosed by

serpentine and magnetite within a serpentine- and actinolite-rich matrix (Fig. 3.4H). The margins of cumulus olivine are outlined by magnetite concentrations (Fig. 3.4H).

Mafic metavolcanic rocks in the Selva greenstone belt are characterised by actinolite-chlorite-quartz-albite assemblages. These parageneses of ultramafic and mafic rocks characterize most greenstone belt terrains worldwide (see review by Arndt et al., 2008).
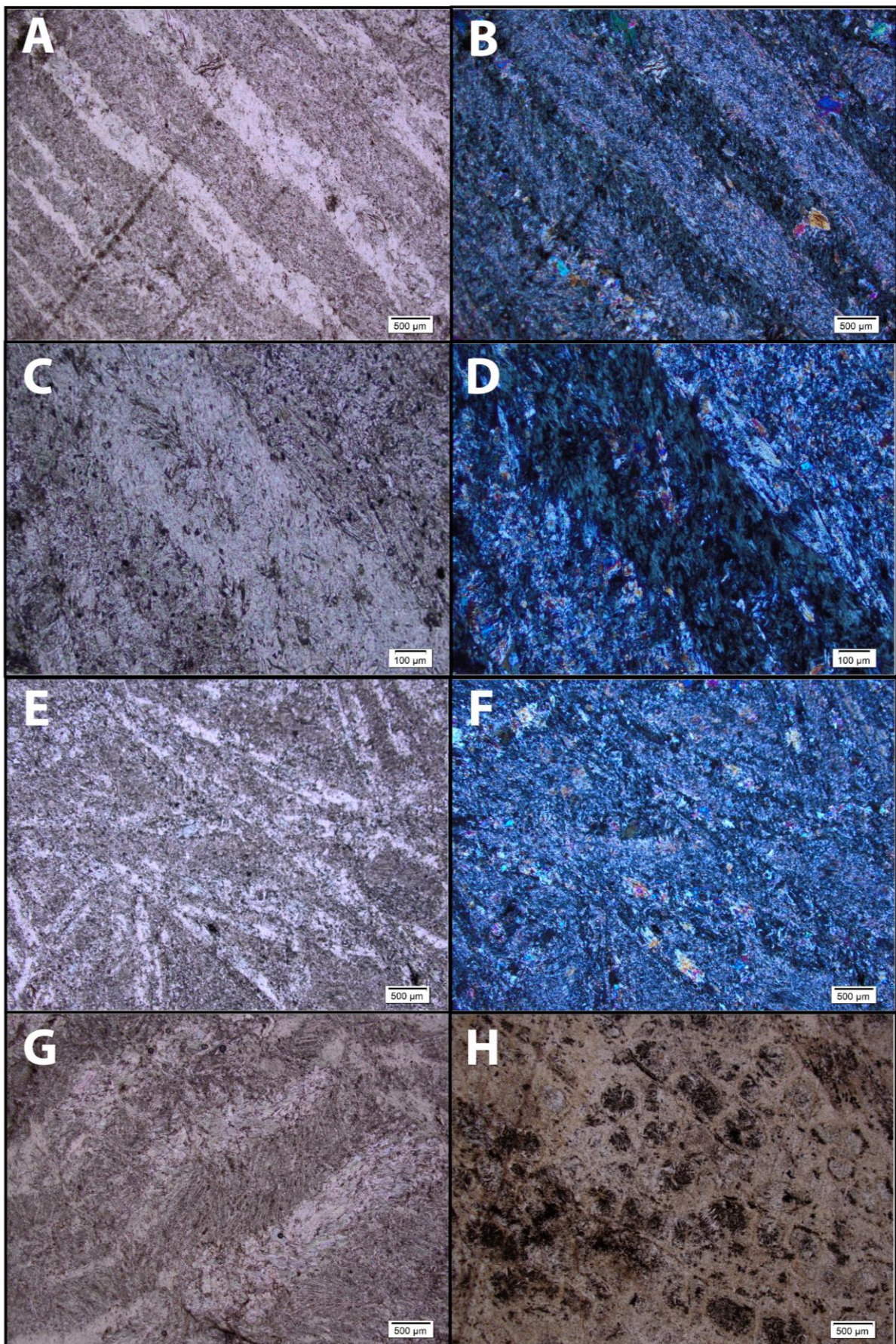
Figure 3.4. A) Photomicrograph of platy spinifex texture. Pseudomorphs of olivine plates (white color) consist mainly of chlorite and serpentine. Dark colored domains between olivine plates consist mainly of actinolite with associated chlorite, serpentine, talc and magnetite. B)

Same as A but with crossed polarizers. C) and D) Detail of A and B, respectively. E) Photomicrograph of random spinifex texture. F) Same as E but with crossed polarizers. G) Photomicrograph of platy spinifex texture. The matrix between plates of olivine shows relicts of irregular arrays of fine-grained parallel actinolite crystals (clinopyroxene pseudomorphs). H) Cumulate zone of spinifex-textured flow. Relicts of cumulus olivine are enhanced by magnetite enriched crystal margins.

Bulk rock geochemistry

Eleven komatiites with spinifex or massive cumulate textures were analysed for major, minor, and trace elements (Table 3.1). These analyses are compared with analyses of twelve spinifex-textured komatiites collected from a sequence of thin (i.e., few meters thick) spinifex-textured flows from the Seringa belt in the Rio Maria Domain (Fig. 3.1; Table 3.1). Compared with komatiites of the Selva greenstone belt, the spinifex-textured komatiites of the Seringa belt have the same type of texture and metamorphic mineralogy, but better-preserved primary textures, particularly fine-grained features of the matrix between olivine plates, including relict cores in skeletal chromite crystals replaced by magnetite (ferrichromite) (Fig. 3.5).
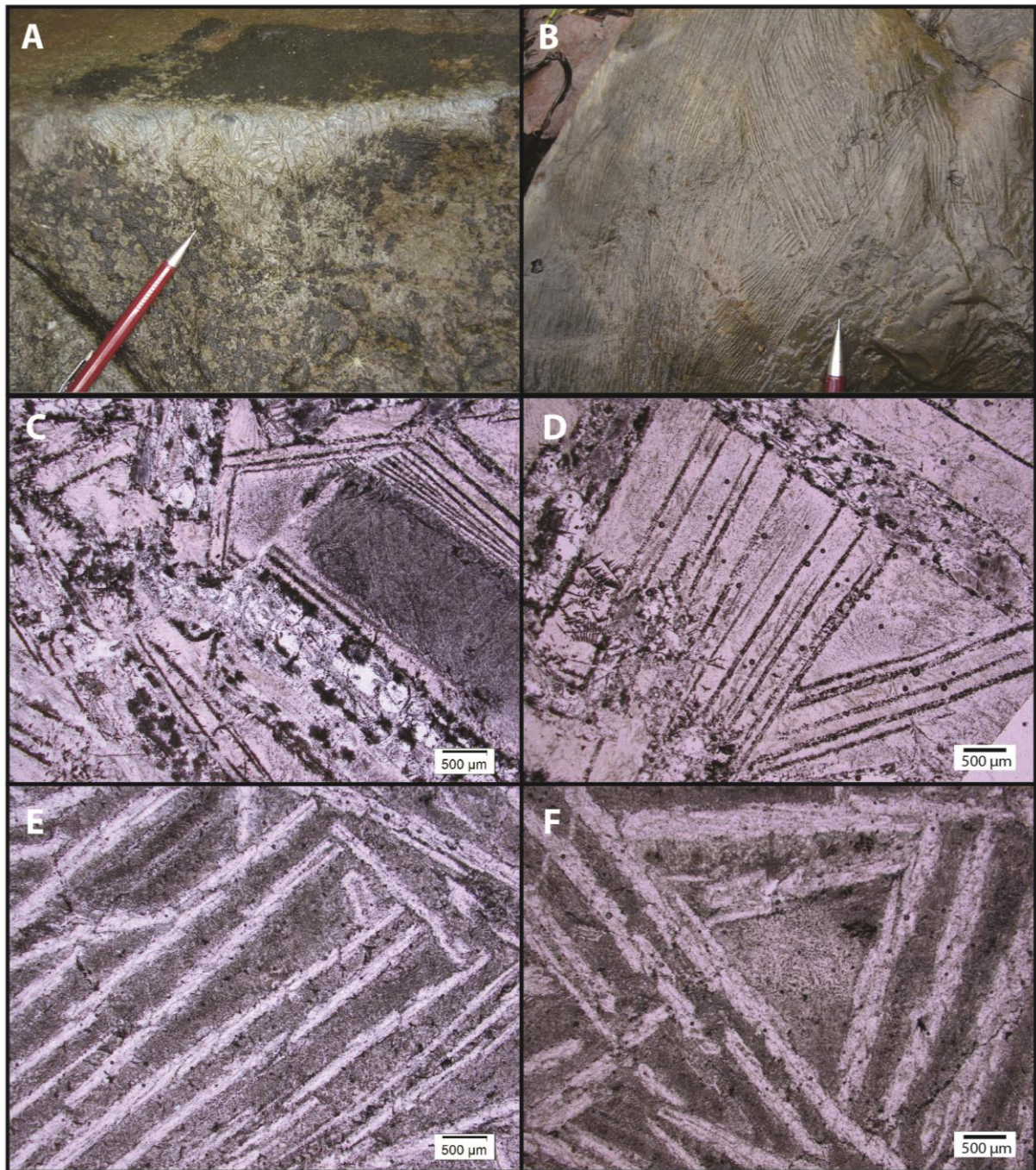
Figure 3.5. Photos from komatiites of the Seringa greenstone belt. A) Komatiite with random spinifex texture. B) Komatiite with centimeter-scale platy spinifex texture. C) and D) Photomicrographs of platy spinifex texture. Note fine skeletal crystals in the matrix between olivine plates, including skeletal chromite in the left hand side of photomicrograph "C". Note also the enrichment of magnetite (opaque minerals) at the border of large olivine plates (whitish color). E) and F) Platy spinifex texture. Olivine plates (whitish color) are replaced by fine-grained aggregates of serpentine, chlorite, magnetite, with minor talc and actinolite.

A plot of MgO vs major oxides and minor elements illustrates the main geochemical characteristics of the komatiites in the Selva greenstone belt (Fig. 3.6). In the following discussion and diagrams, major and minor elements will be quoted as weight percent oxide from analyses (see Table 3.1) normalized to 100% on an anhydrous basis. Spinifex-textured komatiites from the Selva greenstone belt have high MgO contents between 22.8 and 26.9 wt.%, with cumulate textured komatiites ranging in contents up to 40.6 wt. % MgO (Fig. 3.6). The abundances of compatible elements (e.g., Ni, Cr) are correspondingly high, and abundances of incompatible elements (e.g., Al, Ti) are correspondingly low. The compositions of the spinifex-textured komatiites in the Seringa greenstone belt are similar to those in the Selva greenstone belt. In the following discussion the latter will be considered as a comparative reference of less metasomatized komatiites with broadly similar textures and compositions.

The plot of MgO vs Al_2O_3 and MgO vs TiO_2 for komatiites of the Selva greenstone belt fall on well-defined linear trends (r = -0.79 and -0.71, respectively; Fig. 3.6). Because olivine contains insignificant amounts of Al_2O_3 and TiO_2, the MgO intercept gives the MgO content of olivine that accumulated (i.e., olivine cumulate samples) or fractionated (i.e., olivine spinifex samples). The MgO intercepts in these plots are close to the MgO content of an olivine with composition of Fo_{90} (Fig. 3.6). A composition that is intermediate between the Fo_{95-88} range of compositions expected for liquidus olivine in equilibrium with komatiitic magmas (see reviews by Lesher and Stone, 1996; Arndt et al. 2008). The variations of MgO vs SiO_2 and MgO vs Fe_2O_3, are also consistent with olivine fractionation and suggest that the abundances of these elements were not significantly affected by hydrothemal alteration and/or metamorphism. The variation of MgO vs CaO (r = -0.98) and MgO vs Na_2O (r = 0.02), however, are not consistent with fractionation of olivine with composition close to Fo_{90}, suggesting that these elements are affected by hydrothermal alteration and/or metamorphism (Fig. 3.6). The sample with the lowest Ca content (0.02 wt. % CaO; sample SELVA 04 in Table 3.1) is the most magnesian sample (40.6 wt. % MgO; Fig. 3.6), suggesting that Ca has been systematically lost during serpentinization (see discussion in Lesher and Stone, 1996; Arndt et al., 2008). Na_2O and K_2O are lower than expected from comparison with Seringa belt komatiites (Fig. 3.6) and less-altered komatiites worldwide (Arndt et al., 2008), indicating that they have been mobile during seafloor alteration and/or metamorphism.

The plot of MgO vs Ni for komatiites of the Selva greesntone belt falls on well-defined linear trend (r = 0.96; Fig. 3.6), consistent with accumulation or fractionation of an olivine with composition close to Fo_{90} and about 3250 ppm Ni (Fig. 3.6). The plot of MgO vs Cr_2O_3 for komatiites of the Selva greenstone belt falls in a poorly defined linear trend (r = -0.37; Fig. 3.6). Relatively high Cr_2O_3 contents and positive linear trends for spinifex-textured komatiites for Selva and Seringa belts (r = 0.64 for the latter; Fig. 3.6), are consistent with fractionation of olivine and chromite. The positive Cr-Mg trend for the spinifex-textured komatiites indicates that chromite was on the liquidus (Lesher and Stone, 1996; Barnes and Roeder, 2001), but the lower Cr contents in cumulate-textured komatiites indicate that they do not contain much chromite (Fig. 3.6). This suggests that komatiitic magmas reached chromite saturation during fractional crystallization, as discussed by Lesher and Stone (1996).

High-field strength elements (HFSE) and rare-earth elements (REE) are relatively immobile in many altered komatiites (e.g., Arndt and Lesher, 1992; Lesher and Arndt, 1995; Lahaye et al., 1995). Variation diagrams for less mobile major and minor elements (Fig. 3.6) suggest a dominant control by olivine accumulation or fractionation of komatiites from Selva and Seringa komatiites. Therefore, the highly incompatible HFSE and REE should retain constant interelement ratios if alteration and/or processes other than olivine fractionation were not involved. Unfortunately, several HFSE have very low contents that are close to their lower limits of quantification in the analyses of komatiites of this study (e.g., Th, Nb, Ta, U: Table 3.1), and should be considered with discretion. The Zr-Hf plot provides essentially constant interelement ratios (Fig. 3.7) and well-defined linear trends (r = 0.99 and 0.96 for samples from the Selva and Seringa belts, respectively), indicating that they were not affected by significant chemical mobility during alteration. The plots of different REE with Zr (e.g., Ce, Sm and Yb in Fig. 3.7) provide highly variable interelement ratios for komatiites of the Selva belt, with poor linear correlations. This is in variance with results for the Seringa belt, which show positive linear correlation and much less variable interelement ratios (Fig. 3.7). Mantle-normalised REE and selected incompatible element plots are given in Fig. 3.8. Komatiites in the Seringa belt have very similar flat REE patterns at about 1-2 times primitive mantle values. Komatiites in the Selva belt have highly variable REE patterns and REE concentrations (up to 40 times primitive mantle values). Several samples of komatiites from the Selva greenstone belt have pronounced negative Ce and Eu anomalies, suggesting significant mobility of these elements during hydrothermal alteration and/or metamorphism. The mobility of elements such as Cs, Rb and Pb is manifested by positive or negative anomalies in mantle-normalized trace elements plots for komatiites from the Seringa belts

(Fig. 3.8), as commonly observed in komatiites from several localities (see Arndt et al., 2008 for a review). Mantle-normalized trace elements plots for komatiites from the Selva belt (Fig. 3.8), however, have several positive or negative anomalies for elements not usually considered to be mobile. Chemical compositions of komatiites in the Selva greenstone belt are likely to be affected by significant hydrothermal and/or metamorphic alteration. This possibility provides the framework for petrologic and petrogenetic discussions in the following section of this study.

Table 3.1. Chemical composition of komatiite samples from Selva and Seringa belts. Major elements and S are reported in wt. %, while trace elements in ppm. Abreviations: Spx-K = spinifex-textured komatiite, Cum-K = cumulate komatiite, LOI = loss on ignition, bdl = below detection limit, Mg# = Mg number.

| Sample	Selva01	Selva02	Selva03	Selva04	Selva05	Selva06	Selva07	Selva08	Selva10	Selva11	Seringa01	Seringa02	Seringa03	Seringa04	Seringa05	Seringa06	Seringa07	Seringa09	Seringa10	Seringa11	Seringa12	Seringa13
Rock	Spx-K	Spx-K	Spx-K	Cum-K	Spx-K	Spx-K	Spx-K	Cum-K	Spx-K	Spx-K	Spx-K	Spx-K	Spx-K	Spx-K	Spx-K	Spx-K	Spx-K	Spx-K	Spx-K	Spx-K	Spx-K	Spx-K
SiO2	39.76	39.31	43.14	39.17	42.75	44.85	42.27	37.42	42.55	40.77	41.89	41.10	42.24	43.84	40.41	42.33	41.37	42.23	45.44	41.34	41.08	39.86
TiO2	0.44	0.45	0.36	0.11	0.26	0.36	0.37	0.22	0.35	0.49	0.33	0.33	0.40	0.35	0.40	0.38	0.38	0.42	0.26	0.32	0.36	0.44
Al2O3	7.80	7.93	7.21	2.63	5.59	6.03	7.08	4.25	7.89	8.32	5.62	6.28	7.07	6.75	7.72	6.76	7.03	7.40	5.88	6.33	7.40	7.90
Cr2O3	0.39	0.38	0.30	0.21	0.31	0.28	0.32	0.32	0.29	0.31	0.32	0.37	0.34	0.33	0.32	0.37	0.35	0.33	0.24	0.33	0.35	0.30
Fe2O3	11.34	11.80	11.97	9.33	11.67	11.48	11.46	13.80	12.77	9.68	12.71	12.02	12.63	12.77	13.42	13.12	13.30	13.23	12.23	12.45	12.66	12.43
MnO	0.18	0.18	0.24	0.08	0.16	0.22	0.24	0.15	0.27	0.22	0.23	0.21	0.21	0.18	0.20	0.23	0.20	0.22	0.20	0.20	0.20	0.22
MgO	24.27	23.67	22.02	35.42	24.22	21.30	23.36	28.69	21.98	24.58	24.03	24.06	22.54	24.32	22.50	22.82	23.36	20.91	20.80	23.70	24.54	21.09
CaO	7.07	6.92	7.57	0.02	7.41	8.75	7.15	2.71	7.91	6.83	7.72	8.04	8.54	7.99	7.97	7.66	8.12	8.67	9.70	7.63	7.35	9.10
Na2O	0.20	0.19	0.24	0.20	0.14	0.12	0.31	0.16	0.20	0.23	0.45	0.43	0.74	0.31	0.81	0.53	0.75	0.59	0.48	0.35	0.38	0.40
K2O	0.03	0.03	0.05	0.03	0.04	0.02	0.04	0.02	0.03	0.03	0.07	0.06	0.07	0.09	0.07	0.05	0.07	0.08	0.07	0.09	0.05	0.07
P2O5	0.02	0.03	0.06	0.01	0.04	0.03	0.04	0.03	0.02	0.07	0.03	0.04	0.02	0.03	0.04	0.04	0.04	0.04	0.02	0.03	0.04	0.04
BaO	bdl	bdl	0.01	bdl	bdl	bdl	bdl	0.01	bdl	bdl	0.01	bdl	bdl	bdl	bdl	bdl	bdl	bdl	bdl	0.01	bdl	bdl
SrO	0.01	0.01	0.01	bdl	0.01	0.01	0.01	0.01	0.01	bdl	0.01	bdl	0.01	0.01	0.01	0.01	0.02	0.01	0.01	0.01	0.01	0.01
LOI	8.04	7.71	6.86	12.50	7.46	6.27	7.24	11.80	5.41	8.15	6.38	7.03	4.81	2.98	5.64	5.75	4.92	5.15	4.18	6.75	5.43	7.52
Total	99.54	98.61	100.05	99.72	100.05	99.71	99.89	99.58	99.73	99.64	99.80	99.96	99.62	99.95	99.52	100.05	99.92	99.29	99.53	99.54	99.83	99.36
Mg#	65.00	63.00	61.00	77.00	64.00	62.00	64.00	64.00	60.00	69.00	62.00	63.00	61.00	62.00	59.00	60.00	60.00	60.00	58.00	59.00	62.00	59.00
S	bdl	bdl	bdl	bdl	bdl	bdl	bdl	bdl	bdl	bdl	0.06	0.02	0.01	bdl	0.03	bdl	bdl	bdl	bdl	0.02	0.01	bdl
Ag	bdl	bdl	bdl	bdl	bdl	bdl	bdl	bdl	0.02	bdl	0.56	0.15	0.13	0.13	0.11	0.07	0.03	0.03	0.15	0.03	0.04	0.04
As	1.4	2.6	1.2	5.5	0.6	0.4	1.5	4.8	0.8	2.7	bdl	bdl	0.7	4.1	bdl	bdl	1.0	bdl	0.8	1.2	0.5	1.1
Ba	bdl	10	bdl	10	bdl	bdl	bdl	20	bdl	bdl	10	20	bdl	10	10	bdl	10	10	20	10	bdl	30
Be	0.12	0.21	0.13	0.08	0.06	0.09	0.21	0.06	0.19	0.19	0.10	0.09	0.09	0.11	0.11	0.09	0.08	0.07	0.08	0.06	0.10	0.10
Bi	0.01	0.01	0.04	0.3	0.14	-0.01	0.04	0.66	0.04	0.04	0.07	0.05	0.06	0.03	0.03	0.03	0.02	0.01	0.01	bdl	bdl	bdl
Cd	0.02	0.03	bdl	bdl	0.03	0.02	0.03	0.06	0.02	0.04	0.10	0.04	0.05	0.04	0.22	0.04	0.15	0.05	0.10	0.10	0.12	0.09
Co	98.5	101.0	162.5	79.4	77.6	83.8	83.1	108.5	101.5	91.6	99.2	104.5	96.7	107.0	94.2	99.8	121.5	107.0	100.5	97.8	104.5	95.8
Cr	1740	1760	1350	867	1310	1320	1400	1420	1290	1310	1370	1690	1570	1480	1515	1530	1615	1440	1030	1540	1460	1360
Cs	bdl	bdl	0.15	bdl	0.12	0.10	0.12	bdl	0.09	0.07	0.68	0.39	1.03	0.91	0.44	0.42	0.25	0.34	0.35	0.98	0.59	0.67
Cu	13	14	17	7	11	12	12	18	69	16	491	31	45	19	194	9	10	23	154	31	78	53
Ga	7.87	8.01	7.98	2.99	6.26	6.60	7.33	4.76	8.63	7.90	6.16	6.46	7.39	7.67	7.83	6.94	7.76	8.46	7.35	6.76	8.06	8.30
Ge	0.15	0.16	0.13	0.12	0.11	0.11	0.13	0.14	0.14	0.10	0.09	0.09	0.11	0.10	0.13	0.09	0.12	0.11	0.11	0.14	0.13	0.12
Hf	0.2	0.2	0.7	bdl	0.2	0.2	0.6	0.1	0.9	0.6	0.5	0.6	0.7	0.6	0.8	0.6	0.7	0.8	0.5	0.5	0.5	0.7
In	0.04	0.04	0.04	0.03	0.02	0.02	0.04	0.02	0.02	0.03	0.03	0.04	0.04	0.04	0.05	0.04	0.05	0.04	0.03	0.03	0.03	0.03
Li	1.2	1.1	2.3	bdl	0.4	3.5	0.8	0.6	3.1	0.7	1.6	3.0	2.7	10.1	2.5	3.5	6.7	3.7	2.2	2.0	1.7	2.2
Mn	1160	1170	1640	515	1110	1560	1680	993	1950	1450	1435	1295	1510	1150	1290	1405	1415	1455	1350	1380	1350	1530
Mo	0.10	0.12	0.10	0.19	0.15	0.08	0.10	0.15	0.13	0.10	0.35	0.20	0.18	0.27	0.19	0.16	0.38	0.19	0.22	0.18	0.18	0.23
Nb	1.0	1.0	1.4	0.3	0.6	0.7	1.2	0.6	1.3	1.4	0.7	0.9	0.9	1.8	1.0	0.8	0.9	0.9	0.8	0.8	0.9	1.1
Ni	1100	1120	1020	2380	999	831	1120	2000	1110	1110	1140	1100	907	1100	872	873	983	790	1040	1020	999	815
P	60	30	140	10	20	160	110	70	210	130	90	90	100	100	120	90	110	120	80	90	100	120
Pb	bdl	bdl	bdl	bdl	bdl	bdl	bdl	0.5	0.5	1.0	0.9	1.5	2.2	0.9	2.3	1.2	3.5	1.4	2.3	2.1	1.3	1.3
Rb	0.2	0.3	1.2	0.4	1.2	0.6	0.5	0.1	0.4	0.4	0.7	0.2	0.3	2.6	0.2	0.1	0.5	0.5	0.7	2.6	1.0	1.4
Sb	0.06	0.08	0.08	0.13	0.08	0.09	0.11	0.16	0.13	0.44	0.24	0.21	0.33	1.60	0.17	0.19	0.18	0.09	0.18	0.18	0.13	0.09
Sn	0.2	0.3	0.3	0.2	bdl	bdl	0.2	0.2	0.2	0.2	0.2	0.2	0.3	0.2	0.3	0.2	0.2	0.2	0.2	0.2	0.2	0.2
Sr	14.2	13.8	29.7	0.5	12.1	3.9	29.5	21.0	24.4	17.0	23.7	18.4	35.9	21.4	105.5	30.0	116.0	27.9	25.5	20.8	20.7	25.6
Ta	0.08	0.08	0.20	bdl	bdl	0.06	0.09	0.05	0.10	0.11	0.08	0.09	0.07	0.09	0.10	0.09	0.09	0.09	0.05	0.07	0.07	0.08
V	175	184	141	66	132	128	155	105	157	172	129	142	157	146	160	149	162	169	116	145	160	166
W	32.0	30.0	335.0	18.5	15.8	44.0	45.3	66.2	33.3	57.9	47.9	72.1	37.5	116.5	35.8	78.6	108.5	70.8	31.2	19.8	36.6	41.8
Zn	72	60	110	77	45	133	85	143	161	102	94	89	112	88	81	98	97	83	76	80	82	74
Zr	4.8	4.8	18.6	bdl	2.9	3.8	15.6	0.6	23.3	15.9	12.6	16.3	17.6	14.5	24.0	15.8	19.8	22.4	13.5	9.1	9.6	19.8
La	21.80	28.60	2.80	bdl	1.60	bdl	6.10	0.60	3.80	3.20	1.10	1.00	1.00	1.40	1.50	1.00	0.90	0.90	0.90	0.90	0.80	1.30
Ce	8.80	16.40	4.40	0.60	1.20	bdl	10.20	1.00	3.80	2.40	2.70	2.50	3.10	3.60	4.30	3.20	2.70	2.50	2.40	3.40	2.30	3.60
Pr	3.80	4.90	0.90	bdl	0.50	bdl	1.90	0.10	1.00	0.70	0.40	0.30	0.40	0.50	0.50	0.40	0.30	0.40	0.30	0.40	0.30	0.50
Nd	15.00	19.30	4.50	bdl	2.80	0.60	8.80	0.90	4.90	3.90	2.10	2.00	2.30	2.80	2.90	2.30	1.90	2.40	2.00	2.30	1.90	2.60
Sm	3.10	3.70	1.30	0.10	0.90	0.40	1.80	0.30	1.30	1.10	0.60	0.70	0.80	0.90	0.90	0.80	0.70	0.90	0.60	0.70	0.70	0.90
Eu	0.90	1.00	0.30	bdl	0.30	bdl	0.40	bdl	0.40	0.30	0.20	0.20	0.30	0.20	0.20	0.20	0.20	0.30	0.30	0.20	0.20	0.30
Gd	4.00	4.90	1.50	0.20	1.10	0.60	2.20	0.50	1.70	1.60	0.80	1.00	1.00	1.10	1.20	1.00	1.00	1.10	0.90	1.00	0.90	1.10
Tb	0.70	0.80	0.20	bdl	0.20	0.10	0.30	bdl	0.30	0.30	0.10	0.20	0.20	0.20	0.20	0.20	0.20	0.20	0.20	0.20	0.10	0.20
Dy	4.10	4.70	1.80	0.40	1.60	1.00	2.40	0.60	1.90	2.00	1.20	1.30	1.30	1.50	1.70	1.50	1.40	1.60	1.10	1.40	1.20	1.50
Ho	0.80	0.90	0.40	0.10	0.30	0.20	0.50	0.10	0.40	0.40	0.20	0.20	0.30	0.30	0.30	0.30	0.30	0.30	0.20	0.20	0.20	0.30
Er	2.20	2.70	1.20	0.30	0.90	0.60	1.40	0.40	1.10	1.20	0.70	0.80	0.80	0.90	1.00	0.90	0.90	1.00	0.70	0.80	0.70	0.90
Tm	0.30	0.30	0.10	bdl	0.10	bdl	0.20	bdl	0.10	0.10	0.10	0.10	0.10	0.10	0.10	0.10	0.10	0.10	bdl	0.10	bdl	0.10
Yb	1.80	2.10	0.90	0.30	0.80	0.50	1.30	0.40	0.90	1.00	0.70	0.70	0.80	0.90	1.00	0.80	0.90	1.00	0.60	0.80	0.70	0.90
Lu	0.20	0.20	0.10	bdl	0.10	bdl	0.20	bdl	0.10	0.10	bdl	0.10	bdl	0.10	0.10	0.10	0.10	0.10	bdl	0.10	bdl	0.10
Y	25.90	29.90	10.00	3.10	8.80	6.00	13.60	4.70	11.20	13.70	6.70	7.30	7.00	8.30	9.00	8.00	7.20	8.60	6.40	7.60	6.20	7.90
Th	bdl	bdl	0.70	bdl	bdl	bdl	0.60	0.60	0.90	0.30	0.20	bdl	0.20	0.20	0.20	bdl	0.20	0.20	bdl	bdl	dbl	0.20
U	bdl	bdl	bdl	bdl	bdl	bdl	bdl	bdl	bdl	bdl	bdl	bdl	bdl	bdl	bdl	bdl	bdl	bdl	bdl	bdl	bdl	bdl

Figure 3.6. Plot of MgO content versus major oxides and selected minor elements of komatiites from Selva and Seringa belts. See Table 3.1 for chemical analyses. Trendlines correspond to the linear correlation for samples of Selva belt (black dashed line) or Seringa belt (red dashed line). See text for further explanation.
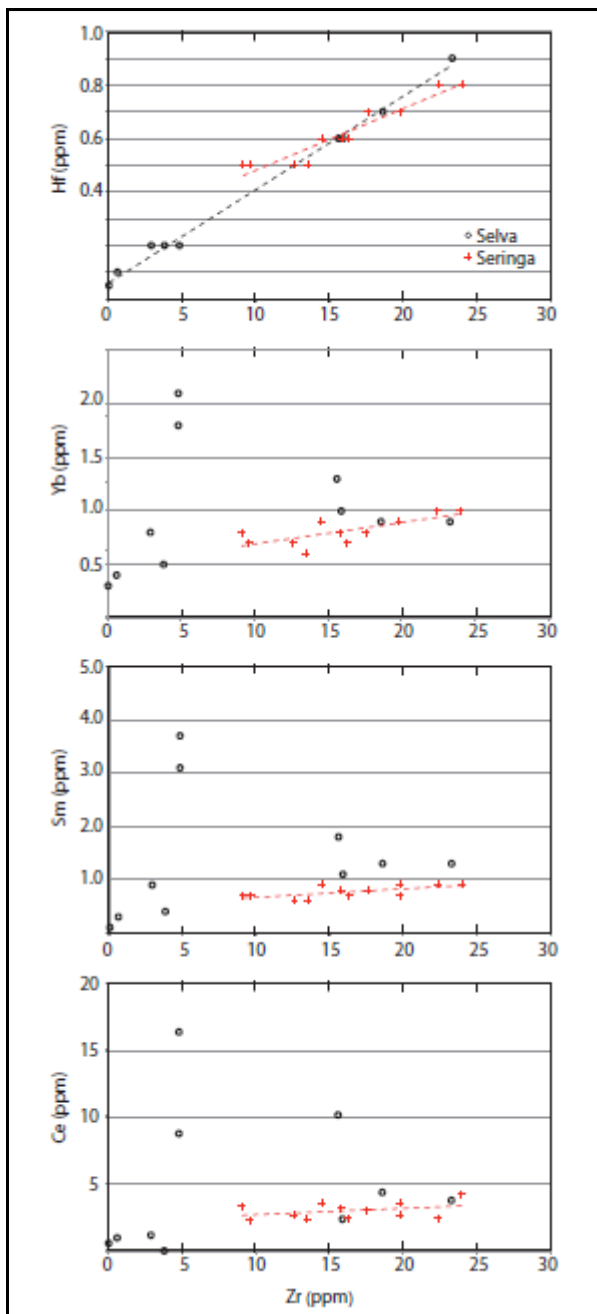
Figure 3.7. Plot of Zr content versus Hf, Ce, Sm and Yb of komatiites from Selva and Seringa belts. See Table 3.1 for chemical analyses. Trendlines correspond to the linear correlation for samples of Selva belt (black dashed line) or Seringa belt (red dashed line). See text for further explanation.
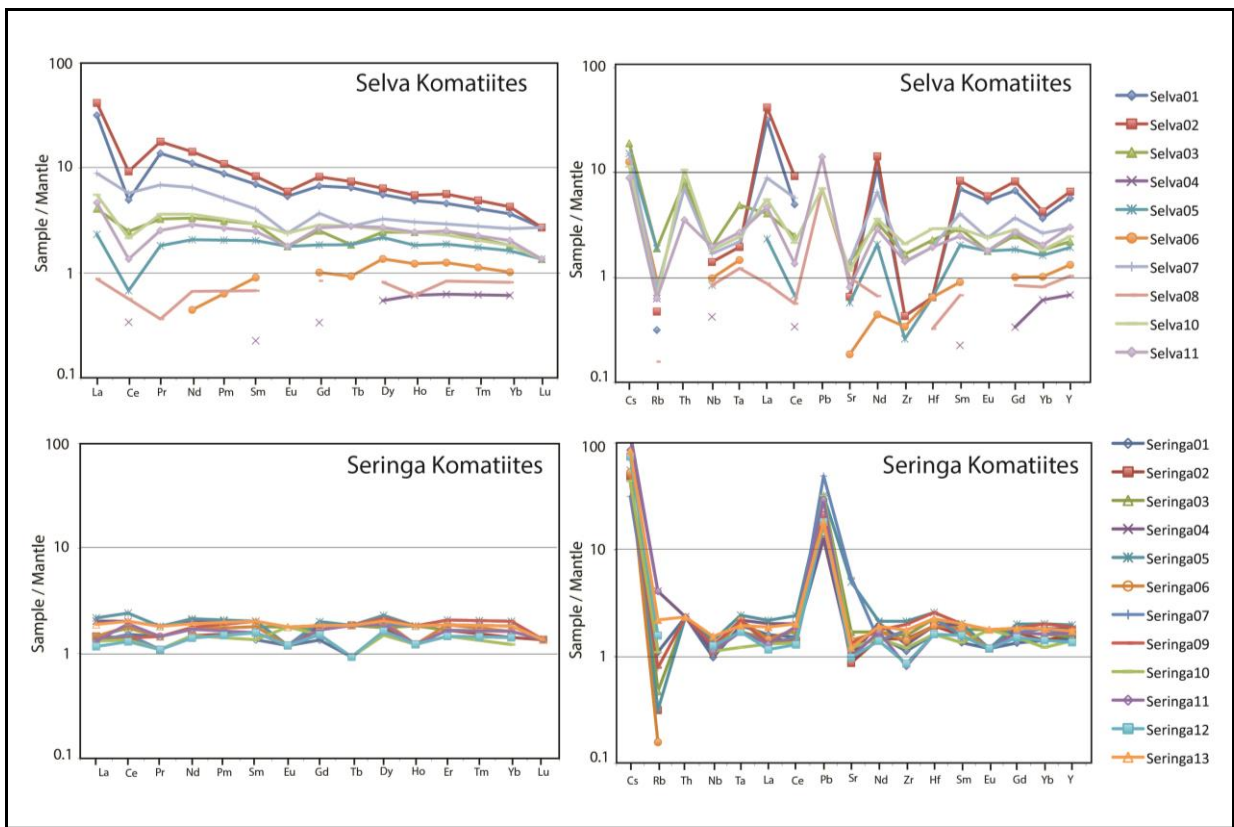
Figure 3.8. Mantle-normalized REE and trace elements patterns of komatiites from Selva and Seringa belts. See Table 3.1 for chemical analyses. Normalization data from Sun and McDonough (1989).

Discussion

The transition of the Carajás and Rio Maria domains

The identification of spinifex-textured komatiites close to the Carajás Basin suggests the continuation of the 3.0-2.9 Ga (Macambira and Lafon, 1995; Souza et al., 2001) greenstone belts of the Rio Maria Domain into the Transition Subdomain. This suggestion is supported by recent dating of metavolcanic rocks close to the IOCG type Sossego Cu-Au deposit at ca. 2.97 Ga (Moreto et al., 2015). These results suggest that at least some of the as yet poorly described volcanic-sedimentary sequences in the Transition Subdomain, many of them containing metabasalts with pillow lavas, may represent the northern continuation of the Rio Maria greenstone belts, and the Transition Subdomain may represent the border zone of the Carajás Basin. The geological processes associated with or characteristic of the Carajás Basin (e.g., Neoarchean mafic-ultramafic magmatism: Machado et al., 1991; Ferreira Filho et

134

al., 2007; hydrothermal alteration associated with IOCG type Cu-Au deposits: Xavier et al., 2012) would also affect this border zone and become progressively less significant toward the south.

The ages of the layered intrusions of the Carajás Mineral Province (2763 ± 6 Ma Luanga Complex: Machado et al., 1991; 2766 ± 6 Ma Serra da Onça Complex: Lafon et al., 2000) overlap with ages of bimodal volcanism in the Grão Pará Group (2759 ± 2 Ma: Machado et al., 1991; 2760 ± 11 Ma: Trendall et al., 1998), supporting the interpretation that mafic volcanics and mafic-ultramafic layered intrusions resulted from coeval major magmatic events in the Carajás region (Machado et al., 1991; Ferreira Filho et al., 2007). The distribution of layered intrusions in the Carajás Domain (Fig. 3.1) suggests that they are abundant close to the south border zone of the Carajás Basin (i.e., the Transition Subdomain) and become progressively less significant toward the Rio Maria Domain. Geological distinction between Neoarchean volcanic-sedimentary sequences from Mesoarchean greenstone belts is not so straightforward, as both volcanic-sedimentary sequences consist of abundant bimodal volcanism. This distinction is especially difficult within highly deformed zones and/or region with extensive lateritic cover and few outcrops, as commonly occurs in the Transition Subdomain. The identification of komatiites (this study) and Mesoarchean acid metavolcanic rocks (Moreto et al., 2015) are critical findings in the Transition Subdomain, providing references for separating these different sequences in the south border zone of the Carajás Basin.

Cu-Au mineralization and associated hydrothermal mineralization is a landmark geological feature of the Carajás Domain (Xavier et al., 2012). This feature includes several large deposits (e.g., Salobo, Sossego, Cristalino, Bahia) and widespread small deposits and occurrences associated with discrete zones of hydrothermal alteration. Regardless of genetic models or ages indicated by different authors for these Cu-Au deposits (generally accepted as IOCG-type) and occurrences (e.g., Tallarico et al., 2005; Grainger et al., 2008; Xavier et al., 2012; Moreto et al., 2015), their abundance close to the southern border zone of the Carajás Basin contrasts with their absence in the Rio Maria Domain. Because IOCG-type deposits are associated with extensive hydrothermal alteration, combined mapping of Cu-Au mineralization and associated hydrothermal alteration, should indicate how much further south of the Carajás Basin this mineralization process occur. In the following discussion we compare the geochemistry of the Selva komatiites, located close to the Carajás Basin, and the

Seringa komatiites, located in the Rio Maria Domain, indicating that some differences result from hydrothermal alteration, possibly associated with Cu-Au mineralization processes.

Contrasting geochemical features of the Selva and Seringa komatiites

Komatiites in different regions or even within different suites in the same region can have significant differences in compositions (e.g., Sproule et al., 2002; Arndt et al., 2008). Al_2O_3/TiO_2 and mantle normalized Gd/Yb ratios, involving two relatively immobile major elements, are particularly useful to illustrate different compositions of komatiites. Based on these ratios komatiites have been subdivided into a group of komatiites with higher Al_2O_3/TiO_2 and lower Gd/Yb_{MN} ratios (usually ~ 20 and ~ 1, respectively) referred to as Al-undepleted komatiites, and another with lower Al_2O_3/TiO_2 and higher Gd/Yb_{MN} ratios (usually 10-15 and 1.5-5, respectively) referred as Al-depleted komatiites (Sun and Nesbitt, 1978; Sproule et al., 2002; Arndt et al., 2008). Al-undepleted komatiites, typified by those in Munro Township in Canada (Sproule et al., 2002; Arndt et al., 2008), are more abundant in younger (2.7 Ga) terrains, whereas Al-depleted komatiites, typified by those in the Barberton greenstone belt, are more abundant in older terrains (ca 3.5 Ga) (see review by Arndt et al., 2008). Komatiites in the Selva and Seringa belts are Al-undepleted with Al_2O_3/TiO_2 ratios close to 20 (Fig. 3.9), and komatiites in the Seringa belt have Gd/Yb_{MN} ratios close to 1 (Fig. 3.10), both of which are characteristic of Al-undepleted komatiites (Arndt et al., 2008).

Komatiites in the Selva belt exhibit considerable scatter in Gd/Yb_{MN} ratios (Fig. 10), over a narrow range of MgO contents for spinifex-textured samples and Al_2O_3/TiO_2 ratios (~ 20) for both spinifex-textured and cumulate samples (Fig. 3.9 and 3.10). Variable HREE patterns are uncommon in komatiite samples collected in closely associated flows, so the more variable REE compositions of komatiites of Selva komatiites (Fig. 3.7 and 3.8) suggest that they were variably affected by hydrothermal and/or metamorphic alteration.

REE contents in specific Selva komatiite samples are very high (up to 40 times primitive mantle values; Fig. 3.8) and the REE patterns vary from flat (La/Yb_{PM} ~ 1) to highly enriched in LREE (La/Yb_{PM} up to ~ 10). Previous studies of komatiitic flows with variable REE contents and distribution patterns have attributed the variations to metasomatic alteration (e.g., Arndt et al., 1989; Tourpin et al., 1991; Gruau et al., 1992; Lahaye et al., 1995) or crustal assimilation (e.g., Lesher and Arndt, 1995; Perring et al., 1996; Lesher et al., 2001).

Distinguishing between these two processes is difficult and demands an evaluation of the composition of potential candidates for contaminant of the magma (i.e., crustal rocks) or alteration of the komatiitic rocks (i.e., hydrothermal fluids), which is not intended in this study. It is worth mentioning, however, that contamination with crustal rocks should increase both the LREE and Th contents. The assimilation of continental crust during the ascent and/or emplacement of the mafic-ultramafic magma of the Lago Grande Complex in Carajás is indicated, together with variably negative εNd (T=2.72 Ga) isotopes, by the relative enrichment in LREE and Th, with pronounced negative Nb and Ta anomalies in gabbroic rocks (Teixeira et al., 2015). The most LREE enriched samples in the Selva belt do not have positive Th anomalies, as well as Nb-Ta negative anomalies (Fig. 3.8), thus suggesting that crustal contamination is not the dominant process leading to LREE enrichment in komatiites. A connection of the hydrothermal alteration identified in samples of the Selva belt with the metasomatic event associated with Cu-Au deposits in Carajás is a possibility that should be considered. Cu-Au deposits and occurrences are abundant close to the south border of Carajás Basin (Xavier et al., 2012; Moreto et al., 2015). These deposits (see Cu and Cu-Au deposits in Fig. 3.1) are particularly abundant close the Selva belt and grouped in the southern copper belt of the Carajás Mineral Province, including several large (e.g., Sossego, 118, Cristalino) and medium-size (e.g., Bacaba, Castanha, Visconde, Bacuri) deposits (Moreto et al., 2015). Despite several differences among Cu-Au deposits in Carajás, most deposits are characterized by metasomatism leading to REE enrichment, which is especially significant for LREE (e.g., Tallarico et al., 2000; Grainger et al., 2008; Xavier et al., 2012). Pronounced LREE enrichment is in fact a distinctive characteristic of IOCG-type deposits worldwide (Groves et al., 2010). Because the REE concentration in komatiitic magmas is very low, the effect of Cu-Au metasomatic alteration in the distribution of REE in komatiitic rocks may be prominent even when distinctive mineralogical and/or major element alteration associated with Cu-Au deposits is not clearly indicated.

Geochemical features discussed in this section indicate that the composition of komatiitic rocks of the Selva belt partially result from metasomatic alteration. We also suggest that this alteration may be associated with processes associated with Cu-Au mineralization. This suggestion imply that contrasting compositional features of komatiitic rocks from the Seringa and the Selva belts are not primary magmatic features, and may result from processes that modified the primary content of usually immobile elements (including REE) in the latter.
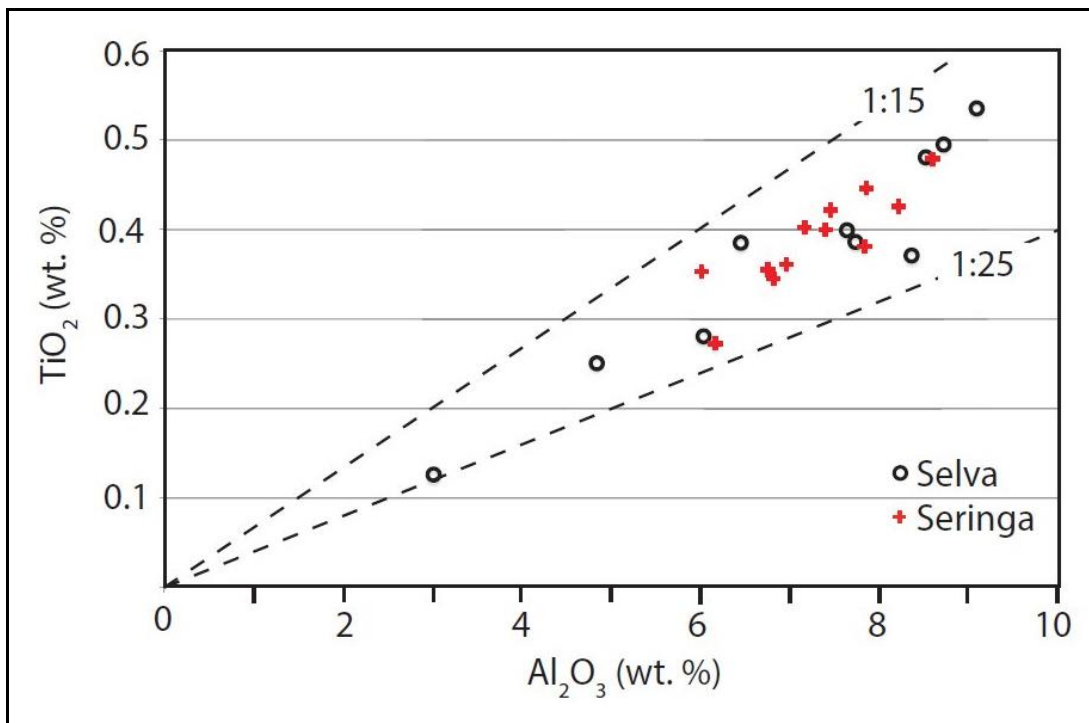
Figure 3.9. Plot of Al_2O_3 vs TiO_2 for komatiites of Selva and Seringa belts. Dashed lines indicate Al_2O_3/TiO_2 ratios. See Table 3.1 for chemical analyses.
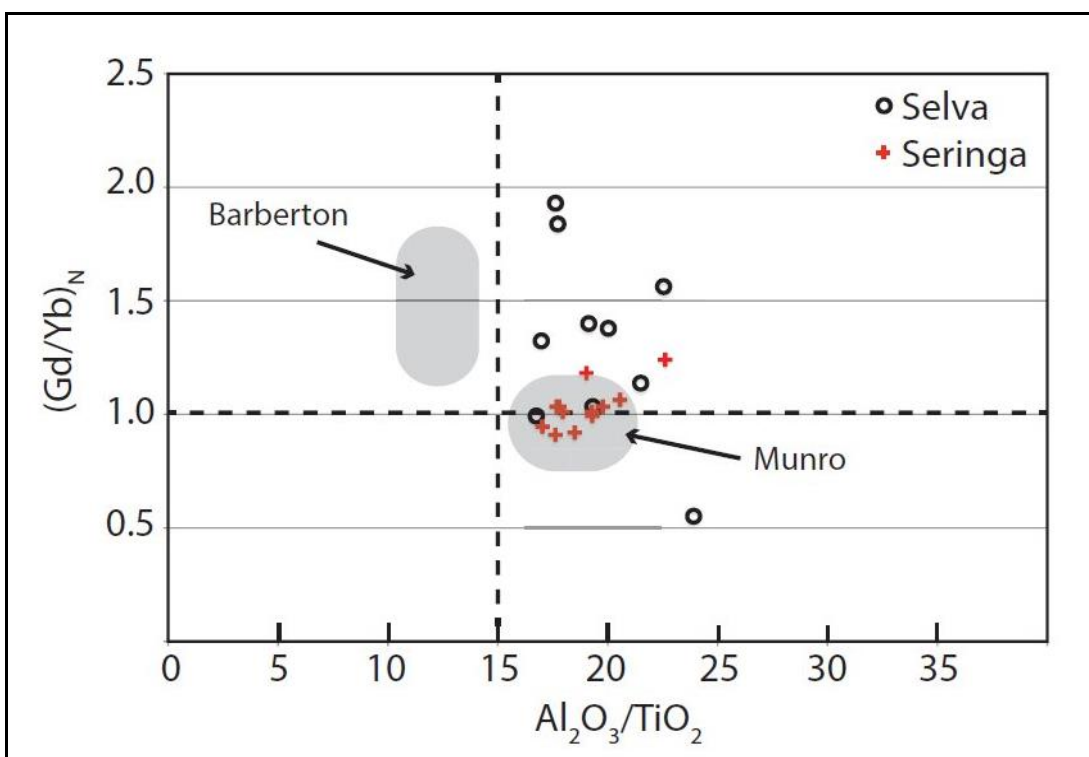
Figure 3.10. Plot of Al_2O_3/TiO_2 vs $(Gd/Yb)_N$ for komatiites of Selva and Seringa belts. The subscript "N" indicates normalization to primitive mantle values of Sun and McDonough (1989). Indicated fields for typical Barberton (UDK) and Munro (AUDK) komatiites are based on Arndt et al. (2008). See text for further explanation and Table 3.1 for chemical analyses.

Implication for mineral exploration

The Carajás and Rio Maria domains have different types of mineral deposits. Whereas the Rio Maria Domain contains typical orogenic gold deposits associated with Mesoarchean greenstone belts (Villas and Santos, 2001), the Carajás Domain has a diversity of mineral deposits, including world-class iron ore, IOCG-type Cu-Au and hydrothermal gold deposits, interpreted to result from a complex Neoarchean to Proterozoic geological evolution (Grainger et al., 2008). The identification of spinifex-textured komatiites in the Transition Subdomain of the Carajás Province indicates that this region has potential to host deposits characteristic from both domains. Apart from this broad regional metallogenetic implication, geological and geochemical features described in komatiites of the Selva greenstone belt provide two implications for exploration of Ni-Cu-PGE deposits associated with mafic-ultramafic bodies within the Transition Subdomain.

The first implication is relevant to the exploration for komatiite-associated Ni-Cu-PGE deposits. It is now well established that a sound understanding of physical volcanology and lithogeochemistry is critical for an effective exploration for Ni-Cu-PGE deposits in greenstone belts (see reviews by Lesher, 1989; Lesher and Keays, 2002; Barnes, 2006; Arndt et al., 2008). Our study indicates that tectonism and hydrothermal alteration in the Selva greenstone create a difficult setting for lithogeochemical exploration, as magmatic structures and compositions were partially to extensively obliterated. It is worth mentioning however that tectonism and alteration are highly heterogeneous within the Transition Subdomain, such that greenstone belts and komatiites with pristine magmatic features may yet be discovered. An example of nicely preserved magmatic structure within the Transition Subdomain is provided by the Vermelho layered complex, located just 10 km to the south of the Selva greenstone belt. Detailed study of the Naoarchean Vermelho Complex indicates a subhorizontal layered intrusion with preserved magmatic textures and minerals (Siepierski et al., in prep.).

The second implication is relevant to the criteria for distinguishing between poorly exposed Neoarchean tholeiitic ultramafic intrusions and komatiitic bodies within the Transition Subdomain in Carajás. Although tholeiitic intrusions and komatiites are favorable targets for Ni-Cu-PGE deposits, their selection and priority within a regional exploration program follow different guidelines. Spinifex textures that provide unequivocal evidence for komatiites are not always present or preserved within extensively weathered and/or deformed

metamorphic terrains, as expected for the Transition Subdomain. Therefore, discrimination of komatiites from tholeiitic ultramafic intrusions based on preserved volcanic textures is likely to be an exception in the Transition Subdomain. Lithogeochemical characterization of komatiites is frequently based upon compositional features used to distinguish komatiites from other types of high-Mg lavas (e.g., Al_2O_3, TiO_2, Na_2O, K_2O). Considering that compositions of komatiites are broadly compared to tholeiitic basalts with a variable but usually high proportion of olivine with high magnesium content, distinguishing komatiitic rocks from olivine cumulates crystallized from tholeiitic magmas may not be straightforward during preliminary phases of an exploration program. It is also no surprise that peridotites have compositions that plot within the ultramafic komatiitic field of geochemical diagrams used to classify volcanic rocks (e.g., Jensen, 1976; Le Bas, 2000). We conclude this discussion with the obvious, but frequently forgotten statement that effective use of geochemical results in exploration demands a sound geological understanding of the rocks.

Conclusions

The principal conclusions of this study are as follows:

a) This paper provides the first description of spinifex-textured komatiites in the Transition Subdomain of the Carajás Mineral Province.

b) Spinifex-textured komatiites occur in the Selva greenstone belt located few kilometers from the south border of the Carajás Basin.

c) Komatiitic rocks of the Selva belt are part of a sequence of thin flows consisting of a spinifex-textured upper layer and an olivine cumulate lower layer. Although the spinifex texture is well preserved in the field, the primary mineralogy of the komatiites is completely replaced by greenschist facies metamorphic minerals.

d) Spinifex-textured komatiites from the Selva greenstone belt have MgO contents bracket between 22.8 and 26.9 wt.%, with higher MgO contents (up to 40.6 wt. %) in cumulate textured komatiites. When plotted vs MgO contents, most major and minor elements for komatiites of the Selva belt fall on well-defined linear trends indicating control by olivine fractionation or accumulation. Komatiites from the Selva and Seringa (located in the Rio Maria Domain) belts are Al-undepleted with Al_2O_3/TiO_2 ratios close to 20.

e) Chemical compositions of komatiites of the Selva greenstone belt indicate that they were variably affected by hydrothermal and/or metamorphic alteration. Results for CaO, Na_2O and REE suggest that these elements were mobile and their contents partially result from metasomatic alteration. REE contents in specific komatiite samples of the Selva belt are very high (up to 40 times primitive mantle values), and REE patterns vary from flat (La/Yb$_{PM}$ ~ 1) to highly enriched in LREE (La/Yb$_{PM}$ up to ~ 10). The most LREE enriched samples in the Selva belt do not have positive Th anomalies, as well as Nb-Ta negative anomalies, thus suggesting that crustal contamination is not the dominant process leading to LREE enrichment in komatiites. These unusual compositional features led to the suggestion that hydrothermal alteration of komatiites from the Selva belt may be associated with processes related to Cu-Au mineralization in the region.

f) The identification of spinifex-textured komatiites close to the Carajás Basin suggests the continuation of the 3.0-2.9 Ga greenstone belts of the Rio Maria Domain within the Transition Subdomain. This also suggests that the Transition Subdomain has potential to host komatiite-associated Ni-Cu-PGE deposits.

g) Our results suggest that exploration for komatiite-associated Ni-Cu-PGE deposits in the Transition Subdomain may be hampered by poorly preserved primary magmatic and compositional features in komatiites.

Acknowledgments

References

Araújo, O.J.B., Maia, R.G.N., João, X.S.J., Costa, J.B.S., 1988. A megaestruturação arqueana da Folha Serra dos Carajás. In: Congresso Latino Americano de Geologia, Anais, Belém-Brasil 1, 324-338.

Araújo, O.J.B. de, Maia R.G.N., 1991. Programa Levantamentos Geológicos Básicos do Brasil. Serra de Carajás. Folha SB.22- Z-A. Estado do Pará. Brasília, DNPM-CPRM, 136 pp.

Arndt, N.T., Brooks, C., 1980. Komatiites: Penrose conference report. Geology 8, 155-156.

Arndt, N.T., Lesher, C.M., 1992. Fractionation of REE by olivine and the origin of Kambalda komatiites, Western Australia. Geochimica et Cosmochimica Acta 56, 4191-4204.

Arndt, N.T., Lesher, C.M., Barnes, S.J., 2008. Komatiite. Cambridge, UK: Cambridge University Press, 467 pp.

Arndt, N.T., Teixeira, N.A., White, W.M., 1989. Bizarre geochemistry of komatiites from the Crixás greenstone belt, Brazil. Contributions to Mineralogy and Petrology, 101, 187–197.

Avelar, V.G., Lafon, J.M., Correia JR., F.C., Macambira, E.M.B., 1999. O magmatismo arqueano da região de Tucumã-Provínica Mineral de Carajás: Novos dados geocronológicos. Revista Brasileira de Geociências 29, 453-460.

Barnes, S.J., 2006. Komatiite-hosted nickel sulfide deposits: geology, geochemistry, and genesis. Society of Economic Geologists Special Publication, 13, 51-118.

Barnes, S.J., Roeder, P.L., 2001. The range of spinel compositions in terrestrial mafic and ultramafic rocks. Journal of Petrology, 42, 2279–2302.

Barros, C.E.M., Sardinha, A.S., Barbosa, J.P.O., Krimski, R., Macambira, M.J.B., 2001. Pb-Pb and U-Pb zircon ages of Archean syntectonic granites of the Carajás metallogenic province, northern Brazil. In: Proceedings of the South American Symposium on Isotopic Geology 3, 94-97.

Brenner, T.L., Teixeira, N.A., Olivera, J.A.L., Franke, N.O., Thompson, J.F.H., 1990. The O'Toole nickel deposit, Morro do Ferro greenstone belt, Brazil. Economic Geology, 85, 904-920.

Brooks, C., Hart, S.R., 1974. On the significance of komatiite. Geology, 2, 107-110.

Costa, C.N., Ferreira-Filho, C.F., Osborne, G.A., Araujo, S.M., Lopes, R.O., 1997. Geology and geochemistry of the Boa Vista Nickel Sulfide Deposit, Crixas Greenstone Belt, Central Brazil. Revista Brasileira de Geociencias, 27, 365-376.

CVRD-Companhia Vale do Rio Doce S.A., 2005. Relatório de mapeamento geológico do Alvo Selva. Relatório Interno-CVRD, Carajás-PA (unpublished), 10 pp.

Dall'Agnol, R., Souza, Z.S., Althoff, F.J., Barros, C.E.M., Leite, A.A.S., João, X.S.J., 1997. General aspects of the granitogenesis of the Carajás metallogenetic province. In: Proceedings of the International Symposium on Granites and Associated Mineralizations, Salvador, Excursion Guide, 135-161.

Dall'Agnol, R., Teixeira, N.P., Rämö, O.T., Moura, C.A.V., Macambira, M.J.B., Oliveira, D.C., 2005. Petrogenesis of the Paleoproterozoic, rapakivi, A-type granites of the Archean Carajás Metallogenic Province, Brazil. Lithos 80, 101-129.

Dall'Agnol, R., Oliveira, M.A., Almeida, J.A.C., Althoff, F.J., Leite, A.A.S., Oliveira D.C., Barros C.E.M., 2006. Archean and Paleoproterozoic granitoids of the Carajás metallogenetic province, eastern Amazonian craton. In: Dall'Agnol R., Rosa-Costa L.T., Klein E.L. (Eds.) Symposium on Magmatism, Crustal Evolution, and Metallogenesis of the Amazonian Craton, Abstracts Volume and Field Trips Guide. Belém, PRONEXUFPA/SBG-NO, 150 pp.

Dias, G.S., Macambira, M.J.B., Dall'Agnol, R., Soares, A.D.V., Barros, C.E.M., 1996. Datação de zircões de Sill de metagabro: Comprovação da idade arqueana da Formação Águas Claras, Carajás, Pará. In: Simpósio de Geologia da Amazônia 5, Belém, Sociedade Brasileira de Geologia, Extended Abstracts, 376-379.

Docegeo-Rio Doce Geologia e Mineração, 1988. Revisão Litoestratigráfica da Província Mineral de Carajás. In: Provincia Mineral de Carajás, Litoestratigrafia e principais depósitos minerais. CVRD/SBG, Congresso Brasileiro de Geologia (Belém), *Anexo aos anais*, 35, 11-59.

Faraco, M.T.L., Vale, A.G., Santos, J.O.S., Luzardo, R., Ferreira, A.L., Oliveira, M.A., Marinho, P.A.C., 2005. Levantamento Geológico da Região ao Norte da Província Carajás In: Souza, V. and Horbe, A.C. (Eds.). Contribuições a Geologia da Amazônia 4, 32-44.

Feio, G.R.L., Dall'Agnol, R., 2012. Geochemistry and petrogenesis of the Mesoarchean granites from the Canaã dos Carajás area, Carajás Province, Brazil: Implications for the origin of Archean granites. Lithos 154, 33-52.

Feio, G.R.L., Dall'Agnol, R., Dantas, E.L., Macambira, M.J.B., Santos, J.O.S., Althoff, F.J., Soares, J.E.B., 2013. Archean granitoid magmatism in the Canaã dos Carajás area: Implications for crustal evolution of the Carajás province, Amazonian craton, Brazil. Precambrian Research 227, 157-185.

Ferreira Filho, C.F., Cançado, F., Correa, C., Macambira, E.M.B., Siepierski, L., Brod, T.C.J., 2007. Mineralizações estratiformes de EGP-Ni associadas a complexos acamadados em Carajás: os exemplos de Luanga e Serra da Onça. In: Contribuições à Geologia da Amazônia, Sociedade Brasileira de Geologia - Núcleo Norte, 5, 01-14.

Figueiredo e Silva, R.C., Lobato, L.M., Rosière, C.A., Zucchetti, M., Hagemann, S.H., Baars, F.J., Morais, R., Andrade, I., 2008. A hydrothermal origin for the jaspilite-hosted, giant iron ore of the Serra Norte deposits in the Carajás Province, Pará State, Brazil. In: Hagemann, S.G., Rosière, C.A., Gutzmer, J., and Beukes, N.J., (Eds.), BIF-related high-grade iron mineralization. Reviews in Economic Geology 15, 255-290.

Grainger, C.J., Groves, D.I., Tallarico, F.H.B., Fletcher, I.R., 2008. Metallogenesis of the Carajás Mineral Province, Southern Amazon Craton, Brazil: varying styles of Archean through Paleoproterozoic to Neoproterozoic base- and precious-metal mineralisation. Ore Geology Reviews 33, 451-489.

Groves, D.I., Bierlein, F.P., Meinert, L.D., Hitzman, M.W., 2010. Iron oxide- copper-gold (IOCG) deposits through Earth history: Implications for origin, lithospheric setting, and distinction from other epigenetic iron oxide deposits. Economic Geology 105, 641-654.

Gruau, G., Tourpin, S., Fourcade, S., Blais, S., 1992. Loss of isotopic (Nd, O) and chemical (REE) memory during metamorphism of komatiites: new evidence from eastern Finland. Contributions to Mineralogy and Petrology 112, 66-82.

Holdsworth, R.E., Pinheiro, R.V.L., 2000. The anatomy of shallow-crustal transpressional structures: insights from the Archean Carajás fault zone, Amazon, Brazil. Journal Structural Geology 22, 1105-1123.

Huhn, S.R.B., Santos, A.B.S., Amaral, A.F., Ledsham, E.J., Gouveia, J.L., Martins, L.P.B., Montalvão, R.M.G., Costa, V.C., 1986. O terreno granito-greenstone da região de Rio Maria-Sul do Pará. In: Congresso Brasileiro de Geologia, 35, Anais, Sociedade Brasileira de Geologia 3, 1438-1452.

Huhn, S.R.B., Macambira, M.J.B., Dall'Agnol, R., 1999. Geologia e Geocronologia Pb/Pb do Granito Alcalino Arqueano Planalto, Região da Serra do Rabo, Carajás-PA. In: Simpósio de Geologia da Amazônia, 6. Manaus, Anais, Sociedade Brasileira de Geologia - Núcleo Norte, 1, 463-466.

Jensen, L.S., 1976. A new cation plot for classifying subalkalic volcanic rocks. Ontario. Ontario Division of Mines, MP 66, 22 pp.

Kerr, A.C., Arndt, N.T., 2001. A note on the IUGS reclassification of the high-Mg and picritic volcanic rocks. Journal of Petrology 42, 2169-2171.

Lafon, J.M., Macambira, M.J.B., Pidgeon R.T., 2000. Zircon U-Pb SHRIMP dating of Neoarchean magmatism in the southwestern part of the Carajás Province (eastern Amazonian Craton, Brazil). In: 31th International Geological Congress, Rio de Janeiro, Brazil, Extended Abstracts, CD-ROM.

Lahaye, Y., Arndt, N.T., Byerly, G., Gruau, G., Fourcade, S., Chauvel, C., 1995. The influence of alteration on the trace-element and Nd isotope compositions of komatiites. Chemical Geology 126, 43-64.

Le Bas, M. J., 2000. IUGS reclassification of the high-Mg and picritic volcanic rocks. Journal of Petrology, 41, 1467-1470.

Lesher, C.M., 1989. Komatiite-associated nickel sulfide deposits. In: J. A. Whitney and A.J. Naldrett (Eds.) Ore Deposition Associated with Magmas. pp. 45–102. Dordrecht: Society of Economic Geologists.

Lesher, C.M., Arnt, N.T., 1995. REE and Nd geochemistry, petrogenesis and volcanic evolution of contaminated komatiites at Kambalda, Western Australia. Lithos 34, 127-157.

Lesher, C.M., Burnham, O.M., Keays, R.R., Barnes, S.J., Hulbert L., 2001. Geochemical discrimination of barren and mineralized komatiites associated with magmatic Ni-Cu-(PGE) sulphide deposits. Canadian Mineralogist 39, 673-696.

Lesher, C.M., Keays, R.R., 2002. Komatiite-associated Ni-Cu-(PGE) deposits: Mineralogy, geochemistry, and genesis. In: L. J. Cabri (ed.) The Geology Geochemistry, Mineralogy, and Mineral Beneficiation of the Platinum-Group Elements, pp. 579-617, Special Volume 54. Montreal: Canadian Institute of Mining, Metallurgy and Petroleum.

Lesher, C.M., Stone W.E., 1996. Exploration geochemistry of komatiites. In: D. A. Wyman (ed.) Igneous Trace Element Geochemistry Applications for Massive Sulphide Exploration, pp. 153-204, Geological Association of Canada Short Course Notes 12. Ottawa: Geological Association of Canada.

Lobato, L.M., Figueiredo e Silva, R.C., Rosière, C.A., Zucchetti, M., Baars, F.J., Seoane, J.C.S., Rios, F.J., Monteiro, A.M., 2005a. Hydrothermal origin for the iron mineralisation, Carajás Province, Pará State, Brazil. In: Proceedings Iron Ore 2005. The Australian Institute of Mining and Metallurgy, Publication Series no 8, 99-110.

Lobato, L.M., Rosière, C.A., Figueiredo e Silva, R.C., Zucchetti, M., Baars, F.J., Seoane, J.C.S., Rios, F.J., Pimentel, M.M., Mendes, G., Monteiro, A.M., 2005b. A mineralização hidrotermal de ferro da Província Mineral de Carajás, controle estrutural e contexto na evolução metalogenética da província. In: Marini, O.J., Queiroz, E.T., Ramos (Eds.), Caracterização de depósitos minerais em distritos mineiros da Amazônia, Brasília, DNPM/FINEP/ADIMB, 1, 21-92.

Macambira, M.J.B., Lafon, J.M., 1995. Geocronologia da Província Mineral de Carajás: síntese dos dados e novos desafios. Boletim Museu Paraense Emílio Goeldi (Série Ciências da Terra) 7, 263-288.

Macambira, M.J.B., Lancelot, J.R., 1996. Time constraints for the formation of the Archean Rio Maria crust, Southeastern Amazonian Craton, Brazil: International Geology Review 38, 1134-1142.

Machado, N., Lindenmayer, Z.G., Krogh, T.E., Lindenmayer, D., 1991. U-Pb geochronology of Archean magmatism and basement reactivation in the Carajás área, Amazon shield, Brazil. Precambrian Research 49, 329-354.

Moreto, C.P.N., Monteiro, L.V.S., Xavier, R.P., Creaser, R.A., DuFrane, S.A., Tassinari, C.C.G., Sato, K., Kemp, A.I.S., Amaral, W.S., 2015. Neoarchean and Paleoproterozoic Iron Oxide-Copper-Gold Events at the Sossego Deposit, Carajás Province, Brazil: Re-Os and U-Pb Geochronological Evidence. Economic Geology 110, 809-835.

Nogueira, A.C.R., Truckenbrod, W., Costa, J.B.S., Pinheiro, R.V.L., 1994. Análise faciológica e estrutural da Formação Águas Claras, Pré-Cambriano da Serra dos Carajás. In: Simpósio de Geologia da Amazônia, 4, Belém, Sociedade Brasileira de Geologia, Resumos Expandidos, 363-364.

Nogueira, A.C.R., Truckenbrod, W., Pinheiro, R.V.L., 2000. Storm and tide-dominated siliciclastic deposits of the Archean Águas Claras Formation, Serra dos Carajás, Brazil. In: 31th International Geological Congress, Rio de Janeiro, Brazil, Extended Abstracts, CD-ROM.

Perring, C.S., Barnes, Stephen J., Hill, R.E.T., 1996. Geochemistry of Archaean komatiites from the Forrestania Greenstone Belt, Western Australia: evidence for supracrustal contamination. Lithos 37, 181-197.

Pidgeon, R.T., Macambira, M.J.B., Lafon, J.M., 2000. Th-U-Pb isotopic systems and internal structures of complex zircons from an enderbite from the Pium Complex, Carajás Province, Brazil: evidence for the ages of granulite facies metamorphism and the protolith of the enderbite. Chemical Geology 166, 159-171.

Pinheiro, R.V.L., Holdsworth, R.E., 1997. Reactivation of Archaean strike-slip fault systems, Amazon region, Brazil. Journal of the Geological Society 154, 99-103.

Pyke, D.R., Naldrett, A.J., Eckstrand, O.R., 1973. Archean ultramafic flows in Munro Township, Ontario. Geol. Soc. Amer. Bull., 84, 955-978.

Saboia, L.A., Teixeira, N.A., 1983. Ultramafic flows of the Crixas greenstone belt, Goias, Brazil. Precambrian Research 22, 23-40.

Santos, J.O.S., Groves, D.I., Hartmann, L.A., Moura, M.A., Mc-Naughton, N.J., 2001. Gold deposits of the Tapajós and Alta Floresta domains, Tapajós-Parima orogenic belt, Amazon craton, Brazil. Mineralium Deposita 36, 278-299.

Sardinha, A.S., Dall'Agnol, R., Gomes, A.C.B., Macambira, M.J.B., Galarza, M.A., 2004. Geocronologia Pb-Pb e U-Pb em zircão de granitóides arqueanos da região de Canaã dos Carajás, Província Mineral de Carajás. Congresso Brasileiro de Geologia, 42. CD-ROM.

Sardinha, A.S., Barros, C.E.M., Krymsky, R., 2006. Geology, geochemistry, and U-Pb geochronology of the Archean (2.74Ga) Serra do Rabo granite stocks, Carajás Province, northern Brazil. Journal of South American Earth Sciences 20, 327-339.

Siepierski, L., Ferreira Filho, C.F., in prep. Stratigraphy and petrology of the Vermelho Complex, Carajás Province, Brazil: evidence for magmatic processes at the lower contact zone of a layered mafic-ultramafic intrusion.

Soares, A.D.V., Santos, A.B., Vieira, E.A., Bella, V.M., Martins, L.P.B., 1994. Área Águas Claras: Contexto geológico e mineralizações. In: Simpósio de Geologia da Amazônia, 4, Belém, Anais, Sociedade Brasileira de Geologia, 379-382.

Souza, Z.S., Dall'Agnol, R., 1996. Caracterização geoquímica e tectônica de rochas meta vulcânicas de "greenstone belts" arqueanos da região de Rio Maria, SE do Pará. Bol. IG-USP, Publ. espec. [online] 18, 97-101. ISSN 0102-6275.

Souza, Z.S., Potrel, A., Lafon, J.M., Althoff, F.J., Pimentel, M.M., Dall'Agnol, R., Oliveira, C.G., 2001. Nd, Pb and Sr isotopes in the Identidade Belt, an Archean greenstone belt of Rio Maria region (Carajás Province, Brazil): implications for the geodynamic evolution of the Amazonian Craton. Precambrian Research, 109, 293-315.

Souza, S.R.B., Macambira, M.J.B., Sheller, T., 1996. Novos dados geocronológicos para os granitos deformados do Rio Itacaiúnas (Serra dos Carajás, PA), implicações estratigráficas. In: Simpósio de Geologia da Amazônia, 5, Belém, Anais, Sociedade Brasileira de Geologia, 380-383.

Sproule, R.A., Lesher, C.M., Ayer, J.A., Thurston, P.C., 2002. Secular variations in the geochemistry of komatiitic rocks from the Abitibi Greenstone Belt, Canada. Precambrian Research 115, 153-186.

Sun, S.S., Nesbitt, R.W., 1978. Petrogenesis of Archean ultrabasic and basic volcanics: evidence from rare earth elements. Contributions to Mineralogy and Petrology 65, 301-325.

Sun, S.S., McDonough W.F., 1989. Chemical and isotopic systematics of oceanic basalts: Implications for mantle composition and processes. In: Saunders, A.D., Norry, M.J. (Eds.), Magmatism in Oceanic Basins, Geol. Soc. London Spec. Pub. 42, p. 313-345.

Tallarico, F.H.B., Oliveira, C.G., Figueiredo, B.R., 2000. The Igarapé Bahia Cu-Au mineralization, Carajás Province: Revista Brasileira de Geociências 30, 230-233.

Tallarico, F.H.B., Figueiredo, B.R., Groves, D.I., Kositcin, N., McNaughton, J., Fletcher, I.R., Rego, J.L., 2005. Geology and SHRIMP U-Pb geochronology of the Igarapé Bahia deposit, Carajás copper-gold belt, Brazil: An Archean (2.57 Ga) example of iron-oxide Cu-Au mineralization. Economic Geology 100, 7-28.

Teixeira, A.S., Ferreira Filho, C.F., Della Giustina, M.E.S., Araujo, S.M., Silva, H.H.A.B., 2015. Geology, petrology and geochronology of the Lago Grande layered complex: Evidence for a

PGE-mineralized magmatic suite in the Carajas Mineral Province, Brazil. Journal of South American Earth Sciences 64, 116-138.

Tourpin, S., Gruau, G., Blais, S., Fourcade, S., 1991. Resetting of REE and Nd and Sr isotopes during carbonatization of a komatiite flow from Finland. Chemical Geology 90, 15-29.

Trendall, A.F., Basei, M.A.S., De Laeter, J.R., Nelson, D.R., 1998. SHRIMP zircon U-Pb constraints on the age of the Carajás Formation, Grão Pará Group, Amazon Craton. Journal of South American Earth Sciences 11, 265-277.

Vasquez, M.L., Rosa-Costa, L.T., Silva, C.G., Ricci, P.F., Barbosa, J.O., Klein, E.L., Lopes, E.S., Macambira, E.B., Chaves, C.L., Carvalho, J.M., Oliveira, J.G., Anjos, G.C., Silva, H.R., 2008. Geologia e Recursos Minerais do Estado do Pará. In: Vasquez, M.L and Rosa-Costa, L.T., (Eds.), Texto Explicativo dos Mapas Geológico e Tectônico e de Recursos Minerais do Estado do Pará: Sistema de Informações Geográficas-SIG, Escala 1:1.000.000, Belém, CPRM, 329 p.

Villas, R.N., Santos, M.D., 2001. Gold deposits of the Carajás mineral province: Deposit types and metallogenesis: Mineralium Deposita 36, 300-331.

Xavier, R.P., Monteiro, L.V.S., Moreto, C.P.N., Pestilho, A.L.S., Melo, G.H.C., Silva, M.A.D., Aires, B., Ribeiro, C., Silva, F.H.F., 2012. The iron oxide copper-gold systems of the Carajás mineral province, Brazil. Society of Economic Geologists, Special Publication 16, 433-454.

CONCLUSÕES

Conclusões Capítulo 1: *Stratigraphy and petrology of the Vermelho Complex, Carajás Province, Brazil: evidence for magmatic processes at the lower contact zone of a layered mafic-ultramafic intrusion*

As principais conclusões referentes ao estudo realizado no Complexo do Vermelho são abaixo elencadas:

a) O Complexo Acamadado do Vermelho corresponde a uma intrusão máfico-ultramáfica localizada a cerca de 10 km ao sul da Serra de Carajás. Apresenta 9,5 km de comprimento por 1,5 km de largura média, e alinhamento segundo a direção NE-SW. Grande parte deste complexo encontra-se erodido, porém destacam-se dois *plateus* conhecidos como V1 (porção NE) e V2 (porção SW), sustentados por rochas ultramáficas lateritizadas que correspondem aos depósitos de Ni laterítico do Vermelho.

b) Os estudos realizados demonstram que o Complexo do Vermelho corresponde a uma câmara magmática sem evidências de deformação e/ou metamorfismo, encaixada em rochas gnáissicas do Complexo Xingú (>2,85 Ga) e granitóides indiferenciados.

c) A arquitetura da intrusão do Complexo do Vermelho abrange um conjunto de rochas máfico-ultramáficas acamadadas com sequência complexa, porém, no geral sub-horizontalizada que foram subdivias em duas unidades estratigráficas distintas: Zona Inferior (LZ) e Zona Superior (UZ).

d) A Zona Inferior (LZ) é caracterizada por apresentar evolução petrológica normal com a seguinte sequência de fracionamento: Ol+Chr $\rightarrow$ Opx+Chr $\rightarrow$ Opx $\rightarrow$ Opx+Pl $\rightarrow$ Opx+Pl+Cpx, com dunitos e harzburgitos primitivos na base (olivina mais primitiva apresentando composição de $Fo_{90,5}$) até gabronoritos e gabros altamente fracionados, com quartzo acessório, na porção superior (ortopiroxênio mais fracionado exibindo $En_{57,5}$). Dados de sondagem nesta Zona demonstram uma espessura de pelo menos 400 m abaixo do plateau V1 e progressivamente mais rasa em direção ao extremo SW da intrusão, indicando que a

estrutura do conduto possa estar situada abaixo do V1. A sequência basal da LZ, junto ao contato com as encaixantes, consiste em dunitos, harzburgitos e ortopiroxenitos interacamadados, possivelmente resultantes das sucessivas injeções de magma primitivo. Nesta sequência basal, o mineral de composição mais primitiva encontra-se localizado a dezenas de metros do contato com as encaixantes, possivelmente devido ao fracionamento do magma parental durante os estágios iniciais do preenchimento da câmara. Apesar disso, as evidências do desenvolvimento de um completo fracionamento reverso não foram claramente indicadas pela sequência de fases cumulus ou trends de fracionamento das sequências de rochas localizadas junto ao contato inferior do Complexo do Vermelho com as encaixantes.

e) A Zona Superior (UZ) ocorre como duas camadas sub-horizontalizadas, totalizando cerca de 175 m de espessura, preservadas da erosão e que compõem os *plateus* V1 e V2. É definida a partir de uma notável interrupção na sequência de fracionamento e na composição mineral da porção superior da LZ, é caracterizada por sequência de fracionamento distinta (Opx+Chr $\rightarrow$ Ol+Chr) iniciada a partir da base com ortopiroxenitos contendo *pods* centimétricos de cromititos, passando a dunitos e harzburgitos intemperizados no topo. Aspectos composicionais do ortopiroxenito da base da UZ são comparáveis àqueles observados na porção inferior da LZ, indicando similaridade entre os magmas e sugerindo que a camada de ortopiroxenito da UZ (ortopiroxênio primitivo apresentando composição de $En_{85,7}$) foi formada a partir da mistura de um novo e volumoso influxo de magma primitivo com um volume reduzido de magma altamente fracionado e rico em sílica residente na câmara magmática, o que seria corroborado pela presença de cromititos resultante da saturação de cromita induzida pela mistura de magmas distintos, conforme modelo proposto para a origem de cromititos em diversas intrusões acamadadas.

f) Os diagramas de correlação do conteúdo de MgO versus demais elementos demonstra que a maioria dos elementos maiores e traços apresentam correlação linear bem definida para as amostras da LZ. O ortopiroxenito primitivo da UZ demonstra significativa diferença com relação aos *trends* de correlação da LZ, como também observado claramente pelos gráficos do percentual de En x Cr_2O_3 wt.% e En x TiO_2 wt.%.

g) O comportamento dos ETR para a LZ indica um enriquecimento progressivo em direção ao topo, porém, significativamente mais acentuado para as ETRL em relação aos ETRP. O ortopiroxenito da UZ, quando comparado com os ortopiroxenitos da LZ, apresenta padrão de

ETR marcadamente distinto com valores mais próximos aos do chondrito, o que indica o caráter mais primitivo para o piroxenito da UZ.

h) Tanto a estratigrafia da câmara magmática, como as características petrológicas e químicas, comprovam que dois principais eventos de injeção de magma foram responsáveis pela evolução do Complexo Acamadado do Vermelho, o primeiro associado à formação da LZ e um segundo evento posterior relacionado à formação da UZ.

i) Apresenta assimilação crustal consistente com a cristalização de Opx preliminarmente ao Cpx, o que indica magma parental saturado em sílica. Portanto, o Complexo Acamadado do Vermelho, à semelhança de outras intrusões em áreas cratônicas no mundo e particularmente na região da Província Mineral de Carajás (e.g., Luanga, Lago Grande, Onça, etc), foi originado pela ascensão de magmas basálticos ricos em MgO através de falhamentos crustais que serviram de condutos, e que se tornaram progressivamente saturados em sílica através da assimilação de crosta continental préexistente. Isto é corroborado com os resultados de εNd, com valores altamente variáveis e predominantemente negativos: LZ (+0,1 to -4,7) e UZ (-7,3), confirmando reação e contaminação do magma máfico do Complexo Vermelho com rochas encaixantes crustais (e.g., granitóides, gnaisses/migmatitos do Complexo Xingú).

j) A análise sistemática de cristais de olivina em dunito e harzburgito da LZ, proveniente de amostras dos furos DDH-14 e DDH-25, apresentaram composições primitivas com conteúdo de Fo variando de $Fo_{88,0}$ a $Fo_{85,6}$ (DDH-14) e $Fo_{90,5}$ a $Fo_{86,6}$ (DDH-25); o conteúdo de Ni nestas olivinas apresenta correlação positiva com o conteúdo de Fo, variando de 2200-3950 ppm e de 1750-3400 ppm respectivamente para os furos DDH-14 e DDH-25. O conteúdo de Ni é menor no furo DDH-25 quando comparado com olivinas com o mesmo conteúdo de Fo. O conteúdo distinto de Ni obtido nas olivinas dos furos DDH-14 e DDH-25 sugere discreto empobrecimento de Ni nas olivinas das porções distais da LZ. Considerando que não foram identificadas mineralizações sulfetadas nos furos exploratórios na LZ, o empobrecimento de Ni pode estar relacionado à segregação subordinada de sulfetos em direção à borda SW da intrusão do Complexo do Vermelho. Portanto, o Complexo Vermelho tem uma evolução magmática marcada por sucessivas injeções de magma, indicando um sistema dinâmico e favorável para a geração de depósitos magmáticos.

Conclusões Capítulo 2: *Stratigraphy and petrology of the Touro Mafic-Ultramafic Complex, Carajás Province, Brazil*

As principais conclusões referentes ao estudo realizado no Complexo do Touro são abaixo apresentadas:

a) O Complexo Acamadado do Touro corresponde a uma intrusão máfico-ultramáfica localizada a cerca de 5 km ao sul da Serra de Carajás. Apresenta 4,2 km de comprimento por 1,2 km de largura média, e alinhamento segundo a direção ENE-WSW.

 b) Os trabalhos realizados demonstram que o Complexo do Touro corresponde a uma câmara magmática sem evidências de deformação e/ou metamorfismo, hospedada em granitóides sin-orogênicos indiferenciados (2,76-2,73 Ga).

c) A arquitetura da intrusão do Complexo do Touro abrange um conjunto de rochas máfico-ultramáficas acamadadas sub-horizontalizadas que foram subdividas em duas unidades estratigráficas distintas da base para o topo: Zona Ultramáfica (UZ) e Zona Máfica (MZ). A UZ é caracterizada por apresentar evolução petrológica com a seguinte sequência de fracionamento: Ol+Chr → Ol+Cpx+Chr, com dunitos e wehrlitos na base (olivina mais primitiva apresentando composição de $Fo_{76,3}$) até clinopiroxenitos na porção superior (clinopiroxênio mais fracionado exibindo $En_{49,5}$); no contato da UZ com o embasamento ocorre rocha gabroica fina a média que aflora de forma descontínua principalmente ao longo da borda sudeste da intrusão, sendo considerada aqui como uma zona de borda à semelhança de outras intrusões mundialmente estudadas. A MZ corresponde a rochas mais fracionadas com evolução petrológica exibindo as seguintes fases cumulus: Ol+Cpx+Pl → Cpx+Pl, com melagabros na base até gabros no topo (clinopiroxênio mais fracionado exibindo $En_{42,5}$).

d) Quando comparado com o Complexo Vermelho, o Complexo Acamadado do Touro apresenta sequência de cristalização distinta, caracterizada pela ausência de Opx como fase cumulus, indicando que o magma primário é subsaturado em sílica. Regionalmente ocorre situação similar descrita para os complexos da Serra da Onça (saturado em sílica) e Serra do Puma (subsaturado em sílica), localizados na porção oeste da PMC.

e) Além do Complexo Touro, regionalmente são observados que tanto os complexos que possuem características petrológicas de magma saturado em sílica como aqueles subsaturado em sílica apresentam similaridade nos dados dos elementos traços, sugerindo fontes mantélicas equivalentes. Para rochas gabroicas de complexos da PMC com estas características, os perfis de elementos traços resistentes à alteração normalizados ao manto primitivo apresentam fracionamento, demonstrado pelo enriquecimento de ETRL e Th, com pronunciadas anomalias negativas de Nb e Ta. Elementos traços e resultados isotópicos de Sm-Nd para os complexos da Serra do Onça (saturado em sílica) e Serra do Puma (subsaturado em sílica) sugerem que ambos são derivados de magmas primitivos similares, porém, que seguiram padrões diferentes de fracionamento durante a ascensão e posicionamento na crosta. Os dados obtidos neste trabalho para o Complexo Touro sugerem também esta premissa.

f) A sequencia basal de rochas ultramáficas sotopostas a rochas gabroicas horizontalizadas, juntamente com a zona de borda, indicam contato em alto ângulo de um possível conduto com as rochas encaixantes. Estas feições abrem potencial ainda inexplorado para pesquisa de depósitos sulfetados de Ni-Cu-EGP que podem estar hospedados na porção basal mais profunda e no conduto da câmara magmática do Complexo Touro.

Conclusões Capítulo 3: *Spinifex-textured komatiites in the south border of the Carajás ridge, Selva Greenstone Belt, Carajás Province, Brazil*

As principais conclusões associadas ao estudo dos komatiitos do *Greenstone Belt* Selva são abaixo elencadas:

a) Este trabalho apresenta as primeiras descrições de rochas komatiíticas com textura *spinifex* no interior da área do Subdomínio de Transição, Província Mineral de Carajás.

b) Os komatiitos com textura *spinifex* ocorrem no *Greenstone Belt* Selva, localizado a poucos quilômetros da borda sul da Serra de Carajás.

c) As rochas komatiíticas do *Greenstone Belt* Selva são parte de uma sequência de derrames estreitos, consistindo de um nível superior com textura *spinifex* e outro nível inferior com cumulado de olivina. Apesar das texturas *spinifex* estarem bem preservadas no campo, a mineralogia primária dos komatiitos encontra-se completamente substituída por minerais característicos da fácies xisto-verde de metamorfismo.

d) Os komatiitos com textura *spinifex* do *Greenstone Belt* Selva possuem conteúdo de MgO variando entre 22,8 and 26,9 % em peso, com valores elevados de MgO (até 40,6% em peso) em komatiitos com textura cumulática. Nos diagramas de dispersão do conteúdo de MgO, a maioria dos elementos maiores e traços apresenta correlação linear bem definida para as amostras dos komatiitos Selva, indicando significativo controle associado ao fracionamento ou acumulação de olivina. Os komatiitos dos *greenstones belts* Selva e Seringa (localizado no Domínio Rio Maria) são Al-não empobrecidos, com razões Al_2O_3/TiO_2 próximas de 20.

e) A composição química dos komatiitos do *greenstone belt* Selva indica que estes foram variavelmente afetados por alteração hidrotermal e/ou metamorfismo. Os resultados de CaO, Na_2O e ETR sugerem mobilidade para estes elementos, e seu conteúdo foi parcialmente afetado por alteração metassomática. O conteúdo de ETR em certas amostras de komatiito do Selva são particularmente elevados (até 40x os valores do manto primitivo), e o padrão de ETR varia de horizontalizado ($La/Yb_{PM} \sim 1$) a altamente enriquecido em ERTL (La/Yb_{PM} até ~ 10). A maioria das amostras mais enriquecidas em ETRL não apresenta anomalias positivas de Th, bem como anomalias negativas de Nb-Ta, sugerindo que contaminação crustal não representa o processo dominante para o enriquecimento de ETRL nos komatiitos do *greenstone belt* Selva. Estas características não usuais na composição química destas rochas indicam que a alteração hidrotermal destes komatiitos pode estar associada ao mesmo processo relacionado às mineralizações de Cu-Au na região de Carajás.

f) A identificação de rochas komatiíticas com textura *spinifex* próximas a Bacia de Carajás sugere a continuação dos *greenstone belts* 3,0-2,9 Ga do Domínio Rio Maria para o Subdomínio de Transição. Isto também indica que o Subdomínio de Transição passa a ter potencial para hospedar depósitos de Ni-Cu-EGP associados a rochas komatiiticas.

g) Os resultados obtidos indicam que os esforços para pesquisa voltados à descoberta de depósitos de Ni-Cu-EGP associados a rochas komatiiticas no interior do Subdomínio de Transição podem ser dificultados em função da baixa preservação das características magmáticas e composicionais destas rochas.

Conclusões Finais

As principais conclusões obtidas no presente estudo sobre os corpos máfico-ultramáficos presentes na região de Canaã dos Carajás, parte importante da PMC, são apresentadas a seguir.

a) A região de Canaã dos Carajás, situada dentro do Subdomínio de Transição, é composta por uma diversidade de corpos máfico-ultramáficos que apresentam evolução petrológica e cronológica distintas, e desta forma importantes para o conhecimento da evolução da geológica da PMC.

b) O Complexo Acamadado do Vermelho corresponde a uma câmara magmática sub-horizontalizada com evolução petrológica que confirma a ocorrência de dois pulsos distintos de magma primitivos (olivina mais primitiva apresentando composição de $Fo_{90,5}$). Apresenta assimilação crustal consistente com a cristalização de Opx preliminarmente ao Cpx, o que indica magma parental saturado em sílica. Portanto, o Complexo Acamadado do Vermelho, à semelhança de outras intrusões em áreas cratônicas no mundo e particularmente na região da Província Mineral de Carajás (e.g., Luanga, Lago Grande, Onça), foi originado pela ascensão de magmas basálticos ricos em MgO através de falhamentos crustais que serviram de condutos, e que se tornaram progressivamente saturados em sílica através da assimilação de crosta continental preexistente. Isto é corroborado com os resultados de εNd, com valores altamente variáveis e predominantemente negativos: LZ (+0,1 to -4,7) e UZ (-7,3). Confirmando reação e contaminação do magma máfico do Complexo Vermelho com rochas encaixantes crustais (e.g., granitóides, gnaisses/migmatitos do Complexo Xingu).

c) O Complexo Acamadado Touro corresponde a uma câmara magmática também sub-horizontalizada, com sequência de fracionamento que indica a formação a partir de um único

pulso magmático moderadamente primitivo (olivina mais primitiva apresentando composição de $Fo_{76,3}$) e sub-saturado em sílica. A sequência de cristalização, onde o Opx é ausente como fase cumulus, é distinta de outras intrusões acamadadas conhecidas na região da PMC. Resultados para elementos traços resistentes à alteração normalizados ao manto, confirmando reação com crosta mais antiga, entretanto, quando comparado com o Complexo Vermelho, exibem menor proporção de contaminação crustal do magma máfico do Complexo Touro com rochas encaixantes. Isto pode indicar que o magma primário do Complexo Touro é o mesmo das demais intrusões da PMC. Porém, a assimilação crustal, embora presente, pode não ter sido suficiente para induzir ao magma parental a cristalização de Opx cumulus.

d) Os complexos acamadados do Vermelho e Touro demonstram que este magmatismo máfico-ultramáfico neoarqueano não apresenta uma evolução petrológica singular na PMC. Esse plutonismo é também cronocorrelato ao extensivo vulcanismo basáltico da região de Carajás (e.g. 2759±2 Ma; 2760±11 Ma), relacionado ao evento que originou o Supergrupo Itacaiúnas. Portanto, o modelo tectônico de *rift* intraplaca em crosta continental antiga fornece uma explicação mais apropriada para assimilação crustal destes magmas primitivos derivados do manto e, por consequência, para a evolução da PMC.

e) Os komatiitos com textura *spinifex* descritos na área Selva fazem parte inequivocamente de uma sequência do tipo *greenstone belt*. Esta sequência está situada dentro do Subdomínio de Transição, a poucos quilômetros ao sul da borda da Serra dos Carajás. Apresenta direção NW-SE, sendo discordante do trend do Supergrupo Itacaiúnas (NE-SW). Apesar das texturas bem preservadas, a mineralogia primária encontra-se totalmente transformada para minerais do fácies metamórfico xisto-verde. À semelhança dos komatiitos da sequência Seringa (Domínio Rio Maria), ambos são Al-não empobrecidos, com razão Al_2O_3/TiO_2 próximo de 20. Análises químicas de rocha total demonstraram, com resultados anômalos para CaO, Na_2O e ETR, este com valores de até 40x os do manto primitivo, sugerem que os komatiitos do Selva foram também afetados pelo mesmo evento hidrotermal responsável pelas mineralizações tipo IOCG da PMC. Apesar da não obtenção de zircões nestas rochas, datações em rochas metavulcânicas ácidas próximas a mina do Sossego forneceram idades mesoarqueanas. Portanto, a identificação de rochas komatiíticas vizinhas a Bacia de Carajás demonstra a continuidade do Domínio Rio Maria (2,9-3,0 Ga) para o interior do Subdomínio de Transição.

f) Corpos intrusivos máfico-ultramáficos e derrames komatiíticos são mundialmente conhecidos como os típicos hospedeiros de mineralizações magmáticas sulfetadas de Ni-Cu-EGP (Naldrett, 2004, e referências nele contidas). O estudo focado na caracterização petrológica, química e estratigráfica das numerosas intrusões máfico-ultramáficas, bem como a presença confirmada de lavas komatiíticas na região do Subdomínio de Transição abrem, portanto, uma excelente janela de oportunidade para a prospecção de depósitos magmáticos de Ni-Cu-EGP neste setor da PMC.